APPLICATION OF KEY-OFF COOLING AND PARTIAL CHARGING IN PLUG-IN ELECTRIC VEHICLES

Sina Shojaei

A thesis submitted in fulfilment of the requirements for the degree of Doctor of Philosophy in Engineering

University of Warwick

September 2018

Abstract

Ambient conditions can have a significant impact on the temperature of the battery of electrified vehicles. In hot geographical locations, high battery temperatures can be experienced when the vehicle is parked and cooling is absent. This has three negative implications for the vehicle performance attributes: first, it accelerates the ageing mechanisms of the battery and leads to short battery lifetime; second, it necessitates inhibition of the battery power as a safety measure and leads to low traction in electric vehicles or poor fuel economy in hybrid electric vehicles; third, it increases the battery cooling load which reduces the cooling power available to the cabin and leads to poor passenger thermal comfort.

Eliminating the high battery temperatures that result from exposure to hot ambient conditions requires a comprehensive battery cooling strategy; one in which the battery can be cooled when the vehicle is driven or when parked. In the current state of the art battery cooling strategy, cooling is only available when the vehicle is driven and when it is plugged in. Practical concerns such as the associated energy consumption have discouraged battery cooling when the vehicle is parked and not plugged in (key-off). Since passenger vehicles typically experience long key-off intervals, the existing battery cooling strategies are insufficient in hot ambient conditions.

The main contribution of this research is proposing the application of key-off battery cooling and developing an underpinning methodology for evaluating the benefits of key-off cooling in a plug-in hybrid electric vehicle. Key-off cooling is defined as an optimal control problem and solved in view of the 24-hour duty cycle of the vehicle evaluated by a representative model. This new methodology enables applying key-off cooling based on the requirements of one or more of the attributes of battery lifetime, thermal comfort and fuel economy, enabling consideration of these attributes in applying battery cooling in an optimal manner. The results show that while the effectiveness of key-off cooling depends on the duty cycle of the vehicle, it generally improves the battery lifetime and benefits the thermal comfort and the fuel economy attributes.

To enable further improvements in the battery lifetime, integration of key-off cooling and partial charging of the battery is proposed, advancing the existing state of the art where partial charging is optimised independently of cooling. A new methodology is developed that determines the combination of the battery charge and key-off cooling control strategy that maximises the battery lifetime, while also considering the thermal comfort and the fuel economy attributes.

Contents

LIST OF FIGURES

LIST OF TABLES

NOMENCLATURE

Notation	Description	Unit
F_T	traction force	N
F_A	aerodynamic resistance (vehicle)	N
F_{RR}	rolling resistance (tyres)	N
M	vehicle mass	kg
v	vehicle speed	$\frac{m}{s}$
C_D	vehicle drag coefficient	C_D
A	vehicle frontal area	m^2
ρ	density (air)	$\frac{kg}{m^3}$
τ_w	wheel torque	Nm
τ_{em}	electric machine torque	Nm
$\tau_{em,max}$	maximum electric machine torque (motoring)	Nm
τ_{eng}	engine torque	Nm
$\tau_{eng,max}$	maximum engine torque (wide-open throttle)	Nm
τ_{loss}	torque loss (gears)	Nm
τ_d	torque demand at gearbox input	Nm
ω_w	wheel speed	$\frac{rad}{s}$
ω_{em}	electric machine speed	rpm
ω_{eng}	engine speed	rpm
I_w	wheel assembly rotational inertia	$kg.m^2$
J_g	gear inertia	$kg.m^2$
J_{em}	electric machine inertia	$kg.m^2$
ϕ	accelerator pedal position	%

Nomenclature *(continued)*

Notation	Description	Unit
$P_{em,mech}$	electric machine mechanical power	W
P_{em}	electric machine electric power	W
$P_{comp,mech}$	AC compressor mechanical power	W
P_{comp}	AC compressor electrical power	W
V	battery voltage (cell)	V
V_{batt}	battery voltage (pack)	V
V_{oc}	open-circuit voltage (cell)	V
i	battery current (cell)	A
i_{batt}	battery current (pack)	A
R_0	battery internal resistance (cell)	Ω
P_{cell}	battery power (cell)	W
P_{batt}	battery power (pack)	W
T_{cabin}	average cabin air temperature	°C
$T_{cabin,max}$	maximum cabin temperature	°C
T_{vent}	cabin vent temperature	°C
T_{batt}	battery temperature (bulk)	°C
$\bar{T}_{batt}$	average battery temperature	°C
$T_{batt,max}$	maximum battery temperature	°C
$\dot{Q}_{amb}$	heat transfer between battery and ambient	W
$\dot{Q}_{clnt}$	heat transfer between battery and coolant	W
$\dot{Q}_{cabin}$	heat transfer between battery and cabin	W
$\dot{Q}_{gen}$	internal heat generation of battery (pack)	W
$\mathcal{C}_{batt}$	battery heat capacity	$\frac{kJ}{K}$
$c_{coolant}$	coolant specific heat capacity	$\frac{kJ}{kgK}$
R_{amb}	thermal resistance between battery and ambient	$\frac{K}{W}$
$R_{coolant}$	thermal resistance between battery and coolant	$\frac{K}{W}$
$R_{cabin,int}$	thermal resistance between battery and cabin interior	$\frac{K}{W}$

Nomenclature *(continued)*

Notation	Description	Unit
$R_{cabin,wall}$	thermal resistance between battery and cabin wall	$\frac{K}{W}$
$\bar{h}_{aw}$	average heat transfer coefficient air side of evaporator/condenser	$\frac{W}{m^2K}$
$\bar{h}_{wr}$	average heat transfer coefficient refrigerant side of evaporator/condenser	$\frac{W}{m^2K}$
A_{aw}	heat transfer area on air side of evaporator/condenser	m^2
A_{rw}	heat transfer area on refrigerant side of heat evaporator/condenser	m^2
$\dot{Q}_{wa}$	heat transfer on air side of heat evaporator/condenser	W
$\dot{Q}_{wr}$	heat transfer on air side of heat evaporator/condenser	W
Nu	Nusselt number	–
Re	Reynolds number	–
Pr	Prandtl number	–
SH	refrigerant superheat	K
SC	refrigerant subcool	K
$\dot{m}_{ref}$	refrigerant flow rate	$\frac{kg}{s}$
p_{ref}	refrigerant pressure	Pa
T_{ref}	refrigerant temperature	K
$hr.$	relative humidity (air)	%
η_{vol}	AC compressor volumetric efficiency	–
η_{isen}	AC compressor isentropic efficiency	–
$\boldsymbol{\omega_{comp}}$	AC compressor speed	rpm or Hz
ζ	state of charge (Sock)	%
ζ_{max}	maximum Sock (level of battery charge)	%
ζ^*_{max}	optimum maximum Sock (optimum level of charge)	%
$\bar{\zeta}$	average of SoC	%
n	number of charge-discharge cycles of battery	–
ΔC_{stor}	storage capacity loss	%
ΔC_{cyc}	cycling capacity loss	%
ΔC	total capacity loss	%
v_{fuel}	fuel consumption (fuel consumed)	L
$I_{discomf}$	discomfort index	–
$Trp1$	Trip 1 (phase of the duty cycle)	–

Nomenclature *(continued)*

Notation	Description	Unit
$Dprk$	Day Park (phase of the duty cycle)	–
$Trp2$	Trip 2 (phase of the duty cycle)	–
$Nprk$	Night Park (phase of the duty cycle)	–
$[\Delta C]_{Trp1}$	total capacity loss in Trip 1	%
$[\Delta C]_{Dprk}$	total capacity loss in Day Park	%
$[\Delta C]_{Trp2}$	total capacity loss in Trip 2	%
$[\Delta C]_{Nprk}$	total capacity loss in Night Park	%
$[v_{fuel}]_{Trp1}$	consumed fuel in Trip 1	L
$[v_{fuel}]_{Trp2}$	consumed fuel in Trip 2	L
t_{Trp1}	time at end of Trip 1	s
t_{Dprk}	time at end of Day Park	s
t_{Trp2}	time at end of Trip 2	s
t_{Nprk}	time at end of Night Park	s
τ_{eng}	engine torque	Nm
x_b	state (vector) of the battery: $[T_{batt}, \zeta]'$	–
x_v	state (vector) of the vehicle: $[T_{cabin}, T_{batt}, \zeta]'$	–
u	*key-off cooling flag trajectory*	–
u^*	optimum trajectory of key-off cooling flag	–
J	total cost minimized in optimal control problems	–
h	terminal cost (used in the definition of cost functions)	–
λ	vector of weights (used in the definition of cost functions)	–

LIST OF ACRONYMS

Acronym	Description
xEV	electrified vehicle
BEV	battery electric vehicle
PHEV	plug-in hybrid electric vehicle
PPHEV	parallel plug-in hybrid electric vehicle
AER	all-electric drive range
AC	air conditioning (system)
SoC	state of charge
DoD	depth of discharge
CD	charge depleting (mode of powertrain operation)
CS	charge sustaining (mode of powertrain operation)
Enol	end of life (of the battery)
DP	Dynamic Programming method

AKNOWLEDGEMENTS

This research would not have been possible without the support and encouragement of Andrew and James. Their experience and insight paved the way when there was seemingly no hope. Andrew spent numerous hours on reviewing and proofreading this thesis and my papers. I am thankful to them both.

I am grateful to Professor Paul Jennings who gave me the opportunity to work within his group, persuaded me to register for this degree, and supported me when writing this thesis affected my work.

This research benefited from the support and the sound technical knowledge of Dr Simon Robinson of Jaguar Land Rover. Simon also facilitated my access to the data that enabled this research.

My journey as a PhD student started in 2011 at Aston University, with the support of Dr Dani Strickland. Although I moved to Warwick soon afterwards, Dani had an important role in shaping my thought process, and I am grateful to her.

I struggle to even begin to thank my parents. When you read this, know that I am sorry for not being with you as much as I liked to in the last five years. That changes with the full stop at the end of this sentence**.**

PEER-REVIEWED PUBLICATIONS

S. Shojaei, S. Robinson, C. Chatham, A. McGordon, J. Marco, Modelling the Electric Air Conditioning System in a Commercially Available Vehicle for Energy Management Optimisation, in: SAE Tech. Pap., 2015. doi:10.4271/2015-01-0331.

S. Shojaei, S. Robinson, A. McGordon, J. Marco, Passengers vs. Battery: Calculation of Cooling Requirements in a PHEV, in: SAE Tech. Pap., 2016. doi:10.4271/2016-01-0241.

S. Shojaei, A. McGordon, S. Robinson, J. Marco, P. Jennings, Developing A Model for Analysis of the Cooling Loads of a Hybrid Electric Vehicle by Using Co-Simulation of Verified Submodels, Proc. Inst. Mech. Eng. Part D J. Automob. Eng. (2017) 954407017707099. doi:10.1177/0954407017707099.

S. Shojaei, A. McGordon, S. Robinson, J. Marco, Improving the Performance Attributes of Plug-in Hybrid Electric Vehicles in Hot Climates through Key-Off Battery Cooling, Energies. 10 (2017) 2058. doi:10.3390/en10122058.

DECLARATION

The research presented within this thesis has been undertaken by me, except where otherwise stated. No part of this thesis has been submitted in support of another degree. The thesis is presented in accordance with the regulations of Warwick University.

Sina Shojaei
September 2018

Dedicated to family

To my parents, Nasrin and Behrouz, for their endless love;

To my sister, Saman, for her kindness and all the laughter we share;

To my brother, Siamak, my partner in crime.

This page is intentionally left blank

CHAPTER 1 INTRODUCTION

1.1 Motivation

With mounting evidence that global warming is posing a fundamental threat to humankind and other species in the near future, stringent reductions in greenhouse gas emissions is indispensable. CO_2, which is the most abundant long-lived greenhouse gas, is a combustion product of fossil fuels [1]. Therefore, to reverse global warming, the dependency of different industries and human activities on fossil fuels should be reduced [2]. Finding economically viable and environmentally friendly alternatives for fossil fuels has been a research priority for over three decades [3].

The transportation sector is responsible for over 14% of the global greenhouse gas (GHG) emissions, a share that is projected to increase to 50% by 2030 [4]. In 2016, the transportation sector was responsible for over 25% of the total GHG emissions in the European Union (EU) countries, over 70% of which was due to road transport [5]. Electrification of road vehicles, combined with de-carbonization of power plants, is most likely the only way for eliminating the environmental impact of road transport [6]. As a result, battery electric vehicles (BEVs) have attracted significant attention over the last decade. Currently, the transition from conventional vehicles (CVs) to BEVs is slowed by the immaturity of the battery technology, which has significant shortcomings in delivering the following three essential requirements [7,8]:

1. sufficient energy density in light, and inexpensive packs;
2. fast charge time, comparable to the refueling of CVs;
3. sufficient lifetime under real-life usage conditions.

Research has shown that the above shortcomings lead to range anxiety which is the lack of confidence on the side of the potential users in sustained practicality of

BEVs [7]. Scarcity of charging infrastructure only adds to the problem [9]. Range anxiety limits the market penetration rate of BEVs [9,10], therefore, advanced battery technologies are a major research priority in road transport. As the battery technology continues its development, plug-in hybrid electric vehicles (PHEVs) which combine the characteristics of BEVs and CVs are deemed as a step in the right direction towards cleaner and greener transportation [11]. BEVs and PHEVs, are referred to as plug-in electric vehicles or PEVs, in that plugging these vehicles to the grid is the main mechanism of charging their battery, distinguishing them from other types of electrified vehicles (xEVs).

Stringent legislation has had a significant role in encouraging the automotive manufacturers to invest in the development of PEVs. The EU standards require the fleet average emissions of 95 grams of CO_2 per kilometre for all new cars by 2021 [12]. Similar targets are currently in place in the US under the corporate average fuel economy (CAFE) standard [13]. As a result, while only 14 PEV models were available from 8 major automotive manufacturers in 2013, 59 PEV models were available in 2017, as all major automotive manufacturers offer PEVs as part of their model range [14]. Electrification is already showing tangible benefits; it has been estimated that in 2012, light duty PEVs in the US saved over 6 million gallons of fuel [15]. The global sales of PEVs are rapidly growing, having increased by 80% in 2015 compared to 2014 [16,17]. In the US, the annual sales of PEVs are expected to exceed 1.2 million vehicles by 2025, reaching more than 7 per cent of the annual vehicle sales in that country [10], while in the UK, all new cars are required to have EV operating mode by 2040 [18].

Ageing of battery cells, defined as the irreversible reduction of their energy storage capacity and power [20,21], is a major challenge for electrification of road vehicles [22]. Lithium-ion cells, which are believed to be the most promising choice for automotive applications [23,24] have ageing mechanisms that are sensitive to real world usage conditions [25]. Cycling ageing (ageing due to the conditions of charge-discharge cycles) accelerates at high temperature, as well as with high depth of discharge, and high charge-discharge rates [26,27]. Storage ageing (ageing due to storage conditions) increases with elevated temperature [20,28] and

state of charge (SoC) [29,30]. Heat transfer from the ambient, the passenger cabin and other adjacent components, in addition to internal heat generation, contributes to high battery temperature [31] that can reach as high as 65°C [32]. It is generally agreed that some form of battery cooling system is necessary for modern BEVs and PHEVs [33]. Battery cooling is traditionally a 'key-on' function, that is, it is only applied when the vehicle is switched on [34]. However, in hot geographical locations, the heat gain from the ambient environment can heat the battery to extreme temperatures [35,36]; a phenomenon that cannot be prevented with key-on cooling only. Since passenger vehicles are typically parked for most of their lifetime, markedly short battery lifetime has been observed in hot geographical locations [32,35].

The observation of short battery lifetime in hot geographical locations indicates the need for extending battery cooling beyond a key-on function by enabling battery cooling even when the vehicle is parked. When the vehicle is plugged in, the 'free' energy of the charger can be used to cool the battery, a strategy that is often referred to as 'plugged-in cooling' or 'stand-by cooling' [32,35,37–41]. Alternatively, the energy of the battery can be used for cooling in the more common scenario that the parked vehicle is not plugged in ('key-off cooling'). However, two critical concerns have discouraged the consideration of key-off cooling in the past. First, using the energy of the battery for cooling reduces the all-electric range (AER) of the vehicle. Second, discharging the battery for key-off cooling increases cycling ageing and can adversely affect the battery lifetime. Therefore, further research is necessary to exploit the potential benefits of key-off cooling while avoiding the above concerns.

Reducing the average SoC of the battery through optimized partial charging is another method that has been used to improve the battery lifetime [42–45]. The method typically involves using *a priori* knowledge of the energy requirement of the vehicle and charging the battery only as much as the vehicle will consume until it is plugged-in next time, eliminating the excess charge. Partial charging has been shown to be especially effective if the vehicle is plugged-in multiple times per day

so the battery can be charged just as much as needed for following trip [44]. In the more common scenario that the vehicle is plugged-in once per day, the battery should be charged enough to support an extended operation, which leaves a limited excess battery charge. The previous studies in this area ignored the benefit of lower SoC relative to lower temperature, and considered controlling the level of charge independent of controlling cooling, even when plugged-in cooling was available. When key-off cooling is to be enabled, understanding the benefit of maintaining a low SoC through partial charging relative to the benefits of key-off cooling (maintaining a low temperature) becomes critical due to two considerations. First, partial charging affects the battery charge that can be allocated to key-off cooling. Second, in the presence of uncertainty in the timing of trips, key-off cooling generally poses a lower risk to the vehicle range compared to partial charging. This is because an early trip start will reduce the need for key-off cooling but closes the window of opportunity for sufficiently charging the battery for the following trip. Further research in this area is required to better establish the relative benefit of key-off cooling and partial charging.

1.2 Contribution to knowledge

This research, for the first time, studies the application of key-off cooling as well as its integration with partial charging. Specifically, the following research question is investigated:

'How can the ultimate benefits of key-off cooling and partial charging be evaluated for a PEV operating in hot climate conditions?'

The research offers the following key contributions to knowledge:

1. Developing a methodology for establishing the ultimate benefits of key-off battery cooling;

2. Considering the implications of battery cooling strategy for passenger thermal comfort

3. Considering the trade-off between fuel economy, battery lifetime, and passenger thermal comfort in controlling battery cooling

4. Integrating partial charging and key-off cooling of battery to improve battery lifetime

5. Developing a methodology for optimising the combination of level of charge and key-off cooling that benefits the fuel economy and passenger thermal comfort while maximising the battery lifetime

6. Elevating battery thermal management (battery cooling) to a supervisory-level function

This research was carried out as part of the energy efficiency workstream of the High Value Manufacturing (HVM) Catapult project (2012- 2017) in partnership with Jaguar Land Rover. The scope and the methodology of the research were defined in alignment with HVM Catapult objectives as well as the strategic priorities of the industry partner.

1.3 Organisation of the thesis

The thesis is organised as follows:

Chapter 2 provides the necessary background information for the remainder of this thesis, including an overview of the design and the energy management requirements in PHEVs, a brief introduction to traction battery technologies, as well as a short review on the design of automotive air conditioning systems.

Chapter 3 reviews the previous research on the impact of hot climate conditions on PEVs, and possible methods for mitigating this impact. This review highlights the gap in the current knowledge of key-off cooling and partial charging of PEV batteries, raising the research question that is addressed in this thesis.

Chapter 4 presents the methodology chosen to investigate the research question, including the key assumptions about the vehicle in addition to explaining the simulation and optimisation techniques used in subsequent analyses.

Chapter 5 explains the process of development and verification of a set of vehicle subsystem models which are used in Chapter 6 to develop a vehicle model for the purpose of this research.

Chapter 6 explains the process of developing a vehicle model from a set of high level assumptions and the subsystems models developed in Chapter 5. The vehicle model is simulated over a set of standard drive cycles and its basic operation metrics are discussed.

Chapter 7 discusses the result of simulating the vehicle model over a set of 24-hour duty cycles that include mild and hot climate conditions. The variability of some key performance attributes of the vehicle with ambient conditions is determined from the simulation results. Analysing the simulation results indicates the potential benefits of key-off (battery) cooling and partial charging.

Chapter 8 focuses on defining key-off cooling as an optimal control problem and describing the selected solution approach. The chapter also provides some initial analysis of the factors affecting the solution of this control problem.

Chapter 9 expands the key-off cooling control problem defined in chapter 8 by proposing a methodology for solving the problem in view of the 24-hour vehicle duty cycle. The solution of this problem is discussed for different duty cycles considering different scenarios to evaluate the implications of key-off cooling for different performance attributes of the vehicle.

Chapter 10 proposes a methodology for integrated optimisation of partial charging and key-off cooling. The benefits of this methodology are discussed for two vehicle duty cycles, while various scenarios are considered to analyse possible implications for different performance attributes of the vehicle.

Chapter 11 discusses the generality of the proposed methodology including its applicability to alternative assumptions about the vehicle type and usage scenarios.

Chapter 12 summarises the key conclusions of the research.

CHAPTER 2 BACKGROUND

Introduction

This chapter provides the necessary background information for this research. In Section 2.1, the high-level considerations related to the design and operation of PHEVs are reviewed. In Section 2.2 the design requirements of the battery of PHEVs and other types of electrified vehicles are reviewed. In addition, the operational principles of the Lithium-ion battery technology including the mechanisms of ageing in these batteries and their cooling requirements are discussed. In Section 2.3, the key aspects of the design and operation of typical automotive air conditioning systems are explained.

2.1 Design considerations in PHEVs

Electrified vehicles or xEVs are the class of vehicles in which some part of the traction torque is delivered by an electric machine in conversion of electrical energy from an on-board source to mechanical energy [46,47]. xEVs therefore differ from CVs in which the entirety of the traction torque is the product of combustion of fuel in an engine [48,49]. The source of the electrical energy in xEVs is typically a battery, although capacitors and super-capacitors can be also used [50].

In addition to having one or more electric machines, xEVs can have a full-size engine, or the engine can be downsized or removed[1], depending on the emphasis on electric traction, also referred to as the degree of electrification [51]. Accordingly, four types of xEVs can be identified[2] [47,52]

[1] A hydrogen fuel cell can be potentially used instead of the engine, forming a fuel cell electric vehicle (FCEV), or it can be used alongside a battery to form a fuel cell hybrid electric vehicle FCHEV [49]. However, the fuel cell technology is currently under-developed [8].

[2] CVs with start-stop technology are occasionally referred to as micro-hybrids and included in this category, especially when the start-stop technology enables regeneration of the engine braking force [270].

- mild hybrid electric vehicles (MHEVs)
- hybrid electric vehicles (HEVs),
- plug-in hybrid electric vehicles (PHEVs),
- battery electric vehicles (BEVs)

In MHEVs and HEVs[1], the battery charge is mainly replenished from the power of the engine (engine charging) [50,53], while plugging the vehicle to the grid is the main charging mechanism in PHEVs and BEVs [54], although PHEVs also benefit from engine charging [53]. The plug-in feature enables application of larger batteries and more powerful electric machines in PHEVs, making the battery the primary energy source [55]. From this point of view, PHEVs and BEVs are similar, and are collectively referred to as plug-in electric vehicles (PEVs).

While BEVs are seen as the long-term focus of the automotive industry, most technology road maps and policy trends indicate that PHEVs will dominate the xEV market for at least the next decade [56–58]. PHEVs typically have one or more electric machines and an engine, each of which can operate independently. From this point of view, PHEVs are similar to HEVs. Based on the existence of a mechanical link between the wheels and the engine or the electric machine, the powertrain architecture in PHEVs (and HEVs) can be categorised as series, parallel, combined series-parallel, and through-the-road [47,59]. Figure 2-1 shows the parallel architecture.

[1] The main difference between MHEVs and HEVs is that the electic machine of MHEVs cannot propel the vehice independently.

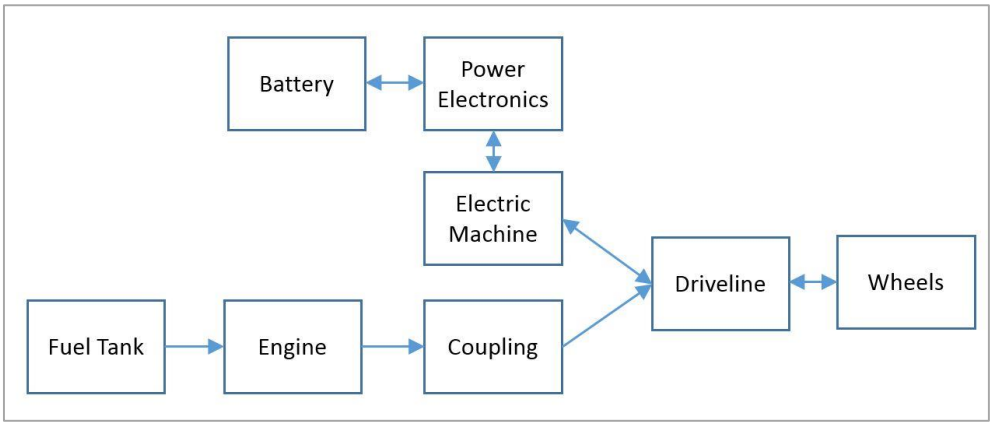

Figure 2-1. Parallel hybrid powertrain architecture

The main feature of parallel architecture is that both the engine and the electric machine can provide traction torque to the wheels. Some form of coupling, such as a friction clutch, creates a mechanical connection from the driveline to the engine and the electric machine. This architecture can deliver the following 5 operating modes [52,60,61]:

1. Electric drive mode (EV mode): the vehicle is driven by the electric machine, while the engine is off and de-coupled from the driveline[1]. This mode is often referred to as "zero-emission" drive

2. Motor assist mode: (hybrid mode): The engine acts as the primary source of traction torque while it is assisted by the electric machine to meet high torque demands

3. Engine charge mode: Electricity is generated from the power of the engine to charge the battery. If the engine can provide traction torque, it drives the vehicle.

4. Conventional drive mode: the vehicle is driven by the engine, like a conventional vehicle, and the electric machine is not used.

[1] 'Driveline' refers to the shafts and gearings that transfer torque from the propeller (engine or motor) to the wheels.

5. Electric braking mode: The engine is decoupled from the drive line while the electric machine provides a resistive torque to the driveline to decelerate the vehicle, subsequently regenerating the kinetic energy of the vehicle in form of electricity which will be stored in the battery. Therefore, electric braking is often referred to as ‘regenerative braking’. Electric braking is often blended with mechanical (friction) braking, thus the term ‘hybrid braking’ mode is also common.

2.1.1 Energy management in PHEVs

The common strategy for controlling the powertrain of PHEVs is the charge-depleting-charge-sustaining (CD-CS) strategy [62–64]. In this strategy, the vehicle is initially propelled by the electric machine, depleting a considerable part of the battery charge. This is referred to as the charge depleting (CD) mode. Once the battery SoC drops below a certain threshold, the vehicle switches to the charge sustaining (CS) mode, in which both the engine and the electric machine are used to propel the vehicle, maintaining a near-constant SoC. Figure 2-2 shows the idealised SoC profile in the CD-CS strategy. The SoC window of the CD mode is determined based on the durability of the battery, and the trade-off between fuel economy, weight, cost, and lifetime [65,66]. The advantage of the CD-CS strategy is that it is simple to realise in real-time, however, it does not lead to maximum fuel economy [62,67]. The ideal alternative to this strategy is to blend the use of the engine and the electric machine throughout the travelled distance so that each one can be used at their respective highest efficiency points. However, this is not possible without advanced knowledge of the drive cycle [68,69].

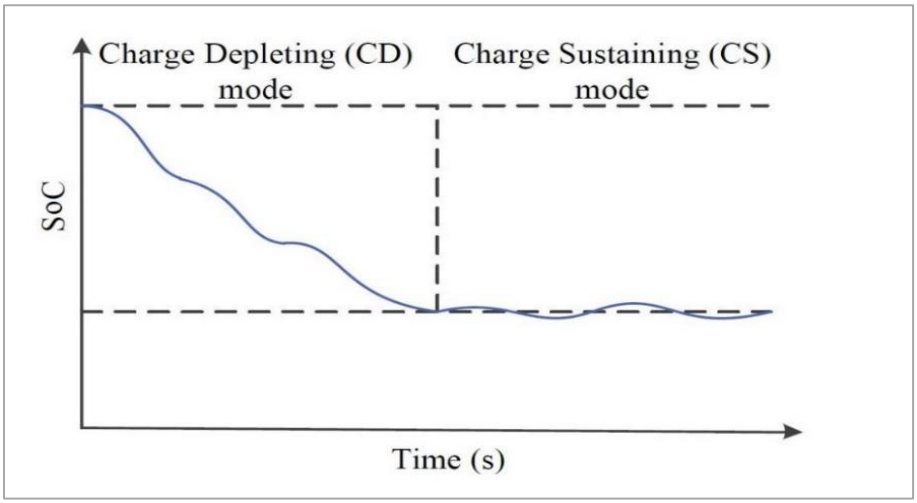

Figure 2-2. Re-created from [63] : Typical PHEV energy management modes

It is important to note that the CD and CS energy management modes encompass the operating modes of the powertrain described previously. For example, in a plug-in parallel hybrid electric vehicle (PPHEV), electric drive, regenerative braking, and mechanical braking will all likely occur during the CD mode. In addition, if the power demand of the drive cycle exceeds the power (torque) capability of the electric machine while the vehicle is in CD mode, the engine will start (motor assist). However, once such periods of high power demand have passed, the CD mode will resume, assuming the battery SoC is still in the CD window [62]. Figure 2-3 illustrates how different powertrain and energy management modes overlap.

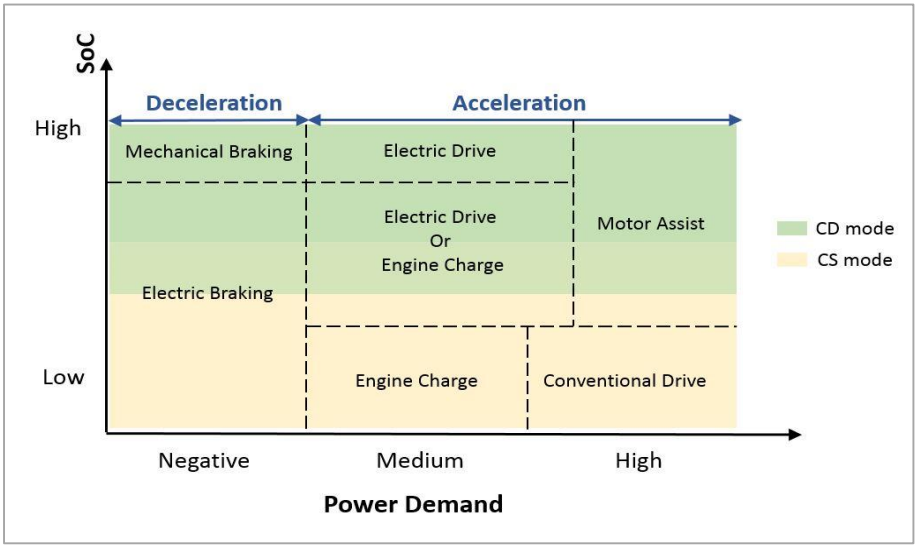

Figure 2-3. Overlap of energy management and powertrain operating modes in a PPHEV

An important consideration in the design of a PHEV is that the vehicle is expected to have better fuel economy and less environmental impact compared to HEVs while demonstrating similar attributes of maximum acceleration and speed both in the CS and the CS operating modes [55,70]. This means that PHEVs need relatively large batteries and powerful electric machines that allow extended CD operation [66]. It also means that a PPHEV will require a full size engine that can propel the vehicle normally as it charges the battery during the CS operation [71]. This can be inferred from Table 2-1 which compares the specifications of the battery pack and the engine of some commercially available xEVs.

Table 2-1 Battery and engine speecifications in some commercially available xEVs based on publically available informtaion from model year 2016

Type	Make and Model	Battery Specifications			Engine Power
		Energy [kWh]	Voltage [V]	Power [kW]	
MHEV	Infiniti QX60	0.6	144	15	2.5 L 170 *kW*
HEV	BWM Series 5	1.4	317	40	3.0 L 253 *kW*
	Range Rover	1.6	270	35	3.0 L 192 *kW*
PHEV	Chevrolet Volt	16.7	370	110	1.5 L 62 *kW*
	Mercedes s-500	8.8	400	85	3.0 L 244 *kW*
BEV	Nissan Leaf	24	360	80	n/a*
	Chevrolet Bolt	60	350	160	n/a*
	Tesla Model S	85	355	310	n/a*

* not applicable

Another implication of the above requirement is that subsystems, such as the air conditioning (AC) subsystem, which are typically powered by the engine in CVs and HEVs, should be electrified in PHEVs to minimise the operation of the engine [72].

2.1.2 Energy efficiency of PHEVs

The energy efficiency of a vehicle is defined as the amount of energy required to drive the vehicle over a certain distance. It depends on factors such as the pattern of driving, the ambient temperature, and the source of energy [73,74]. Regulatory authorities such as the European Commission (EC) or the U.S. Environmental Protection Agency (EPA) have issued standard procedures for measuring the energy efficiency (and emissions) of different vehicles [75,76]. Typically, the vehicle is placed in a test cell at controlled temperature. A chassis dynamometer is then used to mimic driving over pre-defined speed profiles, known as drive cycles.

In current EC test procedure, the measurements are based on driving the vehicle over the New European Drive Cycle (NEDC) at 25°C [76]. The current EPA procedure (the supplementary federal test procedure or SFTP) [77] includes five drive cycles : the FTP-75, the HWFET, the US06, the SC03, and the UDDS. The first three drive cycles are run at 75°F (24°C). The SC03 and the UDDS drive cycle are used to measure the effect of operating the AC and heating systems on energy efficiency, and are carried out at 95°F (35°C) and 20°F (-7°C), respectively. Energy efficiency (and emissions) are measured in these five tests for city and highway parts of the drive cycles. The measurements are weighted and reported separately or as a combined number according to established EPA procedures [77,78].

In CVs and non-plug-in xEVs that have fuel as their single source of energy, the test process is straightforward. In these vehicles, energy efficiency is commonly quoted as miles travelled per gallon of fuel (mpg), or as Litres of fuel required to travel 100 kilometres [76]. The existence of two energy sources in a PHEV necessitates the process outlined below:

- The test is first carried out with a fully charged battery, so the vehicle operates in CD mode during the test. The test continues until the end of the drive cycle, or until the battery is discharged and the engine is turned on. Following the test,

the battery is charged and the energy required to charge the battery is divided by the travelled distance to calculate the CD energy efficiency of the vehicle for the assumed drive cycle (and ambient conditions). The distance travelled in CD mode is the AER of the vehicle for the assumed drive cycle (and ambient conditions) [79].

- The test is then repeated with a fully discharged battery. The fuel consumption of the vehicle is calculated in a similar manner to non-plug-in xEVs. This gives the CS fuel efficiency (economy) of the vehicle.

In the EPA test procedure, the CD energy efficiency and CS fuel economy are calculated for all drive cycles and quoted as an average value. Furthermore, to enable comparison with other vehicle types, an overall fuel economy figure is calculated by converting the electric energy consumption in CD mode to equivalent fuel consumption and calculating the CD equivalent fuel economy [80]. Then, a weighted average formula is applied to the CD and CS fuel economy [80].

2.1.3 Charge patterns

Design standards of PEVs charging stations are still evolving. Currently, three types of charging stations are identified based on the power that they draw from the grid, as summarised in Table 2-2.

Table 2-2. Charger specifications [15,50,81,82]

Type	Voltage [V]	Current rating [A]
Level 1	120	12-15
Level 2	240	12-80
Level 3	400-450	50-220

A comprehensive study carried out by the Idaho National Laboratory in 2015 [83] provides a clear insight into the charging patterns of plug-in xEVs. In this research, 2400 Nissan Leaf BEVs and 1800 Chevrolet Volt PHEVs were monitored as they were used across the U.S. All vehicles were equipped with level 1 charger cables while level 2 chargers were installed at home for all users. In addition, level 2 and level 3 chargers were installed in a variety of locations, including workplaces, stores, restaurants, gas stations, etc. to allow observation of charging patterns. The following key observations were reported:

1. Most vehicles are charged at home. 84% of all Leaf charges and 87% of all Volt charges were at home. Also, more than half of all vehicles were charged at home in 95% of the time. Of all the vehicles, 13% were never charged away from home, while 69% of them were charged away from home up to 30% of the time.

2. On average, the Leafs were charged 1.1 times per day. The Volts were charged 1.5 times per day, in line with their lower AER.

3. Most Leafs were plugged-in with significant charge left in the battery. The Volts were almost fully discharged before being plugged-in, in line with the option to use the engine.

4. On a working day, 57% of the Volts and 65% of the Leafs were charged once, at home.

5. Level 1 charges were preferred. Among the vehicles charged away from home, 63% only used level 1 chargers, while 36% used level 1 or level 2 chargers. Less than 1% of the vehicles used level 3 chargers.

Apart from the charger type, there are two strategies for charging a PEV, 'opportunity charging' and 'timed charging' [9,43,58]. In opportunity charging, the vehicle is plugged in and charging is started whenever a charger is available. In timed charging, the vehicle is plugged-in at a certain time, or electronic control is used schedule charging. These strategies have different practical implications for the vehicle and the users. With opportunity charging, the vehicle will be ready to drive (in EV mode) more frequently [43]. On the other hand, timed charging enables making use of low cost electricity in time-regulated systems and avoiding higher load on the grid at peak demand hours [84]. More importantly, charging can be scheduled to start just in time for the trips, so that the battery can remain at a low SoC for an extended period of time. This is referred to as 'just-in-time charging' and has been shown to enable significant improvements in the battery lifetime compared to opportunity charging [85].

2.2 Battery technologies

In this section, the key aspects of the xEV battery technologies pertinent to the scope of this research are reviewed, focusing on PHEVs. In Section 2.2.1, the high-level battery design requirements and the importance of the Lithium-ion (Li-ion) technology are discussed. In Section 2.2.2, the basic technical terms related to the operation of typical batteries are defined. In Section 2.2.3, the ageing phenomenon in Li-ion batteries is explained while Section 2.2.3 explains the cooling requirements of xEV batteries.

2.2.1 High-level design requirements

The most significant barrier to the commercialization of PEVs is the battery, due to its high cost, low durability, large volume, slow charging rate, and the associated safety concerns [86,87]. In 2008, a consortium led by the U.S. Department of Energy established the requirements for commercialization of PHEVs and identified a set of design targets for a PHEV battery for model-year 2016 [66]. These targets are listed in Table 2-3. Recent analyses show that battery technologies have developed at a fast rate, leading to a rapid decrease in the unit cost of PEVs batteries [58,88]. In other areas such as durability, the battery technology currently underperforms [28,89]. The economic success of PEVs against CVs necessitates more aggressive development of the technology [22], especially considering the recent fall in the global oil price [90] and the continued improvements in the ICE technologies [91,92].

Table 2-3. Battery pack level requirement for a mid-size cross-over PHEV [4]

Specification	Target
Reference equivalent electric range	40 miles
Available Energy for CD mode	11.6 kWh *
Available Energy for CS mode	0.3 kWh
lifetime (at 35°C)	15 years
cycle life (one full cycle per day)	5,000 cycles
Production price (100,000 units/year)	$ 3400
Maximum weight	120 kg
Technology readiness	2016

*sized for a vehicle with energy efficiency of 350Wh/mile

Common battery packs are built up of multiple battery modules which are units formed of several battery cells that are electrically connected and packaged together. Battery packs also encompass the battery management system (BMS) and electronic harnesses [93]. When thermal management is considered, relevant components such as heat sinks or cooling plates are also packaged in the battery pack [94].

The design and chemistry of battery cells for different types of xEVs vary based on their power-to-energy requirements [53]. The power-to-energy ratio of the battery is defined as the ratio of the electrical power of the battery to its energy capacity. MHEVs and HEVs require cells with high-power-to-energy ratio (power dense cells) that can accommodate higher number of charge-discharge events, higher currents and have low resistance to current flow [95]. BEVs on the other hand require batteries with low power-to-energy ratio (or higher energy-to-power ratio or E-rate or energy-dense cells) that can deliver more energy at the cost of enduring much lower cycling rates [93]. PHEV batteries fall between these requirements [93,96].

Currently, most commercial lithium ion batteries have a cathode formed by a lithium metal oxide, an anode made of graphite, and an electrolyte which is typically a solution of a lithium salt (typically $LiPF_6$) in an organic solvent such as ethylene carbonate–dimethyl carbonate [23]. Based on the cathode chemistry, five different types of battery cells are identified: Lithium Iron Phosphate $LiFePO_4$ (LFP), Lithium Nickel Cobalt Aluminium $LiNi_{0.8}Co_{0.15}Al_{0.05}O_2$ (NCA), Lithium Cobalt Oxide $LiCoO_2$ (LCO), Lithium Manganese Oxide Spinel $LiMn_2O_4$ (LMO), Lithium Nickel Cobalt Manganese $LiNi_xCo_yMn_xO_Z$ (NMC) [23,97]. More recently, anodes made from Lithium Titanate Oxide (LTO) have been used in conjunction with different cathode chemistries to improve the endurance of the battery cells. Battery cells are designed in three formats: cylindrical, pouch, and prismatic [97,98]. The physical shape and the manufacturing process of different cell formats leads to different mechanical properties (such as weight, stress durability, etc.), as well as electrical properties (energy density, C-Rate[1], etc.) [94].

The structure of a $LiFePO_4$-graphite battery cell is shown in Figure 2-4. The operation mechanism of this battery can be explained as follows [93,99,100].

[1] C-rate is the measure of the rate at which a battery is discharged relative to its maximum energy capacity and is loosely defined as the ratio of current to nominal capacity [102].

When the battery is charged, the bonds between Li and phosphate in $LiFePO_4$ break as a result of the external potential and Li^+ ions and electrons are released. The electrons are absorbed by the current collector and travel through the external circuit while the Li^+ ions travel through the electrolyte and are stored in the structure of graphite. During discharge, this process is reversed. Other types of lithium-ion batteries function in a similar manner [101,102].

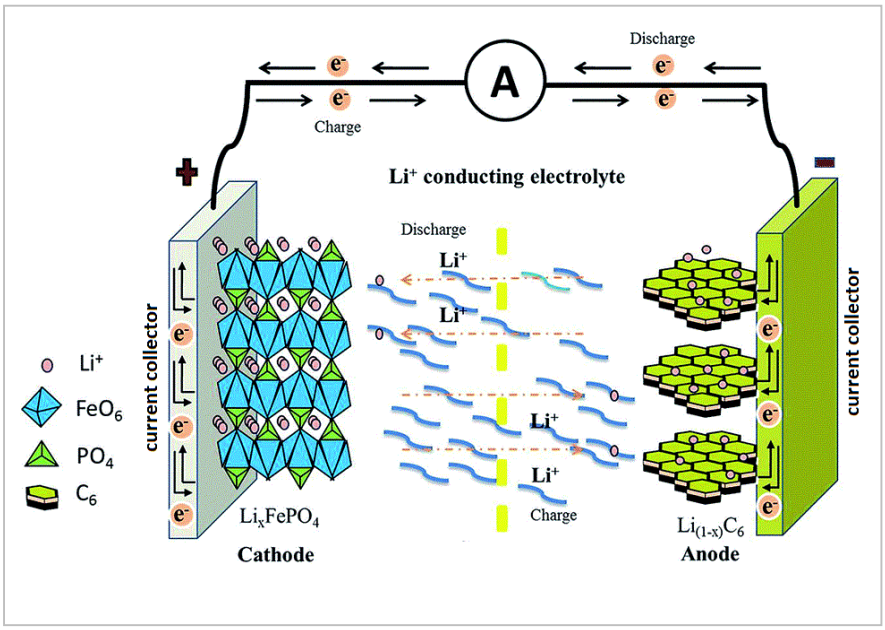

Figure 2-4 Schematics of a $LiFePO_4$ battery cell [100]

2.2.2 Basic technical definitions [99,103]

When describing the operation of a battery, a number of technical terms are commonly employed. To facilitate future discussions defining these terms is necessary.

2.2.2.1 State of charge (SoC)

The SoC (ζ) of a battery is defined as the ratio of the energy (charge) remaining $C(t)$ in the cell, to its nominal energy capacity C_0 (of a new cell)

$$\zeta(t) = \frac{C(t)}{C_0} \tag{2-1}$$

SoC cannot be directly measured but can be estimated, if the total energy capacity of the cell is known. One common method of estimating the SoC is Coulomb counting in which the charge throughput to the cell is calculated by measuring and integrating the cell current to estimate the SoC of the cell as

$$\zeta(t) = \zeta(0) + \frac{1}{C_0} \int_{t_0}^{t} i \, dt. \tag{2-2}$$

where $\zeta(0)$ is the initial SoC and i is the current of the cell.

2.2.2.2 Depth of discharge (DoD)

A parameter that is often used as an alternative to SoC is the depth of discharge (DoD) which is defined as

$$DoD = 1 - \zeta, \tag{2-3}$$

so, for a cells that operate in the SoC range of ζ_{hi} to ζ_{low}, $DoD = \zeta_{hi} - \zeta_{low}$.

2.2.2.3 Charge-discharge cycle

When a fully charged cell ($\zeta = 1$) is completely discharged ($\zeta = 0$) and charged again ($\zeta = 1$), it is said to have undergone one full charge-discharge cycle. This is equivalent to a charge throughput equal to double the capacity of the battery. In general usage when the battery is subject to repetitive micro-cycles rather than a pure discharge and a pure charge, the number of cycles (n) can be calculated based on the total charge throughput as:

$$n = \frac{\int |i| \, dt}{2 \times C_0} \tag{2-4}$$

2.2.3 Ageing of Lithium-ion batteries

During the lifetime of a battery, irreversible physical and chemical changes occur within the battery that reduce its energy storage capacity and power delivery [20,21]. Batteries with reduced capacity or power levels are referred to as aged, compared to new batteries which deliver their rated energy capacity and power.

2.2.3.1 Mechanisms of ageing

The mechanisms of ageing in lithium-ion batteries are complex and depend on various factors such as manufacturing methods, cathode and anode materials, electrolyte composition and the usage conditions [99]. Generally, capacity loss is associated with reduction in active material within the battery, for example due to decomposition of the electrolyte or side reactions between lithium and current collectors which reduce the electrolyte and lithium inventory within the cell [104]. Another major mechanism of ageing in lithium-ion batteries is the formation of a solid film on the surface of the graphite anode as a result of chemical reactions between lithium ions and decomposition products of the electrolyte. Referred to as solid electrolyte interface (SEI) [105,106], the thickness of this film increases over time (SEI growth) as a result of multiple charge and discharge cycles, thereby increasing the battery resistance and continuously reducing the lithium and graphite inventory [107]. It is widely believed that electrolyte decomposition and SEI formation are the dominant storage ageing processes in most graphite-based lithium-ion batteries [108–110].

The phenomena that lead to ageing in lithium ion batteries occur whether the battery is used or not [108]. It is common to refer to ageing that occurs due the conditions of charge discharge cycles of the battery as cycling ageing, and to the ageing that occurs due to storage conditions as storage ageing or calendar ageing [111,112].

2.2.3.2 Factors affecting storage and cycling ageing

Various studies have shown that the rate of storage ageing varies according to the conditions of storage, specifically the temperature and the SoC of the battery [111,113–115], although the sensitivity to storage conditions varies from one cell to another [20,116]. When the temperature is high, secondary reactions such as corrosion are facilitated and lithium loss is more significant than in moderate temperature, inducing capacity loss [28,107]. High SoC is analogous to higher ion proportions present on electrodes, and a high potential disequilibrium on the electrode-electrolyte interface, which promotes chemical reactions [29,110,116,117].

Cycling ageing, among other factors, depends on the charge throughput [30,106], so the battery ages as it is used. Other factors that intensify cycling ageing include high C-rate [104,118], high temperature [107,118] and low temperatures [119,120]. High C-rates, which may occur in regenerative braking or aggressive driving can damage the battery through decomposing the electrolyte or transforming the lithium ions to inactive phases [121]. Low temperature can damage the lattice of the electrodes and lead to a phenomenon known as lithium plating which reduces the active material within the cell and prevents electro-chemical reactions [107,119]. High temperature intensifies the side reactions within the battery and the decomposition of the electrolyte, accelerating the SEI growth [24,27,107,115]. In addition to the above factors, some studies have shown that high DoD can accelerate cycling ageing [115,122] while other studies have disputed this claim [118,123].

In the absence of long term field data from automotive batteries, accelerated ageing methods are currently used to characterise ageing in battery cells [124,125].These methods typically include storing the cells at different conditions (temperature and SoC), or subjecting the cells to repeated cycling at different temperature, C-Rate, etc. The variation is the capacity and the internal resistance of the cells are then measured at certain intervals or after certain number of cycles.

Table 2-4 shows the effect of temperature and SoC on the accelerated storage capacity loss of four typical Li-ion cells according to recent literature. For each cell, a subset of the dataset presented in the relevant reference has been used to compare the variation in capacity loss due to temperature increase at constant SoC. Also, the variation in the capacity loss of the cells due to SoC increase at constant temperature has been calculated and compared. The data suggests that when cell 1 is stored at 60% SoC, the capacity loss will be 133% higher at 40°C compared to 30°C, and 300% higher at 50°C compared to 40°C. When this cell is stored at 30°C, the capacity loss will be 200% higher at 60% SoC compared to 30% SoC, and 200% higher at 90% SoC compared to 60% SoC. The data suggests that although higher temperature and SoC generally intensify the capacity loss, a

consistent relationship may not exist and some irregularities are possible. Analysing effect of temperature and SoC on the power loss (resistance growth) of these or similar cells supports an identical conclusion. This analysis is not included here in the interest of brevity.

Table 2-5 shows the effect of charge throughout and temperature on the accelerated cycling capacity loss of a number of typical Li-ion cells according to recent literature. For each cell, the number of full charge-discharge cycles to 5%, 10%, and 20% capacity loss has been given at different temperature. The table generally suggests that the cells lose their capacity as a result of cycling, while the rate of capacity loss is higher in the cells that are cycled at higher temperature. The data also indicates that the capacity loss is initially fast, but slows down as the cells is cycled more. For example, the table shows that cell 1 loses 5% of its capacity after 800 cycles at 15°C and after 120 cycles at 45°C. At 60°C, the cell loses 5% its capacity before it reaches 120 cycles. Therefore, high temperature accelerates the cycling capacity loss of this cell. Comparing the number of cycles to 5% and 10% capacity loss when the cell is cycled at 45°C shows that the rate of capacity loss has decreased. This is why the cell does not reach 20% capacity loss by the end of the test (800 or more cycles).

Table 2-4. Effect of storage conditons on the capacity loss of a number of Li-ion cells.
Annotations. T : temperature , ζ : SoC, H: High, L : low

Cell	Capacity	Type	Duration†	$\left(\frac{\Delta C^{TH}-\Delta C^{T_L}}{\Delta C^{T_L}}\right)\times 100$		$\left(\frac{\Delta C^{\zeta H}-\Delta C^{\zeta_L}}{\Delta C^{\zeta L}}\right)\times 100$		Ref.
1	1.2 Ah	NMC	200 days	133%	$T_L = 30°C$ $T_H = 40°C$ $\zeta = 60\%$	200%	$\zeta_L = 30\%$ $\zeta_H = 60\%$ $T = 30°C$	[117]
				300%	$T_L = 40°C$ $T_H = 50°C$ $\zeta = 60\%$	200%	$\zeta_L = 60\%$ $\zeta_H = 90\%$ $T = 30°C$	
2	2 Ah	NMC - LMO ††	415 days	116%	$T_L = 35°C$ $T_H = 40°C$ $\zeta = 50\%$	120%	$\zeta_L = 50\%$ $\zeta_H = 10\%$ $T = 50°C$	[110]
				70%	$T_L = 40°C$ $T_H = 50°C$ $\zeta = 50\%$	30%	$\zeta_L = 50\%$ $\zeta_H = 70\%$ $T = 50°C$	
				--		32%	$\zeta_L = 70\%$ $\zeta_H = 95\%$ $T = 50°C$	
3	3 Ah	NCA	140 days	60%	$T_L = 10°C$ $T_H = 25°C$ $\zeta = 45\%$	80%	$\zeta_L = 30\%$ $\zeta_H = 65\%$ $T = 40°C$	[126]
				87%	$T_L = 25°C$ $T_H = 40°C$ $\zeta = 45\%$	0	$\zeta_L = 60\%$ $\zeta_H = 90\%$ $T = 40°C$	
				140%	$T_L = 25°C$ $T_H = 40°C$ $\zeta = 100\%$	113%	$\zeta_L = 30\%$ $\zeta_H = 65\%$ $T = 25°C$	
4	3 Ah	NCA	385 days	-11%	$T_L = 10°C$ $T_H = 25°C$ $\zeta = 50\%$	25%	$\zeta_L = 20\%$ $\zeta_H = 50\%$ $T = 45°C$	[127]
				-16%	$T_L = 10°C$ $T_H = 25°C$ $\zeta = 90\%$	10%	$\zeta_L = 50\%$ $\zeta_H = 90\%$ $T = 45°C$	
				66%	$T_L = 25°C$ $T_H = 45°C$ $\zeta = 50\%$	14%	$\zeta_L = 20\%$ $\zeta_H = 50\%$ $T = 25°C$	
				38%	$T_L = 25°C$ $T_H = 45°C$ $\zeta = 90\%$	25%	$\zeta_L = 50\%$ $\zeta_H = 90\%$ $T = 25°C$	

† Longest duration of storage for which all data points are available
†† blended cathode chemistry

Table 2-5. Effect of charge throughput and temperature on the capacity loss of a number of Li-ion cells. Data is related to cycling at 1C with 80% DoD, unless otherwise stated.

Cell	Capacity	Type	cycle count to 5% ΔC		cycle count to 10% ΔC		cycle count to 20% ΔC		Ref
1	2.2 Ah	LFP	800	15°C	na††	15°C	na	15°C	[120]
			120	45°C	340	45°C	na	45°C	
			120†	60°C	120	60°C	272	60°C	
2	1.5 Ah	NCM	100	0°C	<136	0°C	180	0°C	[107]
			319	25°C	455	25°C	638	25°C	
			100	60°C	182	60°C	<319	60°C	
3†	3 Ah	NCA	83	10°C	229	10°C	na	10°C	[126]
			133	25°C	na	25°C	na	25°C	
			133	40°C	na	40°C	na	40°C	
4†††	3Ah	NCA	83	25°C	166	25°C	533	25°C	[127]
5	0.4	NCA	150	25°C	250	25°C	1000	25°C	[128]
			<150	60°C	<150	60°C	<250	60°C	

† The '<' sign indicates that the measurements have missed the capacity loss and the closest measurement are quoted.

†† The test has terminated before this capacity loss is reached or data not reported

† † † Data related to cycling at 20% DoD around 75% SoC

2.2.3.3 Practical considerations for automotive applications

For model year 2016, most PEVs manufacturers offer battery packs warranties for up to 8 years or 100,000 miles [89]. The widely accepted end of life (EoL) condition for automotive batteries are when either 20% of the energy capacity is lost or the internal resistance is increased by 100% of the original value [66,98,129], albeit more recently it has been argued that this condition is too demanding for the current state of the technology and 30% capacity loss or 200% resistance increase is proposed as EoL condition [28,110,120,130,131].

In the absence of field data from automotive batteries, interpretation of the accelerated ageing test results is critical in determining whether certain cells are appropriate for automotive application. As a general rule, storage and cycling

ageing are considered as additive [108], therefore, the battery lifetime is estimated based on the total capacity loss or total power loss [109,122]. This however leads to under-estimation of the battery lifetime. To explain the issue, consider the dataset shown in Figure 2-5 which has been measured by the authors of reference [126] from accelerated capacity loss of a set of automotive battery cells. Figure 2-5(a) shows the capacity loss after 20 weeks of storage. Figure 2-5(b) shows the capacity loss resulted from 1400 Ah of charge throughput, equivalent to approximately 230 full charge-discharge cycles. The dataset suggests that storing the cells at 25°C and 45% SoC for 20 weeks will reduce their capacity by 1.3%. Also, if the cells are cycled 230 times at 25°C they lose over 7% of their capacity.

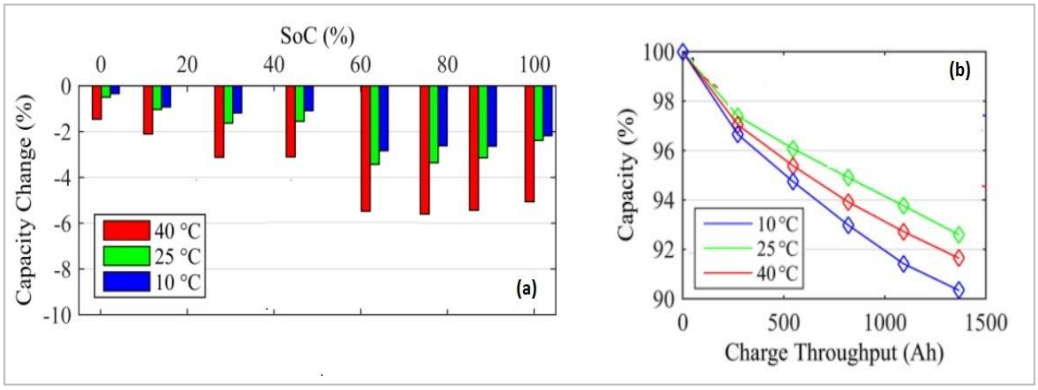

Figure 2-5. Recreated from [126]: (a) capacity loss after 20 weeks stroage, and (b) capacity loss after 1400 Ah cycling (20% DoD around 75% SoC) of 3Ah Panasonic NCR18650PD battery cells

The authors of [126] considered a range requirement of 100,000 km for a BEV and estimated that a 13 kWh battery pack made up of the cells in question an deliver a range of 100,000 with 2800 Ah of charge throughput per cell. Based on extrapolating the cycling capacity loss data in Figure 2-5(b) to 2800 Ah charge throughput, it was concluded that the cells will retain more than 80% of their capacity after 100,000 km of driving and were therefore suitable for automotive application.

The author asserts that the above interpretation of the ageing data is flawed. In addition, in real life, most passenger vehicles travel approximately 10,000 km to 12,000 km per year [132], so the target travelled distance will be reached over 8 to 10 years. Therefore, in a realistic application, the storage component of ageing will

have a major effect on the battery lifetime. In the following calculations, the lifetime of the battery cells tested in [126] are estimated based on annual travelled distance of 10,000 km. It can be seen that the battery cells reach their EoL after approximately 5 years and fail to deliver the required travelled distance. Accounting for temperature and SoC variations will lead to significantly shorter lifetimes. Similar calculations show that for these battery cells to be appropriate for realistic vehicle applications, they should endure approximately 2.5 times more number of cycles and storage length before losing their capacity to the levels seen in Figure 2-5.

Estimating the lifetime of the battery cells tested in [126] **in automotive application:**

Storage condition:	25°C and 45% SoC
Cycling condition:	25°C
Storage capacity loss over 20 weeks:	1.3%.
Annual storage capacity loss:	2.9 % (for 312 days of storage per year)
Charge throughput for 50,000 km	2800 Ah
Charge throughput per year:	560 Ah (assuming 10,000 km driving per year)
Cycling capacity loss per year:	2.8 % (for 10,000 km per year)
Total annual capacity loss:	2.9% + 2.8 % = 5.7 %
EoL:	5.3 years (based on 30% capacity loss)

In the above calculations, the storage and cycling capacity loss data were extrapolated beyond the duration of the test. Extrapolation ignores the fact that the rate of capacity loss slows down over time (see Section 2.2.3.2). In addition, the applicability of the accelerated ageing characterisation method to prediction of battery lifetime can be questioned. In real-life applications, automotive cells will be subject to periodic cycling and storage and this will likely trigger different ageing mechanisms compared to accelerated ageing tests [133]. In fact, the limited data collected from Tesla vehicles since 2013 shows their battery cells have outperformed the estimations based on accelerated ageing [134,135]. Due to the extra time and cost associated with non-accelerated ageing tests, ageing data that can support realisable battery lifetime calculations are currently rare [97]. In the

absence of reliable data, some theoretical ageing models have been developed for estimate the battery lifetime in automotive applications [111]. However, the accuracy of such models can be questioned as they either typically rely on accelerated ageing data for their verification [28], or lack the complexity required to capture the variability in the operation of typical automotive batteries [136].

2.2.4 Battery cooling requirements

The behaviour and performance of battery cells is known to be sensitive to temperature. Lithium-ion battery cells operate best in the range of 15°C-30°C [39,93,94]. Low temperature slows the electro-chemical reactions within the battery cells, reducing their power output and charge acceptancy [137]. High temperatures accelerate the degradation of battery cells, including through initiating or accelerating side reactions (e.g. corrosion or reactions between lithium ions and current collectors), and accelerating the decomposition of the electrolyte [24,106,112,115,118]. Extreme temperatures can lead to thermal runaway, or cause cell swelling and mechanical distortion that can lead to short circuiting the cell and fire [28,39,138].

Internal heat generation as well as heat transfer from adjacent components and ambient, contribute to high battery cell temperature [31,137]. Figure 2-6 shows the heat pathways to the battery in a typical vehicle. In this figure, k_{ab} , k_{ac} , k_{bc} denote the ambient-battery, ambient-cabin, and battery-cabin thermal inductance. T_a and T_b indicate the temperature of the ambient and the battery. M_b and M_c denote the thermal capacities of the battery and the cabin. q_{int} denotes the internal heat generation of the battery.

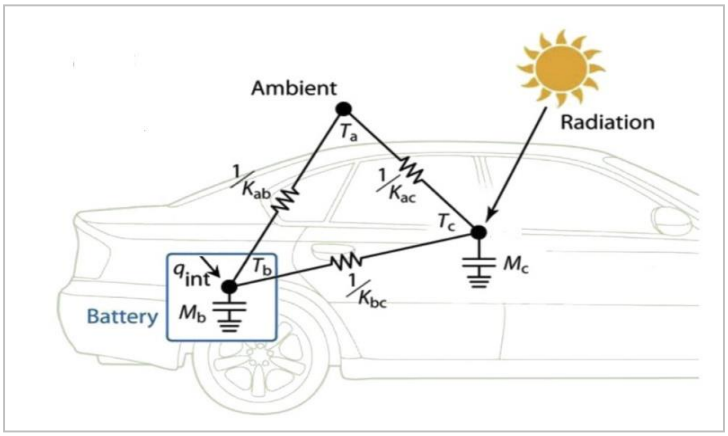

Figure 2-6. Recreated from [31]: heat paths to automotive batteries

Within battery cells, heat is generated as a result of four phenomena [139,140]:

1. chemical reactions
2. entropic reactions
3. energy dissipation for overcoming the internal resistance of the cell
4. change in concentration of species and their partial molar enthalpy during phase change

In automotive applications where battery cells are subject to repeated charge-discharge periods at C-rates of above 1, the only considerable heat generation mechanism is the one associated to overcoming internal resistance of the cell components [41,138,140]. This form of heat generation, which is commonly referred to as Joule heating [139–141], is proportional to the square of the current I and internal resistance R of the cell:

$$\dot{Q}_{gen} = I^2 R \tag{2-5}$$

Due to the dependency of Joule heating on internal resistance of cells, the peak and average heat generation in the battery pack of different vehicles can be different over similar drive cycles. Also, Joule heating increases with higher currents, thus the temperature of the battery can be expected to increase for fast charging [40] and over aggressive drive cycles [142]. The combination of aggressive drive cycles and hot ambient condition can lead to battery temperatures

reaching as high as 65°C [32,40]. Therefore, some form of cooling system is required to ensure that the desired operation range is not exceeded.

The size and design of the cooling system is generally dictated by the overall rate of heat generation in the battery pack when subjected to load [143,144]. Battery cooling is traditionally a 'key-on' function, that is, it is only activated when the vehicle is switched on [34]. Typically, the cooling system should have the capability to maintain the pack at an optimum average temperature with a minimum temperature gradient across different cells [145].

There are several approaches to designing a cooling system for traction batteries. As in any other system, factors such as lightness, compactness, reliability, and maintainability of the cooling system are also considered in their design. From one point of view, cooling systems can be categorised based on the medium used to extract heat from within the battery. Possible options are using air, liquid coolant, refrigerant and phase change material [137]. Practical considerations are associated to each option that will dictate specific pack level designs, ultimately leading to more acceptability of some options over others [146].

Figure 2-7 shows a schematic of a typical liquid-based battery cooling system which includes a pump, a low-temperature radiator (LTR), a coolant-refrigerant chiller, a valve and an expansion tank. The electric pump circulates a coolant (typically a water-glycol mixture) in the system. The coolant passes through cooling jackets or plates that are in thermal contact with battery cells while the valve controls the flow of the coolant between the LTR and the chiller loop. When the battery cooling load is low, the LTR loop is used; which has a low energy requirement, especially when the vehicle is in motion and the LTR fan is used at a reduced power. The chiller is integrated into the refrigeration circuit of the AC system and provides extra cooling power when the cooling load of the battery cooling or the ambient temperature are high.

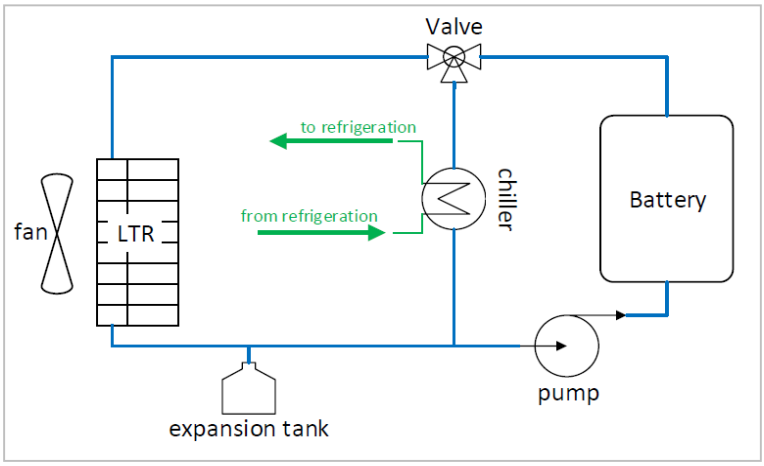

Figure 2-7. Schematic of a typical liquid-based battery cooling system with a low-temperature radiator and a chiller

2.3 Automotive AC systems

Typical automotive AC systems have four primary functions: cooling, circulating, purifying and de-humidifying the air inside the passenger cabin [147,148]. Automotive AC systems are typically composed of air handling units (including a fan and a blower that facilitate air flow, the pipes that carry the air, a heater core, and a recirculation air flap), and a refrigeration circuit [149,150]. Schematically, the top-level view of a typical automotive AC system is as shown in Figure 2-8. Briefly, the system operates as follows:

1. Cabin air, mixed with ambient air, is sent to the refrigeration circuit by the blower, and is cooled to near-freezing temperatures.
2. Cold air exits the refrigeration circuit and enters the heater core, where it is reheated to temperatures comfortable for the occupants of the vehicle.
3. The reheated air enters the cabin.
4. Ambient air is flown to the refrigeration circuit where it absorbs heat. Hot air is rejected to the ambient.

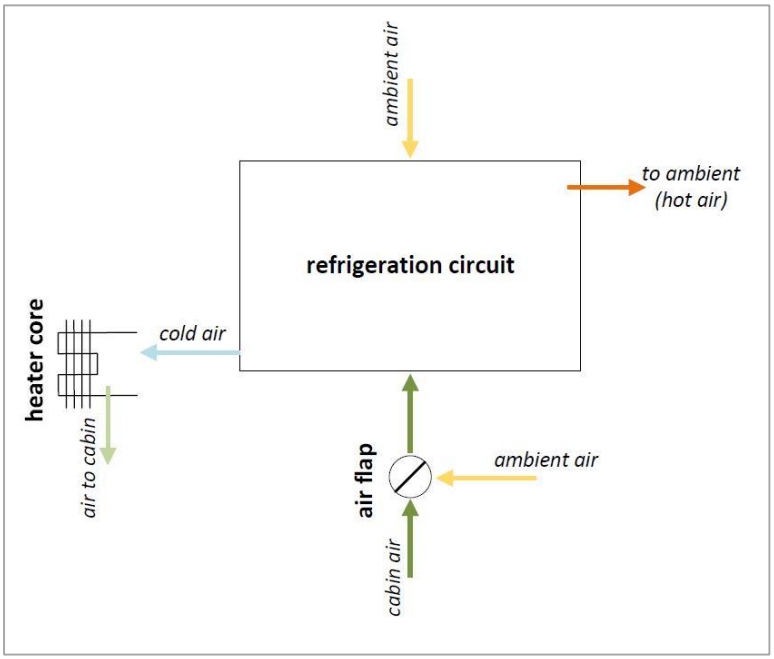

Figure 2-8. High level schematic a typical automotive AC system

Purifying the cabin air from dust and odour is typically achieved by filtering the air that enters the AC system [147]. Another aspect of purification is preventing the CO_2 that results from respiration to build up inside the cabin [147]. Mixing the cabin air with fresh air is the main CO_2 reduction mechanism and one of the two dehumidification mechanisms in common automotive AC systems [147,151]. It is enabled by an air flap (as shown in Figure 2-8) which can change between full re-circulation mode and full fresh mode. In full re-circulation, only the cabin air is cooled and sent back to the cabin. Since the cabin is generally at a lower temperature than the ambient, the system is more energy efficient in the full re-circulation mode and the cabin can be cooled faster [72]. In fresh mode, only ambient air enters the AC system, where it is cooled and sent to the cabin, while some of the air previously in the cabin is extracted to the ambient, so the carbon dioxide build-up is avoided. Carbon dioxide and humidity sensors can be used to optimise the amount of fresh air allowed to enter the system [152].

Cooling the air to near-freezing temperatures is in the interest of the dehumidification [147,153] of the cabin. Since the capacity of air in carrying moisture is significantly low at near-freezing temperatures ($6.8\,\frac{g}{m^3}$ at $5°C$

compared to 30.4 $\frac{g}{m^3}$ at $30°C$ [154]), the moisture content of the air condenses inside the refrigeration circuit, and the cabin is gradually dried.

Cold air can cause thermal discomfort if it comes to direct contact with human skin [155], therefore it should be reheated before entering the cabin [153]. The technology of the heater core depends on the vehicle type, and varies from an exhaust gas heat exchanger in CVs [156] to a positive temperature coefficient (PTC) heater in BEVs [157]. Other technologies have been also promoted for BEVs in recent years due to the high energy demand of the PTC heaters [156,158].

Vapour compression refrigeration circuits are the most ubiquitous technology of refrigeration employed in the automotive industry. Figure 2-9 shows a schematic of a vapour compression refrigeration circuit in its most general form, which is composed of two heat exchanger cores: condenser and evaporator, an expansion valve, and a compressor. A working fluid such as one from the hydrofluorocarbons family is used in the system as the heat transfer medium. The refrigeration circuit operates between a high temperature and a low temperature environment. The refrigerant undergoes a series of cyclic thermodynamic processes, as a result of which, heat is absorbed from the low temperature environment and rejected to the high temperature environment. The cooling power of the refrigeration circuit depends on the power of the compressor which is a function of its displacement and speed.

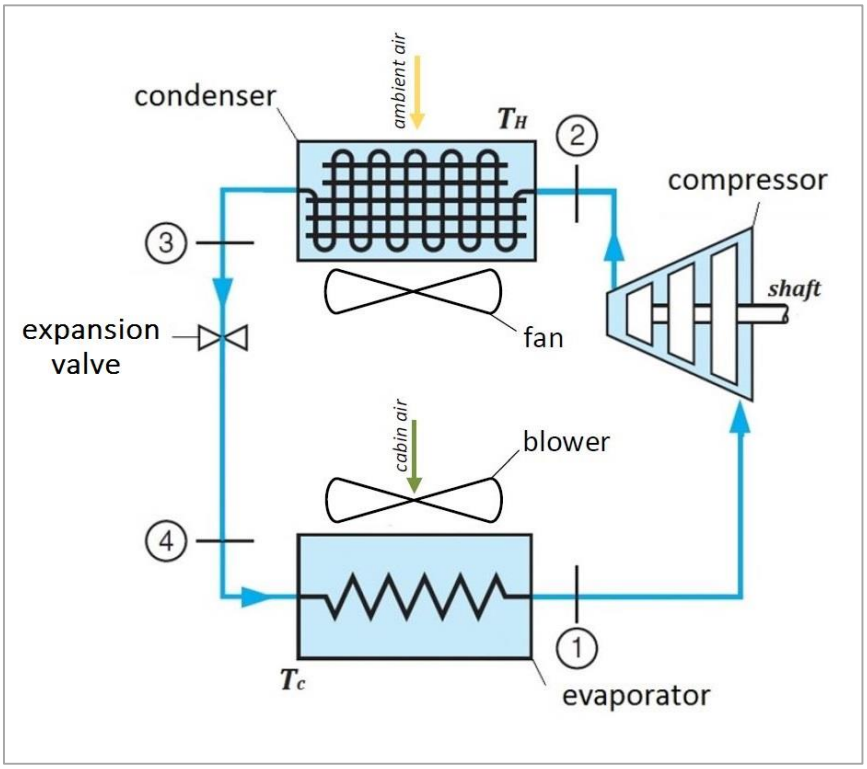

Figure 2-9. Recreated from [159] : schematics of a vapour compression refrigeration circuit. The high temperature and the low temperature sides are denoted as T_H and T_C respectively.

In CVs, variable displacement mechanical compressor are commonly used [160,161] which are driven by the engine through a mechanical coupling [147,162]. In PEVs where the engine does not exist or is commonly switched off, variable speed electric compressors are used which are driven by an electric motor supported by the high voltage battery [163–165].

Most refrigeration circuits are controlled as a single-input-single-output (SISO) system, i.e. the compressor is the only component that is controlled [166]. The expansion valve is most commonly of a thermostatic type (thermostatic expansion valves or TXV), which open or close based on a pre-defined difference between the temperature of the refrigerant at the inlet and the outlet of the evaporator [153]. More modern electronic expansion valves are an alternative that can be independently controlled, to allow a more efficient multi-input-multi-output (MIMO) control scheme [150,153,167].

The main purpose of automotive AC systems is to create thermal comfort for the passengers. Thermal comfort is defined as psychological satisfaction with the thermal environment and is assessed by subjective evaluation [168]. Thermal comfort has two primary requirements: First, thermal equilibrium of the body, that is, the net loss of thermal energy from the body is equal to the heat generation within the body; second, correct relationship between generation of heat within the body, evaporation of perspiration, and skin temperature [169,170]. Therefore, the main physical factors that affect thermal comfort are those that determine the heat gain and loss, namely the metabolic rate[1], clothing (thermal) insulation, (mean) radiant temperature[2], air temperature, air speed, and relative humidity[3] [171,172]. In addition, behavioural and psychological parameters such as personal expectations also affect thermal comfort [171]. In the context of vehicle passenger cabins, only the last three physical factors can be altered by the AC system [173].

Due to its subjective nature, thermal comfort can be only predicted with statistical models which are based on the perception of a large number of people subject to certain thermal conditions [169]. The Predicted Mean Vote (PMV) model, or its equivalent, the Predicted Percentage of Dissatisfied (PPD) model, are the most recognised thermal comfort models within the literature [169,174–178].

Recently, incorporating thermal comfort models in the control of building and automotive AC systems has been proposed [175,176,179]. This approach can potentially enhance the passengers' thermal comfort, as the cabin temperature and blower speed set points can be controlled to follow thermal comfort needs more closely [180]. In addition, using thermal comfort models can help avoid over-cooling the cabin, reducing the energy consumption of the AC system [176]. However, the thermal complexities of the cabin are a large obstacle on the way of

[1] **Metabolic rate** is the rate of energy conversion within the human body which depends on the metabolism [271]

[2] **Mean Radiant Temperature:** is a measure of the average temperature of the surfaces that surround the human body and exchange thermal radiation with it [272].

[3] **Relative humidity (RH)** is the ratio of the partial pressure of water vapour to the equilibrium vapour pressure of water at a given temperature [154]

adopting this approach, as extra instrumentation will be required to measure the heat influx to the cabin and the temperature of different surfaces around it [148,181]. In addition, a detailed model of the cabin will be required to calculate the regime of air flow within the cabin [177,181] as well as the heat fluxes that affect different parts of the passengers' bodies [182–184]. The long convergence time of such models, that typically spans from several minutes to a few hours [177,185], makes them unsuitable for control applications.

In the absence of a thermal comfort model, the passengers can directly control the cabin temperature and the blower speed [147,150]. The acceptable range of average air temperature for a person in summer clothing pursuing sedentary activity could be between 22°C to 26°C [160,173,179,182].

2.4 Summary

This chapter presented the background information relevant to the scope of the research. The high-level operational consideration of PHEVs and the key requirements of PHEV batteries was discussed. The ageing mechanisms of Li-ion batteries were explained and the impact of factors such as high temperature and high SoC on the ageing of typical Li-ion batteries were established through presenting a subset of the ageing characterisation data available in the public domain. Also, the requirement for cooling the battery was discussed and the requirement for integration of typical battery cooling systems to the AC system of the vehicle was discussed together with a brief explanation of the operation of typical automotive AC systems.

CHAPTER 3 LITERATURE REVIEW: EFFECT OF HOT CLIMATE CONDITIONS ON THE PERFORMANCE ATTRIBUTES OF PEVS

Introduction

In this chapter, the previous research that has investigated the effect of hot climate conditions on PEVs is reviewed to identify the gap in knowledge.

Hot geographical locations, where high air temperature and high solar irradiance are combined, create challenging operating conditions for passenger vehicles [74]. With the exception of Europe, extremely hot climate conditions are experienced in major cities across all continents [186]. In Phoenix, Arizona (AZ), US, for example, hot days with air temperatures higher than 40°C and solar irradiance in excess of 950 $\frac{W}{m^2}$ frequently occur over three months of the year [187]. Therefore, understanding and mitigating any impact of hot ambient conditions on the performance attributes of PEVs has attracted considerable attention.

3.1 Effect of hot ambient conditions on cabin and battery temperatures

In the automotive industry, a common procedure for determining the effect of hot ambient on the cabin is a hot soak of the vehicle [188,189] which includes 3-4 hours of exposure to the reference conditions given in Table 3-1. When undergoing a hot soak, the average cabin air temperature can exceed 60°C [173,190–193]. The temperature of the interior surfaces of the cabin varies depending on the level of exposure to solar irradiance [175,183,191]. The surfaces that are more exposed to solar irradiance, such as the dashboard, steering wheel, etc., can experience temperatures in the range of 90°C -110°C [194,195].

Table 3-1. Reference hot soak conditions

Air Temperature	Solar Irradiance	Humidity	Duration	Reference
43°C	1000 $\frac{W}{m2}$	50%	4 hours	[183,189,192,196]

Similarly, hot ambient conditions have been shown to have a significant effect on the temperature of PEV batteries. This effect is evaluated over 24-hour vehicle duty cycles, either experimentally or through simulation. A typical duty cycle can be defined by three elements:

1. The usage scenario, which includes details such as the number and timing of the trips, charge pattern, where the vehicle is parked (i.e. garage or open space), etc.;
2. The drive cycles of the trips;
3. The ambient conditions in which the vehicle operates

Many previous investigations of the effect of ambient conditions on PEV batteries have considered the climate conditions of Phoenix and other US locations as reference. To facilitate the forthcoming review of these investigations, the said locations are rated from hottest to coldest in Table 3-2.

Table 3-2. Rating of US locations from hottest to coldest, based on the data in [197,198]

Location	Rating *(1: hottest, 5: coldest)*
Phoenix, Arizona	1
Miami, Florida	2
San Francisco, California	3
Los Angles, California	3
Seattle, Washington	4
Baltimore, MD	4
Charleston, West Virginia	4
Portland, Maine	5
Minneapolis, Minnesota	5

In [36] a number of BEVs equipped with 24 kWh batteries were monitored as they were used in Phoenix. Recording the battery temperature in these vehicles at the start of every trip for 250 consecutive days showed a variation of more than 30°C

between the colder and the warmer days of the year. In the warmer days, starting temperatures as high as 45°C were observed, while in the colder days, the starting temperature could be as low as 15°C. However, the climate conditions on the specific days were not reported.

In [199], a mid-size PHEV with a 16 kWh battery was simulated in the ambient conditions of various US locations. Different daily duty cycles were assumed, composed of trips on real-life drive cycles as well as park phases, including an 8-hour park in daytime. It was shown that for a vehicle operating in Phoenix over 1 year, the median of peak battery temperature was up to 24°C higher than the average ambient temperature. The same study showed that in Los Angeles, the median of peak battery temperature was up to 17°C higher than the average ambient temperature. However, the absolute battery temperature was not reported.

In [40] the operation of a mid-size BEV with a 24 kWh battery was simulated over a number of real-life duty cycles in the climate conditions of Phoenix and Seattle. In the absence of active cooling, the median of the average, and the maximum battery temperatures were respectively 26°C and 64°C, in Phoenix. In Seattle, the median of average and maximum battery temperatures were 14°C and 47°C, respectively. Therefore, the median of the average, and the maximum battery temperature in Phoenix were 12°C and 17°C higher than in Seattle. A similar study was conducted in [32] assuming a set of real-life usage cases and the climate conditions of various US locations. It was shown that in the absence of active cooling, the battery temperature reached as high as 65°C in Phoenix. It was also shown that the annual average battery temperature in Phoenix, Los Angeles and Minneapolis were approximately 27°C, 20°C and 10°C, respectively.

The high cabin and battery temperatures that result from hot ambient condition can deteriorate the performance attributes of PEVs. In the following sections, some of the affected attributes will be reviewed.

3.2 Performance attributes affected by the high cabin temperature

High cabin temperature and the associated high AC load can lead to poor energy efficiency, thermal comfort and battery lifetime. These aspects are discussed in the following sections.

3.2.1 Energy efficiency

Automotive AC systems are designed based on peak cooling load in hot soak conditions [190,200] similar to those given in Table 3-1. The peak cooling load corresponds to the maximum time that it should take to cool the cabin to a thermally comfortable set point, typically 22°C [201]. The process of cooling a hot-soaked cabin to this set point is commonly referred to as cabin pull-down [166]. The time required for a complete pull-down depends on different factors (e.g. the initial temperature and size of the cabin, as well as the speed of the vehicle during pull-down [202,203]) but can be between 20 to 30 minutes in case of mid-size vehicle [175,202], to 1 hour, in case of large sport utility vehicle [173].

Cabin pull-down requires a significant amount of energy that can even outweigh the energy loss due to rolling resistance, aerodynamic drag and driveline losses [160,204,205]. In a mid-size vehicle, power demand air conditioning during pull-down is in the range of 6 kW- 7 kW [192,206,207]. In a conventional vehicle with a mechanical compressor, this power translates to approximately 4 kW- 5 kW of extra load on the engine [192,207], which is greater than the engine power required for 35mph cruise of the vehicle [207]. Inevitably, the fuel consumption (also the emissions) of the vehicle will increase as a result of this load- every 400W increase in engine load reduces the fuel economy by 1 mile per gallon (US) [204,208].

The effect of AC loads on energy efficiency is even more significant in PEVs [74]. In a mid-size PEV, the power required from the battery to operate a high performance electric AC compressor is in the range of 3 kW-5kW during pull-down [175,207], while the steady-state compressor power required to maintain a low cabin temperature can exceed 1 kW [192,209]. This load can reduce the AER

by 20% to 40%, depending on the assumed drive cycle. In [207], the 3kW load of the AC compressor during pull-down of a mid-size BEV was shown to reduce the AER of the vehicle by 18% on the US06, and by 36% on the SC03. In [175], experimental studies on the AC system of a mid-size BEV were used to generate a compressor load profile. This load profile represented a 10-minute high power operation (cabin pull-down with average value of 4.2 kW), and a 16-minute low power operation (constant cabin temperature control with average value of 600 W). Simulating the vehicle over different drive cycles with this AC compressor load profile showed that the AER of the vehicle was reduced by approximately 37% on the SC03 and UDDC, and by approximately 16% on the HWFET.

In a hybrid vehicle, any reduction in range will result in higher fuel consumption. In [188], the 3 kW electrical load of the AC compressor of a mid-size PHEV was shown to decrease the fuel economy by 40 % on the FUDS and by 28% on the SC03.

3.2.2 Thermal comfort

As mentioned in Section 3.2.1, the pull down of a hot soaked cabin takes between 30 minutes to 1 hour, depending on the thermal load and the cooling power of the AC system. The passengers experience poor thermal comfort during most of this time.

In [177], a 3D type cabin model was used to simulate the internal thermal conditions of the cabin of a mid-size vehicle during pull-down from 60°C while a variation of the PPD model was used to assess the thermal comfort within the cabin. The simulation results showed that a complete pull-down took more than 30 minutes. The cabin was hot in the initial 10 minute of the pull-down, and remained warm in the following 20 minutes.

In [182], temperature and air flow measurements taken from a passenger vehicle were used to estimate thermal comfort during the pull-down of the hot soaked cabin. The measurements suggested that the complete pull-down of the cabin (from 65°C) took over 50 minutes. The thermal comfort calculations based on a

heat balance model of human skin showed that the cabin remained ‘very hot’ or ‘hot’ during the initial 30 minutes of the pull-down.

3.2.3 Battery lifetime

The energy requirement of the AC system affects the battery lifetime of PEVs. Limited research has been conducted on quantifying this effect. In [209], a mid-size BEV with a 24 kWh battery was simulated over real-life usage scenarios under the climate conditions of various US locations. It was shown that for similar driving conditions, the vehicle requires approximately 1000 kWh more electrical energy per year for conditioning the cabin. It was also estimated that to meet this additional energy requirement, the vehicle needed to be charged 54 times more per year in Arizona compared to West Virginia. This is equivalent to 54 more charge-discharge cycles per year, which inevitably accelerates the degradation of the battery.

In [210,211], a BEV was simulated for 27,500 km over different drive cycles. The simulations accounted for the compressor load which was generated from a separate simulation of cabin pull down from 55°C and steady state air conditioning. It was shown that the AC compressor load increased the capacity loss of the battery by 10% -35%, depending on the assumed drive cycle.

3.2.4 Mitigation methods

Various technologies have been developed for mitigating the effect of hot climate conditions on the cabin temperature, and the subsequent impact on performance attributes such as energy efficiency, thermal comfort and battery lifetime. From one perspective, these technologies can be categorised as those that reduce the hot soak temperature of the cabin, and those that enhance cabin cooling.

3.2.4.1 Reducing the hot soak temperature of the cabin

Solar irradiance is the major contributor to the maximum soak temperature of the cabin.

The solar irradiance incident on the windows can be transmitted, reflected or absorbed. The transmitted component enters the cabin directly, while a fraction of the absorbed component enters the cabin through convection with the cabin air or through subsequent inward radiation. Advanced glazing technologies, such as spectrally selective coatings[1] [212] and double-pane glasses[2] [192] have been shown to limit the inward flow of solar energy through the windows and reduce the hot soak temperature of the cabin.

The solar irradiance incident on the opaque segments of the cabin, such as the roof, door panels, side posts, etc. (simply referred to as cabin wall, hereafter) can be reflected or absorbed. The absorbed component enters the cabin through inward conductance and convection with cabin air. It has been shown that using solar reflective paint [192] and insulating the cabin wall [190] can limit the inward flow of heat and reduce the hot soak temperature of the cabin.

Although limiting the heat gain from the ambient reduces the hot soak temperature of the cabin, and therefore can help improve the affected performance attributes, the widespread adoption of the technologies cited above has been restricted by practical considerations [188]. For example, absorption of solar energy in winter accelerates cabin warm-up. Therefore, using spectrally selective coatings to block solar energy increases the heating load of the cabin and can reduce the energy efficiency of the vehicle [175,190] especially in PEVs [209]. 'Active' spectrally selective coating technologies can be used as an alternative, but they are currently at the early stages of their development [213].Ventilating the cabin when the vehicle is parked (parked ventilation) [214] is another method that can reduce the accumulation of heat inside the cabin without reducing the ability to warm up the cabin in winter. The effectiveness of this method is however limited in extremely hot climate conditions [215].

[1] Spectrally selective coatings reflect the invisible solar irradiance wavelengths (infrared and ultraviolet), but transmit the visible wavelengths.

[2] Double-pane glass limits the heat flow into the cabin by reducing the temperature of the glass surface that is in contact with cabin air

3.2.4.2 Enhanced cabin cooling

The technologies that enhance cabin cooling include those that enable faster, and more efficient fulfilment of the cabin cooling requirements. Advanced designs of the refrigeration circuit and its elements [216], such as heat exchangers, compressors and refrigerants, that facilitate more efficient extraction of heat from the cabin, fall into this category.

Another group of the technologies that enhance cabin cooling are those that are concerned with efficient delivery of cooling power to the passengers. Zonal cooling [149,175], conductive cooling (e.g. cooled seats [217]), and radiative cooling (e.g. cooled dashboards [218]) are examples of such technologies that enable the creation of local comfort for the passengers. These technologies reduce the need for maintaining the entire cabin at low temperatures, thus reducing the associated energy demand.

To improve thermal comfort during trips, precooling the cabin to a thermally comfortable temperature has been considered [219,220]. To pre-cool a hot-soaked cabin effectively, cooling power from the refrigeration circuit is required [193]. Therefore, pre-cooling will deteriorate the fuel economy of CVs, and the AER of PEVs. In PEVs, the grid power can be used to pre-cool the cabin (plugged-in precooling), which, in addition to improving thermal comfort [221], improves the energy efficiency of the vehicle through reducing the AC loads on the battery [222].

In addition to the technologies cited above, optimal (active) control methods have been applied to reduce the energy demand of air conditioning [69,151,176,223–225]. This typically includes using a thermal comfort model to dynamically define the set points of the AC system. For example, in [176], the cabin temperature set point was dynamically defined based on thermal comfort predictions. This enabled reducing the AC power, within the limit of the passengers' thermal comfort which led to higher energy efficiency. However, the method is not applicable during pull-down when the vehicle is hot and the AC system needs to operate at maximum power.

The technologies that prevent high cabin temperature and enhance cabin cooling are well established, as they are not exclusive to PEVs, or even to the automotive industry. Rather, extensive experience has been gained from application of these technologies in other industries. For example, window glazing technologies [226], insulation of walls [227], zonal cooling [228] , pre-cooling [229], and active control methods [179], have been widely applied in thermal management of buildings. Nevertheless, widespread adoption of these technologies in the automotive industry has been slowed down by the associated cost and the technical complexities of integrating them to a vehicle [230].

3.3 Performance attributes affected by the high battery temperature

The high battery temperatures that result from hot climate condition and the associated cooling load can negatively affect the performance attributes such as the energy efficiency, the thermal comfort and the battery lifetime of PEVs. In this section, the literature that has investigated such effects and possible methods of mitigating them is reviewed. This review highlights the shortcomings in the existing mitigation methods and the requirement for further research.

3.3.1 Energy efficiency

One consequence of the high battery temperatures experienced in hot climates is high battery cooling loads, which inevitably affects the energy efficiency and the electric range of the vehicle. Very few examples of quantifying the battery cooling loads are available in the literature.

The simulation results presented in [32] show that on aggressive drive cycles, key-on battery cooling increases the energy consumption of a mid-size BEV by approximately 8%. In [143], the battery cooling load of a Chevrolet Volt simulated in hot climate conditions on two back-to-back US06 drive cycles after a hot soak was estimated to be approximately 700 Wh (compared to the approximately 250

$Wh/mile$ energy efficiency of a mid-size PHEV operating in CD mode [66]). In [231], the battery cooling loads of a mild hybrid vehicle with a 1.1 kWh battery and a liquid cooling system was investigated. It was shown that when the vehicle was simulated on the Artemis Urban drive cycle in hot ambient conditions, the battery cooling increased the energy consumption of the compressor of the refrigeration circuit by approximately 10%.

Another consequence of high battery temperature that has not been studied in the literature concerns the electric traction capability of the vehicle. As a safety function, and to avoid damage to the battery, typical automotive battery management systems limit the power output of the battery at high temperatures [38,93,102]. This reduces the electric traction capability until the cooling system brings the temperature of the battery back into the prescribed range [232]. Reduced electric traction means that BEVs may not be driven over aggressive drive cycles. In PHEVs, this can lead to poor fuel economy on aggressive drive cycles as the engine will be used more.

3.3.2 Thermal comfort

When the AC loads are high, for example during pull-down following a hot soak, allocating a part of the refrigeration power to the battery reduces the cooling power of the evaporator. This leads to a noticeable rise in the vent temperature [231], and subsequently the average cabin air temperature [38,231,233]. Therefore, (key-on) battery cooling can cause thermal discomfort for the passengers.

3.3.3 Battery lifetime

As mentioned earlier, the heat extraction capability of active liquid cooling systems is sufficient to ensure that typical PEV batteries operate in the prescribed temperature range over typical real-world load profiles [234]. However, since battery cooling is commonly a key-on function [232], and given that typical passenger vehicles are parked (key-off) for most of their lifetime [35,83,235], key-on cooling is insufficient for preventing the high battery temperatures that can be experienced in hot ambient conditions. This is shown in [32,40] in which the

operation of a mid-size BEV was simulated over a set of real-life usage cases in Phoenix. Key-on cooling was assumed with coolant temperature set point of 20°C. It was shown that with key-on cooling, the absolute maximum daily temperature of the battery was only reduced from 65°C to 47°C, while the median of its maximum temperature was only reduced from 51°C to 46°C. Key-on cooling was also shown to reduce the median of the annual time-average battery temperature from 27°C to 23°C.

The significant effect of the ambient conditions on battery temperature leads to a variability in battery lifetime with geographical location. Below, the literature that has investigated this variability is reviewed. The key aspects of the method and conclusions of the relevant literature are summarised in Table 3-3. All comparisons within the table, and in the discussions that follow, assume the availability of key-on cooling.

In [199] a PHEV was simulated over a range of real-life drive cycles. Average ambient temperatures of various US locations were assumed in the simulations. It was shown that after an 8-year period, the capacity loss of the battery was as low as 14% in colder locations, and as high as 20% in warmer locations.

In [35], the lifetime of a PHEV battery was compared for different duty cycles with the climate conditions of 100 US locations. It was shown that the climate conditions caused a relative variation of up to 75% in the of capacity loss of the battery after 10 years.

In [32] a BEV was simulated over a set of duty cycles composed of long-term travel data and the ambient conditions of Phoenix and Minneapolis. It was shown that after 10 years, the capacity loss of the battery was in the range of 30%-37% in Phoenix, and in the range of 20%-25% in Minneapolis. It was also shown that in the presence of key-on liquid cooling, the cycling component of capacity loss has a negligible sensitivity to ambient temperature. A similar analysis in [40] using a set of duty cycles composed of three trips per day and one overnight charge, in the

ambient conditions of Phoenix and Seattle revealed the average difference in the capacity loss between these two locations was 8%.

In [41] operation of a BEV was simulated over a number of duty cycles composed of trips on the US06, UDDS and other drive cycle, in the ambient conditions of Phoenix and Minneapolis. The drive cycles were blended to create a range of annual mileages. Depending on the mileage of the vehicle, the battery lifetime was between 1.3 to 4.6 years shorter in Phoenix.

In [236] two PHEVs (one with a 11.5 kWh and one with a 2.7 kWh battery) were simulated over a set of duty cycles composed of real-life travel data, the ambient conditions of various US locations including those of Phoenix and Baltimore, and three different charging strategies. It was shown that on average, the capacity loss was between 30% and 50% higher in Phoenix, compared to Baltimore, depending on the charge strategy and battery size.

In [237], the operation of a PHEV over a working day usage scenario was compared in the climate conditions of Phoenix and San Francisco. It was shown that the battery lifetime was approximately 3 years shorter in Phoenix. Simulating the same vehicle and usage scenario in [25] showed that and the battery lifetime was 2 years shorter in Phoenix compared to Miami.

3.3.4 Mitigation methods

Generally, two methods can be considered to reduce the hot soak temperature of the battery, which subsequently mitigate the impact on the vehicle's performance attributes. These methods are described in Sections 3.3.4.1 and 3.3.4.2

3.3.4.1 Thermal insulation

The thermal interactions of the battery and its ambient can be limited through insulation[145], which helps reduce the hot soak temperature of the battery. However, common methods of insulation are not sufficient to eliminate the effect of hot ambient on the battery [31]. In addition, insulation reduces the natural

rejection of heat from the battery [137] and this can lead to faster ageing if the battery is left at a high temperature following driving or charging [35]. Nevertheless, when combined with sufficient cooling, thermal insulation can help reduce battery ageing in hot climates [39,199].

3.3.4.2 Plugged-in cooling

Observation of short battery lifetime in hot geographical locations indicates the need for extending battery cooling beyond a key-on function. Previous research in this area has assumed that vehicles can always be plugged in (when they are parked). Therefore, combining key-on cooling with additional 'plugged-in cooling' (cooling using the grid energy) has been proposed to enable frequent and aggressive cooling [32,35,37–41]. Since it uses an external energy source, plugged-in cooling is effectively 'free' for the vehicle, so it does not reduce the AER or lead to extra cycling ageing. Therefore, the only practical consideration for enabling plugged-in cooling is the additional cost of electricity.

Table 3-3 Summary of literature investigating the sensitivity of battery lifetime to ambient conditions

Vehicle Type	Duty Cycle			Battery lifetime variability	Ageing measure	Cooling strategy	Reference
	Usage Scenario	Drive Cycle	Ambient				
BEV (24kWh) PHEV(16kWh)	real-life travel data + • 1 opportunity overnight charge • opportunity charges at every park event	GPS records	average temperature of various US locations	capacity loss varies across US locations between 14% to 20%	capacity and resistance	active key-on	Wood et al. 2012 [199]
PHEV	real-life travel data and • 1 trip + opportunity charge • 2 trips + 1 just-in-time charge • 2 trips + 2 opportunity charge • 2 trips + 1 overnight opportunity charge	GPS records, UDDS, US06, HWY	hourly temperature and solar radiation 100 US locations	capacity loss varies by up to 75 % with climate conditions	capacity loss	active key-on	Smith et al. 2012 [35]
BEV (24kWh)	real-life travel data and 1 opportunity overnight charge	GPS records	Phoenix, Los Angeles Minneapolis	capacity loss Phoenix: 30-37% Minneapolis 20-25%	capacity and resistance	key-on + plugged-in	Neubauer et al. 2014 [32]
BEV (24kWh)	3 trips per day + • 1 opportunity overnight charge • 1 opportunity midday fast charge 1 opportunity overnight charge	GPS records	Phoenix, Seattle	capacity loss Phoenix :25% Seattle: 17%	capacity loss	key-on + plugged-in	Neubauer et al. 2015 [40]
BEV (22.5kWh)	• 2 trips + 1 opportunity overnight charge • 2 trips +2 opportunity charge • 2 trips + 1 opportunity charge	US06, UDDS	Phoenix, Minneapolis	lifetime shorter in Phoenix by 1.3 to 4.6 years depending on mileage	capacity and resistance	active key-on	Gross et al. 2011 [41]
PHEV (2.7kWh) PHEV (11.5kWh)	• 2 trips + 1 opportunity overnight charge • 2 trips + 1 JIT overnight charge • 2 trips + 2 opportunity charge	GPS records	Phoenix, Baltimore	capacity loss between 30% to 50% higher in Phoenix depending on the charging strategy and size of the battery	capacity loss	active key-on	Smith et al. 2012 [236]
PHEV (5kWh)	real-life travel data + • 2 trips + 1 opportunity overnight charge	GPS records, US06	Phoenix, San Francisco	3 years	capacity loss	active key-on	Yuksel et al. 2017 [237]
PHEV (5kWh)	• 2 trips +1 opportunity overnight charge	US06, UDDS	Phoenix, Miami	2 years	capacity loss	active key-on	Yuksel et al. 2012 [25]

It has been shown that compared to key-on cooling alone, combining key-on and plugged-in cooling can lead to significant improvements in battery lifetime through enabling significantly lower battery temperatures during hot soak and throughout the day. In [32,40], combining key-on and plugged-in cooling was shown to reduce the capacity loss of a BEV battery operating in Phoenix by 3%-5%, over 10 years, depending on the assumed duty cycle.

In addition to other factors, the sensitivity of battery temperature to climate conditions depends on the heat capacity of the battery, therefore, the benefits realised from combining key-on and plugged-in cooling vary with battery size. This is shown in [39] where the effectiveness of combining key-off and plugged-in cooling in reducing the power loss was approximately 3 times higher for a 4kWh battery compared to a 14 kWh battery. Nevertheless, this variability of the sensitivity of the battery to climate conditions with size does not mean that over-sizing the battery can be considered as a practical method of avoiding high temperature [236]. Over-sizing the battery incurs significant costs, including the disproportionate impact of the added weight on the energy efficiency of the vehicle [91,238].

In addition to improving the battery lifetime, enabling plugged-in cooling also benefits the energy efficiency and thermal comfort attributes of the vehicle, as the 'free' nature of plugged-in cooling encourages intensive precooling of the battery for every trip to reduce the any subsequent need for key-on cooling [37,39,40,239].

A further benefit of pre-cooling that battery that has not been directly acknowledged in the literature is that it helps maximise the electric traction capability of the vehicle at the onset of every trip by eliminating battery overheating, thus avoiding traction loss in BEVs or any unwanted extra fuel consumption in PHEVs.

3.3.5 Requirement for key-off cooling

A key shortcoming in previous research that proposed the strategy of combining key-on and plugged-in cooling is the assumption that vehicles can be plugged in

every time they are parked. If this is the case, the cooling strategy will be sufficient for maintaining a low battery temperature throughout the day. However, the opportunity for plugged-in cooling is limited in practice, given that most vehicles are only plugged in once per day, typically overnight [83,240]. Therefore, the benefits previously reported for plugged-in cooling, especially its benefit for the battery lifetime, have been likely overestimated.

A comprehensive battery cooling strategy should therefore combine key-on and plugged-in cooling with additional cooling when the vehicle is parked and not plugged-in (key-off cooling) [35,38]. With this strategy, the battery can be maintained at a low temperature throughout the day, while precooling (key-off or plugged-in) can always be applied. However, two critical concerns have discouraged the consideration of key-off cooling in the past. First, as key-off cooling is supported by the battery, it will reduce the AER. Second, discharging the battery to support key-off cooling increases cycling ageing, which may adversely affect the battery lifetime. Therefore, further research in this area is required.

3.3.6 Partial charging and the implication of key-off cooling

As discussed is Section 2.2.3, high SoC can be detrimental to the battery. Therefore, optimised partial charging has been proposed as a method to maintain a low SoC throughout the vehicle duty cycle and improve the battery lifetime, [40,42,44,45,241]. Therefore, this method can be potentially used to compensate for the low battery lifetime in hot climate conditions. The method typically includes using *a priori* knowledge of the duty cycle and charging the battery only as much as the vehicle consumes until it is plugged in again, eliminating the excess charge. Partial charging is especially effective if the vehicle is plugged in multiple times per day [44]. In the more common scenario that the vehicle is plugged in once per day, the battery should be charged enough to support an extended operation, so the excess battery charge will be lower and the window of partial charging will be limited.

Previous studies of partial charging have not considered the benefits of maintaining a low SoC relative to maintaining a low temperature. In other words, even when the vehicle was always plugged in, partial charging was optimised, while (plugged-in) cooling was either completely ignored [44], or was not optimised [40]. This is a significant shortcoming. To explain this, consider that when the vehicle is always plugged in, optimised partial charging uses *a priori* knowledge of the duty cycle (including the exact timing of the trips) to schedule charging in time for every trip to maintain a low SoC for an extended period of time [242]. Thus, the battery will not have sufficient charge for an early trip start. Plugged-in cooling, on the other hand, does not cause this issue. Therefore, if battery lifetime can be improved by optimal control of (plugged-in) cooling, this method is preferred to similar improvements realised from partial charging.

When the vehicle is not always plugged-in, understanding the relative benefit of partial charging and key-off cooling is critical. This is because partial charging affects the battery charge available for key-off cooling, while enabling key-off cooling further limits the window of partial charging. In addition, since key-off cooling can enable precooling, it can benefit more than one performance attribute. This suggests that improving the battery lifetime by key-off cooling can be preferable to improving it by partial charging. Therefore, more research on the relative importance of partial charging and cooling is required.

3.4 Research question

As explained above, application of key-off battery cooling has been previously ignored due to its potential implications for the vehicle AER in spite of its perceived benefits for battery lifetime. Furthermore, in previous application of partial battery charging for improving battery lifetime, analysing its benefits relative to that of cooling the battery have been overlooked. Therefore, further research is required to establish the absolute and relative benefits of key-off cooling and partial charging, hence, this research will focus on addressing the following question:

‘How can the ultimate benefits of key-off cooling and partial charging be evaluated for a PEV operating in hot climate conditions?’

3.5 Summary

In this chapter, the effect of hot climate conditions on three performance attributes of PEVs, namely their energy efficiency, thermal comfort, and battery lifetime, were established through reviewing the relevant literature. This review revealed that the high cabin and battery temperatures that result from hot climate conditions, and the associated cooling loads, reduce the energy efficiency, battery lifetime, and thermal comfort of PEVs. Possible methods for reducing the hot soak temperature of the cabin and the battery and reducing their cooling loads were reviewed. It was observed that various methods are available for reducing the heat gain of the cabin and improving cabin cooling. However, the only two methods that have been proposed for reducing the hot soak temperature of the battery, namely insulation and plugged-in cooling, are prone to important practical limitations. Specifically, the opportunity for plugged-in cooling is limited in real-life. This indicated the need for considering key-off cooling which has been neglected in the past. It was also observed that optimised partial charging is another method that has been proposed for improving the battery lifetime in hot climates, although the relative importance of partial charging and cooling the battery has not been considered. Therefore, this research will focus on finding a method to realise and evaluate the benefits of key-off cooling and partial charging in hot climates.

CHAPTER 4
RESEARCH METHODOLOGY

Introduction

This chapter outlines the methodology selected to answer the research question defined in Chapter 3, that is:

'How can the ultimate benefits of key-off cooling and partial charging be realised and evaluated for a PEV operating in hot climate conditions?'

As discussed in Chapter 3, key-off cooling can benefit vehicle performance attributes such as energy efficiency, battery lifetime and thermal comfort, while partial charging can benefit the battery lifetime. Therefore, answering the above question requires applying key-off cooling based on consideration of the individual, and the combinations of, the concerned performance attributes. It also requires analysing various combinations of partial charging and key-off cooling based on their implications for battery lifetime. These requirements are best satisfied by model-based optimisation techniques. Therefore, a representative PEV model is developed in this research to enable simulation of the performance attributes of a vehicle over a set of duty cycles. Then, model-based optimisation techniques are used to control key-off cooling and partial charging based on their benefits for the vehicle performance attributes. The assumptions about the vehicle and the approach to evaluating its performance attributes are outlined in Sections 4.1 and 4.2. The applicability of mode-based optimisation techniques for controlling key-off cooling and partial charging is explained in Section 4.3.

4.1 High-level assumptions

This section outlines the high-level assumptions about the type of the vehicle and the duty cycles considered for evaluating the vehicle performance attributes.

4.1.1 Vehicle type

This research focuses on application of key-off cooling and partial charging in a PPHEV. The specifications assumed for the vehicle are introduced in Chapters 5 and 6. While only one set of vehicle specifications including a certain battery type and cooling system architecture are considered in demonstrating the control methodologies within this thesis, the proposed methodologies are applicable to any PEVs given that the vehicle specifications only represent the boundary conditions of the problem at hand.

4.1.2 The duty cycles

For evaluating the performance attributes of the vehicle, a set of duty cycles are required that include a period of hot soak in which the vehicle is not plugged-in, followed by a trip. This is to allow capturing the effect of exposure to hot climate conditions on the performance attributes of the vehicle and to maximise the relevance of key-off cooling.

To achieve this, the following assumptions about the duty cycles of the vehicle were considered:

1. The common work commute usage case was assumed which typically includes an early morning trip (Trip 1), followed by an 8-hour-long park between 8am and 4 pm (Day Park), a second trip in the afternoon (Trip 2), and an overnight park until next day (Night Park).

2. For simplicity, identical drive cycles were assumed for Trip 1 and Trip 2. To investigate the effect of the travelled distance, energy demand, aggressiveness, etc. on the developed methods, the following four different drive cycles were considered:

- The NEDC which is the legislative drive cycle in Europe [76];
- The WLTC which will replace NEDC in the European legislation tests [243];
- The US06 which represents the aggressiveness of most real-life drive cycles, but is short [35];
- The Artemis, which combines aggressiveness with longer distance [244].

3. The operation of the vehicle in Phoenix, AZ and Seattle, WA were simulated and compared in this research. Phoenix has been commonly used in the literature as the reference hot geographical location [32,35,40,41]. Seattle has been used as the reference mild location in the literature [40,229,239] and has climate conditions similar to London, UK [198]. The climate conditions of these locations were represented by hourly profiles of air temperature, solar irradiance, and air humidity, as is the common practice [35,204], using the database available in [197]. In the interest of the generality of the analyses, hourly climate conditions are averaged over 6 months to arrive at a warm and a cold season for each location, rather than considering the hottest or coldest day of the year.

4. The vehicle was assumed to be plugged in once per day, in Night Park, in line with most common charging patterns (see Section 2.1.3). The just-in-time charging strategy was assumed to maximise the battery lifetime [35,199].

Considering the four drive cycles and four seasonal climate conditions (two per location) defined above gives a total of sixteen duty cycles for the vehicle. The idealised profile of the battery SoC and the phase sequence of the duty cycles are as shown in Figure 4-1.

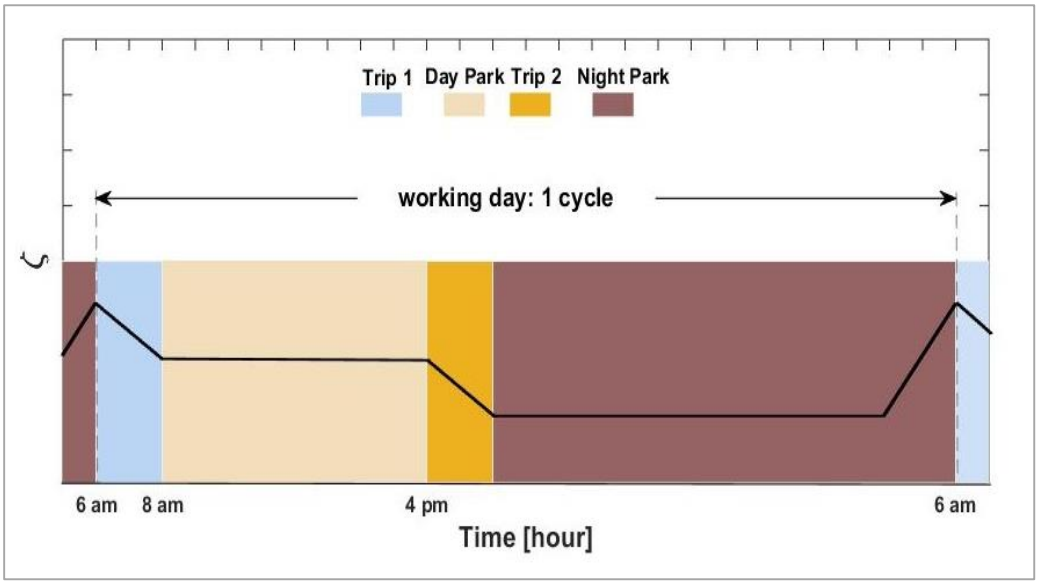

Figure 4-1. Structure of the duty cycles and the approximate variations in battery SoC

4.1.2.1 Applicability of key-off cooling

From the duty cycle assumptions, it follows that the vehicle undergoes a hot soak in Day Park, until the start of Trip 2. Given that the vehicle is not plugged in, the application of key-off cooling can be considered in Day Park to avoid accelerated battery ageing in this phase of the duty cycle, as well as minimising any impact on thermal comfort and fuel consumption in Trip 2. Clearly, key-off cooling affects the battery charge available for Trip 2. Therefore, the battery charge that can be allocated to key-off cooling without increasing the fuel consumption in Trip 2 is equal to the excess battery charge, which depends on the capacity of the battery, and the energy demand of the duty cycles.

4.1.2.2 Applicability of partial charging

In the duty cycles described above, partial charging involves determining the level of SoC to which the battery is charged in Night Park. Given the sequence of the phases of the duty cycle, charging the battery partially in Night Park will reduce the SoC in Day Park as well as in Night Park, and will likely reduce the storage ageing. The window of partial charging should be limited by the excess charge of the battery over the duty cycle, or it can deteriorate the fuel economy. In addition, partial charging reduces the charge available for key-off cooling. Therefore, considering the need for key-off cooling is essential in applying partial charging.

4.1.3 Evaluation of the duty cycles

The operation of the vehicle over the assumed duty cycle can be evaluated experimentally, or through simulation. The experimental approach will require access to a vehicle, as well as test facilities that can repeatedly replicate details of different vehicle duty cycles while providing control over key-off cooling and partial charging. Clearly, this approach will be time-consuming and disproportionately expensive, while lacking flexibility to any change in the high-level assumptions. The simulation approach is a faster, cheaper, and a more flexible alternative which has been commonly used in the past for similar research (as discussed in Chapter 3) and is therefore the preferred approach in the present research.

4.2 System simulation

The simulations should capture the behaviour of the vehicle subsystems that either are most affected by climate conditions, or contribute most to the concerned performance attributes (i.e. the energy efficiency, the battery lifetime and the thermal comfort attributes). In a typical vehicle, these subsystems include the powertrain, the cabin, the AC and the battery cooling subsystems. Therefore, a vehicle model is required that integrates models of these subsystems. Figure 4-2 shows the system-level block diagram of such a vehicle model including the key interactions between the subsystems.

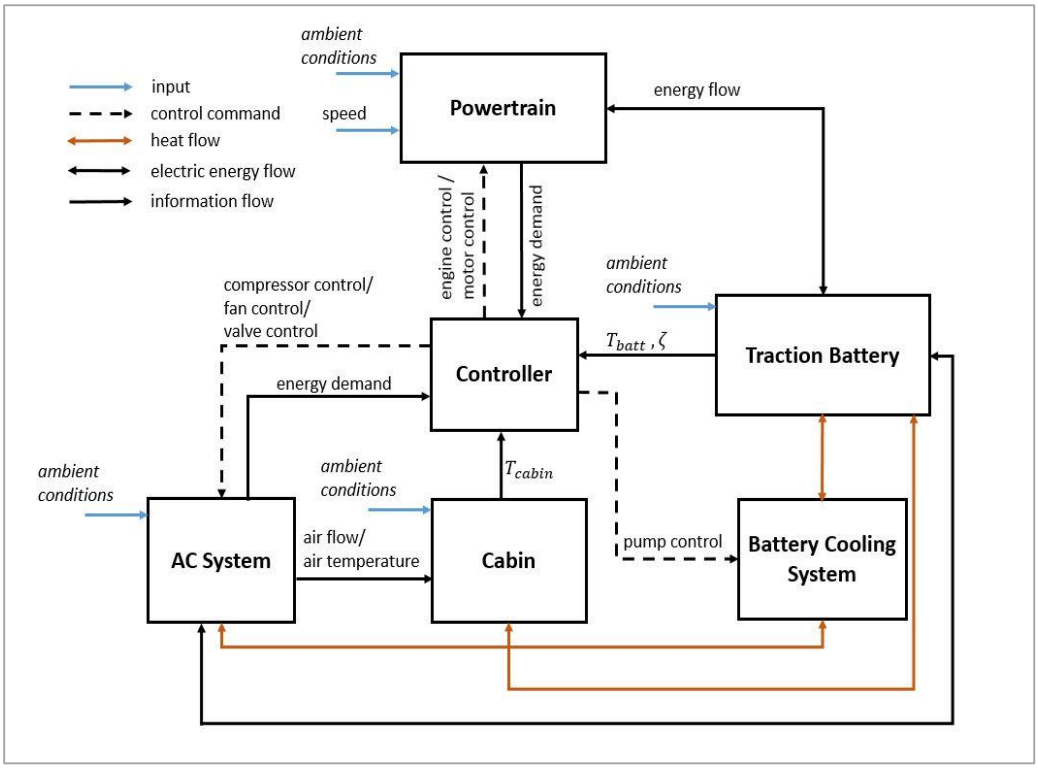

Figure 4-2. Proposed methodology: block diagram of the PHEV model

4.2.1 Model development

The ideal approach for ensuring that the PHEV model is representative of real-life vehicles is to develop the model to represent a commercially available vehicle. This requires knowledge of the specifications of the vehicle components and subsystems, as well as knowledge of the control algorithms, which are not available in the public domain. However, detailed specifications and test data from the current-model Range Rover HEV and some key information about a similar platform future-model Range Rover PHEV were available through the industry partner. The most significant differences between these two vehicles are in their powertrain (specifically the electric machine) and traction batteries, as well as in their control algorithms. Therefore, in developing the PHEV model of Figure 4-2, the subsystems are initially modelled based on the specifications of Range Rover HEV. The simulation results of the subsystem models are compared against the test data available from Range Rover HEV. Such comparisons enable verification of the overall performance of the models and their suitability for the purpose of this research, while highlighting any simulation discrepancies to support future

improvement of the models. Then, a limited number of modifications were applied to the models of the electric machine, the battery, and the control algorithms according to the information available from the future-model PHEV. The PHEV model is created from integration of the 'modified' subsystem models and is used in the subsequent analyses.

The thermal subsystems, i.e. the cabin, the AC, and the battery cooling subsystems, are developed in Modelica/Dymola (release 2015 FD01) to exploit the modular nature of the object-oriented modelling tool [245] and make use of the inbuilt specialised model libraries such as the AirConditioning [246,247] and the ThermoFluid libraries [248]. These libraries include basic models of the various heat exchanger types that are used in typical AC and battery cooling systems, as well as methods for efficient implementation of the thermodynamic properties of air, various refrigerants, and coolants.

MATLAB (release 2014b) and its inbuilt tools such as Simulink and Stateflow are widely used in model-based studies of the powertrain and control algorithms [249,250], therefore they are used in this work for modelling the powertrain and the control algorithms.

The thermal subsystems are integrated in Dymola, and imported to Simulink as one unit, where they are co-simulated with the powertrain and the controller subsystem using the Functional Mock-up Interface (FMI) standard [251]. The Claytex FMI toolbox (FMI 2, release 2016) is used for this purpose. Co-simulation allows using Dymola solvers for the thermal subsystems while using MATLAB solvers for the powertrain and the controller subsystems. This approach improves the performance of the vehicle model given the higher compatibility of Dymola models with Dymola solvers [252].

4.2.2 Evaluation of the performance attributes

Following the common approach explored in recent literature [37,40,41,236,253,254], battery lifetime is calculated based on the capacity loss measure, accepting 30% capacity loss as the EoL condition of the battery

[28,110,120,130,131]. The absolute fuel consumption over the vehicle drive cycles is used as the measure of fuel economy. Also, the cabin temperature is assumed to be a direct indicator of the passengers' thermal comfort, as is a typically accepted approach [223,255]. This allows for any increase in the cabin temperature to be associated to thermal discomfort.

4.3 Application of optimisation methods

4.3.1 Optimal control of key-off cooling

Key-off cooling is defined as an optimal control problem and is solved numerically using the method of Dynamic Programming (DP). A brief introduction to the optimal control theory is provided in Appendix 4. The principles of the DP method are also explained in Appendix 4. To minimise the computation effort to facilitate solving the problem on an ordinary desktop computer, it is assumed that key-off cooling is applied at maximum cooling power. This allows controlling key-off cooling with a control flag (a binary signal representing an on/off switch), limiting the number of the control variables to one. Therefore, the solution of the optimal control problem is the (key-off) cooling flag trajectory that minimises a specified cost function. Including low level control of the compressor, pump and fan may improve the energy efficiency of the key-off cooling but will disproportionately increase the computation effort of the DP problem.

Since key-off cooling, which is applicable to Day Park, also affects the vehicle over the subsequent phases of the duty cycle, *a priori* knowledge about the operation of the vehicle over Trip 2 and Night Park is required to solve the control problem. This is enabled by assuming that the key-on control algorithms of the vehicle (including algorithms of torque control, AC control, and the battery cooling control) are previously optimised, and remain unaffected by key-off cooling. Therefore, the operation of the vehicle over Trip 2 and Night Park can be simulated for a range of possible conditions in advance, and this information is used to solve the DP problem.

To investigate the adaptability of the above control method to different prioritisation of the performance attributes, a range of carefully selected scenarios are solved and analysed. The effect of key-off cooling on individual performance attributes, as well as any potential trade-off, is determined through these analyses.

4.3.2 Integrating the optimisation of partial charging and key-off cooling

Once a method for optimal control of key-off cooling is developed and proven, integration of optimised partial charging is considered. For the duty cycles assumed in this research, partial charging involves determining how much the battery should be charged in Night Park. Therefore, partial charging is approached as a parametric optimisation and solved with the Simulated Annealing (SA) method [256] which is proven to be a fast and efficient method for solving similar problems [257]. The just-in-time charging strategy is considered as default, given the benefits that were outlined in Section 2.1.3.

To integrate partial charging and key-off cooling, the SA algorithm iterates over different choices for the level of charge. For any level of charge, key-off cooling is optimally applied, following the method developed previously. A cost function is specified and evaluated and the optimum combination of the level of charge and key-off cooling flag trajectory is determined. It is assumed that the key-on cooling algorithms of the vehicle are not affected by partial charging (nor by key-off cooling) to facilitate a global solution.

The effectiveness of integrating partial charging and key-off cooling for improving the battery lifetime is demonstrated for different duty cycles. In each case, a range of carefully selected scenarios are solved and analysed to demonstrate the adaptability of the methods to different prioritisation of the relevant vehicle performance attributes.

4.4 Summary

This chapter outlined the methodology that is applied in this research to investigate the benefits of key-off cooling and partial charging. The high-level assumptions

made about the type of the vehicle and its duty cycles were explained, along with the tools that are used to develop a vehicle model that supports this investigation. Application of optimisation methods in this research and the overall approach that are used to evaluate the benefits of key-off cooling and partial charging were discussed.

CHAPTER 5 THE SUBSYSTEM MODELS

Introduction

In this chapter, the subsystem models developed towards creating the vehicle model required for this research are introduced. Through the industry partner, specifications and test data related to Range Rover HEV were available and were used to develop and verify the subsystem models. Section 5.1 gives the key details of the subsystems of the target vehicle. The development process of the powertrain, the cabin, the battery cooling, and the AC subsystems models are discussed in Sections 5.2 to 5.5. Where applicable, the process used for verifying the models is explained. In Section 5.6, the thermal subsystem models are integrated and simulated to show their ability in capturing the required thermal interactions. The discussions are summarised in Section 5.7.

5.1 The target vehicle

The vehicle has an all-wheel-drive parallel hybrid electric powertrain propelled by a diesel engine and an electric machine, which are mounted on a common shaft in a pre-gearbox arrangement. A friction clutch couples the engine and the driveline. The battery is liquid cooled, with cooling power provided by a chiller integrated in the refrigeration circuit of the AC system. The refrigeration circuit is composed of an electric compressor, an evaporator, a condenser, an internal heat exchanger (IHX), the chiller, and two TXVs with integrated shut-off function which regulate the flow of the refrigerant to the evaporator and the chiller.

A simplified illustration of the subsystems of Range Rover HEV is shown in Figure 5-1. The specifications of the key components of the vehicle are given in Table 5-1. Additional parameters and specifications used in developing the model are given in Appendix 1.

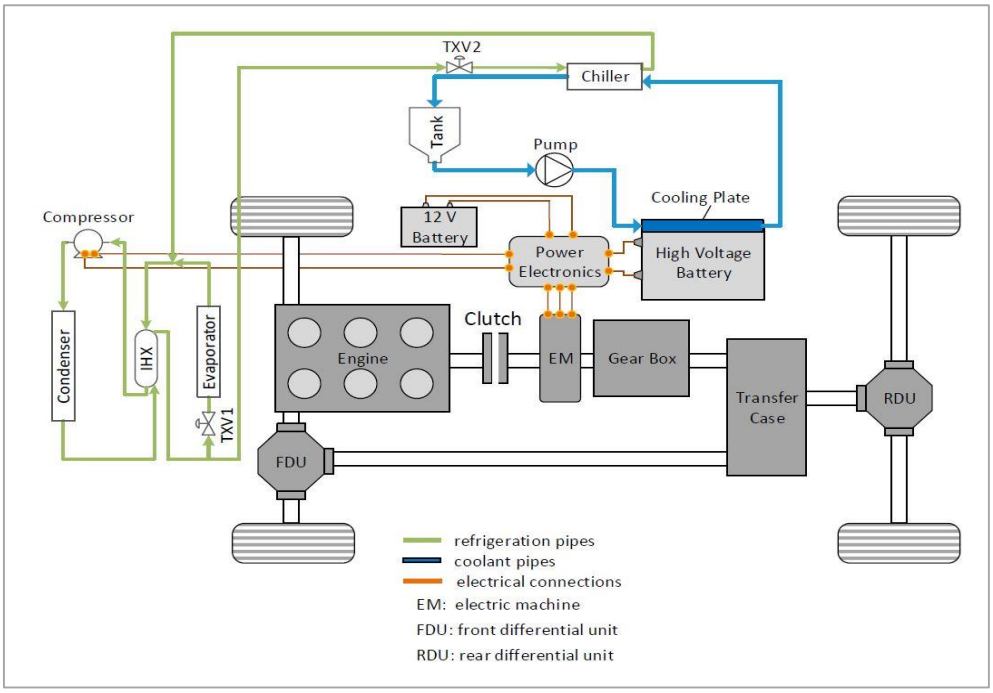

Figure 5-1. Layout of the subsystems in the target vehicle (the passenger cabin is not shown)

Table 5-1. Specifications of Range Rover HEV (provided by the industry partner)

Subsystem	Specification	
Powertrain	architecture	parallel (All-Wheel-Drive)
	EU test weight	2270 kg
	engine size	3.0 L v6 diesel, 140 kW
	electric machine size	35 kW , 180 Nm @ 2500 rpm
Battery	energy capacity	1.9 kWh
	voltage	260 V
	thermal capacity	1480 $\frac{J}{K}$
	cell type	6.5 Ah cylindrical NCA
	cell weight	0.34 kg
	pack electrical architecture	72 cells in series (6 modules of 12 cells)
AC system	compressor displacement	33 cc
	condenser cooling capacity	19 kW
	evaporator cooling capacity	9 kW
	chiller cooling capacity	3 kW
Battery cooling system	Coolant flow rate	0.1 $\frac{L}{s}$
	coolant type	40% Water-glycol solution
Cabin	number of seats	7
	internal air volume	3.5 L

5.2 The powertrain subsystem

This section introduces the powertrain model. The architecture of the powertrain of the target vehicle is shown in Figure 5-2.

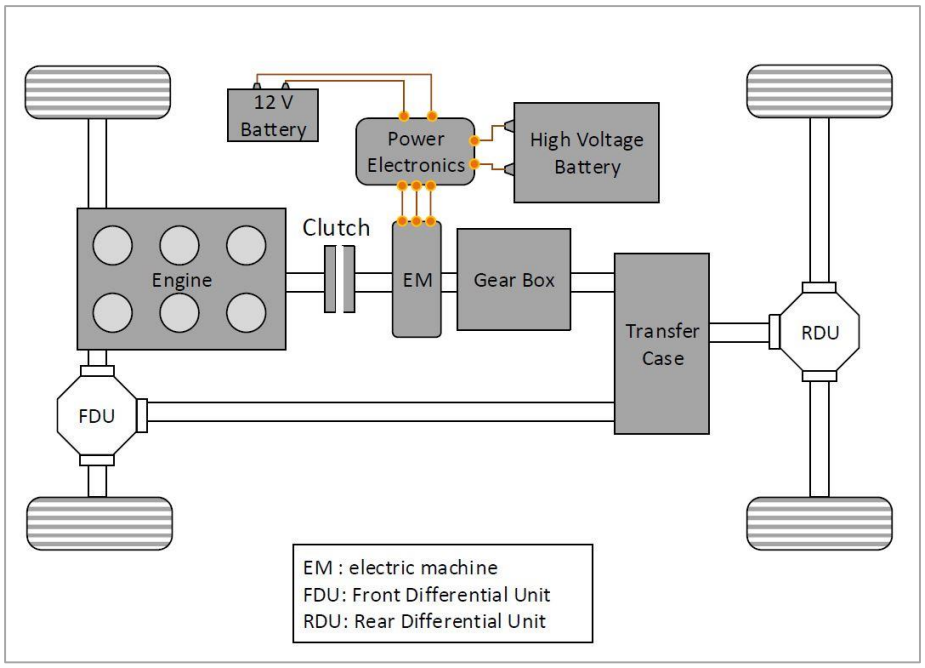

Figure 5-2. Architecture of the powertrain subsystem

The all-wheel-drive powertrain of the is comprised of an eight-speed gearbox, a transfer case and two differential units on the front (FDU) and rear (RDU) axles. The electrical architecture of the vehicle includes the high voltage battery and power electronics (including dc-dc converters and a three phase inverter), as well as a 12-volt battery.

In modelling of the powertrain, the following high level assumptions were considered:

1. Traction torque was distributed evenly between the front and rear axles and between the right and left wheel of each axle. Therefore, the transfer case and the differential units operate as simple torque split gears.

2. The clutch was modelled as an ideal unit, ignoring the synchronization process during engagement/ disengagement

3. The dynamics of tyres were neglected, and the wheels were modelled as rigid discs with negligible slip

4. Low voltage loads were neglected, allowing to ignore the electrical connection between the low and high voltage batteries.

Details of the key components of the model and the implemented control logic are explained in Sections 5.2.1 to 5.2.6. The underlying equations have been taken from references [258–260].

5.2.1 The vehicle dynamics

The powertrain model was developed based on the longitudinal dynamics of the vehicle. Ignoring the dynamics of the tyres, the traction force required at the wheels F_T was given by

$$F_T = M\frac{dv}{dt} + F_A + F_{RR}. \tag{5-1}$$

In the above equation, M is the equivalent vehicle mass, v is the longitudinal speed. Also, F_A is the aerodynamic resistance given by

$$F_A = \frac{1}{2}\rho C_D A v^2 \tag{5-2}$$

where ρ denotes air density, C_D denotes the drag coefficient, and A is the frontal area of the vehicle. F_{RR} in equation (5-1) is the rolling resistance which had been mapped onto the load on each wheel and the vehicle speed (see Appendix 1). The map was implemented in the model in form of a look-up table.

The traction torque delivered to the wheels was calculated from the traction force as:

$$\tau_w = F_T r + I_w \frac{d\omega_w}{dt} \tag{5-3}$$

in which τ_w is the wheel torque, I_w represents the wheel inertia, and ω_w is the wheel speed.

5.2.2 The driveline

In modelling of the driveline, all shafts are assumed to be rigid. Gears are modelled with their ratio, inertia, and losses. Torque transfer across a gear with ratio of B_g can be described by

$$B_g \tau_{in} - \tau_{loss} - \tau_{out} = J_g \frac{d\omega}{dt}, \tag{5-4}$$

in which ω is the gear speed, τ_{in} and τ_{out} denote the torque acting on its input and output shafts, respectively, τ_{loss} denotes losses, while J_g represents its inertia. All gear losses had been mapped on the speed and torque of the gear (see Appendix 1), and were implemented in the model in form of look-up tables.

Knowing the total driveline gear ratio and losses, the torque and angular velocity at gearbox input were calculated from the torque and speed of the wheels using (5-4). The differentials and the transfer box have constant gear rations. The gear ratio of the gear box was determined based on shift maps which specify the gear speed of upshifts or downshifts for every gear and different accelerator pedal positions (see Appendix 1). The shift maps were implemented in the model in form of look-up tables.

The pedal position in this model was reconstructed by dividing the torque demand calculated at the gearbox input τ_d by the total torque capability of the vehicle as

$$\theta\% = \frac{\tau_d}{\tau_{em,max} + \tau_{eng,max}} * 100 \tag{5-5}$$

where $\tau_{em,max}$ and $\tau_{eng,max}$ denote the maximum torque of the electric machine and depend on their speed (see Appendix 1) and were implemented in the model, in form of look-up tables.

The speed of the electric machine is known as it is integrated to the driveline. The model assumes that the engine is either off and decoupled from the driveline, or on and rigidly coupled to it by the clutch; so the engine speed was calculated accordingly. The torque demand at the input of the gearbox is distributed between the engine and the electric machine ($\tau_d = \tau_{eng} + \tau_{em}$), depending on the operating mode of the vehicle.

5.2.3 The electric machine

In modelling of the electric machine, it was assumed that the torque demanded from the machine was readily met, thus, the purpose of the model is to calculate the electric power of the machine in motoring and generation. From its speed and torque, the mechanical power of the machine was calculated as

$$P_{em,mech} = \left(\tau_{em} + J_{em}\frac{d\omega_{em}}{dt}\right)\omega_{em}, \tag{5-6}$$

and the corresponding electric power (at battery terminals) was calculated as blow using the combined efficiency map of the electric machine and the power electronics

$$P_{em} = \begin{cases} \frac{P_{em,mech}}{\eta_{em}} & motoring \\ P_{em,mech} \cdot \eta_{em} & generation \end{cases}. \tag{5-7}$$

5.2.4 The engine

As in the case of the electric machine, the engine model assumes that the torque demanded from the engine is readily delivered. The model calculates the fuel consumption from the steady-state fuel flow map of the engine, which gives the fuel flow at different engine torques and speeds (see Appendix 1). The map was implemented in the model in form of a look-up table.

5.2.5 The battery (electrical model)

In developing the electrical model of the battery, it was assumed that all cells within the pack have identical behaviour. A zero-order equivalent electric circuit cell model which considered to be suitable for the purpose of the research. As shown in Figure 5-3, the model includes an ideal voltage source and a resistance, with the following voltage balance model

$$V_{cell} = V_{oc} - i\,R_0 \tag{5-8}$$

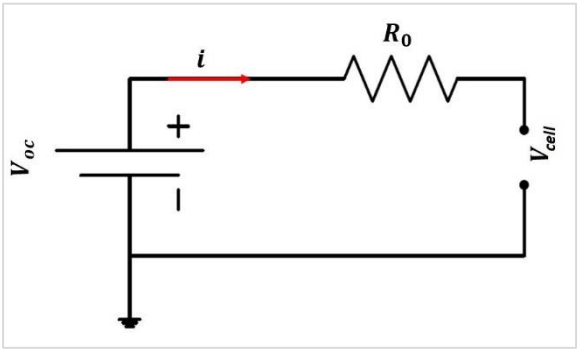

Figure 5-3. Zero-order equivalent electric circuit model of a battery cell

Given the electrical architecture of the battery in which all cells are connected in series, the relation between the voltage and current of the battery and its cells is as follows

$$\begin{cases} V_{batt} = N\,V_{cell} \\ i_{batt} = i \end{cases} \tag{5-9}$$

where V_{batt} denotes the battery voltage and N is the number of cells (72 cells). Writing equation (5-8) for power of the cell gives

$$P_{cell} = V_{oc}\,i - i^2 R_0\,. \tag{5-10}$$

The power of the cells was calculated from the power of the battery which is the sum of the power demand of the electric machine and the AC compressor:

$$P_{cell} = \frac{P_{batt}}{N} = \frac{P_{em} + P_{comp}}{N} \tag{5-11}$$

It is known that the internal resistance and the open-circuit voltage depend on the characteristics of the cells, and are typically determined as functions of SoC and temperature. The data available from the cells captures the dependency of the open-circuit voltage and the internal resistance on SoC, while only the dependency of resistance on temperature is captured. This is however acceptable as the dependency of the open-circuit voltage on temperature is negligible above 20°C [261,262] where this research is focused. The open-circuit voltage and resistance of the cells (see Appendix 1) were implemented in the model as look-up tables.

To calculate the SoC of the cell, the coulomb counting method was used. Assuming that all cells within the battery pack are identical and receive equal currents follows that the SoC of the battery pack is equal to the SoC of each of the cells.

Heat generation within the cell is associated to Joule heating. The total heat generation within the battery is

$$\dot{Q}_{gen} = N\, R_0\, i^2 \tag{5-12}$$

The generated heat is used to calculate the thermal conditions of the battery pack. This will be discussed in Section 5.4.1.

5.2.6 The control logic

The purpose of the control logic is to distribute the torque demand (at the gearbox input) between the engine and electric machine, in the most efficient manner. The control algorithms of the target vehicle could not be accessed for the purpose of this work. The approach chosen here is to develop a rule-based algorithm based on the general operating modes of a parallel HEV, as explained in Section 2.1 The control logic has three modules:

1. The mode controller, which is a state machine that defines the operating mode of the vehicle by comparing the torque demand with the limits of

operation of the electric machine, the engine, and the battery. The parameters used in the control logic are described in

2. Table 5-2.

3. The torque distributor, which allocates positive torque demands to the engine and the electric machine based on the selected operating mode.

4. The brake controller, which blends electric and mechanical braking.

Table 5-2. Parameters used in controlling the powertrain operating modes (as provided by the industry partner)

Parameter Description	Value
maximum vehicle speed for electric drive: beyond this limit engine starts	6.5 $\frac{m}{s}$
maximum vehicle speed for hybrid mode operation: beyond this limit conventional mode is selected	30 $\frac{m}{s}$
maximum vehicle speed for electric braking: below this limit electric braking stops	1.5 $\frac{m}{s}$
maximum vehicle speed for electric braking: above this limit electric braking stops	30 $\frac{m}{s}$
minimum SoC for staying in electric drive	50 %
maximum SoC for charging the battery with the engine	60 %
maximum SoC for regenerative braking: beyond this limit regeneration is deactivated	70%
maximum regenerative braking torque of the electric	70 Nm
minimum duration of engine on: when engine starts, it remains on for this duration (unless brake occurs)	10 s
battery overheat threshold (power cap): above this limit the battery's power is limited at 50%	45°C
battery overheat (power cut-off): the battery is not used above this limit	50°C

5.2.7 Verification of the powertrain model

For verifying the powertrain model, a data set obtained through characterisation test of the target vehicle on a chassis dynamometer was available. The overall

procedure followed in the test is consistent with the EU emission test procedures explained in Section 2.1.2. More specific test conditions are given in Table 5-3.

Table 5-3. Conditions of powertrin characterisation test

Condition	Setting	Condition	Setting
ambient temperature	25°C	battery coolant pump	active
initial battery temperature	30°C	Low voltage dc-dc converter	disconnected
initial battery SoC	54.7%	12 volt loads	free
initial engine oil temperature	25°C	AC compressor	disconnected

The verification of the models was first carried out at component level; for the engine, the electric machine, and the battery, which proved acceptable accuracy of the models. In each case, a set of signals logged from the vehicle were provided as inputs to the model, and the outputs of the model were verified. For example, the engine model was simulated using the logged engine torque and speed signals. Comparing the calculated (simulated) and measured fuel flow showed that the accuracy of the model was within 2%.

Although the control logic implemented within the model is not representative of the algorithm within the vehicle, comparing the response of the complete powertrain model against test results can help verify whether the control logic can replicate the operating modes of the powertrain. To achieve this, the model was simulated using the logged speed and gear shift signals as inputs. A constant battery temperature of 30°C was forced since the battery cooling system model was not included in the simulation. Figure 5-4 compares the key simulation and test results. Despite some discrepancies, the model closely follows the key operating modes of the vehicle. The following observations can be made:

1. The vehicle operates in EV mode within the limits of operation defined by the control rules ($v < 6.5\ \frac{m}{s}$ and $\zeta > 50\%$);

2. The engine starts when the vehicle speed exceeds 6.5 $\frac{m}{s}$. When the engine is on, it is coupled with the electric machine and acts as the primary propeller;

3. When battery SoC is low ($\zeta < 50\%$), the engine provides 70 Nm extra torque to charge the battery;

4. The engine stops with deceleration events (when brake torque is required);

5. Regenerative braking takes place at all braking events (given that the vehicle operates within the operating limits set by the rules);

6. The Battery is discharged in EV mode, and charged through regenerative braking or through engine charge.

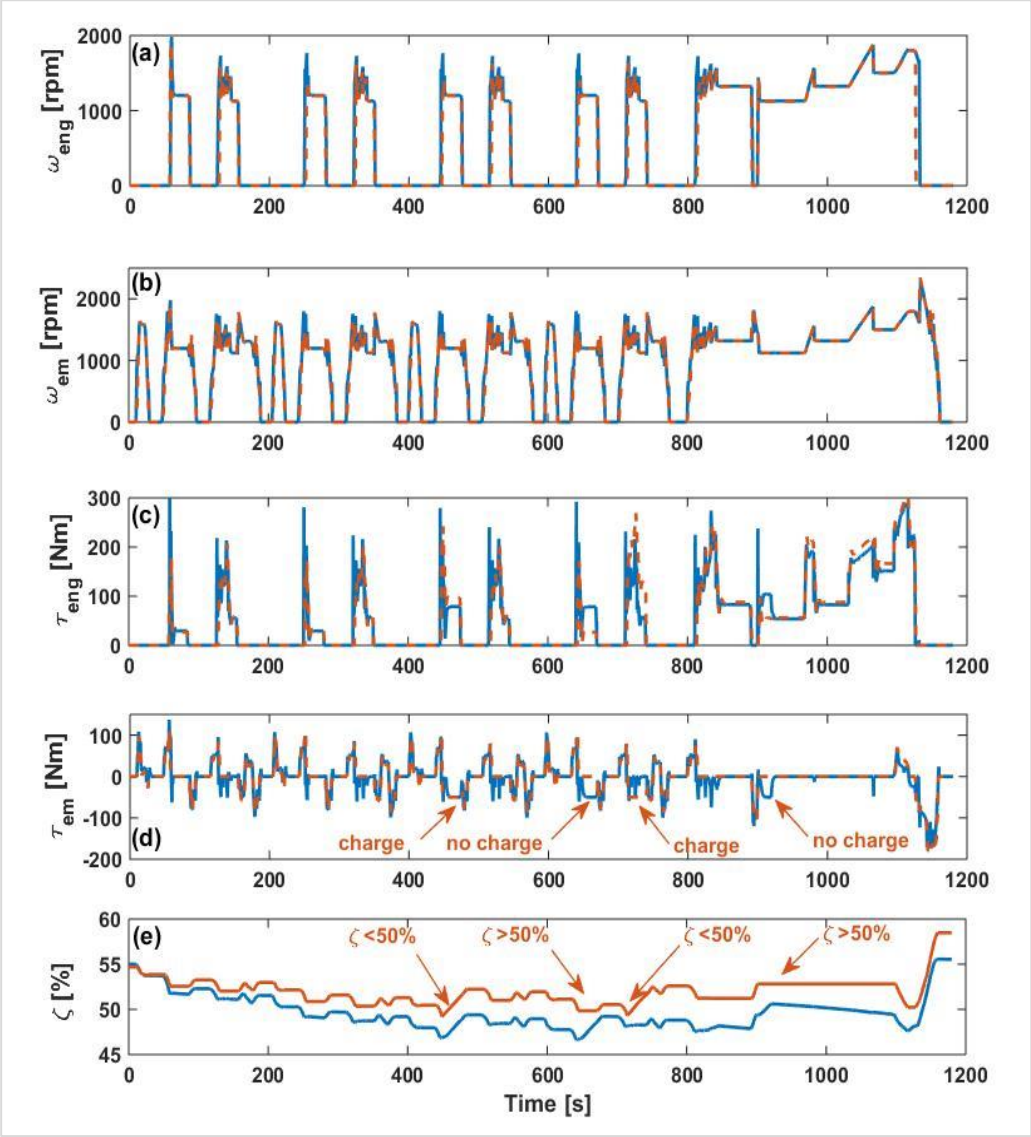

Figure 5-4. Verification of the the powertrain model (final 200 seconds of the results) (a) engine angular velocity, (b) electric machine angular velocity, (c) engine torque, (d) electric machine torque and (e) SoC. ***Annotation- blue: test, red: simulation***

The most significant discrepancy observed in the above results is due to an error between the simulated and logged SoC. As Figure 5-4(e) shows, the first charge event is common between the simulation and the test results, but the subsequent charge events are shifted in time, creating inconsistencies between the simulated and logged torque profiles. Further investigations indicated that these discrepancies are due to an inaccuracy in the measurements, rather than in the models. This can be inferred from Figure 5-5 which shows the torque and speed of the electric machine, as wells the current, voltage, and the SoC of the battery, as logged in the final 200 seconds of the test. It can be seen that when the electric

machine is not used (zero torque), the battery is discharged (positive current and decreasing voltage and SoC), which defies the expectation as no other load exists on the battery (see Table 5-3).

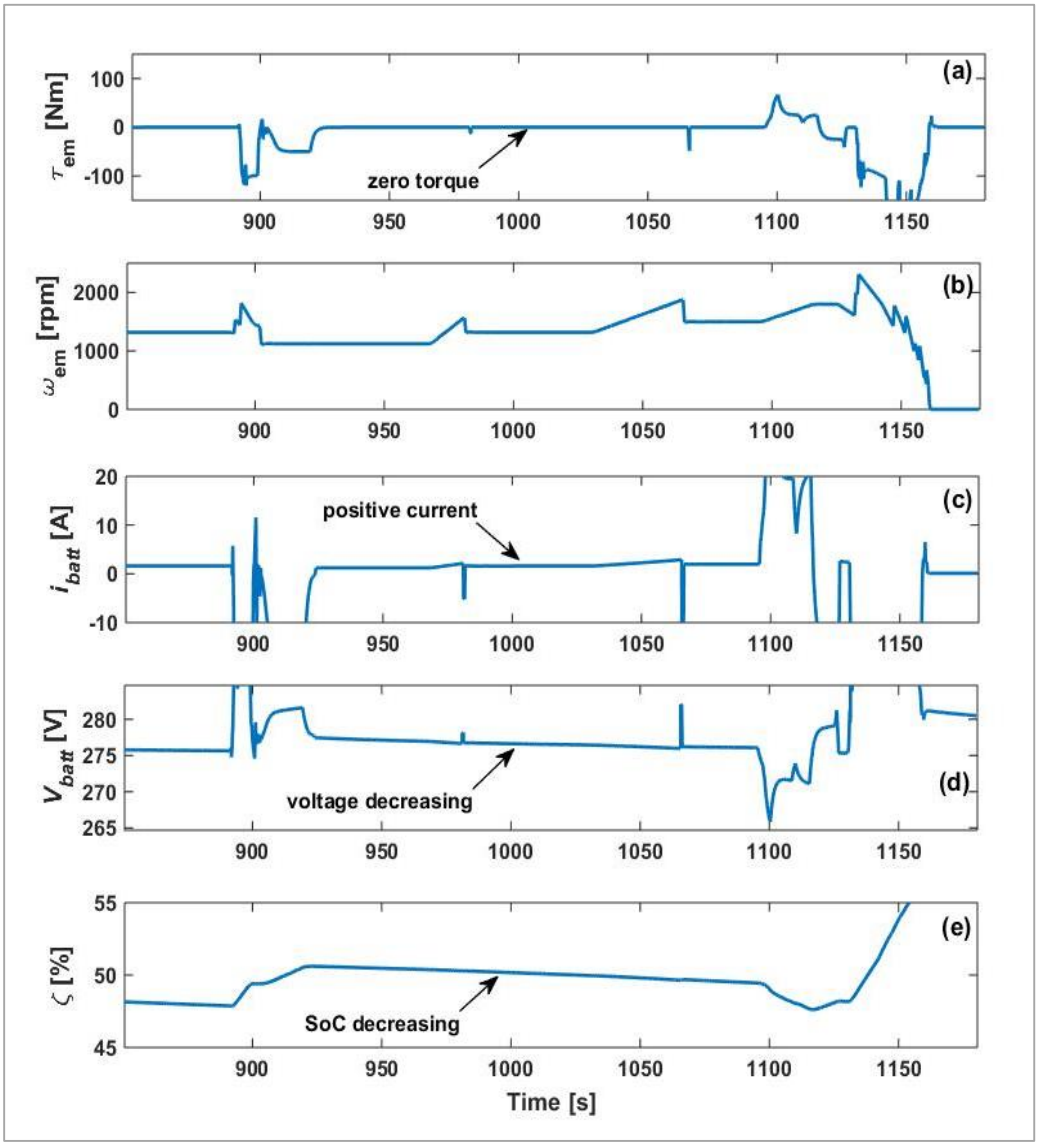

Figure 5-5. Showing the signals logged in the final 200 seconds of the test: (a) torque, and (b) speed of the electric machine, as well as (c) current, (d) voltage, and (e) SoC of the battery.

Other than the above discrepancy, four discrepancies periodically repeat in Figure 5-4. These are all captured in Figure 5-6 which shows the final 200 seconds of Figure 5-4. The following observations can be made:

- point A on Figure 5-6(b): The engine is started early, before the speed limit is reached, with no apparent influence from the battery or electric machine

constraints. This discrepancy occurs in two occasions throughout the test and suggests that more sophisticated algorithms are used within the vehicle for controlling the engine.

- point B on Figure 5-6(b): engine de-clutched from the driveline at brake events before stopping. The model neglects couplings and assumes that the engine stops immediately therefore such discrepancies are consistent with the fidelity of the model.

- point C on Figure 5-6(d): The vehicle enters a charging mode that is not captured by the model due to current measurement error, as discussed earlier.

- point D and E on Figure 5-6(e): during gear shifts, highly transient electric machine torques are detected in the test which are not captured by the model. These transient torques are likely a result of synchronization process of the transmission which are not considered in the model.

Although some discrepancies between the test and simulation results at this fine degree of detail remain unexplained, they do not affect subsequent analyses and conclusions. Improving the accuracy of the model can be addressed as part of a future project.

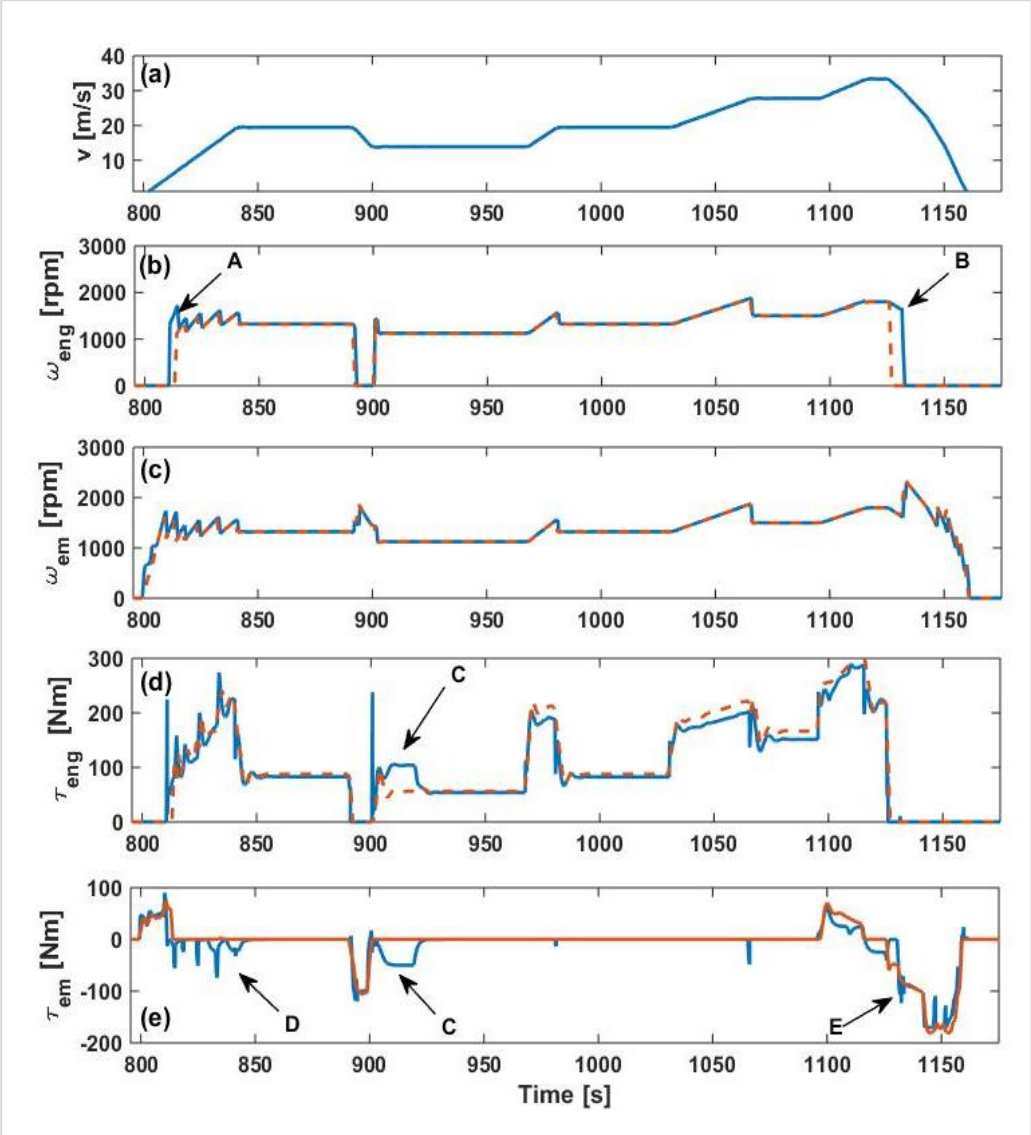

Figure 5-6. Verification of the powertrain model: (a) vehicle speed, (b) engine speed, (c) electric machine speed, (d) engine torque, (e) electric machine torque

5.3 The cabin subsystem

The cabin model was adapted from a model created by the industry partner for the conventional equivalent of the target vehicle. In this section, first the key features of the original model are introduced then, the modifications made to the model to adapt it to the target vehicle are explained. Finally, the verification result of the modified model is discussed.

5.3.1 Key features of the original cabin model

Figure 5-7 shows the thermal network of the original cabin model. In this model, the thermal conditions of the cabin are associated the following interactions:

1. convection between ambient air and the cabin shell
2. solar irradiance incident on the cabin shell
3. conductance through the shell
4. transmittance of solar irradiance through the cabin shell
5. convection inside the cabin,
6. radiation from the cabin shell to ambient
7. heat exchange with the AC subsystem (not shown in Figure 5-7)

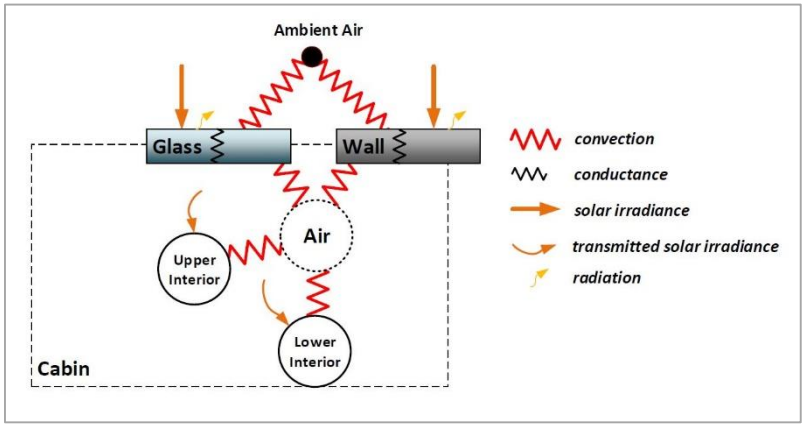

Figure 5-7. The thermal network of the cabin model as provided by the industrial partner

To model the thermal interactions with ambient (i.e. convection and solar irradiance) the model assumes that the cabin shell is composed of two horizontal blocks, representing the glass and wall segments within the shell. The blocks are parameterised for the total area and average material properties of the relevant segment of the shell.

Heat transfers to cabin air (air enclosed within the cabin) is through convection with the shell and the interior of the cabin. The interiors of the cabin (seats, dashboard, etc.) are represented by two heat capacities, representing the upper and lower interior of the cabin. The interiors exchange heat with cabin air as well as receiving the component of solar irradiance transmitted through the cabin glass.

The cabin air is represented by a lumped air volume with ideal mixing. It is assumed that air enters and exits the cabin at the same flow rate. So, once the total heat flow to cabin air is calculated, its net internal energy and temperature is calculated based the first law of thermodynamics knowing the enthalpy of the air stream entering and exiting the cabin.

5.3.2 Modifications to the model

In addition to the thermal interactions considered in the original model, the cabin of Range Rover has thermal interactions with the battery pack. Therefore, two heat transfer paths were added to the model, from the lower interior and the wall of the cabin to the battery, as shown in Figure 5-8. The thermal resistance between the cabin and the battery were available. These and other key parameters used within the model are given in Table 5-4.

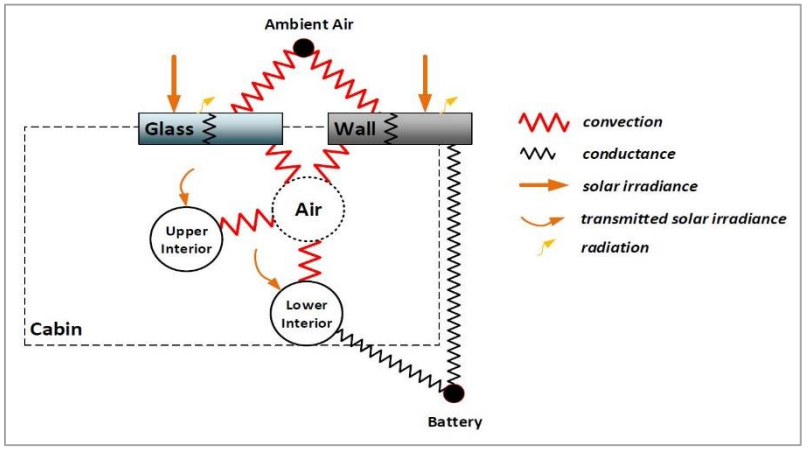

Figure 5-8. Thermal network of the modified cabin model

Table 5-4. The parameters used in the cabin model as provided by the industry partner

Parameter	Value	Unit
Cabin length	3.2	m
Glass area	4.8	m^2
Wall area	5.5	m^2
Glass absorptance	0.5	--
Glass transmissivity	0.1	
Glass emissivity	0.9	
Glass heat capacity	1090	$\frac{J}{kgK}$

Table 5-4 (continued). The parameters used in the cabin model as provided by the industry partner

Parameter	Value	Unit
Sheet metal absorptance (cabin wall)	0.4	--
Sheet metal emissivity (cabin wall)	0.07	--
Cabin wall heat capacity	800	$\frac{J}{kgK}$
Cabin wall conductivity	0.04	$\frac{W}{mk}$
Shell-ambient natural convection coefficient	1	$\frac{W}{m^2K}$
Cabin shell convection coefficient (30 kph)	25	
Cabin interior natural convection coefficient	2	
Cabin interior convection coefficient (130 $\frac{L}{s}$ air flow)	10	
Cabin interior- battery thermal resistance	0.06	$\frac{K}{W}$
Cabin panel- battery thermal resistance	0.1	$\frac{K}{W}$

5.3.3 Verification of the cabin model

For verifying the cabin model, a dataset related to the climatic test of the target vehicle was provided by the industry partner. The test includes a pull-down and a hot soak and is are part of the standard procedure for evaluating automotive AC systems. Details of the test procedures are outlined in [263]. To facilitate the interpretation of the results, a brief explanation will be provided here.

The vehicle is placed in a climatic chamber (schematically shown in Figure 5-9) equipped with wind tunnels, solar lamps, and a chassis dynamometer. The chassis dynamometer is used to load the powertrain, while the wind tunnel and the solar lamps emulate the effect of air flow and solar load on the vehicle.

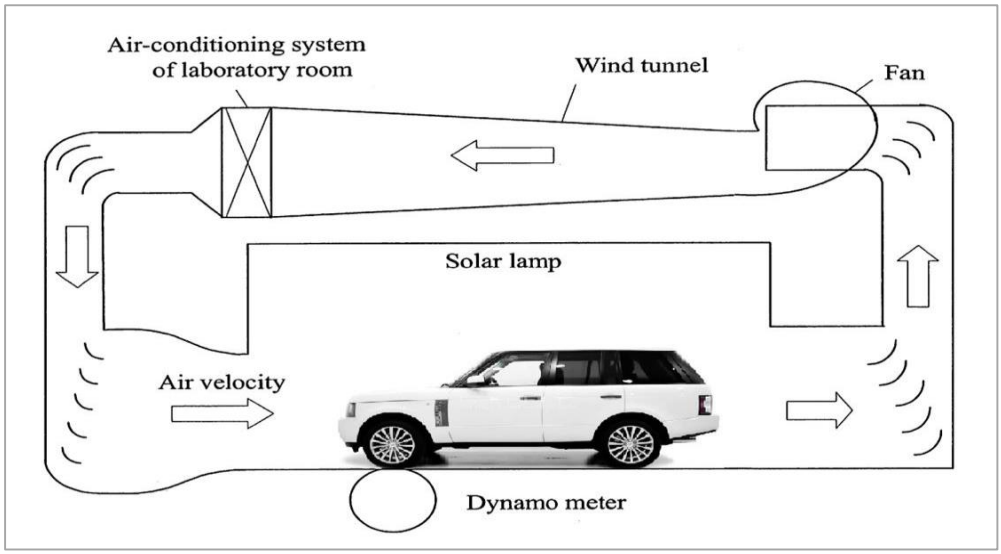

Figure 5-9. Schematics of a typical climatic chamber

In the pull-down test, the vehicle is placed in the climatic chamber for approximately three hours under the conditions given in Table 5-5. At the start of the test, the AC system is switched on at maximum power in recirculation mode, and as the vehicle is driven over a purpose-built drive cycle[1]

Table 5-5. Climate chamber conditions for pulldown and hot soak

Air Temperature	Solar Irradiance	Relative Humidity
[°C]	$[W/m^2]$	[%]
43	850	60%

Figure 5-10 shows the vehicle speed profile as well as the average temperature of cabin air [2], average battery temperature [3], and temperature of the air stream flowing into the cabin [4], during the pull-down test carried out on the vehicle. It can be seen that the cabin temperature is approximately 59°C at the start of the test, and a complete pull-down of the cabin (to 24°C) takes more than 3000 seconds. The battery cooling system is controlled manually in this test, and is activated twice, once after approximately 1000 seconds into the test (remaining active for approximately 2000 seconds), and once after approximately 4000 seconds into the

[1] The aim of the pull-down test is to determine the time and energy required to cool the cabin to 24°C under hot climate conditions.
[2] This will be referred to as 'cabin temperature' and denoted by (T_{cabin}) hereafter.
[3] This will be referred to as 'battery temperature' and denoted by (T_{batt}) hereafter.
[4] This will be referred to as 'vent temperature' and denoted by (T_{vent}) hereafter.

test (remaining active until the end of the test). It is worth noting that activation of battery cooling leads to a noticeable increase in cabin and vent temperatures, due to the distribution of cooling power between AC and battery cooling.

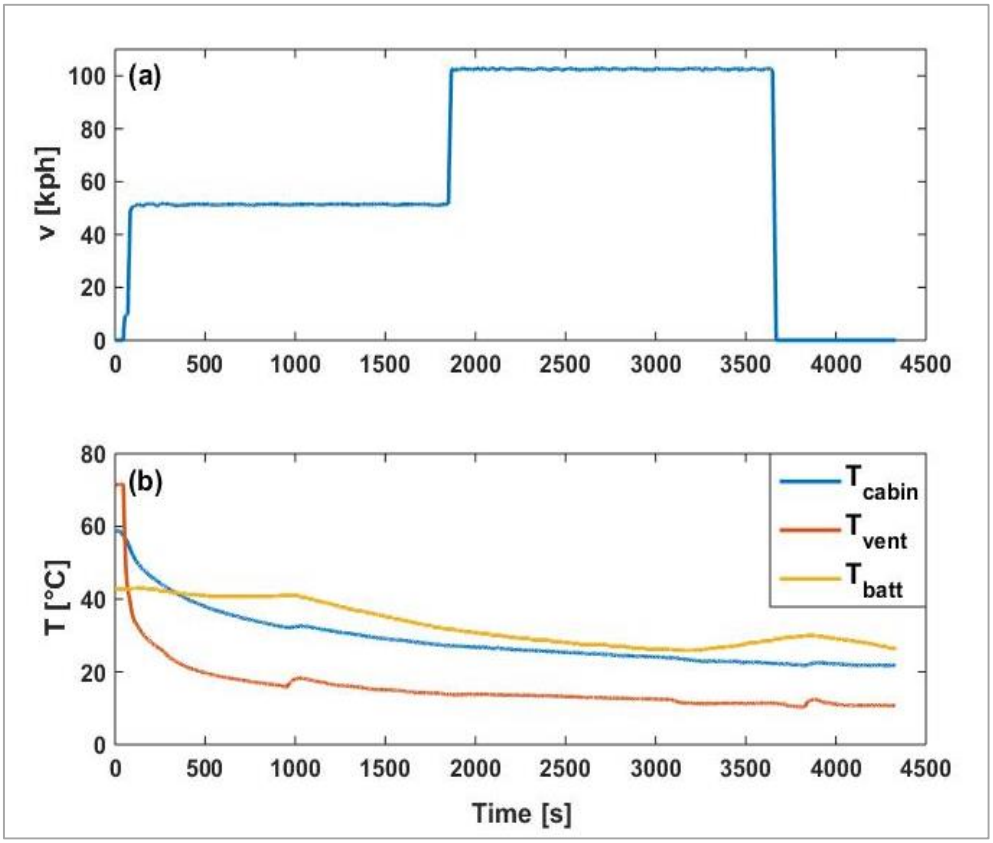

Figure 5-10. (a) vehicle speed (b) cabin, vent and battery temperature during the pull down test

In the hot soak test, the vehicle remains passive inside the climatic chamber, under the conditions given in Table 5-5, and the cabin temperature is measured. Figure 5-11 shows the profile of the cabin temperature in a hot soak test on the target vehicle. In this test, the vehicle was left with open doors overnight inside the chamber at 43°C, reaching thermal equilibrium with the chamber. Then the doors were closed and the solar lamps were switched on. Within three hours, the cabin temperature reaches approximately 68°C.

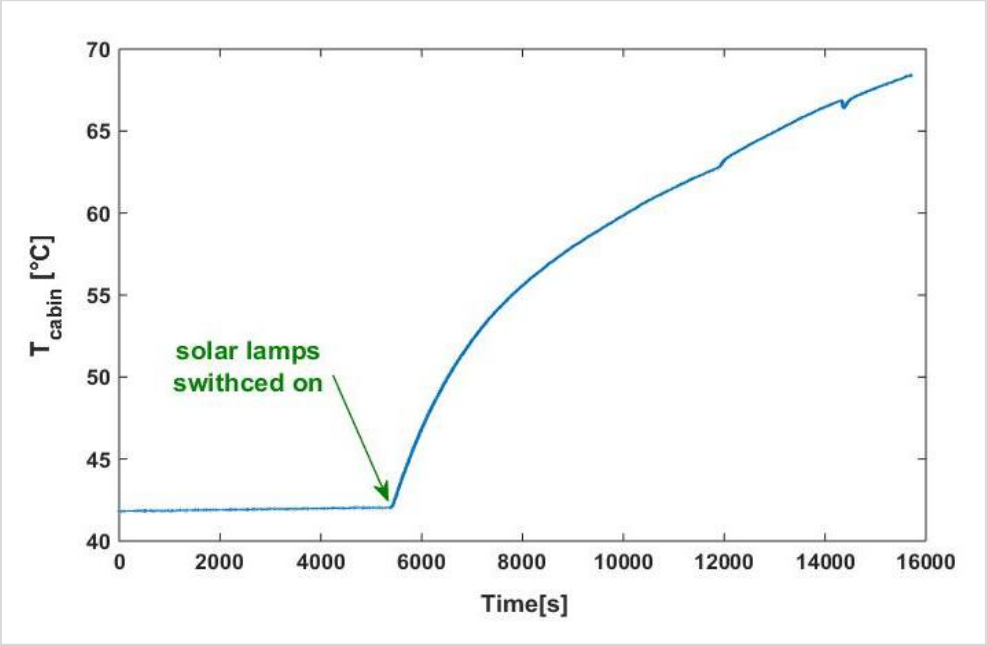

Figure 5-11. Variations in the average cabin temperature during hot soak test

The pull-down and hot soak tests encompass all of the conditions that the cabin model is expected to simulate. For simulating the hot soak test, the conditions of the chamber (Table 5-5) and the initial conditions of the cabin should be provided to the model as inputs. In addition to these inputs, simulating the pull-down test requires the vehicle speed, battery and vent temperatures (Figure 5-10), as well as the vent flow rate (130 $\frac{L}{s}$) as inputs.

The simulated and measured cabin temperatures are compared in Figure 5-12. It can be seen that the model is able to simulate both tests and capture the effect of the variations in the vent temperature and ambient conditions (solar load). In the first 500 seconds of the pull-down test, the simulated cabin temperature reduces faster than the measured values. This is likely due to the transients of air flow and vent temperature at the start of the tests that have been ignored in this simulation. Nevertheless, the absolute error of the model is approximately 2.2°C. After the initial transients, the accuracy of the simulation increased. The absolute error of the hot soak simulation in 1°C. These observations confirm the model is suitable for the purpose of the intended research.

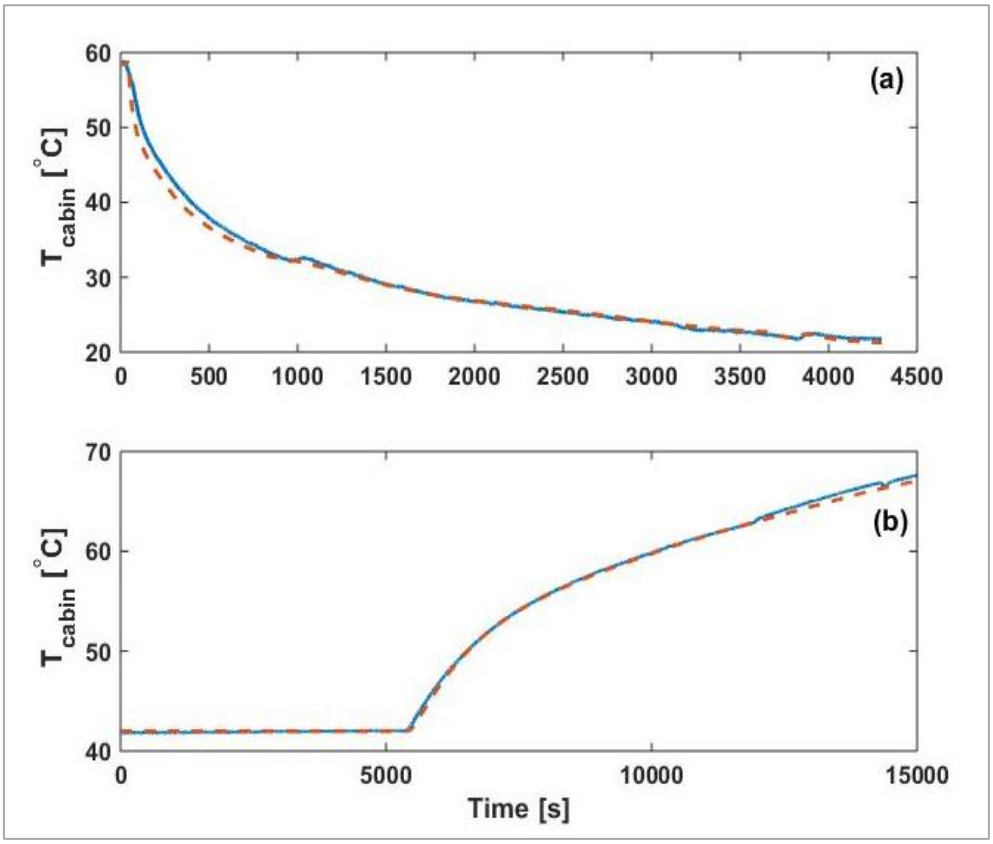

Figure 5-12. Calibration and validation of cabin model against (a) pull-down test, (b) soak test. (Annotations- blue line: test results, red line: simulation results)

5.4 The battery cooling subsystem

Figure 5-13 shows the layout of the battery cooling subsystem of the target vehicle. This section explains details of the model developed for this subsystem, specifically the battery pack, pump and the tank. The chiller model will be explained as part of the explanation of the refrigeration circuit in Section 5.5.2.

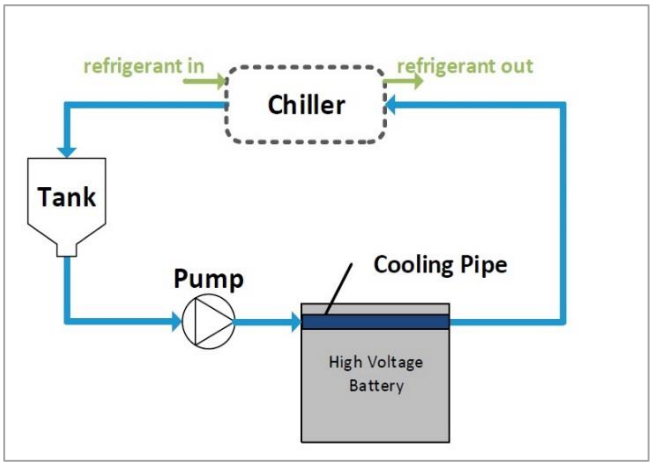

Figure 5-13. Layout of the battery cooling circuit

5.4.1 The battery (thermal model)[1]

The thermal model of the battery pack was represented by a heat capacity with thermal interaction with the coolant within the cooling plates, the ambient air, and the cabin. The model does not distinguish between individual cells of the battery pack. The following heat balance model is assumed

$$\dot{Q}_{amb} + \dot{Q}_{clnt} + \dot{Q}_{cabin} + \dot{Q}_{gen} - \mathcal{C}_{batt}\frac{dT_{batt}}{dt} = 0. \tag{5-13}$$

The first three terms on the right hand side of equation (5-13) denote heat transfer between the battery and the ambient air, the coolant, and the cabin, respectively, while the fourth term represents the internal heat generation discussed in Section 5.2.5. Also $\mathcal{C}_{batt}$ in equation (5-13) is the (bulk) thermal capacity of the battery while T_{batt} is its temperature. The key parameters used in developing the model are listed in Table 5-6.

The heat transfer from ambient air can be expressed as

$$\dot{Q}_{amb} = \frac{(T_{amb} - T_{batt})}{R_{amb}} \tag{5-14}$$

[1] The equations used to develop this model were taken from chapter 8 of reference [264].

where T_{amb} is the ambient (air) temperature while R_{amb} denotes the total thermal resistance between the battery and ambient and was provided to the model as a function of the vehicle speed. To model the heat transfer path between the battery pack and the coolant, the following assumptions were made, according to the method described in Section 8.3.2 of [264]:

1. The coolant flows through a straight cooling pipe with circular cross section;
2. The conductance through the pipe wall pipe is infinite (i.e. the wall is massless);
3. The coolant is incompressible and viscous dissipation is negligible;
4. The heat flow from the battery to the coolant is constant along the length of the cooling pipe.

Assumption 2 follows that temperature of the cooling pipe wall is constant along the length of the pipe and equal to the temperature of the battery. Assumption 3 follows that any change in the temperature of the coolant, as it flows through the battery, is only due to convection with the battery. With these assumptions, heat transfer from the wall of the pipe to the coolant were calculated as:

$$\dot{Q}_{coolant} = \frac{\Delta T_{lm}}{R_{clnt}} = \dot{m}_{clnt}\ c_{clnt}\left(T_{clnt,out} - T_{clnt,in}\right). \tag{5-15}$$

In the above equation, $T_{clnt,in}$ and $T_{clnt,out}$ denote the mean temperature of coolant at the inlet and outlet to the battery, respectively and R_{clnt} is the thermal resistance for convection between coolant and the pipe's wall. Also $\dot{m}_{clnt}$ and c_{clnt} represent the flow rate of coolant and its specific heat capacity, respectively. ΔT_{lm} in equation (5-15) is the logarithmic mean temperature difference of the battery and the coolant along the length of the cooling pipe which can be calculated as

$$\Delta T_{lm} = \frac{\Delta T_i - \Delta T_o}{\ln(\frac{\Delta T_i}{\Delta T_o})} \tag{5-16}$$

in which ΔT_i and ΔT_o denote the difference between the temperature of coolant and battery at the inlet and outlet of the pipe, respectively.

Table 5-6. Parameters of the battery thermal model (provided by the industry partner)

Parameter	Value	Unit	Parameter	Value	Unit
C_{batt}	21.6	$\frac{kJ}{K}$	R_{clnt}	0.014	$\frac{K}{W}$
R_{amb}(0 kph)	0.9	$\frac{K}{W}$	$R_{cabin,int}$	0.06	$\frac{K}{W}$
R_{amb}(50 kph)	0.7	$\frac{K}{W}$	$R_{cabin,wall}$	0.1	$\frac{K}{W}$
c_{clnt} (at 25°C)	3.6	$\frac{kJ}{kgK}$			

5.4.2 The coolant circuit

The coolant circuit includes the coolant pump, the tank and the connection pipes. The pump was modelled as an ideal coolant source, which is operated thermostatically in the temperature band of 25°C-30°C by an on/off flag signal. It provides a constant coolant flow of 0.1 $\frac{L}{s}$ when it is operated. The coolant tank was modelled as an ideal open tank based on conservation of mass (sum of inlet and outlet flows are zero). The tank is made of re-enforced polyethylene and has negligible heat transfer with the ambient. The connection pipes were modelled as ideal volumes, neglecting any potential pressure loss that may occur within them.

5.4.3 Simulation results

Here, the functionality of the battery cooling subsystem model is illustrated through a simple simulation. In the absence of cooling power of the chiller, this simulation was enabled by assuming a low initial temperature for the coolant within the tank (10°C). The following scenario was simulated: the ambient temperature is 37°C and the battery is at 25°C at the start of the simulation. In the first 100 seconds of the simulation, no heat is generated within the battery and the battery is subject to natural convection. Then, an internal heat generation of 300 W and vehicle speed of 50 $\frac{km}{h}$ is prescribed. The simulation results are shown in Figure 5-14.

Figure 5-14(a) shows that the variation in the battery temperature is insignificant in the first 100 seconds of the simulation, but when heat generation and forced convection starts, the temperature rises by 5°C within 500 second.

Figure 5-14(b) shows the control flag of the pump (‘0’ indicates ‘off’ and ‘1’ indicates ‘on’). When the temperature reaches 30°C, the pump is switched on, circulating the cold coolant to the battery, and stops once the battery temperature reduces to 25°C. Acceptable performance of pump control logic can be concluded from these results.

Figure 5-14(c) shows the variation in coolant temperature at the inlet and outlet of the battery. Note that the coolant at inlet and outlet are initially in thermal equilibrium with the battery. As the battery starts to warm up and while the pump is off, heat transfer from the battery to coolant causes the temperature of the coolant at battery outlet to rise with battery temperature. Coolant temperature at battery inlet in fact represents that of the coolant stored in the internal volume of the pump and is less affected by battery temperature. When coolant starts to flow for the first time, the warmer coolant close to the battery is quickly mixed by the cold coolant from the tank. Absorbing heat from the battery warms up the coolant gradually. When the flow stops, the coolant at battery inlet is much colder than before cooling started. The coolant at battery outlet warms up together with the battery. The third cooling event starts with much warmer coolant in the circuit, lacking sufficient cooling power to cool the battery. Thus, after complete mixing, the coolant continues to circulate for the remaining duration of the simulation (as the lower temperature set point in not achieved) and gradually warms up with the battery.

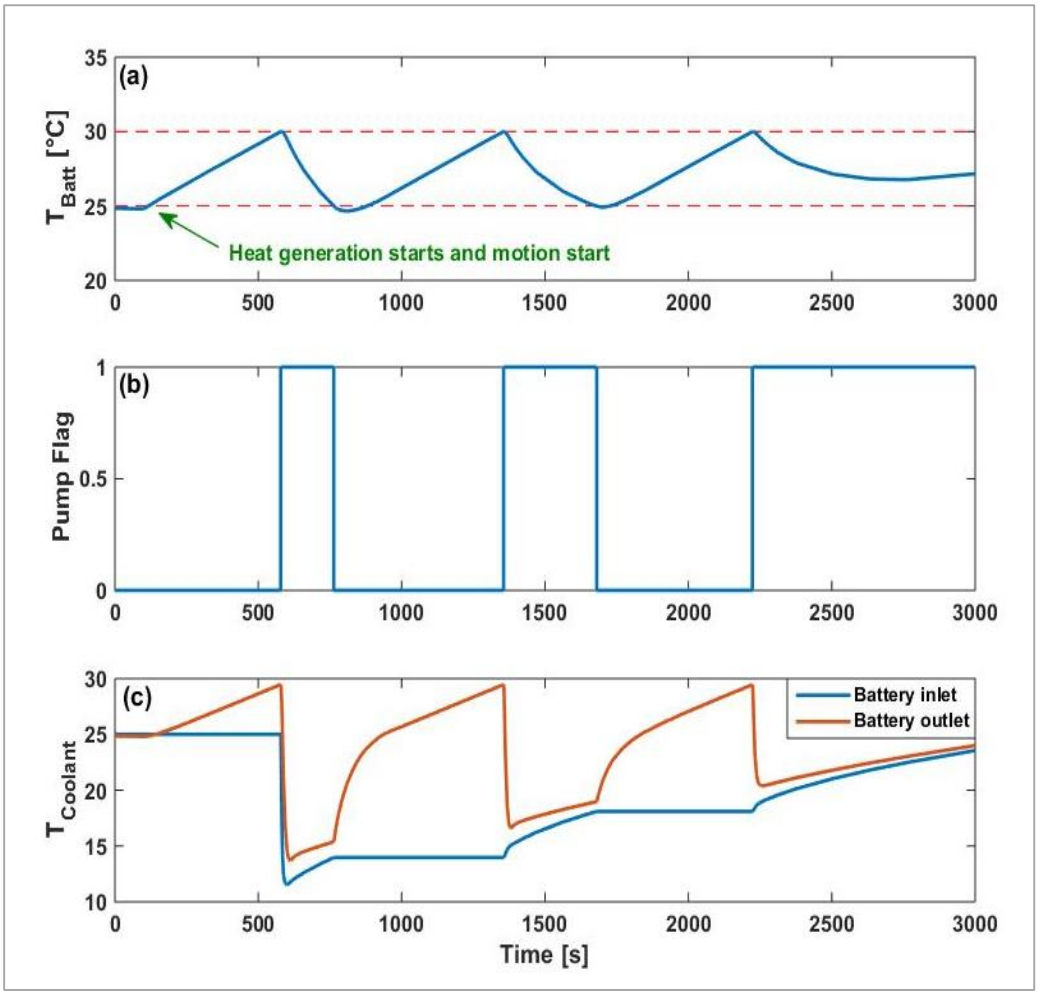

Figure 5-14. Simulation results of battery cooling subsystem model (a) battery temperature, (b) pump velocity, (c) coolant temperature

5.5 The AC subsystem

This section introduces the model of the AC subsystem. Developing the models if the air handling units and a refrigeration circuit are explained in Sections 5.5.1 and 5.5.2, respectively. The verification of the model is then discussed in Sections 5.5.3 and 5.5.4.

5.5.1 The air handling unit

In modelling of the air handling unit, ideal conditions were assumed for air flow within these components, neglecting details such as the dynamics of the flow, leakage and heat transfer from adjacent components. Therefore, the ducts and the

vents were modelled as ideal mass transfer components, i.e. volumes with mass conservation. The heater matrix was modelled as an ideal heat source. Similarly, the blower and fan were modelled as ideal air sources. The flow capacity of the blower is 120 $\frac{L}{s}$, while the flow capacity of the fan depends on the vehicle speed and varying from 600 $\frac{L}{s}$ to approximately 1600 $\frac{L}{s}$, based on the target vehicle specifications.

5.5.2 The refrigeration circuit

Figure 5-15 shows the layout of the refrigeration circuit of the vehicle. Modelling the refrigeration circuit involves customising the components models available in Dymola libraries and using them to build up the circuit of Figure 5-15. The extent of the customisation process depends on the complexity of the components and varies from a simple parameterisation in the case of the mass flow devices (compressor and valves) to detailed parameterisation and calibration in case of the heat exchangers. The customisation process is explained for each component type in Sections 5.5.2.1 to 5.5.2.3 . In each case, necessary explanations about the details of the original models are also provided.

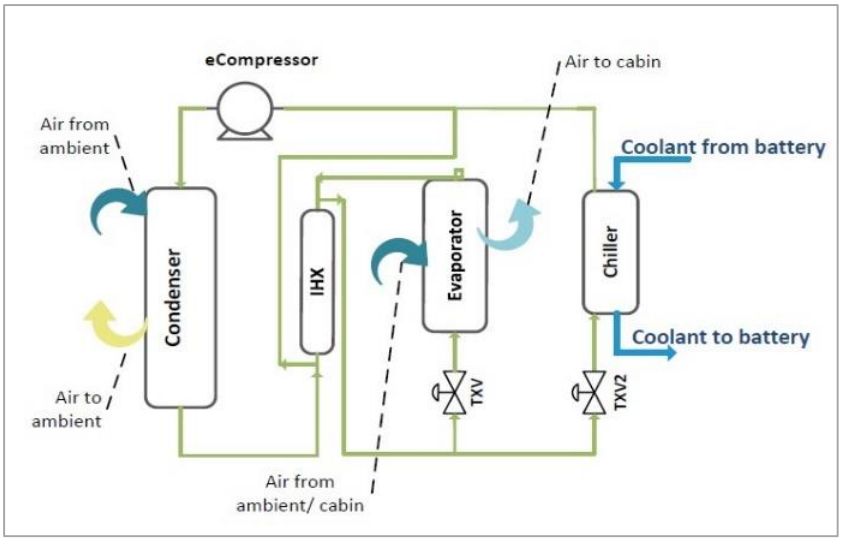

Figure 5-15. Layout of the refrigeration cycle of the target vehicle

5.5.2.1 The air-refrigerant heat exchangers

The heat exchanger models in the Dymola library have been developed based on the basic thermodynamic equations that govern thermo-hydraulic systems. The base element of the air-refrigerant heat exchanger models is shown in Figure 5-16. This element includes two flow channels that carry the air and the refrigerant passing through the component. The channels are thermally connected by a heat conducting wall. The heat exchanger models have been built from an array of this element. A simple heat transfer model has been assumed between the individual elements while the connectors carry the properties of the flow.

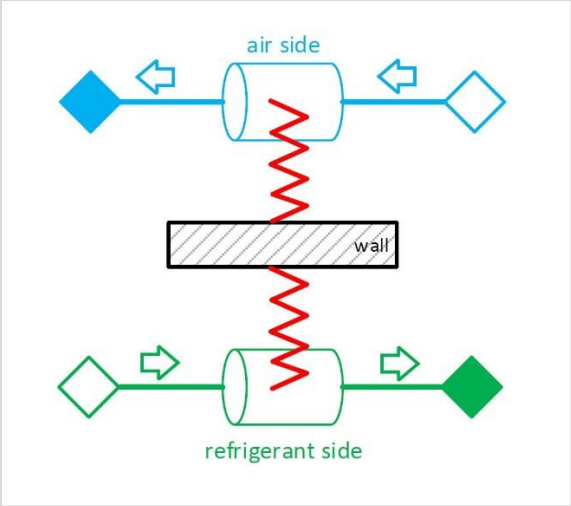

Figure 5-16. Heat exchanger base element:
An array of this element is formed to represent the heat exchanger

Heat transfer, on the air side of the wall has been modelled as

$$\dot{Q}_{wa} = \bar{h}_{aw}\, A_{aw}(T_a - T_w), \tag{5-17}$$

and on the refrigerant side as

$$\dot{Q}_{wr} = \bar{h}_{wr} A_{wr}(T_w - T_r) \tag{5-18}$$

in which $\bar{h}_{aw}$ and $\bar{h}_{wr}$ are the average heat transfer coefficient, A_{aw} and A_{wr} denote the heat transfer area, while T_a, T_w and T_r represent the temperature of the air stream, the wall and the refrigerant, respectively.

In the above equations, T_a is an input, while A_{wr}, and A_{wa} depend on the geometric specifications of the heat exchanger. These specifications were available for the target vehicle and were used to parameterise the models. As an example, the geometric specifications used in parameterising the evaporator model are given in Table 5-7. Similar specifications were also used to define the geometry of the condenser.

Table 5-7. Geometry specifications of the evaporator (provided by the industry partner)

	Parameter Name	Value
Core Geometry 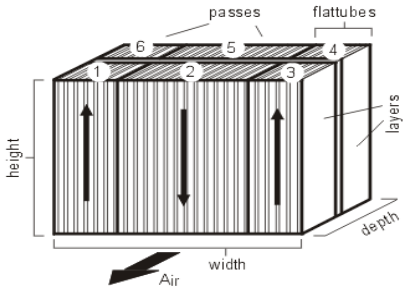	core material	Aluminium
	number of refrigerant Passes	4
	number of flat tubes in each pass	{22,22,22,22}
	core depth	50 mm
	core height	235 mm
	core Width	293 mm
Flat Tubes Geometry 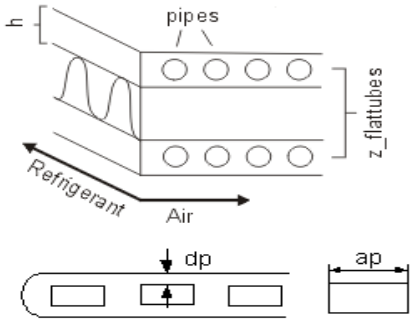	flat tube material	Aluminium
	height of tubes *(h)*	1.7 mm
	centre to centre distance of tubes	6.6 mm
	pipes in each tube	14
	wall thickness of flat tubes (*dp*)	0.22 mm
	shape of pipe cross section	rectangular
	length of pipe cross section (*ap*)	1.0 mm
Fin Geometry 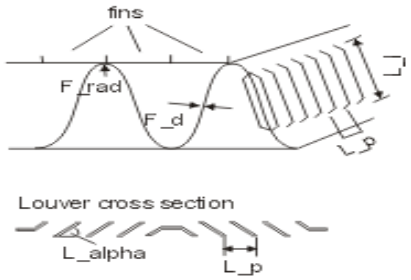	fins per 10 cm length of flat tube	72
	length of louver (*L_l*)	1 mm
	pitch of louver (*L_p*)	1 mm
	thickness of fins *(F_d)*	0.7 mm
	louvre angle (*L_alpha*)	39 degrees

$\bar{h}_{aw}$ and $\bar{h}_{wr}$ in equations (5-17) and (5-18) are functions of Nusselt number, fluid properties, and heat exchanger geometry. Once geometries are parameterised, Nusselt number will be the only unknown but one that can be defined through

calibration against experimental data from the target component. To achieve this, the calibration method outlined in [265] was adopted in this work. In this method, for the refrigerant side heat transfer, the Nusselt number is assumed to be consistent with the Dittus-Boelter correlation (equation 8.60 of [264]):

$$Nu = 0.023\, Re^{4/5}\, Pr^{\alpha}. \tag{5-19}$$

where Nu, Re, and Pr denote the Nusselt number, the Reynolds number, and the Prandtl number respectively. Also, the exponent α in equation (5-19) is 0.3 for heat absorption (evaporator) and 0.4 for heat rejection (condenser). For the air side heat transfer, the Nusselt number is implemented in the model in the general form of (equation 7.1 in [264]) :

$$Nu = C_1\, Re^{C_2}\, Pr^{\alpha}. \tag{5-20}$$

Constants C_1 and C_2 are then calibrated against experimental data obtained from the target components. Here, a dataset related to characterisation of the heat exchangers under steady-state conditions was used in calibration of the model. The characterisation procedure is briefly as follows: refrigerant flows through the evaporator at controlled inlet and outlet conditions (inlet pressure and subcooling, and outlet pressure). A stream of air at specified temperature and humidity is blown onto the heat exchanger, absorbing or rejecting heat. The mass flow rate of the refrigerant is adjusted to achieve the required superheat for any air flow rate and the resulting cooling power is measured. Table 5-8 summarizes the conditions and measurements in one evaporator characterisation test case.

Table 5-8. Conditions and measurements in one evaporator characterisation test case

Conditions		Refrigerant		Air	
$T_{air,in}$	27°C	$T_{ref,in}$	1.04°C	$T_{air,out}$	6°C
$RH_{air,in}$	50%	$T_{ref,out}$	8.85°C	$p_{air,out}$	1 bar
$p_{ref,out}$	0.18 MPa	$p_{ref,in}$	0.3 MPa		
SC	3 K	$\dot{m}_{ref}$	0.018 $\frac{kg}{s}$		
SH	10 K				
$\dot{m}_{air}$	0.05 $\frac{kg}{s}$				

Given that Nu cannot be measured directly, the following approach was adopted:

a) From the test results, the heat flow to the air stream was calculated using the relationship $\dot{Q}_{air} = \left(\dot{m} c_p \Delta T\right)_{air}$.

b) The conditions of the characterisation test were simulated, a parameterised heat exchanger model with inversed heat transfer model was used in this simulation to allow calculating the heat transfer coefficient and the corresponding Nusselt number from $\dot{Q}_{air}$, while the Reynolds number is calculated from the flow conditions for the geometry of the heat exchanger.

c) Repeating this process for a number of available test cases, and using linear regression, coefficients C_1 and C_2 were determined.

Figure 5-17 shows the result of the fitting for the evaporator and condenser.

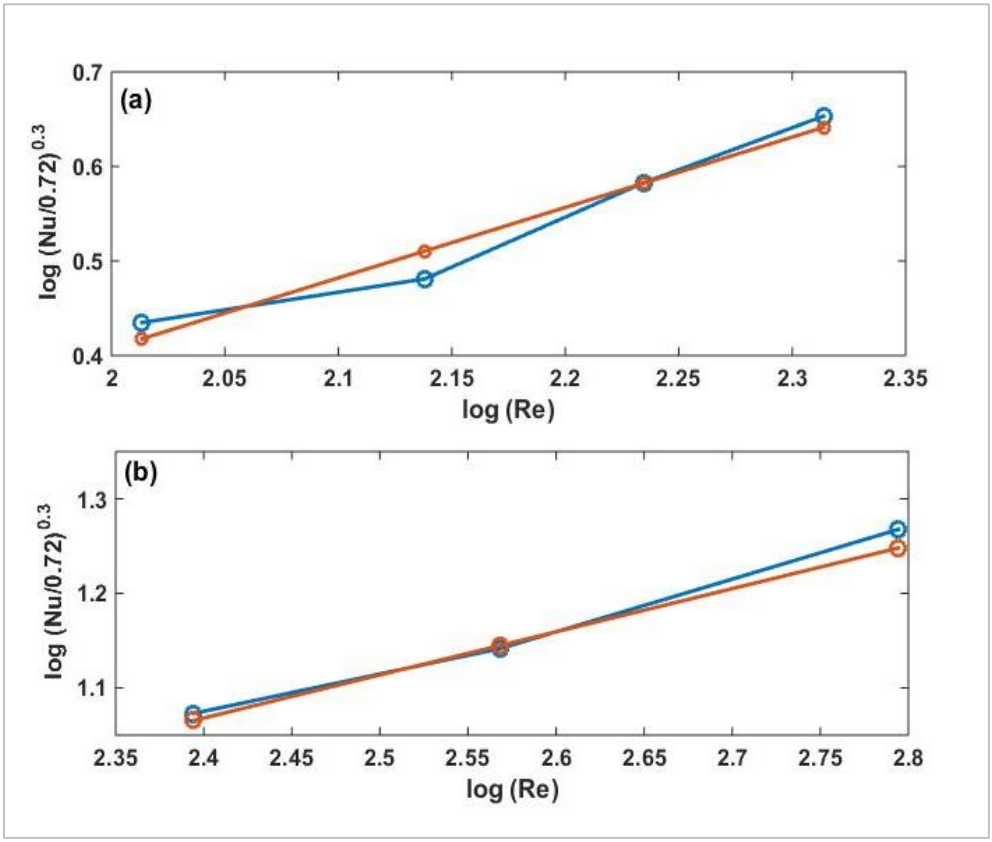

Figure 5-17. Linear regression result for calibrating Nusselt number in air-refrigerant heat exchanger models (a) evaporator (b) condenser. ***Annotations- blue: test data, red: simulation results***

In addition to calibrating the heat transfer models, calibration of refrigerant and air pressure loss across the heat exchangers is required. In this work, pressure loss on the air and refrigerant sides were calculated based on nominal conditions as:

$$\frac{\Delta p}{\Delta p_0} = C_3 \left(\frac{\dot{m}}{\dot{m}_0}\right)^{C_4} \left(\frac{\rho_0}{\rho}\right) \tag{5-21}$$

in which $\dot{m}$ and ρ denote the mass flow rate and the density, Δp denotes pressure loss and the subscript '0' denotes the nominal condition. C_3 and C_4 in the above equation are constant that were calibrated against the component test data as explained above for calibration of (5-20). To verify that the models are representative of the target components, the calibrated models were used to simulate the remaining characterisation tests cases. Comparing the simulation and test results in Figure 5-18 shows that an accuracy of approximately $\pm$5% is achieved, which is considered sufficient for the purpose of this work.

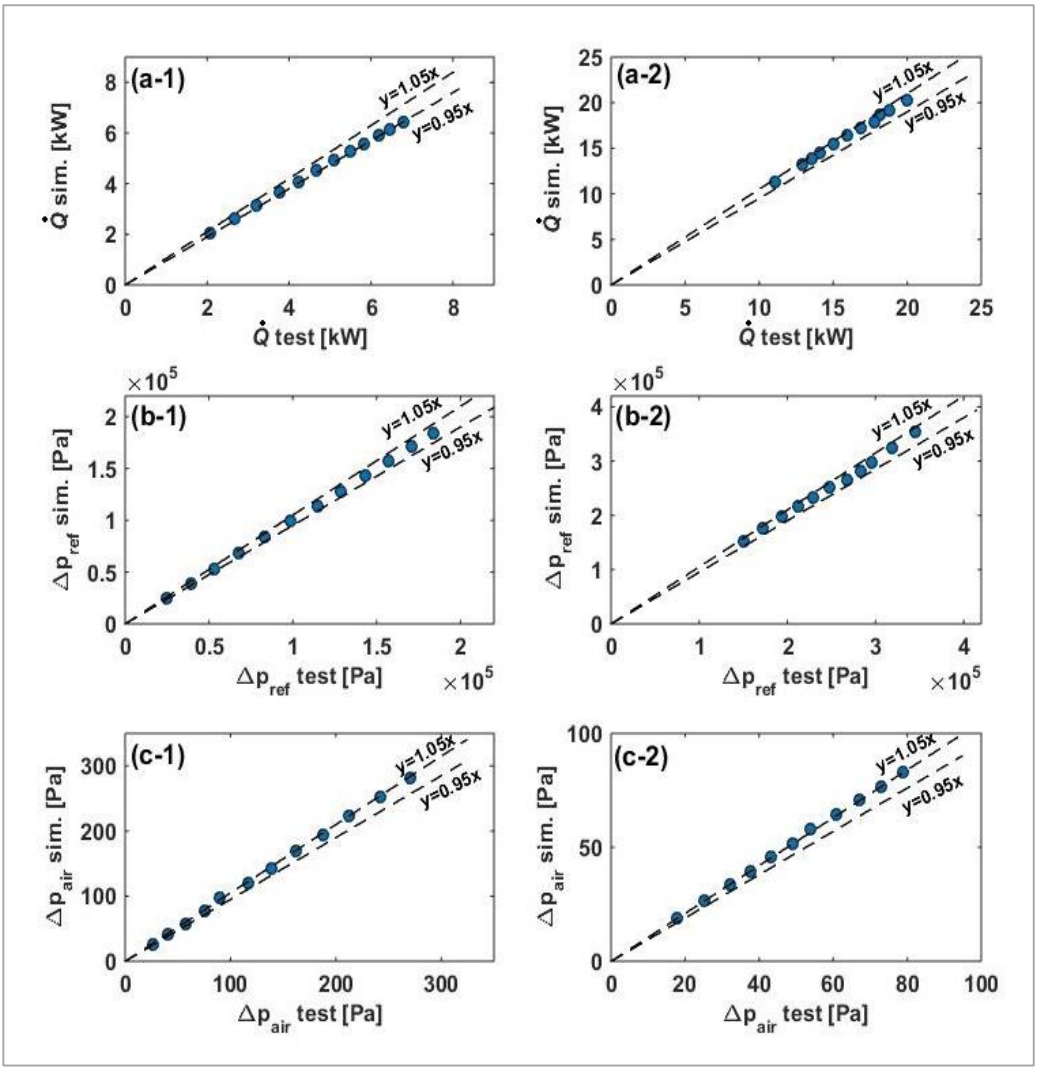

Figure 5-18. Verification of the heat exchanger models: evaporator (left) and condenser (right) (a) heat flow, (b) refrigerant pressure loss, (c) air side pressure loss

5.5.2.2 Internal flow heat exchanger models

The base element of the internal flow heat exchanger models (i.e. the IHX and the chiller in Figure 5-15) is similar to that of the air-refrigerant heat exchangers Figure 5-16 except that the air channel is replaced with a second refrigerant channel or with a liquid channel. The models are customised through a process similar to that in the case of the evaporator and the condenser: i.e. defining the geometries and calibrating the heat transfer and pressure loss models. After calibrating the models against a subset of the characterisation test cases, the models were used to simulate the remaining test cases. Figure 5-19 compares the results of the simulation and the tests. It can be seen that the accuracy achieved in

simulating the power of heat flows is approximately ±5% in case of the IHX and ±10% in case of the chiller, which is considered sufficient for the purpose of this work.

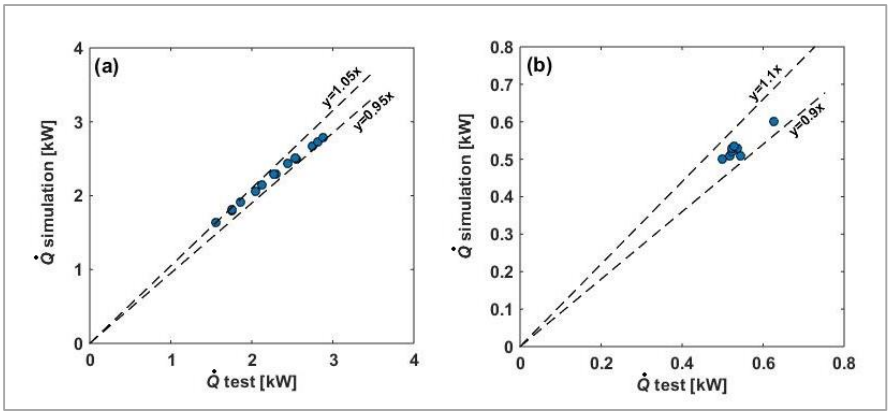

Figure 5-19. Verification of heat transfer model in internal flow heat exchangers against test data (a) IHX (b) chiller.

5.5.2.3 Mass flow devices

In modelling of the compressor and the valves, the dynamics of these devices are neglected, sine these dynamics are considerably faster than the dominant dynamics of the refrigeration circuit [233,266]. The mass flow rate of the refrigerant through the compressor ($\dot{m}_{ref,comp}$) is calculated as:

$$\dot{m}_{ref,comp} = 60\, \rho_{ref}\, \eta_{vol}\, \mathrm{V_{comp}}\, \omega_{comp} \tag{5-22}$$

where ρ_{ref} denotes the refrigerant density, η_{vol} is the volumetric efficiency of the compressor, $\mathrm{V_{comp}}$ is its displacement and ω_{comp} denotes its speed. The outlet enthalpy is initially calculated for an isentropic process as

$$h_{out,isentropic} = h(p_{out}, s_{in}) \tag{5-23}$$

where p and s denote the pressure and the entropy of the refrigerant, respectively. The subscripts in and out denote the inlet and the outlet side of the compressor, respectively.

The isentropic enthalpy is then corrected using the isentropic efficiency (η_{isen}) of the compressor as (equation 7-27 of [154]):

$$\eta_{isen} = \frac{h_{out,isen} - h_{in}}{h_{out} - h_{in}}. \quad (5\text{-}24)$$

where h_{in} denotes the enthalpy of the inlet refrigerant while h_{out} denotes the actual enthalpy of the outlet refrigerant. The efficiency maps of the compressor were available (see Appendix 1), and were implemented in the model in form of look-up tables.

The mechanical power of the compressor is calculated within the model from the change in the enthalpy of the flow. An overall efficiency of 80% for the electrical path between the battery and the compressor (combination of the DC-DC converter and the electric machine of the compressor) was assumed based on the recommendations of the industry partner. Therefore, the electrical power demand of the compressor (P_{comp}) from the battery was calculated from the mechanical power ($P_{comp,mech}$) as:

$$P_{comp} = 1.2 * P_{comp,mech}. \quad (5\text{-}25)$$

In modelling of the TXVs, isenthalpic flow through an orifice is assumed in which mass flow rate through the valve is related to nominal conditions as

$$\frac{\dot{m}}{\dot{m}_0} = \sqrt{\frac{\Delta P}{\Delta P_0}\frac{\rho}{\rho_0}} \quad (5\text{-}26)$$

in which ΔP denotes the refrigerant pressure drop across the valve and subscript 0 denotes nominal conditions. A variable flow coefficient, k_v, is assumed to relate the flow rate through the valve ($\dot{m}_{ref,valve}$) to its opening as

$$\dot{m}_{ref,valve} = k_v \dot{m} = k_v \sqrt{\frac{\Delta P}{\Delta P_0}\frac{\rho}{\rho_0}} \dot{m}_0. \quad (5\text{-}27)$$

A PI controller is built in the model that controls $\dot{m}_{valve}$ by varying k_v to achieve the required superheat conditions of the refrigerant at evaporator and chiller outlet conditions.

In modelling of the refrigerant pipes, since the exact dimensions of transfer pipes was not available, a constant small pressure and enthalpy loss was implemented between components, as suggested in [266] to account for the effect of friction. Possible heat transfer between the flow and ambient was neglected, assuming ideal insulation.

5.5.3 Steady-state verification of the refrigeration circuit model

For verifying the refrigeration circuit model, the dataset given in Table 5-9 was available, which is related to characterisation of the refrigeration circuit of the target vehicle. The characterisation briefly involves measuring the temperature of the evaporator and the chiller, as well as the pressure of the refrigerant at the inlet and outlet sides of the compressor, under different steady state conditions of air flow, coolant flow and compressor speed. In the first three test cases, both the evaporator and the chiller are in the cycle, in test cases 4-6 the chiller is isolated, while in test cases 7-9 the evaporator is isolated.

Table 5-9. Boundary conditions of the refrigeration cycle characterisation test

Test case	ω_{comp}	$\dot{m}_{air,cond}$	$\dot{m}_{air,evap}$	T_{air}	$\dot{m}_{coolant}$	$T_{clnt,chlr,in}$
	rpm	$\frac{kg}{s}$	$\frac{kg}{s}$	°C	$\frac{kg}{s}$	°C
1	6500	0.51	0.137	44	0.1	30
2	6500	1.0	0.137	44	0.1	30
3	8000	1.35	0.137	44	0.1	30
4	8000	0.51	0.137	44	0	30
5	8000	1.0	0.137	44	0	30
6	8000	1.35	0.137	44	0	30
7	4000	0.51	0	44	0.1	30
8	4000	1.0	0	44	0.1	30
9	4000	1.35	0	44	0.1	30

To verify the model, the model was set up and simulated according to the conditions of each test case. The simulation and test results are compared in Figure 5-20. As Figure 5-20(a) and Figure 5-20(b) show, the absolute error in calculation of chiller and evaporator temperature is less than 2.5 degrees. In addition, Figure

5-20(c) and Figure 5-20(d) show that the pressure of the refrigerant is modelled with absolute error of 1.5 bar.

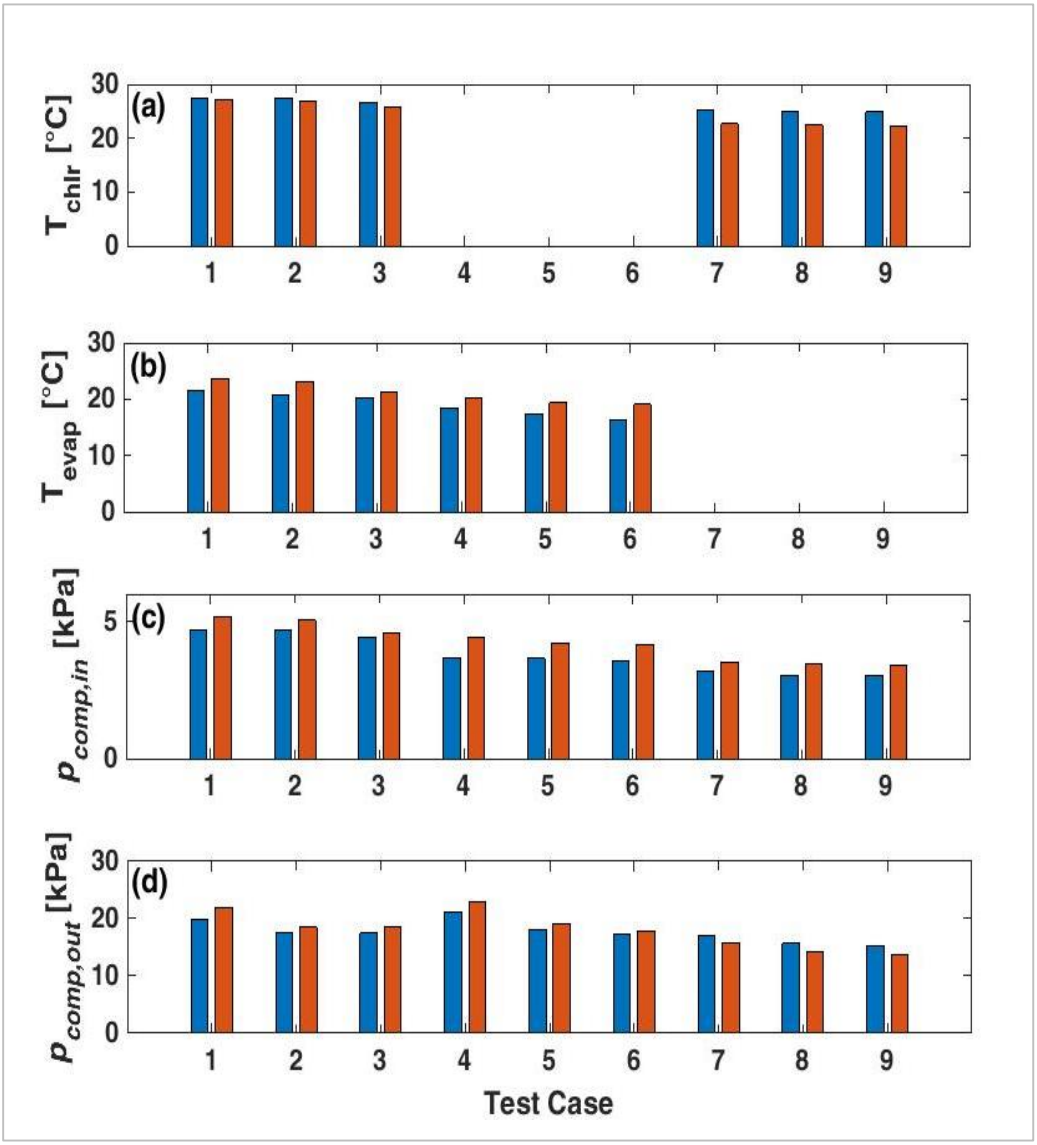

Figure 5-20. Verification of the refrigeration circuit model against test rig measurement: (a) coolant temperature at chiller outlet, (c) average evaporator air temperature, (d) compressor inlet pressure, (e) compressor outlet pressure. ***Annotation- blue: test results, red: simulation results***

5.5.4 Transient verification of the refrigeration circuit

For transient verification of the refrigeration circuit, a dataset is available which was obtained from the vehicle placed in a climatic chamber at 43°C for 5 hours, before switching the AC system on at maximum power and driving the drive cycle

of Figure 5-10(a) with the help of a dynamometer. The signals listed in Table 5-10 were logged from the vehicle.

Table 5-10. Measurements taken in thermal test of the target vehicle

	Measurement	Location
1	Ambient temperature / humidity	Climatic chamber controls
2	Cabin temperature	HVAC ECU
3	Battery temperature	BMS
4	Vehicle speed	Dynamometer
5	Compressor speed	HVAC ECU
6	Coolant pump flag	BMS
7	Coolant temperature	Thermocouple at chiller inlet and outlet
8	Condenser temperature	Thermocouples behind condenser (air outlet)
9	Evaporator temperature	Thermocouples behind evaporator (air outlet)
10	Compressor power	HVAC ECU

Figure 5-21, shows the measured profiles of battery and evaporator inlet air temperature, TXV_2 open-close flag, and compressor speed during the test. Figure 5-21(a) shows that the temperature of the air stream entering the evaporator decreases from 43°C to 27°C (since the cabin is gradually cooled down). It can be also inferred from this figure that the battery cooling has been applied thermostatically, maintaining the battery in the temperature range of 25°C-30°C. To avoid freezing, TXV_2 is shut off (chiller is isolated) when the temperature of the chiller temperature decreases to 10°C, and is reopened once it reaches 20°C, causing the TXV_2 flag to change nine times, as shown in Figure 5-21(b). The compressor controller reacts to the evaporator temperature (not plotted here) as well as disturbances such as valve events and variations in vehicle speed. Figure 5-21(c) shows that the compressor runs at maximum speed in the first half of the test when the evaporator inlet air (and therefore the evaporator temperature) is warm, and at lower speeds in the second half of the test.

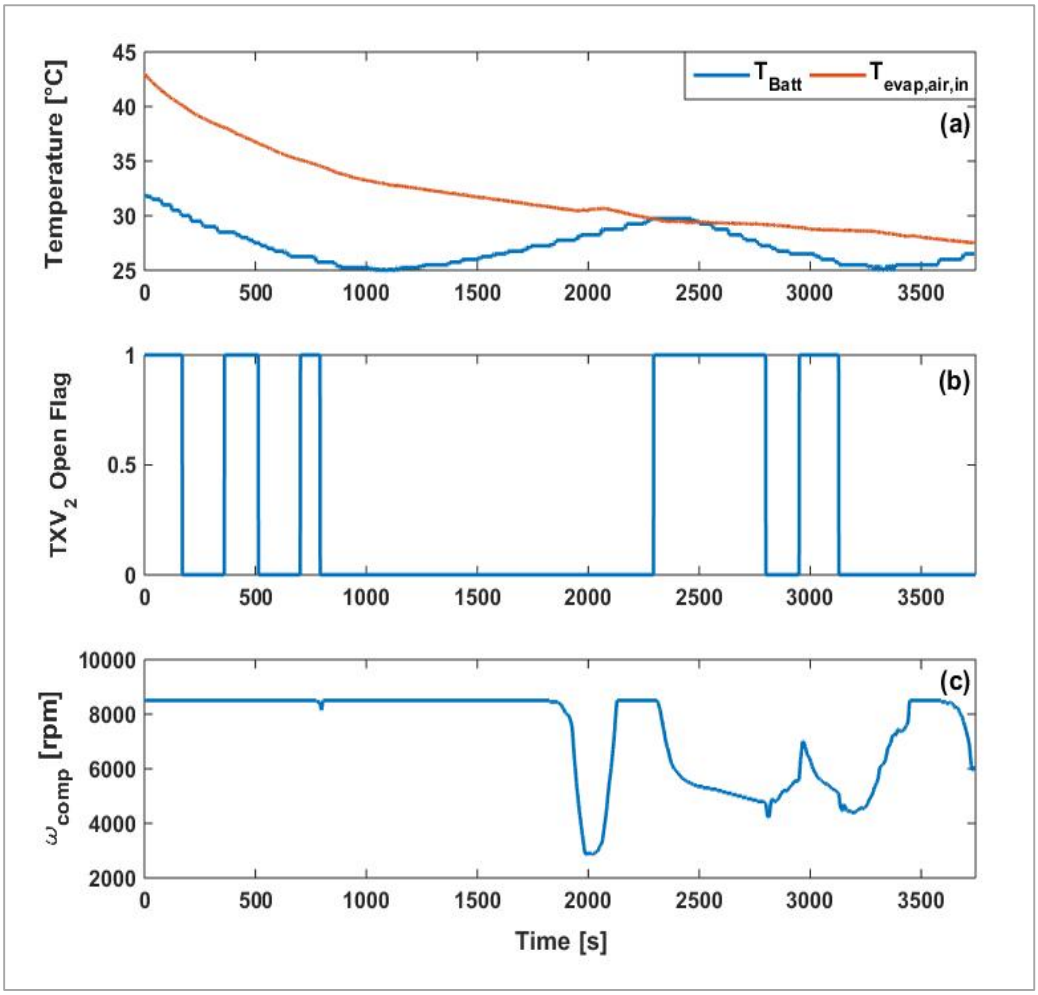

Figure 5-21. Signals used as input for verification of AC and battery cooling subsystem models (a) average temperature of battery evaporator inlet air (b) battery cooling flag and (c) compressor speed

The AC and battery cooling subsystem models were integrated as shown in Figure 5-22, and simulated as one unit, using the signals shown in Figure 5-21 and the speed profile of the vehicle as inputs. In addition, the condenser air flow is calculated within the model from vehicle speed, while the evaporator air flow is known from the fan specifications.

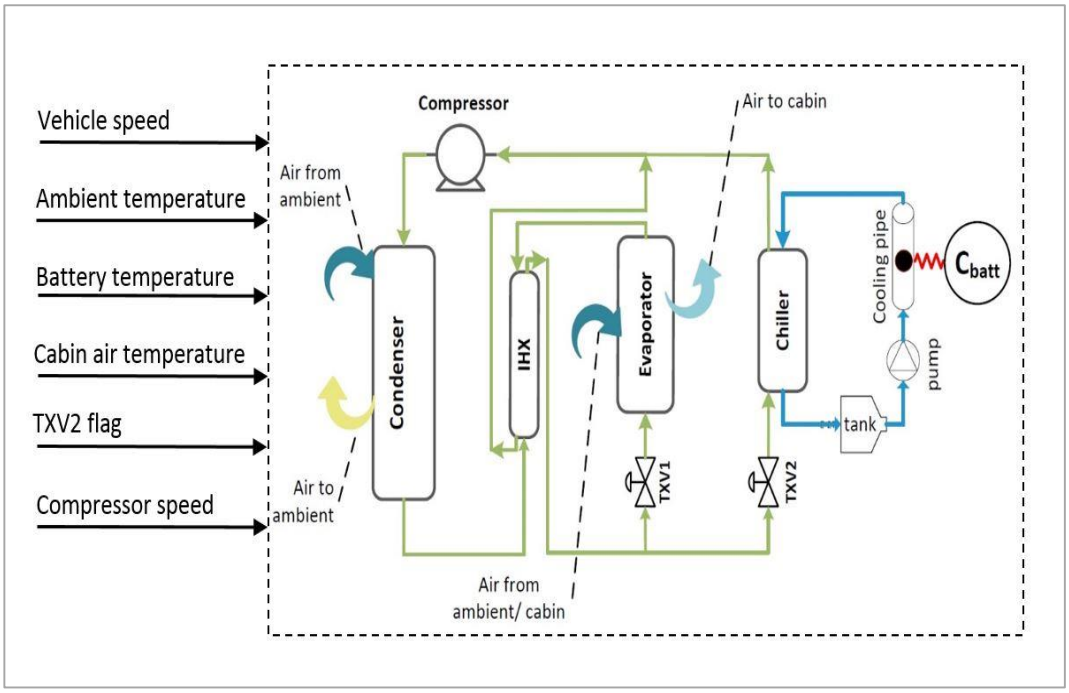

Figure 5-22. Integrated refrigeration and coolant circuits as assumed for transient verification

The simulated and measured evaporator, condenser and chiller temperatures, are shown in Figure 5-23. Comparing Figure 5-23 with Figure 5-21(b) shows that most of the dynamics seen in this figure are caused by changes in battery cooling flag and its subsequent effect on the distribution of cooling power and the operation of the compressor. Despite the discrepancies observed during short transients, Figure 5-23 shows that the model closely captures these dynamics. It can be seen from the test results that the evaporator temperature increases when TXV_2 opens (cooling flag changes from 0 to 1 in Figure 5-21(b)), and decreases when TXV_2 is closed. The temperature of the condenser changes in a similar fashion. The maximum absolute error in the temperature of the evaporator and condenser are approximately 1.5°C and 3.5°C, respectively. Also, Figure 5-23(c), shows that the effect of opening and closing TXV_2 on coolant temperature is captured, although the model over-estimates the rate of cooling (likely due to neglecting the volume of the pipes in the cooling circuit). Additionally, comparing the simulated compressor power against test results in Figure 5-23(d) shows that the model occasionally over-estimates the compressor power by up to 1 kW.

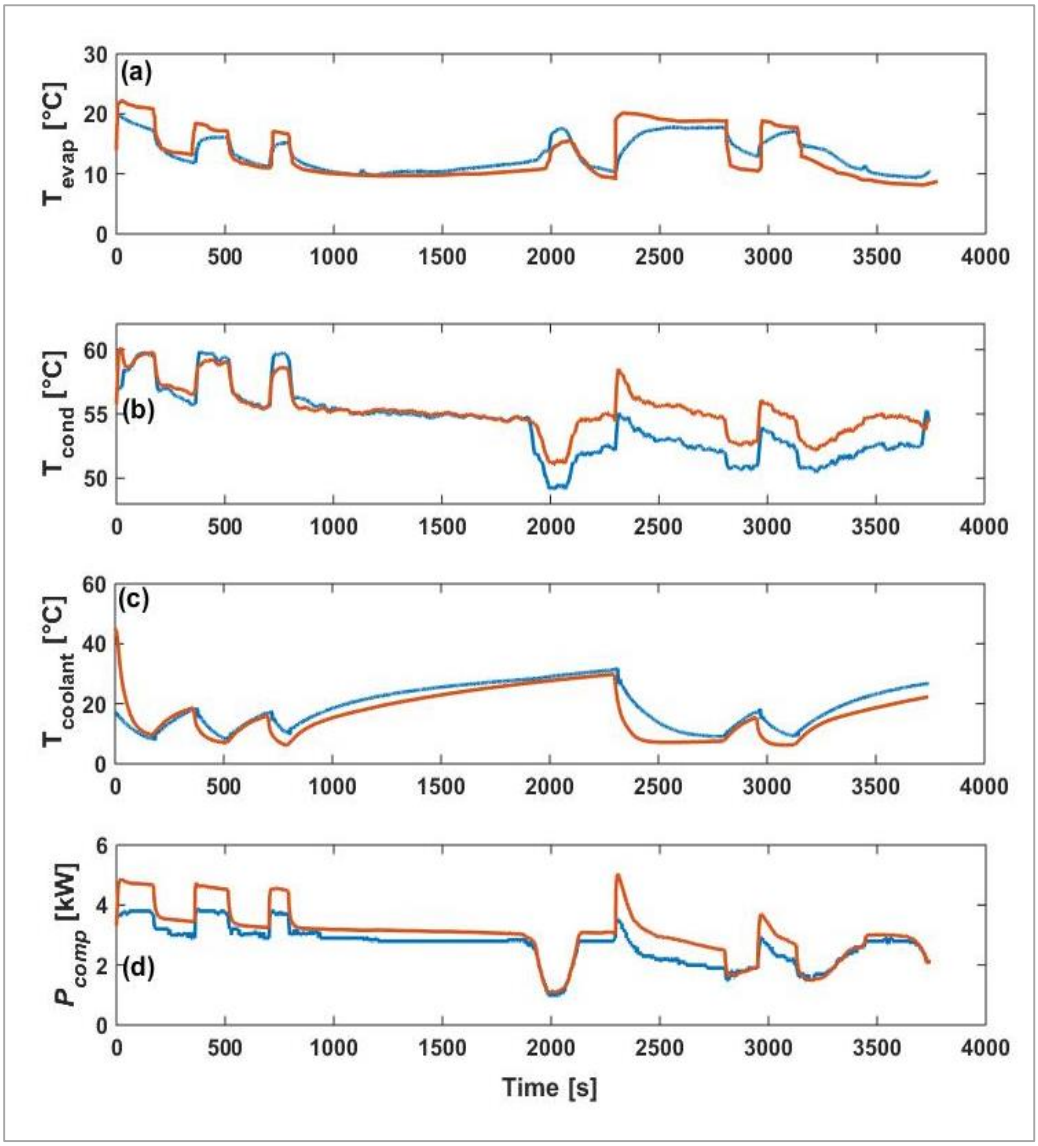

Figure 5-23. Verification of refrigeration and battery cooling circuit models. Temperature of (a) evaporator air, (b) condenser air, (c) coolant at battery inlet. ***Annotations: test result are plotted in blue and simulation results are plotted in red***

5.6 Integration of the thermal subsystem models

The models developed for the cabin, battery cooling, and the AC subsystems were integrated in Dymola as shown in Figure 5-24. A simplified controller was developed to operate the model, that is, for controlling the AC and the battery cooling subsystems. The details of the control strategy implemented within the controller is explained in Section 5.6.1. The model is simulated with this control strategy in Section 5.6.2.

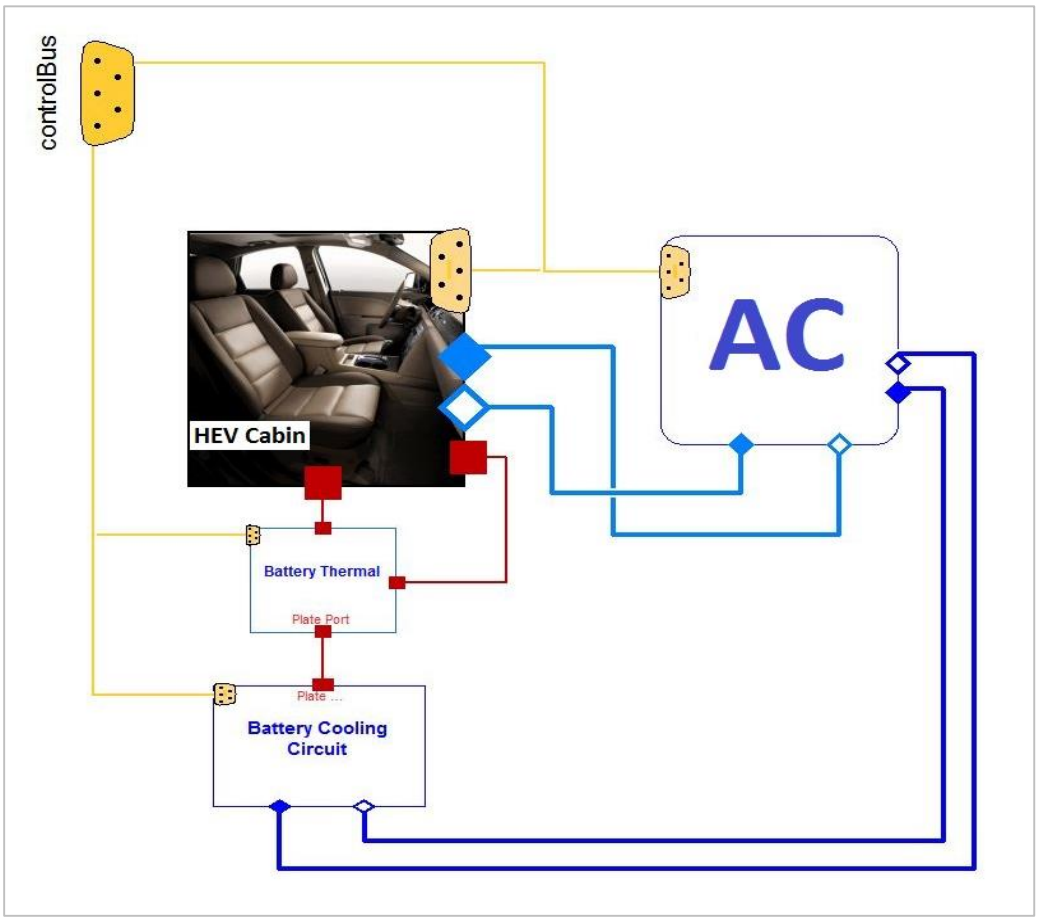

Figure 5-24. Integration of thermal subsystem models

5.6.1 The control strategy

In developing the control strategy, two high-level objectives were considered:

1. Maintaining the cabin air temperature at 22°C
2. Maintaining the battery in the temperature band of 25°C-30°C.

The following four operating modes were defined for controlling the thermal subsystems

- mode 0: AC and battery cooling disabled;
- mode 1: AC and battery cooling enabled;
- mode 2: AC enabled (while battery cooling disabled);

- mode 3: battery cooling enabled (while AC disabled).

The above control modes are chosen by a state machine in which transitions between the modes take place based on the temperature of the cabin and the battery. Once a control model is selected, low-level controllers are used to operate the relevant components. Briefly, the function of the low-level controllers is as follows:

1. The on-off operation of the fan is controlled by a binary switch signal. In modes 1-3 air is supplied to the condenser at a minimum rate of 600 $\frac{L}{s}$, with additional air supply depending on the speed of the vehicle, as discussed in Section 5.5.1.

2. The shut-off operation of the TXVs are controlled based on the operating modes 0-4: TXV_1 is opened in modes 1 and 2 when the evaporator is loaded, while TXV_2 is opened in modes 2 and 3 when the chiller is loaded.

3. The on-off operation of the pump is controlled based on the operating modes: pump is on in modes 1 and 3 and off in other modes.

4. The air flow of the blower is controlled by a PI controller based on the offset between the actual cabin temperature and its set point of 22 °C. Air flow increases when high cooling power is required to cool the cabin (when cabin is warm) and decreases when less cooling power is needed.

5. The compressor speed is controlled by a PI controller which ensures that the evaporator and the chiller temperatures do not drop below 5°C and 10°C, respectively.

6. The heater is controlled by a PI controller. When the evaporator temperature drops below 7°C, the air is reheated to maintain the vent temperature at 7°C.

5.6.2 Simulation results

To illustrate the functionality of the model of Figure 5-24 and the implemented control strategy, AC and battery cooling in a hot-soaked vehicle is simulated with the conditions given in Table 5-11. As indicated in the table, the cabin and the battery are initialised at $60°C$and $42°C$, respectively. Also, in the absence of a powertrain model, a constant internal battery heat generation of 300 W and constant vehicle speed of 55 $\frac{km}{h}$ are assumed.

Table 5-11. Conditions assumed for simulation of the thermal subsystem models

Boundary Conditions		**Initial Conditions**	
Condition	**Setting**	**Condition**	**Setting**
$\dot{Q}_{gen}$	300 W	T_{cabin}	$60°C$
v	55 $\frac{km}{h}$	T_{batt}	$42°C$
T_{amb}	$38°C$	$T_{coolant}$	$42°C$
RH	25%		
Solar load	0 $\frac{W}{m^2}$		

Simulating the above conditions lead to the results shown in Figure 5-25. The following observations can be made:

1. Figure 5-25(a) shows that the cabin is cooled from 60°C to 22°C and maintained at this temperature.

2. According to Figure 5-25(b), the evaporator temperature is reduced to, and maintained at 5°C, while the air is reheated and a minimum vent temperature of 7 °C is maintained.

3. Comparing Figure 5-25(c) and Figure 5-25(d) shows that in the initial 1100 seconds of the simulation, when the evaporator temperature is higher than 5°C, the compressor operates at maximum velocity. Once the evaporator temperature is reduced to 5°C, the speed of the compressor is gradually reduced.

4. Comparing Figure 5-25(b) and Figure 5-25(c) shows that the compressor controller reacts to the variations in the evaporator temperature. These variations are due to the dynamics created by the battery cooling system (see point 7 below).

5. Figure 5-25(d) indicates that the condenser receives a flow of air at constant rate of 830 $\frac{L}{s}$, which is consistent with the air flow capacity of the fan and the vehicle speed of 55$\frac{km}{h}$ (see Section 5.5.1).

6. Figure 5-25(d) shows that the evaporator air flow is 120 $\frac{L}{s}$ in the first 2000 seconds of the simulation when the cabin is warm, and gradually reduces as the temperature of cabin approaches its set point.

7. Figure 5-25(e) shows that the battery is cooled from 42°C to 25°C. Cooling is then thermostatically applied and the battery is maintained between 25°C to 30°C.

8. Allocating cooling power to the battery has a negative effect on the evaporator temperature. Comparing Figure 5-25(b) and Figure 5-25(e) shows that when battery cooling starts, the evaporator temperature increases due to reduced cooling power. When battery cooling stops, more cooling power is made available to the evaporator, leading to lower air temperature. When the cabin is relatively cold, the cooling load of the battery has a negligible effect on cabin temperature.

9. In the first 700 seconds of the simulation, the coolant within the cooling circuit is gradually cooled together with the battery. A minimum coolant temperature of 5°C is maintained through valve and pump control. Comparing Figure 5-25(e) to Figure 5-25-h shows that the operation of TXV_2 and the pump are consistent with the battery temperature set points.

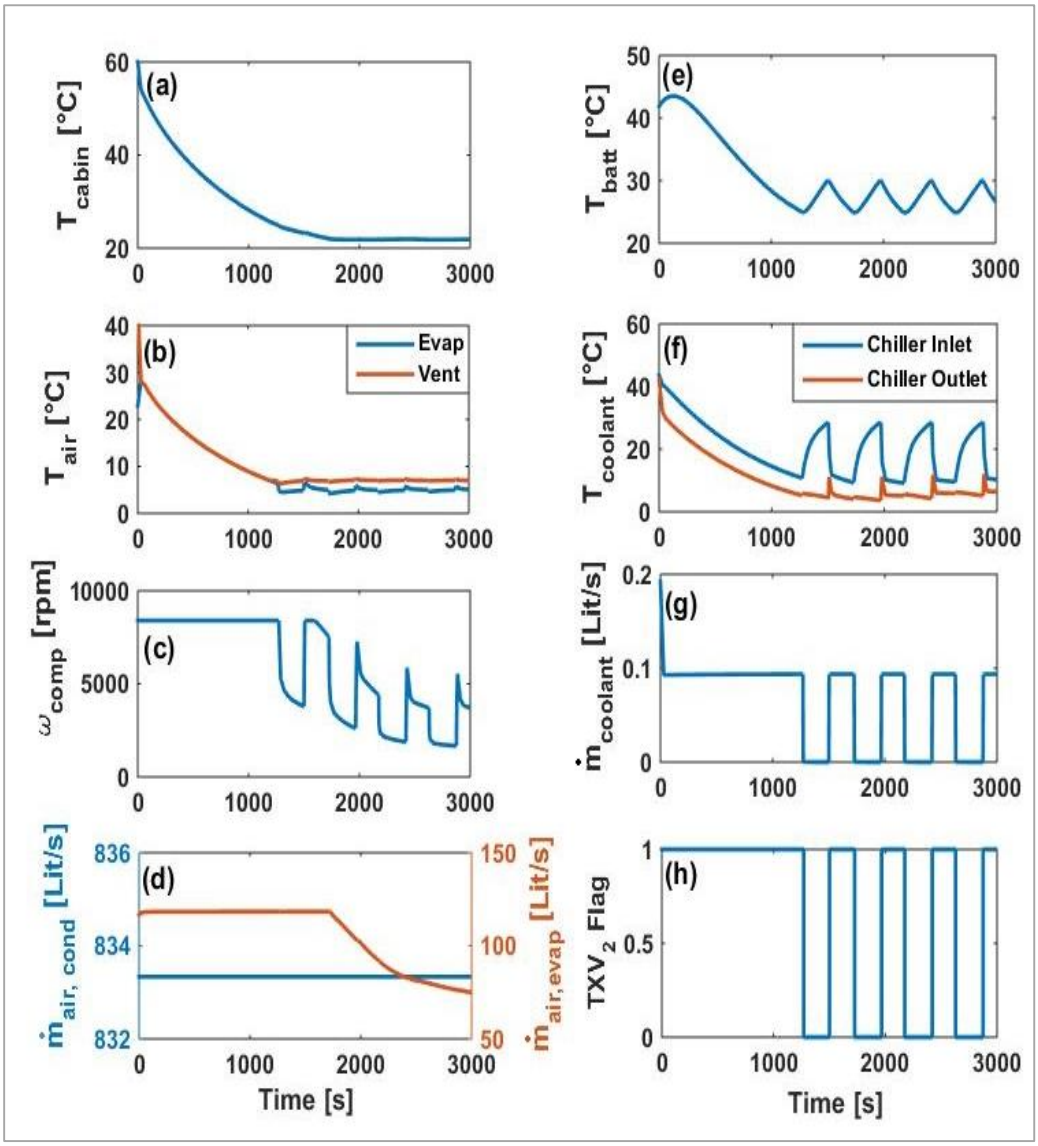

Figure 5-25. Simulation results of thermal submodel (a) cabin temperature, (b) battery temperature, (c) evaporator and vent air temperature, (d) coolant temperature, (g) air flow rate onto evaporator and condenser, (h) coolant flow rate

The simulation results demonstrate that the developed models developed can capture the interactions between the key thermal subsystems. These results also indicate that the implemented control strategies replicate the expected operation of the respective subsystems.

5.7 Summary

In this chapter, the key details of the subsystem models developed for this research were discussed. The models were developed to represent the subsystems of the Range Rover HEV, due to the availability of specifications and parameters, as well

as test data from the vehicle through the industry partner of this research. The powertrain subsystem was modelled in Simulink using the component efficiency maps. The thermal subsystems, including the AC, the battery cooling, and the cabin subsystems were developed and integrated in Dymola. Where experimental data from the vehicle was available, it was used to verify the overall performance of the models, confirming their suitability for the purpose of this research.

CHAPTER 6 THE PHEV MODEL

Introduction

In this chapter, the development of the PHEV model required for the purpose of this research is discussed. In Section 6.1, the high-level assumptions of the PHEV considered as target are explained and the process of developing the PHEV subsystem models from the Range Rover HEV subsystem models is discussed. The process of integrating the subsystem models to arrive at the required PHEV model are discussed in Section 6.2. In Section 6.3, the model is simulated over a number of drive cycles to demonstrate its performance. In Section 6.4, the method of calculating the battery lifetime of the PHEV is explained. The discussions are summarised in Section 6.5.

6.1 PHEV assumptions and modifications of the HEV subsystem models

For the purpose of developing the PHEV model required for this research, approximate specifications of the future-model Range Rover PHEV which will have a similar platform to that of the Range Rover HEV. The key difference between the two vehicles will be in the size of their electric machine and battery. Therefore, to model the PHEV, it was sufficient to modify the specifications of the battery, the electric machine, and a subset of the control parameters within the Range Rover HEV powertrain mode while the remaining subsystem models could be reused. Table 6-1 compares the key specifications of the HEV and the PHEV Range Rover.

Table 6-1. Comparing the specifications of the battery and powertrain subsystem in Range Rover HEV (modelled in Chapter 5) and the future-model Range Rover PHEV

Subsystem	Specification	Range Rover HEV	Range Rover PHEV (concept)
Battery	Energy capacity	1.8 kWh	14-16 kWh
	Voltage	260 V	400 V
Powertrain	Architecture	Parallel	Parallel
	Engine Size	3.0 lit v6 diesel, 140 kW	3.0 lit v6 diesel, 140 kW
	Electric Machine	35kW , 180 Nm @ 2500 rpm	75kW , 420 Nm @ 2500 rpm

6.1.1 The electric machine and the powertrain control rules

As shown in Table 6-1, the PHEV will benefit from a 75 kW electric machine. The torque and the energy efficiency maps of the component were available, as shown in Appendix 1. These maps were replaced in the powertrain model. In addition, the control rules of the powertrain were modified to enable PHEV specific operating modes. Table 6-2 lists the key parameters that were implemented in the control rules based on recommendations of the industry partner.

Table 6-2. Parameters used in the PHEV powertrain control rules

Parameter	Value
SoC window - CD Mode	95%-10%
SoC window - CS Mode	10%-13%
minimum SoC for start in EV mode	11%
battery overheat threshold (power cap): above this limit the battery power is limited at 50%	45°C
battery overheat (power cut-off): the battery is not used above this temperature	55°C

In addition, more rules were implemented to allow simulation of a plugged-in vehicle. These rules provide control over the strategy of charging the battery, including timing and the level of charge.

6.1.2 The Battery Pack

The design of the PHEV battery was not finalised when the research was conducted, however, an energy capacity of 14kWh -16 kWh, and a voltage of 400 V were specified as targets. In the absence of sufficient information about the design of the pack and the specifications of the cells, the PHEV battery was assumed to be created from modules of the Range Rover HEV battery. To arrive at a design close to the required specifications, 54 HEV modules were assumed to be arranged in 6 parallel strings of 9 modules, as shown in Figure 6-1. The resulting pack level specifications are given in Table 6-3. The heat capacity of the battery pack was also updated within the thermal model. Other assumptions of the model are consistent with those given in Sections 5.2.5 and 5.4.1.

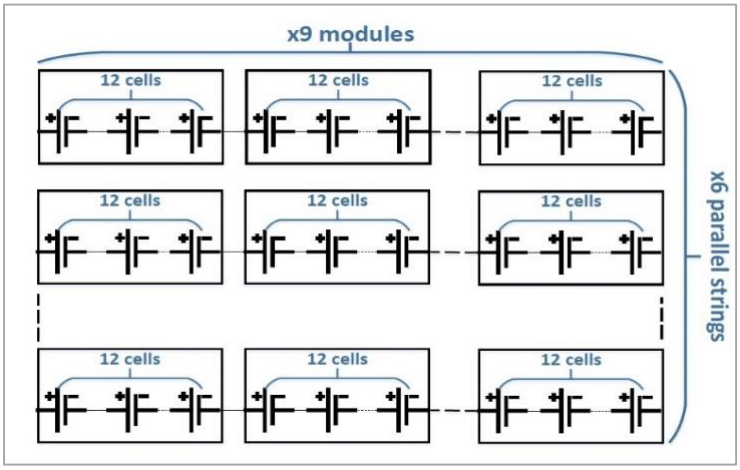

Figure 6-1. Electrical architecture of the battery pack

Table 6-3. Assumtions of the PHEV battery

Specification	Value
Cell type	6.5 Ah cylindrical NCA
Cell weight	0.34 kg
Electrical Architecture	6 parallel strings each with 108 cells in series
Number of Cells	648
Voltage	432 Volt
Energy Capacity	16.8 kWh
Weight	450 kg
Heat Capacity	194.4 kJ/K

6.1.2.1 Verification of the battery pack design

To verify that the above battery pack assumptions are representative of a typical PHEV battery, the performance of this battery was compared with the battery packs of the Chevrolet Volt and the BMW i8, two commercially available PHEVs. The specifications of these vehicles are given in Appendix 1

The traction power required to drive a vehicle over any given drive cycle is

$$P_T(t) = F_T v(t) \tag{6-1}$$

where $v(t)$ is the speed profile given by the drive cycle and F_T is the traction force, which based on equation (5-1) can be calculated as follows:

$$F_T = M\frac{dv}{dt} + F_A + F_{RR}. \tag{6-2}$$

In CD mode, the electric machine provides all the power required at the input shaft of the gearbox. This power can be calculated from the for the driveline efficiency η_T as

$$P_{em,mech}(t) = \eta_T \ P_T(t). \tag{6-3}$$

The total power drawn from the battery to deliver the above mechanical power at gearbox input is

$$P_{batt}\,(t) = \eta_{em}\, P_{em,mech}(t). \tag{6-4}$$

It is worth mentioning that the above relationships may overestimate the battery power since high power demands may be partly loaded on the engine. However, the assumption that the vehicle remains in CD mode throughout the drive cycle allows for eliminating the dependency of the analysis to powertrain capabilities and control strategies.

To enable a comparison of different battery packs, η_T and η_{em} were assumed to be equal in all vehicles. η_T was calculated from the driveline efficiency maps of Range Rover HEV at gear number 6 (total driveline gear ratio of 3.21:1). η_{em} was

assumed to be constant at 72%, assuming electric motors and inverters are each 85% efficient. Also, it was assumed that in braking events 30% of the mechanical power available at the gearbox input can be regenerated to the battery, thus,

$$P_{batt,regen}\,(t) = \; 0.3\,P_{em}(t). \tag{6-5}$$

Once the power of the battery pack was calculated, the C-rate of the cells and the corresponding heat generation was determined from the electrical architecture of the pack. The average and maximum values of terminal power, heat generation and C-rate calculated through the method outlined above for Chevy Volt, BMW i8 and the PHEV are given in Table 6-4. As in the case of power, heat generation and C-rate are likely overestimated here as a result of neglecting the operation of the engine. It is shown later in this chapter that when the PHEV is simulated over the US06 and the Artemis, the engine is used in the high power demanding sections of the drive cycle, reducing the battery load and subsequently its heat generation and C-rate. Still, the simplifications considered here are suitable for a comparison between the battery packs of these vehicles.

Table 6-4 indicates that the power demand of the PHEV is noticeably higher than the Volt and the i8, given its significantly higher weight. The rate of heat generation in the PHEV battery is between that of the Volt and of the i8, on all drive cycle. Similar trends are seen in the C-rates. Therefore, the design of the battery does not represent a special condition and is acceptable for the purpose of this research.

Table 6-4. Battery performance in Chevy Volt, BMW i8 and Range Rover PHEV

	Drive Cycle	Mean Power [kW]	Max Power [kW]	Mean Heat Gen. [kW]	Max Heat Gen. [kW]	Mean C-rate	Max C-rate
Volt	**WLTP**	11.81	74.19	0.30	4.02	0.71	4.46
	US06	24.96	144.85	0.98	15.33	1.50	8.70
	Artemis	18.58	97.62	0.64	6.96	1.12	5.86
i8	**WLTP**	11.58	69.42	1.43	18.36	1.63	9.78
	US06	24.26	131.04	4.51	65.40	3.42	18.5
	Artemis	18.29	90.30	3.11	31.05	2.58	12.7
Range Rover PHEV	**WLTP**	14.40	94.90	0.71	9.99	0.85	5.63
	US06	31.36	186.02	2.37	38.38	1.86	11.04
	Artemis	23.55	125.55	1.58	17.48	1.40	7.45

6.2 Model Integration

As the final step in the development of the PHEV model, the subsystem models were integrated in Simulink where the models of the powertrain and thermal subsystems were co-simulated. To achieve this, a functional mock-up unit (FMU) was created from the thermal subsystem models (the unit shown in Figure 5-24), and imported to Simulink using an FMI tool. The control algorithms of the AC and battery cooling subsystems (as explained in Section 5.6.1) were replicated in Simulink and integrated with the control algorithms of the powertrain subsystem. Figure 6-2 shows the block-diagram of the model. The 'powertrain sub-model' is simulated with an explicit MATLAB solver at fixed time-steps of 0.5 seconds (global solver). The FMI block is simulated with a local variable step solver (CVODE solver of Dymola) and communicates with Simulink at fixed intervals of 5 seconds. The controller block is solved with the global solver. The powertrain control algorithms are updated every 0.5 seconds, while the control algorithms of the thermal subsystems are updated every 5 seconds.

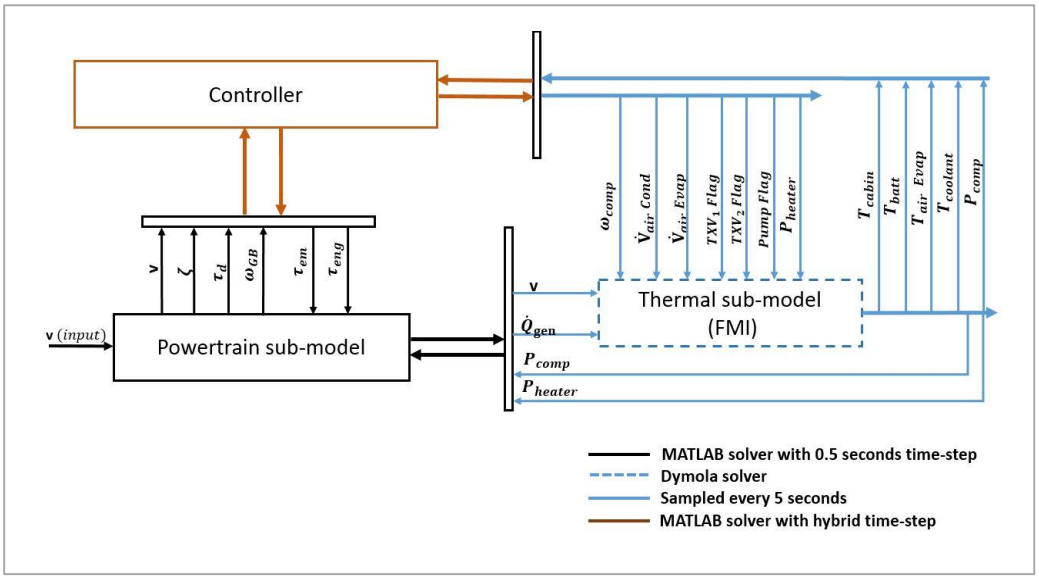

Figure 6-2. Integration of the subsystem models in Simulink

6.3 Drive cycle simulation

In this section, the PHEV model is simulated over four drive cycles; WLTC, US06, Artemis, and the NEDC, and the operating modes of the powertrain are discussed. Where the entire drive cycle is achieved in EV mode, consecutive instances of the drive cycles are used until the engine is turned on. The energy efficiency of the vehicle and the internal heat generation of the battery over different drive cycles are compared based on the simulation results.

6.3.1 WLTC

WLTC is an ideal drive cycle for demonstrating distinct CD and CS operating modes of the vehicle as its torque demand is suitably low, allowing all-electric operation. Figure 6-3 shows the result of simulating the PHEV over 3 consecutive instances of the WLTC. The vehicle has an AER of approximately 55 kilometres on this drive cycle, during which the engine remains off and the battery depletes from 95% SoC to approximately 10% SoC. The vehicle then enters its CS mode when the engine is repeatedly used, maintaining the battery SoC in the window of 10%-13%.

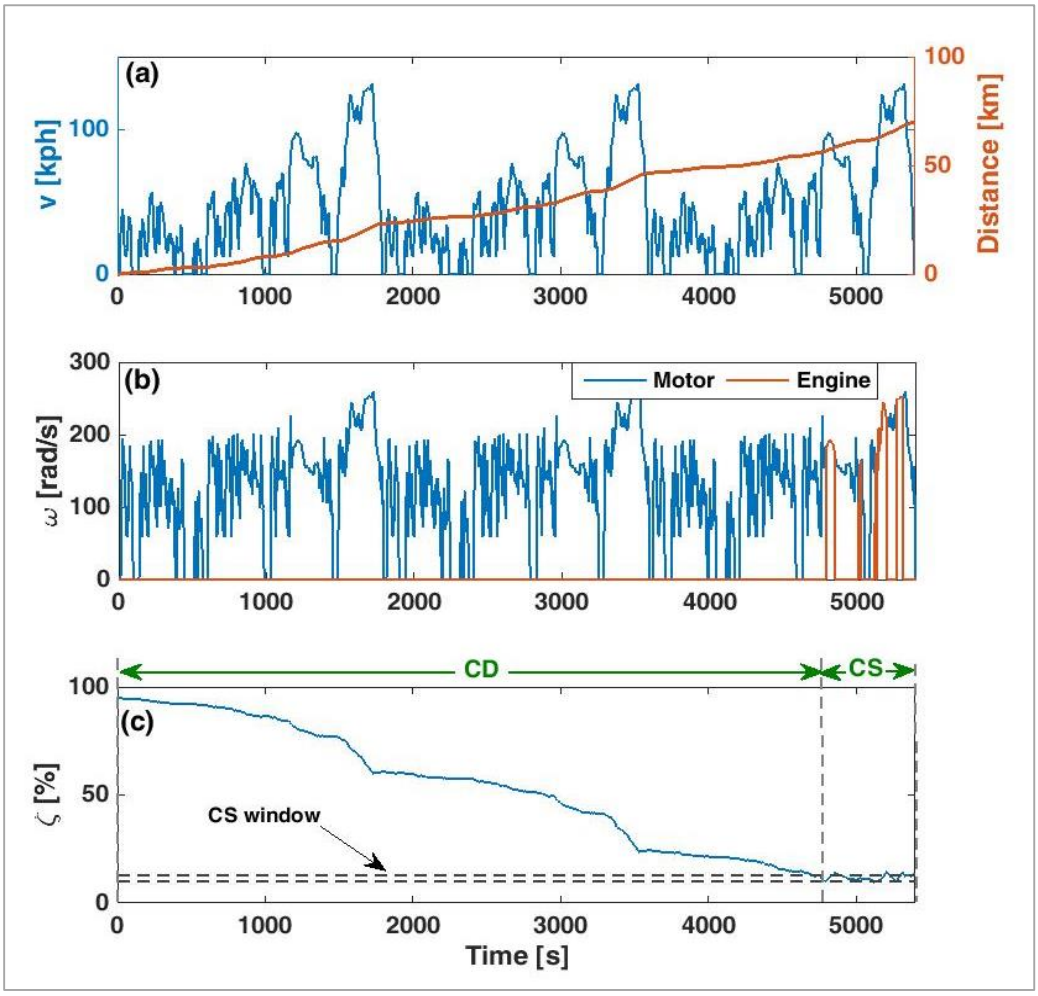

Figure 6-3: Simulation results over 3 WLTC cycles: (a) drive cycle and distance, (b) electric machine and engine speed, and (c) SoC

6.3.2 S06

For more aggressive drive cycles, such as the US06, the engine can be used to assist in accelerating the vehicle (Engine Assist Mode). This is illustrated in Figure 6-4 where the vehicle enters a hybrid mode at 5 instances during the drive cycle, despite sufficient battery charge availability. Note that load balancing is performed to allow more efficient operation of the engine. The net depletion of battery charge over this drive cycle is approximately 21%.

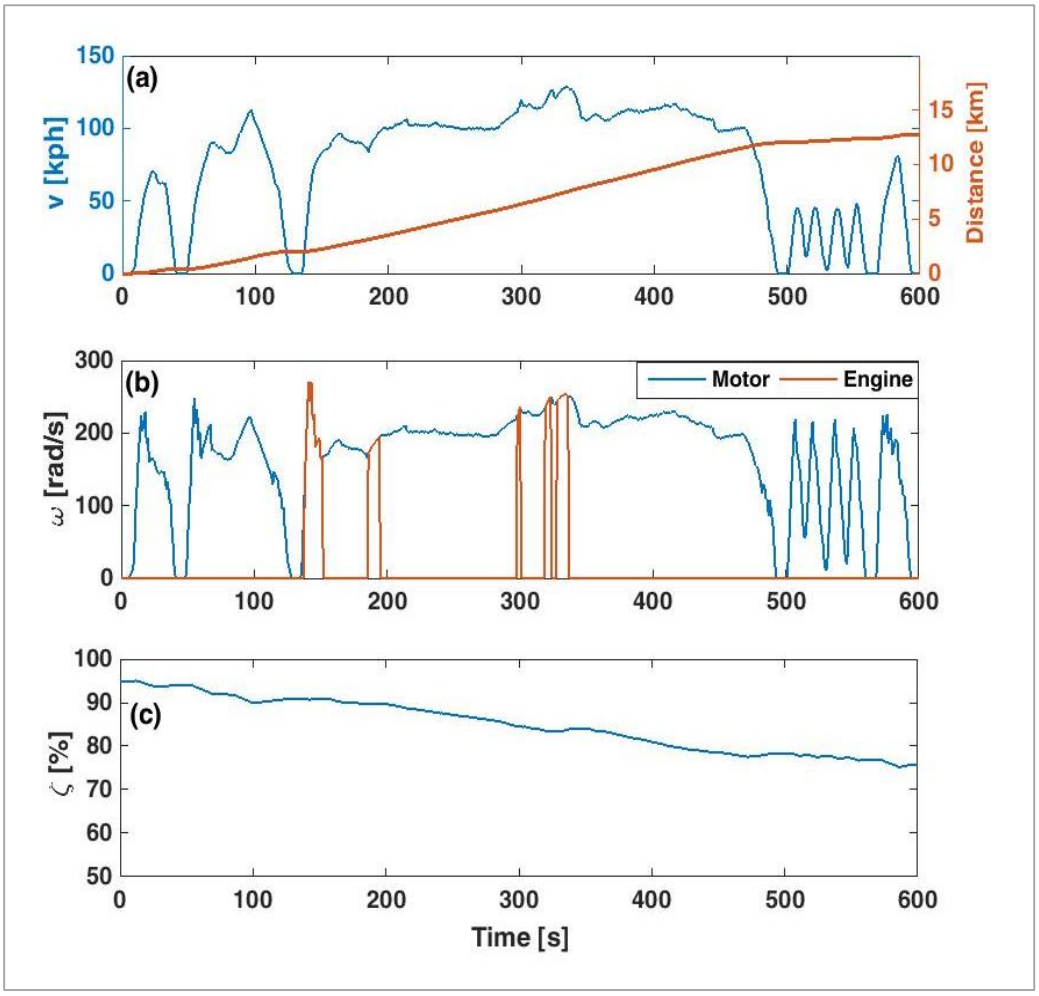

Figure 6-4. Simulation result over US06: (a) drive cycle, (b) electric machine and engine speed, and (c) SoC

6.3.3 ARTEMIS

Operating modes of the vehicle on the Artemis are similar to those on the US06. As Figure 6-5 shows, the vehicle operates in EV mode over the urban part of the drive cycle, while engine assist mode is occasionally activated in the extra-urban part of the cycle. The net depletion of the battery charge over this drive cycle is approximately 57%.

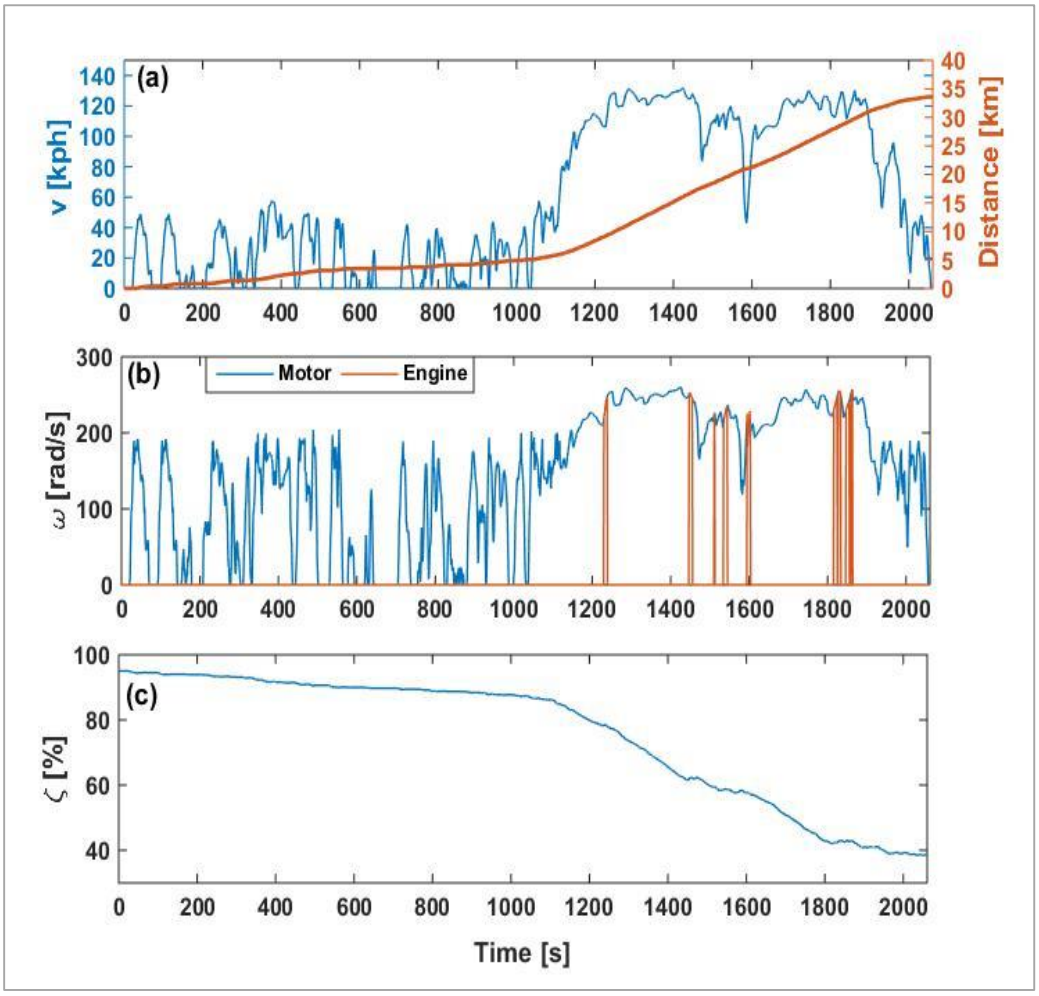

Figure 6-5. Simulation results over Artemis: (a) drive cycle, (b) electric machine and engine speed, and (c) SoC

6.3.4 NEDC

Figure 6-6 shows the result of simulating the model over 7 consecutive instances of NEDC. The operation of the vehicle over the NEDC is qualitatively similar to its operation over the WLTC, in that the vehicle has a long AER (approximately 65 km), before entering the CS operating mode when the battery is maintained in the SoC window of 10%-13%

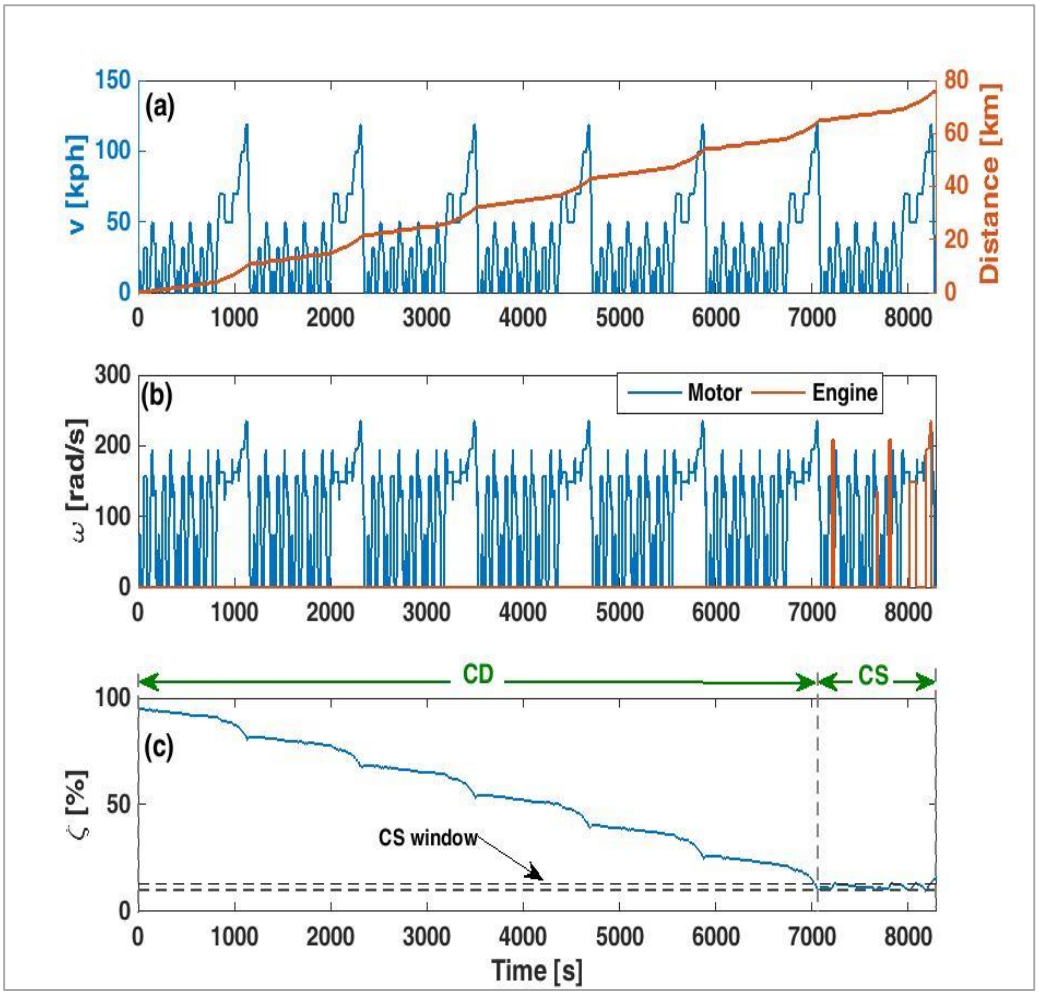

Figure 6-6. Simulation results over NEDC: (a) drive cycle, (b) a electric machine and engine speed, and (c) SoC

Simulation results in Figure 6-3 to Figure 6-6 suggest acceptable functionally of the control rules in replicating the standard PHEV operating modes.

6.3.5 Energy efficiency over different drive cycles

The energy consumption measures of the vehicle over standard drive cycles are compared in Table 6-5. It can be seen that Artemis is the most demanding drive cycle, as indicated by the energy requirement of the driveline. Considering the overall converted energy indicates that the engine operates inefficiently on the US06 (at lower speed), leading to higher energy conversion compared to the Artemis. Table 6-5 also compares the CS energy efficiency of the vehicle over different drive cycles. As expected, the highest fuel economy is achieved over the NEDC, followed by the WLTC.

Table 6-5. Energy consumption metrics over different drive cycles

Drive Cycle	Driveline Energy $[Wh/\ km]$	Converted Energy $[Wh/\ km]$	AER $[km]$	CS FE * $[L/100km]$
WLTC	185	274	55	6.9
US06	243	460	n/a**	8.31
Artemis	253	430	n/a**	8.49
NEDC	150	224	65	6.25

* obtained by simulating the drive cycle with 10% initial SoC.

6.3.6 Heat Generation over different drive cycles

Figure 6-7 compares the temperature and the internal heat generation of the battery over the drive cycles. To obtain these results, the vehicle was assumed to be at 27°C. The temperature variation in the presence and the absence of cooling are given for comparison. The effect of the battery cooling load on the heat generation is however neglected. Over the US06, the battery temperature rises to approximately 31.5°C despite the short length of the drive cycle. The Artemis and the WLTC result in similar heat generations over their urban parts leading to similar evolution of temperature, but since the Artemis highway is more demanding than the extra urban part of WLTC, the battery temperature rises to approximately 35.5°C over the Artemis, compared to 31.5°C over the WLTC. Over the NEDC, the battery temperature only rises to approximately 28.5°C, given the low aggressiveness and short length of the drive cycle, therefore, cooling is not activated.

Table 6-6 compares the temperature rise, the heat generation and the heat extraction from the battery for different drive cycles. The average and peak rates of heat generation are highest over the US06, indicating the most power demanding EV operation. Note however that despite the higher heat generation over the US06, the total amount of the heat generated over the two other drive cycles is higher due to their longer durations. Comparing the peak heat generations and extractions suggests that if the battery is constantly subject to currents as high as the highest transient currents of these drive cycles, the cooling power will be

insufficient to limit temperature rise. The total amount of heat extraction varies depending on the duration of cooling. Over the Artemis, cooling is activated well before the end of the drive cycle, hence heat extraction is sufficient to cool the battery to its initial temperature.

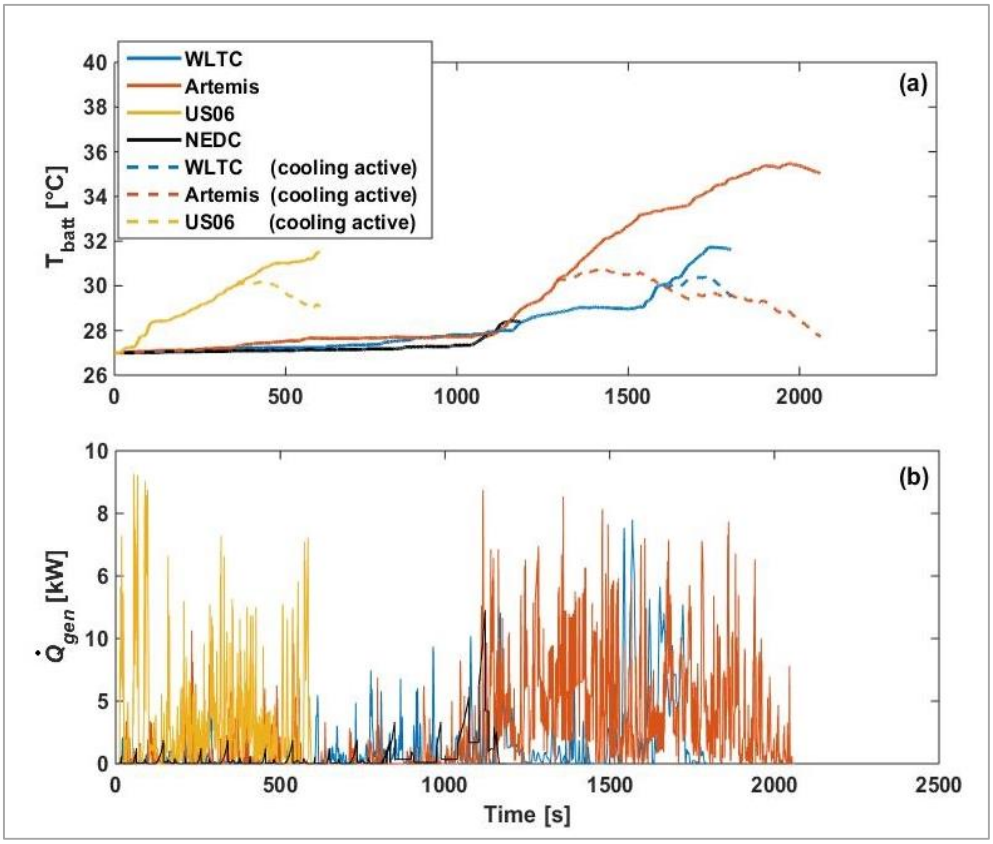

Figure 6-7. Comparison of (a) temperature rise and (b) heat generation in battery between different drive cycles

Table 6-6. Effect of drive cycle on the temperature and internal heat generation of the battery

Drive Cycle	Temperature Rise	Peak Heat Generation	Average Heat Generation	Total Generated Heat	Peak Extracted Heat	Total Extracted Heat
	[°C]	[W]	[W]	[kJ]	[W]	[kJ]
WLTP	4.6	7796	549	989	2926	500
US06	4.5	9244	1449	870	2810	572
Artemis	8	8743	1026	2116	3382	2331
NEDC	1.4	4906	228	270	0	0

6.4 Estimation of the battery lifetime

Subsequent analyses within this research require a method for estimating the effect of storage conditions (temperature and SoC) and cycling conditions (temperature and charge-discharge cycling) on battery lifetime. To enable this estimation, the dataset given in [126] was used as reference. The dataset is related to NCA type cylindrical cells (a similar technology to the cells assumed for the PHEV) and gives the capacity loss of the cells after 20 weeks of storage, as well as after 500 accelerated cycles. As discussed in Section 2.2.3.3 calculating the battery lifetime based on extrapolation of the test data and superposition of cycling and storage capacity losses leads to underestimation of the battery lifetime. While the absolute battery lifetime is not of direct concern to this research, in the interest of consistency between the analyses within this research and the warranty periods set for the PHEV, the capacity loss dataset was scaled by a factor of 2.5, in line with the estimate discussion presented in Section 2.2.3.3 . In other words, it was assumed that the given dataset was representative of 50 weeks of storage (rather than 20 weeks) and 580 cycles (rather than 230 cycles). Figure 6-8 shows the scaled data that is used in the subsequent analyses.

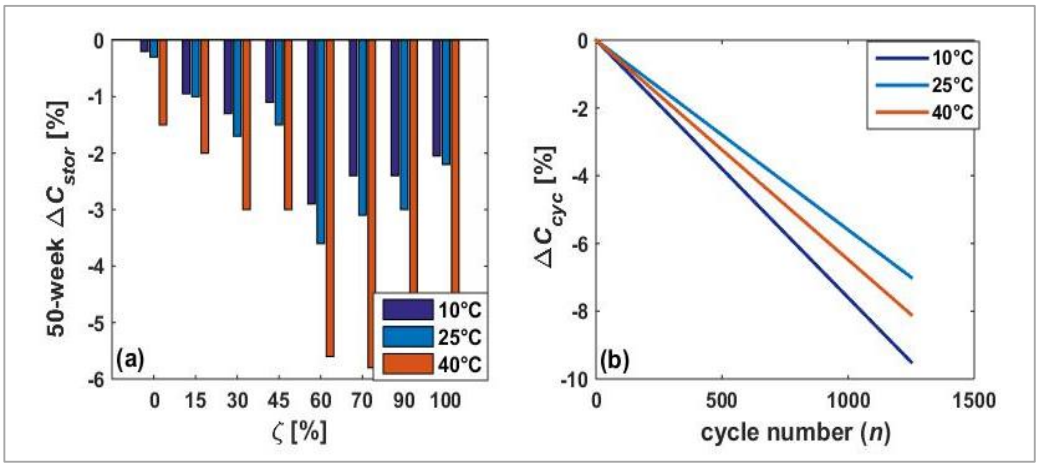

Figure 6-8. The capacity loss data used for battery lifetime calculation (a) effect of temperature and SoC after storage for 50 weeks, and (b) effect of temperature after 1250 charge-discgarge cycles. Data derived from the dataset in [126]

For notational expediency, calculation of capacity loss is described as follows

$$\begin{cases} \Delta C = \Delta C_{stor}(T_{batt}, \zeta) + \Delta C_{cyc}(T_{batt}, n) = \Delta C(x_b, n) \\ \text{where } \Delta C_{stor}, \Delta C_{cyc} \rightarrow data\ shown\ in \text{ Figure 6-8} \end{cases} \quad (6\text{-}6)$$

where ΔC_{stor} and ΔC_{cyc} denote the storage and cycling capacity loss, respectively, while $x_b = \begin{bmatrix} T_{batt} \\ \zeta \end{bmatrix}$, is the state of the battery. Chapter 7 provides further details about calculation of capacity loss and estimation of the battery lifetime of the PHEV.

6.5 Summary

In this chapter, the steps taken for developing a PHEV model from Range Rover HEV subsystem models were discussed. These steps included upsizing the 1.6 kWh battery of Range Rover HEV to a 16.8 kWh battery and changing the 35 kW electric machine of Range Rover HEV with a 75 kWh machine. Appropriate control rules were implemented to replicate the operating modes of PHEVs, i.e. the CS and CD operating modes. An FMU was generated from the thermal subsystem models and imported to Simulink where it was integrated with the powertrain subsystem model to complete the model of the PHEV. Simulating the PHEV model over a number of standard drive cycles helped verify that the model was able to simulate the operating modes of typical PHEVs. Based on these simulation results, some key metrics related to the energy efficiency of the vehicle and cooling power of the battery cooling subsystem was analysed. In addition, the method used on this research for calculating the battery lifetime of the PHEV was explained.

CHAPTER 7 SIMULATION OF THE PHEV IN HOT CLIMATE CONDITIONS

Introduction

In this chapter, the effects of hot climate conditions on the performance attributes of the PHEV are quantified through simulating a number of 24-hour duty cycles, using the model developed in Chapter 6. Details of the duty cycles are explained in Section 7.1. In Section 7.2, the simulation results are presented and three vehicle performance attributes of fuel economy, battery lifetime, and (passenger) thermal comfort are evaluated. The results help further establish the need for key-off cooling. In Section 7.3, different strategies of key-off cooling are investigated and their benefits for the vehicle are evaluated. Also, the benefit of partial charging for improving the battery lifetime is discussed.

7.1 Defining 24-hour duty cycles for the PHEV

This section will introduce the duty cycles defined for simulating the PHEV. The duty cycles assume similar usage scenarios and charge patterns, but different climate conditions and drive cycles.

7.1.1 The usage scenario

The duty cycles assumed a work commute usage case, comprising of four phases: two trip and two parks. In Figure 7-1, different phases of the scenario are marked on the vehicle speed profile. The details of each phase are as follows:

Trip 1 starts in the early hours of the morning, though the exact start time is adjusted for the length of the trip to allow completing the trip at 7:30. The vehicle is initially soaked at the temperature of the garage, and the battery is fully charged. The vehicle is driven on a specific drive cycle while being subject to ambient conditions.

Day Park lasts for 8 hours from 7:30 to 15:30. The vehicle is parked in the open, subject to ambient conditions without being plugged in.

Trip 2 starts at 15:30. The vehicle is subject to ambient conditions as it is driven on a drive cycle identical to that of Trip 1.

Night Park follows Trip 2 and lasts between 14 hours to 15 hours depending on the length of the trips. The vehicle is parked and plugged in until the next day in a garage with constant temperature.

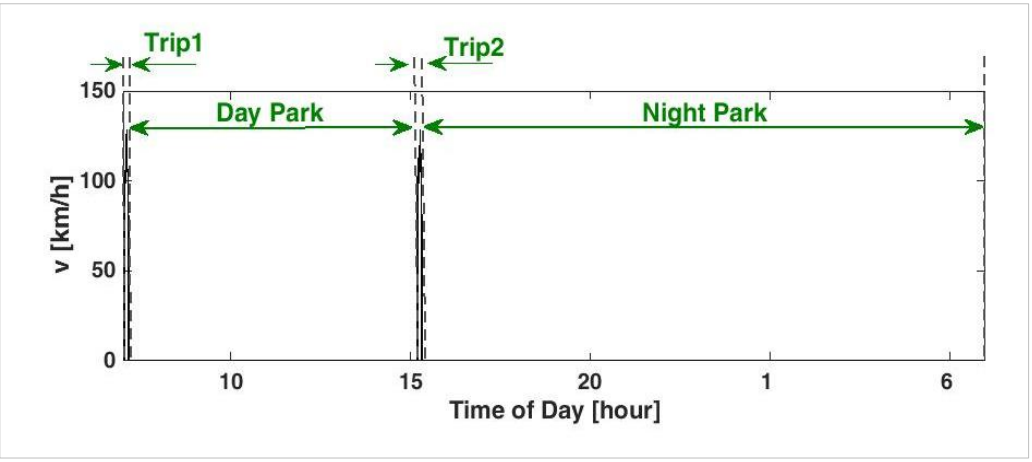

Figure 7-1. 24-hour speed profile of the vehicle

It was assumed that battery cooling is available during the trips as well as during Night Park (key-on and plugged-in cooling). Also, air conditioning is available during the trips. The control of the battery cooling and the AC subsystems follows the strategy explained in Section 5.6.1, while the powertrain control strategies are consistent with those explained in Section 5.2.

7.1.2 The drive cycles

In the interest of clarity, Trip 1 and Trip 2 were assumed to have identical drive cycles. Four standard drive cycles, the WLTC, the US06, the Artemis, and the NEDC were assumed for the trips. In case of the NEDC, two instances of the drive cycle were combined (referred to as NEDCx2 hereafter) to create a more energy demanding commute.

7.1.3 The ambient conditions

The ambient conditions were derived from the climate conditions of Phoenix and Seattle given in [2]. Rather than considering the hottest or coldest day of the year in each location, the hourly profiles of the air temperature, solar irradiance, and humidity were averaged between April to September and between October to March, to define a warm and a cold season, respectively. These are loosely referred to as summer and winter. Although the above assumptions neglect the stochastic nature of real-world climate conditions, they enable the analyses intended in this research and facilitate the evaluation of the ultimate benefits of key-off battery cooling.

Figure 7-2 shows the hourly variation of seasonal climate conditions in these locations based on the assumptions described above. Air temperature and solar irradiance are highest in Phoenix summer and lowest in Seattle winter, as seen in Figure 7-2(a) and Figure 7-2(b). The climate of Phoenix in winter is very similar to climate of Seattle in summer, as far as the air temperature and solar load are concerned, despite higher peak air temperature in Phoenix and higher cumulative solar load in Seattle. As Figure 7-2(c) shows that Seattle is generally more humid than Phoenix.

The ambient conditions in which the vehicle operates were defined as follows. In Trip 1, Trip 2 and Day Park, the vehicle is subject to the hourly climate conditions of Figure 7-2. In Night Park, the vehicle is parked in a garage maintained at the constant temperature of 25°C in summer, and 15°C in winter, in both locations. This assumption helps contain any effect of temperature on battery ageing in Night Park and facilitates the forthcoming analyses.

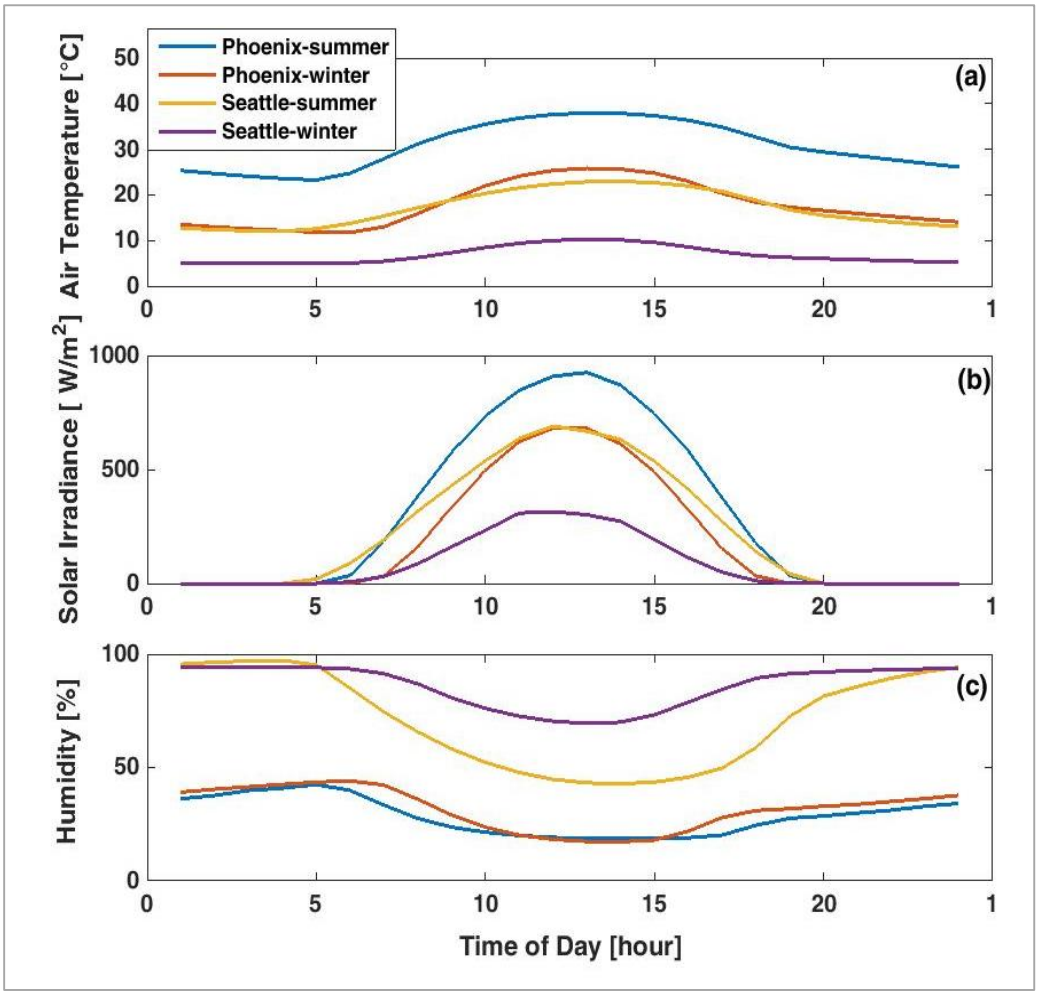

Figure 7-2. (a) air temperature, (b) solar irradiance, and (c) humidity in Phoenix, and Seattle over summer and winter.

7.1.4 The pattern of charge

The battery was assumed to be charged once every 24 hours, in Night Park. An ideal level 2 charger with a constant power of 13.2 kW was assumed. While the vehicle is plugged in to the charger throughout Night Park, the just-in-time charging strategy is applied, which initiates charging in the morning, in time for Trip 1.

The key assumptions of the duty cycles are summarised in Table 7-1. Different combinations of the drive cycles (four) and climate conditions (four, two season per location) define 16 unique duty cycles for simulating the PHEV.

Table 7-1. Summary of duty cycle assumptions

	Phase	Duration	Ambient	Plugged In	Battery Cooling
Duty cycle assumption	Trip1	variable	seasonal hourly mean Figure 7-2	--	yes
	Day Park	8 hrs		no	no
	Trip 2	variable		--	yes
	Night Park	~14 hrs	25°C (summer) 15°C (winter)	yes 13.2 kW charger	yes
Initial Conditions	**Parameter**	**Value**			
	Battery SoC	95 %			
	Battery/Cabin temperature	25°C (summer) 15°C (winter)			

7.2 Simulation results: the duty cycles with US06 trips

In this sections, the results of simulating the duty cycles comprising of US06 trips are discussed. Figure 7-3 is related to the operation of the vehicle in Phoenix summer, and shows the profiles of the cabin and the battery temperature (Figure 7-3(a)), as well as the profile of the battery SoC (Figure 7-3(b)). The following observations can be made with respect to each phase of the duty cycle:

Trip 1: As Figure 7-3(a) shows, the cabin and battery are both at 25°C at the start of Trip 1. AC maintains the cabin at approximately 22°C. The battery gradually warms up and reaches 30°C, at which point battery cooling is initiated. Figure 7-3(b) shows that the vehicle operates mostly in CD mode in Trip 1 (depleting the battery by 21% from 95% to approximately 74%), apart from the high torque demanding parts of the drive cycle (see expected from the results presented in Figure 6-4).

Day Park: Influenced by the ambient conditions, the vehicle undergoes a hot soak in Day Park. The temperature of the cabin and the battery rise to 60°C, and 48°C,

respectively. The SoC remains constant. The peak cabin temperature occurs slightly before the end of Day Park, while the battery temperature rises consistently.

Trip 2: AC and battery cooling are applied to cool down the hot-soaked vehicle. Figure 7-3(a) shows that within the duration of the trip, the cabin and battery are only cooled to approximately 33°C and 39°C, respectively, and remain significantly warmer than their desired temperatures. During this trip, the battery is discharged by a further 19% to approximately 54% SoC [1].

Night Park: When the vehicle is parked again, AC terminates, thus, the cabin temperature, influenced by the high temperature of its shell, rises to 45°C. The battery however, is cooled to 25°C, (plugged-in cooling). Both the cabin and the battery continue to exchange heat with the ambient until stabilising at 25°C. The battery is charged to its maximum allowable SoC in time for the next trip (Trip 1)[2].

[1] The underlying reason for lower depletion of battery charge in trip 2 compared to trip 1 is discussed in Section 7.2.1.1

[2] As Figure 7-3-a shows, charging leads to a slight increase in the battery temperature. This is however neglected in the forthcoming analyses.

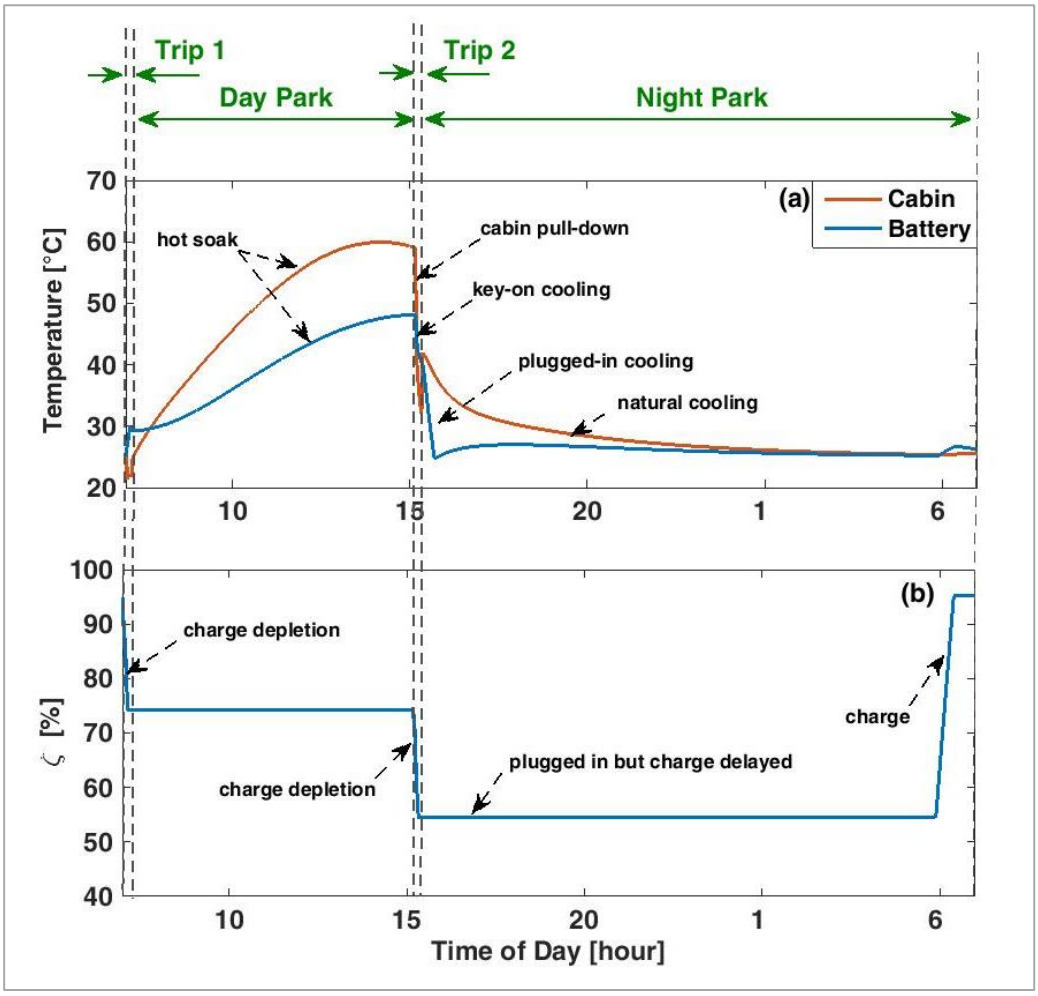

Figure 7-3. Profiles of (a) cabin and battery temperature, and (b) battery SoC in Phoenix summer with US06 trips

Repeating the simulations with the climate conditions of Phoenix winter, and Seattle summer produces results that are qualitatively similar to Figure 7-3, and are not shown. Table 7-2 summarises the key features of the simulation results. Assuming the climate conditions of Seattle winter however leads to a noticeably different cabin and battery temperature profiles. As shown in Figure 7-4, the cabin is generally colder than its set point, therefore AC is not applied (heating the cabin may be necessary but it is ignored in this research). Similarly, the battery temperature remains below 20°C throughout the day, therefore, battery cooling is not activated. Note that the variations in temperatures are due to natural cooling (as well as internal heat generation in the case of the battery).

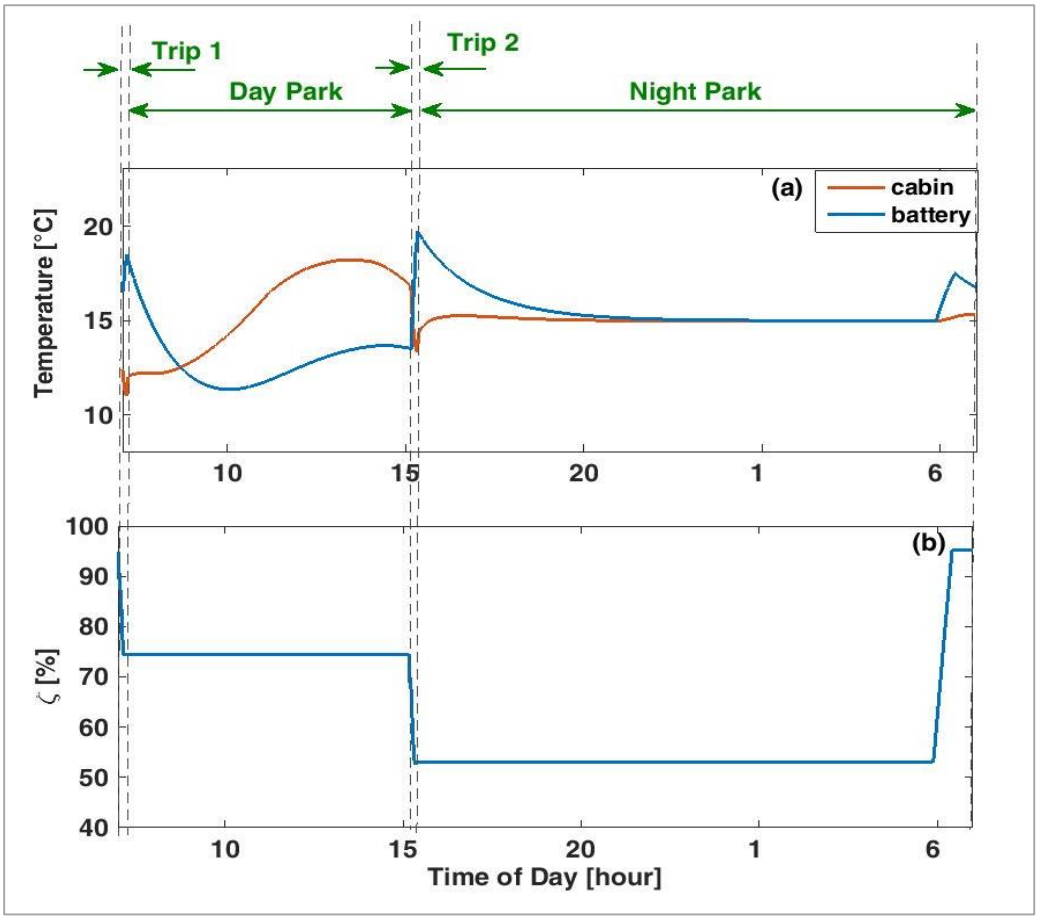

Figure 7-4. Profiles of (a) cabin and battery temperature and (b) battery SoC is Seattle winter with US06 trips

The average and maximum temperature of the cabin and the battery under different climate condition are given in Table 7-2. The following observation can be made:

1. The battery and the cabin are hottest in Phoenix summer and coldest in Seattle winter.

2. Comparing Day Park temperatures in Phoenix winter and Seattle summer indicates similar effects on the temperature of the battery (with average temperatures reaching 25°C in Phoenix compared to 26.5°C in Seattle) due to the similarity in air temperature. The higher cumulative solar load in Seattle leads to higher cabin temperature during Day Park (with average temperatures reaching 18.2°C in Phoenix compared to 34°C in Seattle). However, the maximum temperatures are higher in Phoenix winter.

3. Comparing the winter seasons in both locations shows that while no cooling is required in Seattle, both the battery and cabin should be cooled throughout Trip 2 in Phoenix (as the temperatures exceed their set points). The low cabin temperature in the first trips may in fact demand heating which is neglected in this work.

4. The higher heat gain from the ambient environment has led to different cooling regimes in Phoenix summer compared to Seattle summer. During the first trips, the increase in battery temperature is sufficient to trigger battery cooling in Phoenix but not in Seattle. Also contrary to Phoenix summer, plugged-in cooling is not applied in Seattle summer as the maximum battery temperature in Night Park is below 30°C.

The above observations indicate that geographical locations such as Phoenix can create a challenging environment for the vehicle and can potentially impact its performance attributes.

Table 7-2. Comparion of battery and cabin temperatures for different locations and seasons

Loc.	Parameter	Winter				Summer			
		Trip 1	Day Park	Trip 2	Night Park	Trip 1	Day Park	Trip 2	Night Park
Phoenix	$\overline{T}_{cabin}$	13.6	31.1	24.2	17.5	22.2	50.4	37.0	28.0
	$T_{cabin,max}$	15.0	40.8	39.4	27.4	25.0	61.9	58.1	41.8
	$\overline{T}_{batt}$	18.5	24.9	29.6	17.4	28.0	39.0	43.0	26.2
	$T_{batt,max}$	21.0	32.0	32.0	28.6	30.0	48.4	48.4	41.0
	Cooling	None	NA*	Both	None	Both	NA	Both	Battery
Seattle	$\overline{T}_{cabin}$	12.1	15.6	14.2	15.0	21.2	34.0	24.4	25.8
	$T_{cabin,max}$	15.0	18.2	16.8	15.3	25.0	40.1	39.1	27.4
	$\overline{T}_{batt}$	17.0	13.0	17.1	15.6	25.6	26.4	29.2	25.7
	$T_{batt,max}$	18.5	18.4	19.7	19.7	26.1	30.4	30.4	28.3
	Cooling	None	NA	None	None	Cabin**	NA	both	None

* not applicable
** AC is activated in the initial 200 seconds of the trip

7.2.1 Calculation of the PHEV performance attributes

In this section, the impact of the high battery temperature in Phoenix summer on the performance attributes of the PHEV is determined for the duty cycle comprising of US06 trips.

7.2.1.1 Impact on fuel economy

During Day Park in Phoenix summer, the battery temperature can reach as high as 48°C, which is higher than the 45°C overheating threshold of the battery (see Table 6-2). Therefore, limited battery power will be available at the onset of Trip 2, which on a power demanding drive cycle such as the US06, will reduce the electric traction capability of the vehicle and forces the vehicle to operate in hybrid mode leading to higher fuel consumption. This can be inferred from Figure 7-5 which gives more details about the two daily trips of vehicle. It can be seen that despite having identical drive cycles, the vehicle operates differently in Trip 1 and Trip 2. In Trip 1, the operation of the vehicle is similar to that explained in Section 6.3.2, that is, the vehicle operates mostly in CD mode, depleting approximately 21% of the battery SoC, while the engine starting five times in the high power demanding parts of the drive cycle. With the battery overheated in Day Park, the vehicle is forced to enter hybrid mode twice in the first 100 seconds of Trip 2, as Figure 7-5(b) shows. Once the battery is sufficiently cooled, the engine operates in a similar manner to that in Trip 1, while the battery is gradually discharged as it is cooled.

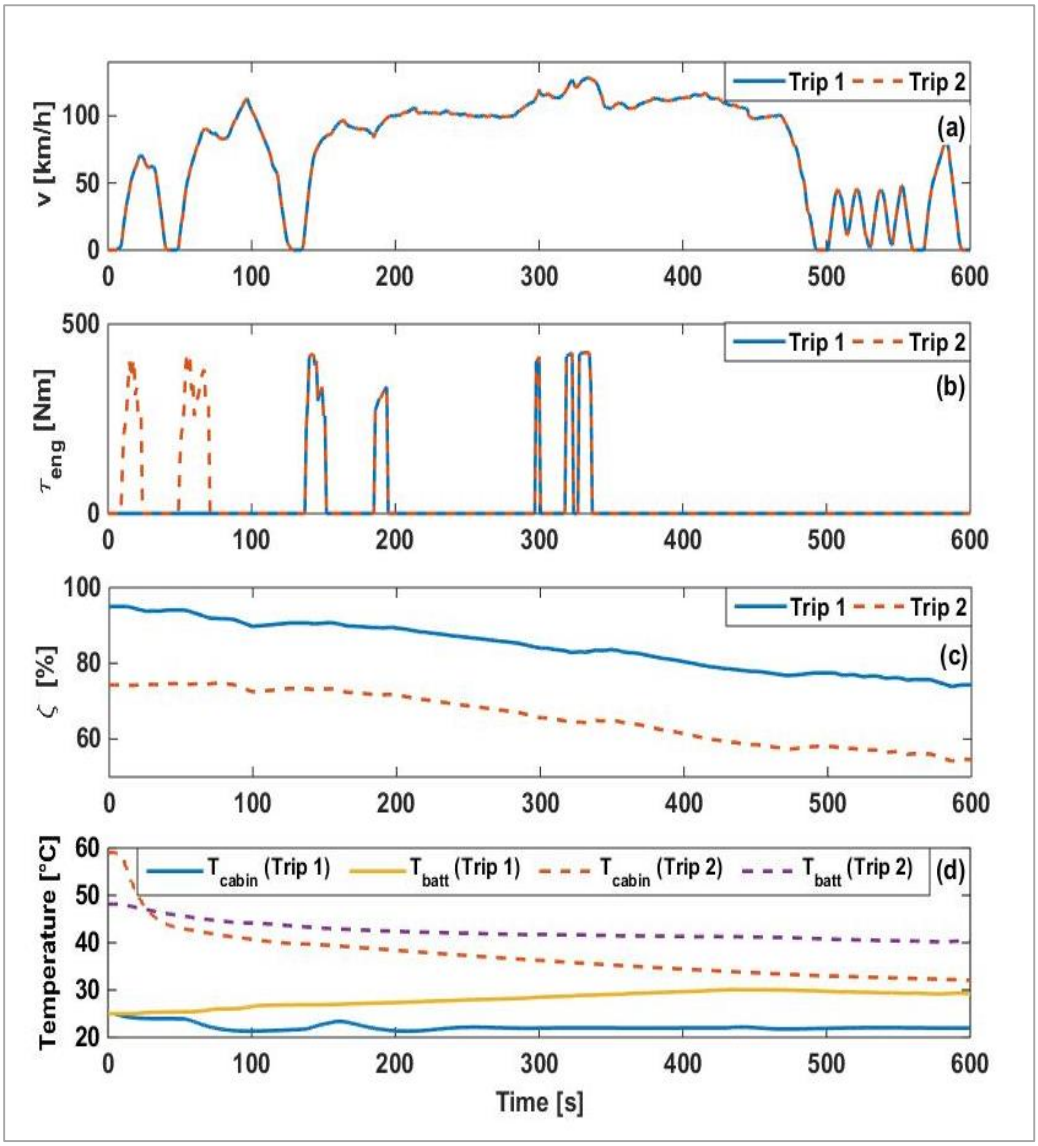

Figure 7-5. Simulation results - (a) vehicle speed, (b) engine torque, (c) battery SoC and (d) temperature of cabin and battery over the duty cycle comprising of Phoenix summer climate and US06 trips

Table 7-3 compares the SoC variation and fuel consumption over the two trips on the US06 for different climate conditions. It can be seen that with the exception of operation in Phoenix summer, 0.23 l of fuel is consumed in both trips of all duty cycles.

With the exception of operation in Phoenix summer, SoC decreases more over Trip 2 compared to Trip 1[1]. The above observations confirm that the climate conditions of Phoenix summer affect the operating mode and therefore the fuel economy of the vehicle.

Table 7-3. SoC change and fuel consumption over two US06 trips for different locations and seasons. Values are related to one day operation under each condition

Loc.	Season	Trip 1		Trip 2	
		$\Delta\zeta$ [%]	v_{fuel} [l]	$\Delta\zeta$ [%]	v_{fuel} [l]
Phoenix	**Summer**	-20.42	0.23	-19.63	0.37
	Winter	-20.29	0.23	-23.67	0.23
Seattle	**Summer**	-19.63	0.23	-23.70	0.23
	Winter	-20.47	0.23	-21.60	0.23

7.2.1.2 Impact on battery lifetime

The battery lifetime of the vehicle undergoing its daily duty cycle can be calculated from the simulation results. Table 7-4 gives the time average of the battery temperature and SoC as well as the number of charge-discharge cycles in each phase of the duty cycle, in Phoenix summer and winter. The number of cycles follow the trends of SoC changes given in Table 7-3. The seasonal storage and cycling capacity losses of the battery are also given for each phase. It can be seen that in Day Park in phoenix summer, the battery remains at an average SoC of 74.6% and at an average temperature of 39 °C without being cycled. Due to the storage conditions, the battery loses 1.07% of its capacity, while the cycling capacity loss is zero.

[1] It is worth noting that the further depletion of the battery in Trip 2 in Phoenix winter and Seattle Summer is a result of higher cooling loads after the day park, but in Seattle winter, the dominant effect on the SoC is the lower voltage of the battery pack. Comparing battery depletion over the first trips in winter of the two locations, the slightly higher battery depletion in Seattle is due to higher internal resistance of the battery at lower temperature.

Adding the cycling and storage capacity losses for different phases of the duty cycle in each season leads to 2.72% capacity loss in summer, compared to 2.05% in winter. The total capacity loss in one year is therefore 4.76%. Accepting 30% capacity loss as the EoL condition, the above calculations indicate a battery lifetime of just over six years.

Table 7-5 gives similar information about the battery of the vehicle operating in Seattle. It can be seen that the battery lifetime of over 7 years can be expected.

The following observation can be made from Table 7-4 and Table 7-5:

1. The conditions of storage are the main contributors to the capacity loss. This is predictable as the vehicle is parked for a significant part of the duty cycle.

2. In summer duty cycles in both locations, cycling capacity loss is higher in Trip 2 compared to Trip 1, due to the higher temperature of the battery. This difference is less significant in Phoenix due to operation in hybrid mode in Trip 2, as previously discussed.

3. In Seattle winter, cycling capacity loss is higher in Trip 2 compared to Trip 1 since the battery is cycled more due to lower voltage (lower average SoC). Lower voltage in Trip 2 of Phoenix winter has a similar effect on capacity fade but is outweighed by the effect of the higher temperature.

4. Comparing Day Park in summer seasons shows that the battery loses approximately 1.1% of its capacity during Day Park in Phoenix compared to 0.65% in Seattle.

5. While Day Park capacity losses in each location are less significant in winter than in summer, Day Park capacity loss in Phoenix winter is as significant as that in Seattle summer, due to the similarity of the climate conditions.

6. The battery will last one year less in the vehicle operating in Phoenix compared to the one in Seattle. The most significant contributor to this shorter lifetime is the higher capacity loss during park phases in Phoenix due to higher temperature of the battery.

Table 7-4. Battery capacity loss and lifetime calculations in Phoenix (trips on the US06)

	Winter				Summer			
	Trip1	**Day Park**	**Trip2**	**Night Park**	**Trip1**	**Day Park**	**Trip2**	**Night Park**
$\overline{SoC}$ **[%]**	84.4	74.7	62.6	53.4	84.51	74.58	68.75	58.98
$\overline{T_{batt}}$ **[°C]**	18.5	24.9	29.6	17.4	28.03	39.00	43.02	26.00
Number of cycles (per season)	28.4	0.0	30.7	40.2	28.21	0.00	27.85	36.4
Storage ΔC **[%]** ***(per season)***	0.00	0.64	0.00	0.86	0.00	1.07	0.00	1.17
Cycling ΔC **[%]** ***(per season)***	0.16	0.00	0.16	0.23	0.15	0.00	0.16	0.17
Total ΔC **[%]** ***(per season)***	2.05				2.72			
Year 1 ΔC **[%]**	4.76							
Life [years]	6.3							

Table 7-5. Battery capacity loss and lifetime calculations in Seattle (trips on the US06)

	Winter				Summer			
	Trip1	**Day Park**	**Trip2**	**Night Park**	**Trip1**	**Day Park**	**Trip2**	**Night Park**
$\overline{SoC}$ **[%]**	84.4	74.5	63.3	55.2	84.8	75.44	63.29	54.1
$\overline{T_{batt}}$ **[°C]**	17.0	13.0	17.1	15.6	25.7	26.5	29.5	25.7
Number of cycles (per season)	28.6	0.0	30.0	38.5	27.9	0.0	30.7	39.6
Storage ΔC **[%]** ***(per season)***	0.00	0.48	0.00	0.92	0.00	0.65	0.00	1.0
Cycling ΔC **[%]** ***(per season)***	0.16	0.00	0.17	0.22	0.14	0.0	0.16	0.20
Total ΔC **[%]** ***(per season)***	1.96				2.16			
Year 1 ΔC **[%]**	4.12							
Life [years]	7.3							

7.2.1.3 Impact on thermal comfort

In Phoenix summer, the cabin temperature in Trip 1 is maintained close to the set point of 22°C. This can be seen in both Figure 7-3(a) and Figure 7-5(b). Therefore, the cabin is thermally comfortable for passengers. However, following the hot soak in Day Park, the thermal load of the cabin is so high that the cabin remains hot throughout Trip 2 and the compressor is fully loaded. As a result, allocating some of the compressor power to key-on (battery) cooling affects the cabin temperature. To illustrate this effect, the battery was removed from the PHEV model to create its equivalent CV model. This model was then used to simulate Trip 2, for identical conditions. Figure 7-6 compares the vent temperature and the average cabin temperature in the PHEV and in the CV. It can be seen than in comparison with the CV equivalent, the key-on battery cooling load in the PHEV increases the cabin and vent temperatures by approximately 3 and 8 degrees, respectively.

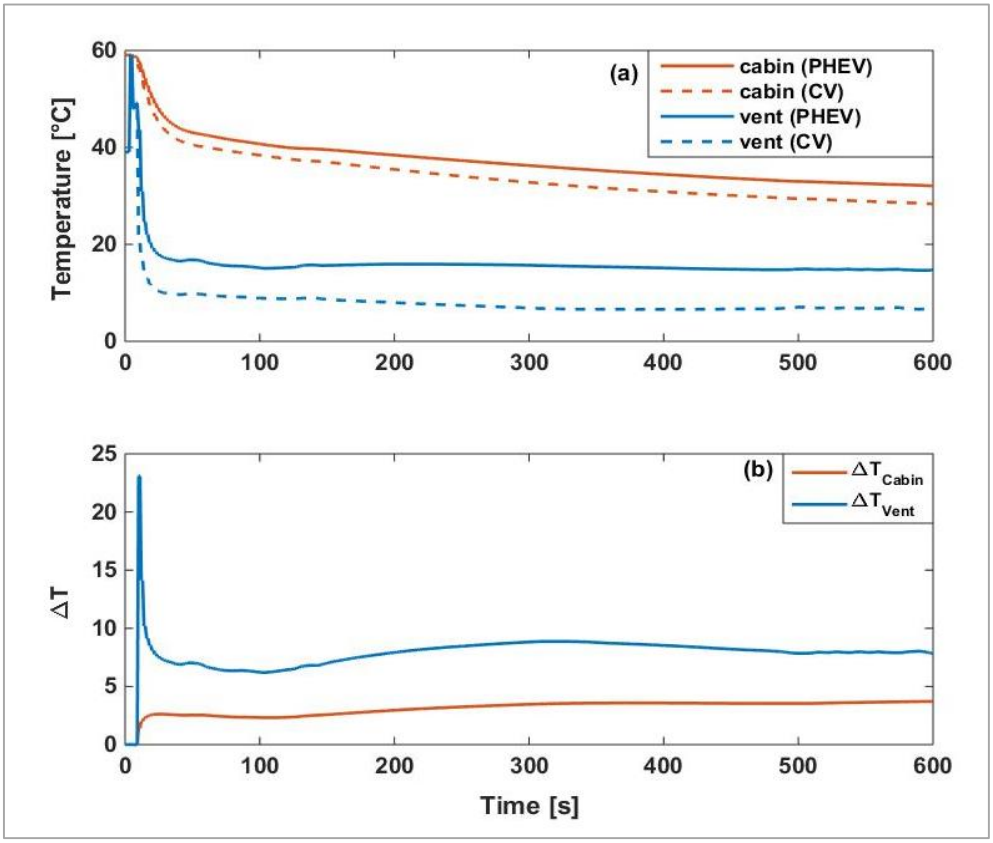

Figure 7-6. Effect of key-on cooling load of the battery on the thermal conditions of the cabin after hot soak (Trip 2) (a) absolute cabin and vent temperatures, (b) temperature error.

To quantify the impact of the key-on cooling on thermal comfort, the discomfort index of the PHEV was defined in this work as the increase in the cabin temperature due to the existence of the battery in the vehicle, and is calculated as:

$$I_{discomf} = \sum \left(\frac{T_{cabin}^{PHEV} - T_{cabin}^{CV}}{T_{cabin}^{CV}} \right). \quad (7\text{-}1)$$

In the above equation, T_{cabin}^{PHEV} and T_{cabin}^{CONV} are the time histories of cabin temperature in the PHEV and the equivalent CV, respectively. $I_{discomf}$ is primarily applicable to Trip 2 in summer seasons as the cooling demand of the cabin is otherwise low and the impact of the battery on cabin temperature is negligible. $I_{discomf}$ is a positive integer, with an ideal value of zero which will indicate that the PHEV cabin is cooled at a rate similar to, or faster than, the conventional vehicle cabin.

It is evident from the above observation that an opportunity exists for minimising the discomfort index through reducing the key-on cooling load of the battery, for example, by precooling the battery for Trip 2. Pre-cooling reduces, or ideally eliminates the requirement for key-on cooling and shift the cooling load of the battery to after the trip. It is noteworthy that the potential for improving the thermal comfort through precooling the battery is limited to the level of thermal comfort in the still thermally uncomfortable cabin of the conventional vehicle.

Table 7-6 compares the discomfort index of the PHEV operating in Phoenix and Seattle summer.

Table 7-6. Thermal discomfort index across diffferent climate conditions

Location	$I_{discomf}$	
	Summer	**Winter**
Phoenix	57	22
Seattle	16	n/a

7.2.2 Simulation results: alternative duty cycles

In this section, the operation of the vehicle over alternative duty cycles is discussed. Figure 7-7 shows the key features of the vehicle operation in Phoenix summer and the duty cycles comprising of WLTC, US06, Artemis, and NEDCx2 trips. Among these, the duty cycle with US06 trips was previously explained in Section 7.2.1 but is included in Figure 7-7 in the interest of completeness. For each duty cycle, the daily profile of the battery temperature and SoC are plotted on the left hand side of Figure 7-7, while the engine torque profile in Trip 1 and Trip 2 are plotted on the right hand side of Figure 7-7. The following observations can be made from these results:

1. The daily profile of battery temperature shows a small sensitivity to the drive cycle, especially, the drive cycle has a negligible effect on the maximum temperature of the battery in Day Park.

2. When the trips are on the WLTC or the Artemis, (Figure 7-7(a) and Figure 7-7(b)), the vehicle enters the CS mode during Trip 2, as can be inferred from the SoC and engine torque profiles. Therefore, the battery has no excess charge when the vehicle operates in Phoenix summer and its trips are on the WLTC or the Artemis.

3. The operation of the vehicle over the duty cycle with US06 trips was previously explained in Section 7.2.1 and is plotted in Figure 7-7(c) for completeness. By the end of Trip 2, the battery is only discharged to 54%, due to the short length of the drive cycle and reduced electric traction due to battery overheating. Considering that the CS operating mode can commence below 13% SoC, the battery has over 41% excess charge over this duty cycle.

4. Figure 7-7(d) shows that when the trips are on the NEDCx2, the vehicle operates in EV mode in both trips. The battery is depleted to approximately 23% by the end of Trip 2. This suggests an excess charge of over 10%.

5. Comparing the engine torque profiles across all drive cycles shows that battery overheating in Day Park only impacts the operating mode of the vehicle over the US06. This is because the urban parts of other drive cycles are less aggressive than that of US06, so even an inhibited battery power is sufficient to start the trip in EV mode. The battery is sufficiently cooled before the vehicle reaches higher power demanding sections of the drive cycle.

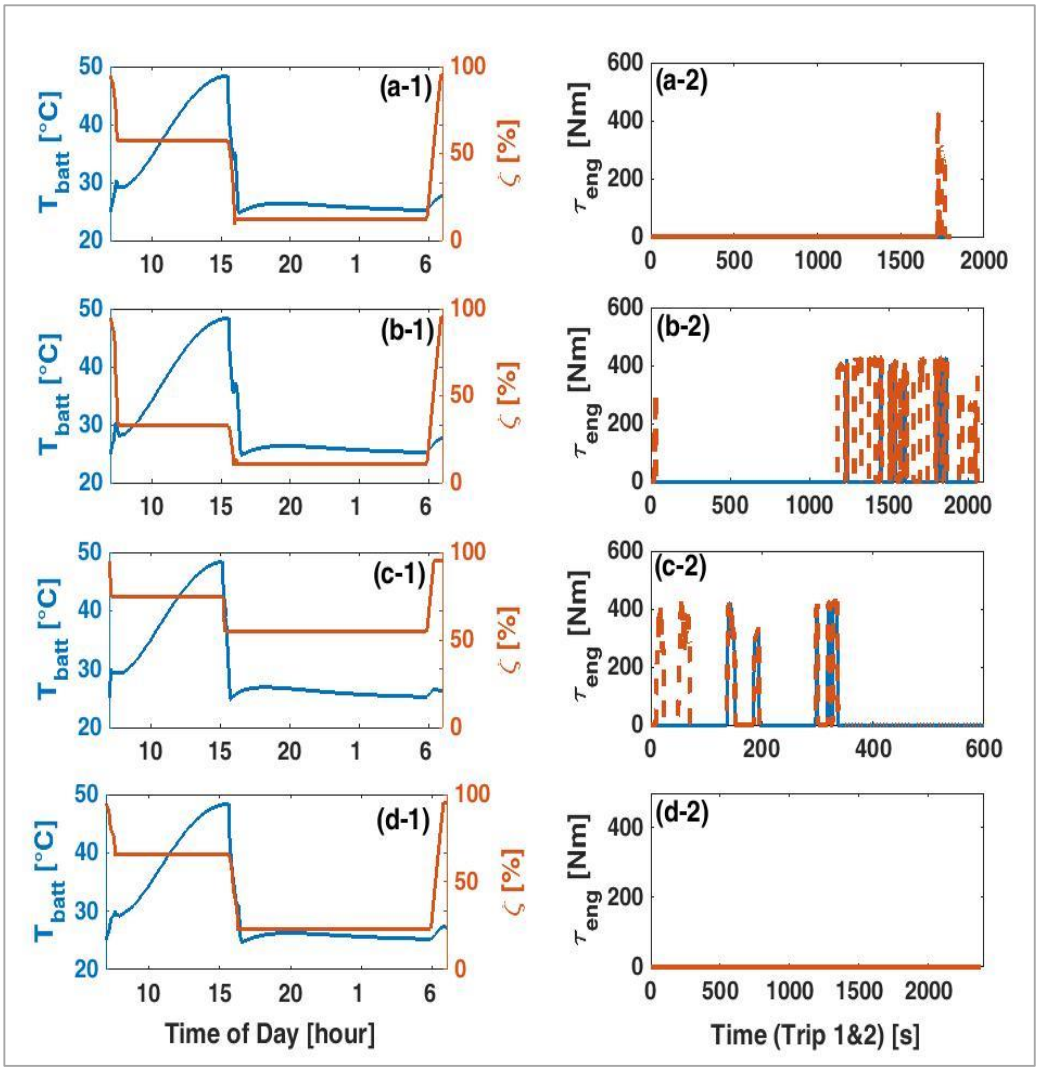

Figure 7-7. Duty cycle simulation result for the vehicle operating in Phoenix summer with different drive cycles: (a) WLTC, (b) Artemis, (c) US06, (d) NEDCx2. Left hand side: the daily profile of battery temperature (in blue) and SoC (in red). Right hand side: comparison between engine torque in Trip 1 (in blue) and Trip 2 (in red)

Table 7-7 summarises key features of the vehicle operation for other climate conditions and drive cycles. Some key observations are:

1. During Day Park, the peak temperature of the battery reaches approximately 48°C in Phoenix summer and 30°C in Seattle summer, while the average battery temperature is 40 ± 0.5 °C in Phoenix summer and 27± 0.6 °C in Seattle summer, irrespective of the drive cycle. This is mainly due to the fact that the heat gained from the ambient environment during Day Park is significantly higher than the total heat generated in the preceding trip.

2. During Day Park in Phoenix winter, the peak temperature of the battery reaches approximately 32°C, irrespective of the drive cycle. However, the average battery temperature is somewhat affected by the drive cycle and ranges from 24.8°C in case of the NEDCx2 to 26.7°C in case of the Artemis.

3. During Day Park in Seattle winter, the battery rejects heat to the cold ambient environment. Therefore, the peak battery temperature in Day Park depends on the final temperature of the preceding trip (which depends on the drive cycle). The average battery temperature is approximately 13±0.7°C.

4. Across all drive cycles and locations, the energy allocated to the duty cycle (in the form of fuel and battery charge) is higher in summer, compared to winter, as a result of the AC and the battery cooling loads

5. In Phoenix, fuel consumption in Trip 2 is higher in summer than in winter, except for the duty cycle with NEDCx2 trips. This difference is highest when the trips are on the Artemis given the higher energy demand of the duty cycle.

6. Comparing the operating mode of the vehicle across different drive cycles and climate conditions shows that with NEDCx2 trips, the operating mode is not affected by the climate conditions (the vehicle achieves both trips in EV mode). With WLTC trips, the vehicle enters CS operating mode in Trip 2 in Phoenix summer, but it can achieve both trips in CD mode under all other climate conditions. With Artemis trips, the vehicle enters CS mode in Trip 2 irrespective of the climate conditions. With US06, the effect of climate condition on the operating mode is only seen in Phoenix summer.

7. In Phoenix, since AC is required in Trip 2 in winter as well as in summer, the cooling load of the battery affects the cabin in both seasons, leading to thermal discomfort. In Seattle, AC and battery cooling are only applied in summer, so the discomfort index is not defined for Seattle winter.

8. In Seattle, the difference between the converted energy (fuel and battery charge) in Trip 2 in summer compared to winter represents the battery cooling and AC loads. When the trip is on the WLTC, US06 and NEDCx2, these loads amount to 3.5%, 2%, and 4.9% of the battery charge, respectively. When the trip is on the Artemis, the loads lead to 2.2% mode discharge of the battery, and approximately 0.1 L more fuel consumption.

9. Comparing the discomfort indices between different locations shows that the negative impact of key-on battery cooling on thermal comfort is more pronounced in Phoenix. This impact is even more pronounced in Phoenix winter than in Seattle summer, given that the battery reaches higher temperatures during Day Park in Phoenix summer than in Seattle winter.

10. The effect of battery temperature on its internal resistance is evident from comparing the SoC reductions in Trip 1 in Seattle between winter and summer. The battery is discharged more in winter due to the higher resistance of cells at low temperature. Note however that the absolute effect of resistance is partly overshadowed by the higher AC load in summer trips.

11. In Night Park, application of plugged-in cooling and the assumption of similar garage temperatures leads to limited variation in the average battery temperature between similar seasons in different locations. Nevertheless, the maximum battery temperatures in Night Park is affected by preceding trips.

12. Each simulation ends with charging the battery to approximately 95% SoC. Thus, the variation of SoC in Night Park is approximately equal to sum of the charge depleted in the two trips.

Table 7-7. Summary of simulation results over different drive cycles and across various climates

Scenario			Trip1				Day Park			Trip2					Night Park		
			ΔSoC [%]	Fuel [L]	$T_{batt,max}$ [°C]	$\overline{T_{batt}}$ [°C]	ΔSoC [%]	$T_{batt,max}$ [°C]	$\overline{T_{batt}}$ [°C]	ΔSoC [%]	Fuel [L]	$T_{batt,max}$ [°C]	$\overline{T_{batt}}$ [°C]	$I_{discomf}$ –	ΔSoC [%]	$T_{batt,max}$ [°C]	$\overline{T_{batt}}$ [°C]
Phoenix	WLTC	Summer	-37.24	0.00	30.29	27.6	0.00	48.35	39.42	-45.18	0.14	48.35	37.73	214	82.95	34.88	25.94
		Winter	-35.49	0.00	21.33	16.2	0.00	32.02	25.66	-42.10	0.00	31.85	26.64	30	77.86	29.19	17.53
	US06	Summer	-20.69	0.23	30.01	28.0	0.00	48.42	39.00	-19.63	0.37	48.42	42.65	57	40.61	40.73	26.18
		Winter	-20.29	0.23	21.02	18.47	0.00	32.00	24.92	-23.67	0.23	31.99	29.55	22	44.22	28.56	17.44
	Artemis	Summer	-62.57	0.45	30.33	27.90	0.00	48.32	39.28	-21.62	2.45	48.32	37.95	243	84.45	36.10	25.93
		Winter	-58.52	0.45	25.87	18.66	0.00	32.11	26.72	-25.35	2.13	31.86	27.04	36	84.14	25.56	17.11
	NEDCx2	Summer	-29.18	0.00	30.02	27.75	0.00	48.31	39.66	-42.78	0.00	48.31	33.79	579	72.22	30.85	25.81
		Winter	-26.71	0.00	17.60	15.57	0.00	31.57	24.84	-33.37	0.00	31.42	25.68	188	60.35	25.78	17.28
Seattle	WLTC	Summer	-35.04	0.00	25.00	22.34	0.00	30.56	26.47	-42.24	0.00	30.49	26.37	21	77.55	28.56	25.65
		Winter	-36.18	0.00	16.84	12.93	0.00	16.40	12.73	-38.71	0.00	19.12	13.76	n/a	75.16	18.87	15.55
	US06	Summer	-19.56	0.23	26.20	25.67	0.00	30.61	26.55	-23.66	0.23	30.61	29.47	16	43.49	28.51	25.71
		Winter	-20.47	0.23	18.47	17.00	0.00	18.43	12.99	-21.60	0.23	19.72	17.12	n/a	42.32	19.70	15.61
	Artemis	Summer	-57.63	0.45	28.24	24.21	0.00	30.62	27.33	-26.01	2.08	30.51	26.99	27	83.90	27.80	25.27
		Winter	-59.86	0.45	21.85	15.66	0.00	20.91	13.76	-23.76	1.99	24.06	16.77	n/a	83.91	22.95	16.04
	NEDCx2	Summer	-26.53	0.00	25.00	21.76	0.00	30.25	25.78	-33.55	0.00	30.19	25.49	151	60.34	27.00	25.24
		Winter	-27.06	0.00	15.00	12.04	0.00	13.42	11.80	-28.68	0.00	13.77	12.61	n/a	56.01	17.83	15.00

* $I_{discomf}$ not applicable to this duty cycle

Table 7-8 compares the lifetime of the battery for different locations and trip drive cycles. For all drive cycles, variations in the battery lifetime with climate conditions is observed. The battery lifetime is also shorter when the excess charge is more (i.e. when the drive cycles are on US06 and the NEDCx2), as the battery is stored at higher SoC, accelerating the capacity loss. The noticeably lower battery lifetime achieved with US06 trips, compared to other drive cycles in both location is due to a similar effect.

Table 7-8. Battery lifetime for different PHEV duty cycles

Location	Drive Cycle			
	WLTC	**US06**	**Artemis**	**NEDCx2**
Phoenix	7.3 years	6.3 years	7.5 years	7.2 years
Seattle	7.7 years	7.3 years	7.9 years	8.6 years

It is worth highlighting the variations in energy flows during the two trips of the day for different duty cycles. Figure 7-8 compares the ratio of energy flows between the two daily trips for the vehicle operating in Phoenix summer on different drive cycles. An increase in the converted energy, representing the total chemical energy conversion (sum of fuel energy and the energy discharged from the battery), is noticeable for all drive cycles after the vehicle undergoes the hot soak in Day Park. The higher increase in energy conversion on Artemis is due to operation in CS mode. The driveline energy, representing the net mechanical energy required at the gearbox input to meet the drive cycles, remains constant between the two trips, as expected. On the other hand, the energy allocated to run the compressor increases significantly in the second trip to deliver the required cooling power to the evaporator and the chiller. The cooling energy of the evaporator is approximately three times more in Trip 2, compared to Trip 1, irrespective of the drive cycle. Similarly, the cooling energy delivered to the chiller increases in Trip 2 compared to Trip 1, with the highest increase occurring over the NEDCx2 given that battery cooling is only briefly applied in Trip 1 when this drive cycle is assumed.

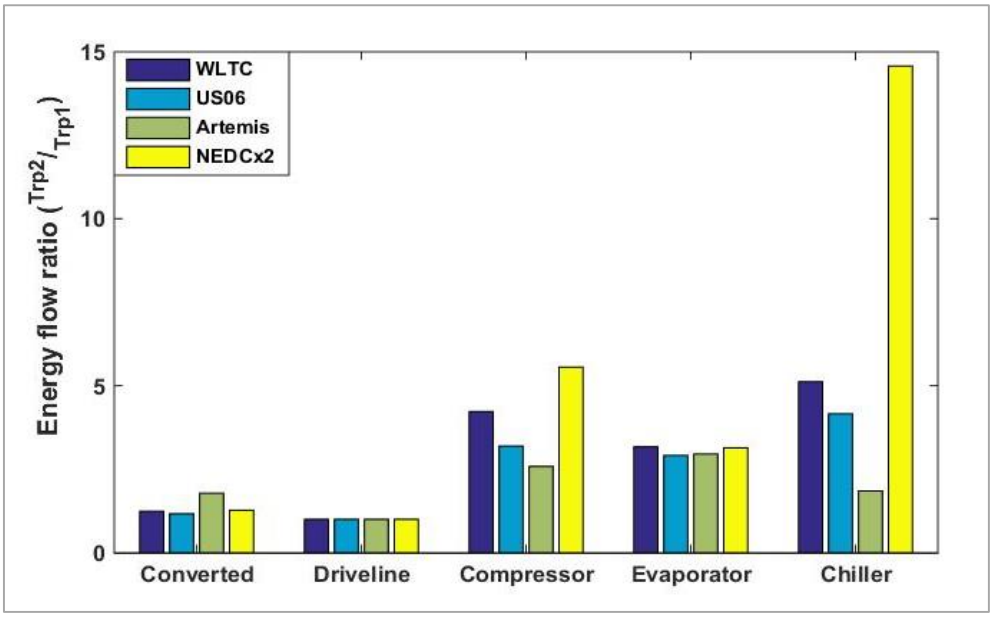

Figure 7-8. Breakdown of the ratio of energy flows (trip 2 to trip 1) for the vehicle operating in Phoenix summer.

7.2.3 Discussion

The above analyses indicate that the hot soak temperature of the battery in Phoenix summer can negatively affect the fuel economy, battery lifetime, and thermal comfort attributes in PHEVs. Similar trends can be expected in other xEVs types, including in BEVs, although rather than fuel economy, it is the range and traction capability of BEVs that will be affected by battery overheating. The above analyses also suggest that cooling the battery during hot soak can improve the affected performance attributes. Since the vehicle is not plugged in during Day Park in the duty cycles assumed here, key-off cooling is the only available option. Therefore, application of key-off cooling is investigated in Section 7.3.

When the battery has excess charge over a duty cycle, partial charging can be applied to reduce the battery SoC in Day Park and Night Park without affecting the operation of the vehicle. As discussed in Chapter 3, this method can improve the battery lifetime. Therefore, in addition to key-off cooling, the potential of partial charging for improving the battery lifetime over the assumed duty cycles is investigated in Section 7.3.

7.2.4 Summary

The operation of the PHEV was simulated over a set of 24-hour duty cycles and the impact of climate conditions on three performance attributes of the vehicle, namely its fuel economy, battery lifetime and passenger thermal comfort, were studied.

The effect of climate conditions on the temperature of the battery the cabin and consequently on their cooling requirements was discussed. It was shown that when the vehicle operates in hot climate conditions, such as in Phoenix summer, its battery temperature can regularly reach 48°C, as a result of the heat gain from the ambient. This can reduce electric traction capability since the power of the battery is limited at such high temperatures due to practical considerations. The simulation results showed that following Day Park in Phoenix summer, the vehicle was forced to operate in CS mode on the US06 drive cycle, due to the high battery temperature. This lower electric traction capability lead to poorer the fuel economy. On other drive cycles, i.e. the WLTC, Artemis, and the NEDCx2 overheating of the battery in Day Park did not affect the operating mode of the vehicle, as these drive cycles have milder urban section compared to the US06.

Comparing the simulation results for different climate conditions showed a noticeable variability in battery lifetime with climate conditions. Depending on the assumed drive cycle for the trips, the battery lifetime in Phoenix was between 0.4 years to 1.4 years shorter than in Seattle.

The simulation results showed that key-on battery cooling can have a negative impact on the thermal comfort of the passengers. Due to the cooling load of the battery, the average cabin and vent temperatures in the PHEV were higher than those in an equivalent conventional vehicle, by approximately 3 and 8 degrees, respectively. To further quantify this impact, the discomfort index was introduced as the normalised accumulative difference between the cabin temperatures of the PHEV and the equivalent conventional vehicle. It was shown that both in Phoenix and in Seattle, the cooling load of the battery impacted the thermal comfort in Trip 2 during summer. Irrespective of the drive cycle, the discomfort index was very

high in Phoenix summer, suggesting a significant impact of the battery cooling loads on thermal comfort. This impact is even more significant in Phoenix winter compared to Seattle summer.

7.3 Strategies for improving PHEV performance attributes in hot geographical locations

In this section, the benefit of key-off cooling and partial charging for the PHEV operating in Phoenix summer is analysed. The duty cycle comprising of US06 trips is considered for the purpose of the forthcoming analyses.

7.3.1 Key-off cooling

Since key-off cooling consumes the energy of the battery, choosing the duration of cooling and temperature set points can be critical. Here, different strategies for applying key-off cooling will be examined to quantify the limits of achievable improvements in the performance attributes.

For simplicity, it is assumed here that key-off battery cooling is conducted at maximum cooling power. Therefore, key-off cooling can be controlled by a flag command. Given the design of the battery cooling system defined in Chapter 5, a cooling flag of 1 will be interpreted by the low level controller as

a) the compressor works at maximum speed;
b) the condenser fan works and maximum speed;
c) the shut-off valve of TXV 2 is open;
d) the cooling pump is switched on.

A cooling flag of 0 indicates a passive system (i.e. no cooling).

Based on duration, key-off cooling can be categorised as follows:

1. after-run cooling
2. extended key-off cooling
3. pre-cooling (pre-run cooling)

7.3.1.1 After-run cooling

In after-run cooling, the battery is only cooled for a short period of time following a trip. In Figure 7-9(a), the profile of battery temperature in Day Park is shown for various degrees of after-run cooling. The strategy hardly affects the maximum battery temperature in the assumed ambient condition, but the average temperature can be noticeably reduced. Figure 7-9(b) shows the total seasonal (storage and cycling) capacity loss in Day Park for different degrees of after-run cooling. The storage capacity loss decreases as the intensity of cooling is increased (i.e. the degree of after-run cooling is reduced) but the increasingly higher cycling capacity loss reduces the benefit of cooling. In Figure 7-9(c), the daily energy requirement of after-run cooling is normalised on the percentage of reduction in capacity loss, indicating that the energy requirement increases for higher intensity cooling.

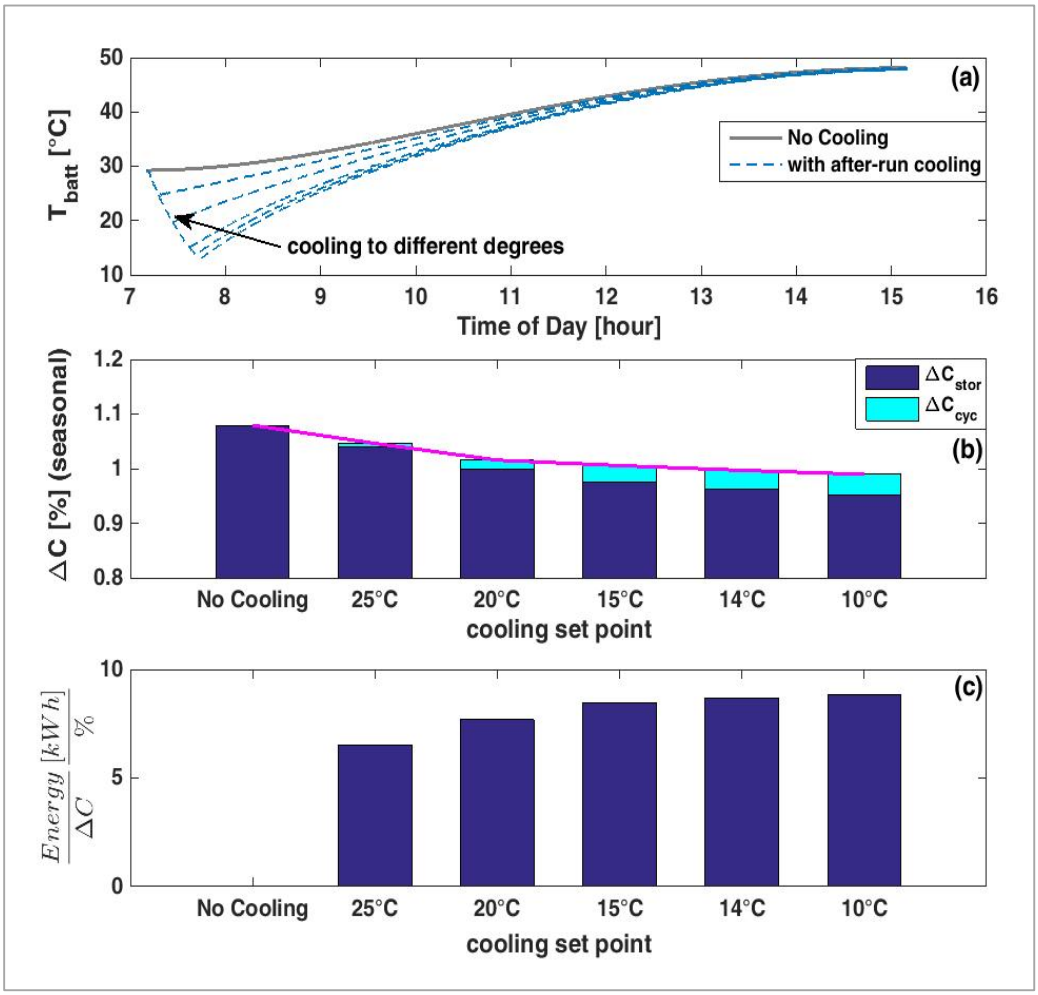

Figure 7-9. After-run key-off cooling (a) temperature profile (b) seasonal capacity loss (c) daily energy requirement for 1% reduction of capacity loss

The above observations indicate that limited benefits can be expected from after-run cooling, while the energy requirements suggest that cooling below 20 °C cannot be justified.

7.3.1.2 Extended key-off cooling

Key-off cooling can be potentially applied for an extended period of time to reduce the average and maximum temperature of the battery. Since the heat gain from the ambient peaks at approximately 12 pm, one option is to start key-off cooling after this peak when cooling seems most critical. To investigate this, different temperature set point (bands) were tested with a 5-degree hysteresis, as shown in Figure 7-10(a). Figure 7-10(b) shows that the capacity loss reduces as a result of cooling. While more intense cooling reduces the storage capacity fade, the resulting cycling capacity loss limits the realised benefit of cooling. As Figure 7-10(b) shows, maintaining the battery within the temperature band of 25°-30° reduces the seasonal capacity loss by 0.25% (from 1.08% to 0.82%). Lower temperature bands require significantly higher energies, as Figure 7-10(c) suggests, without leading to a noticeable reduction in the capacity loss.

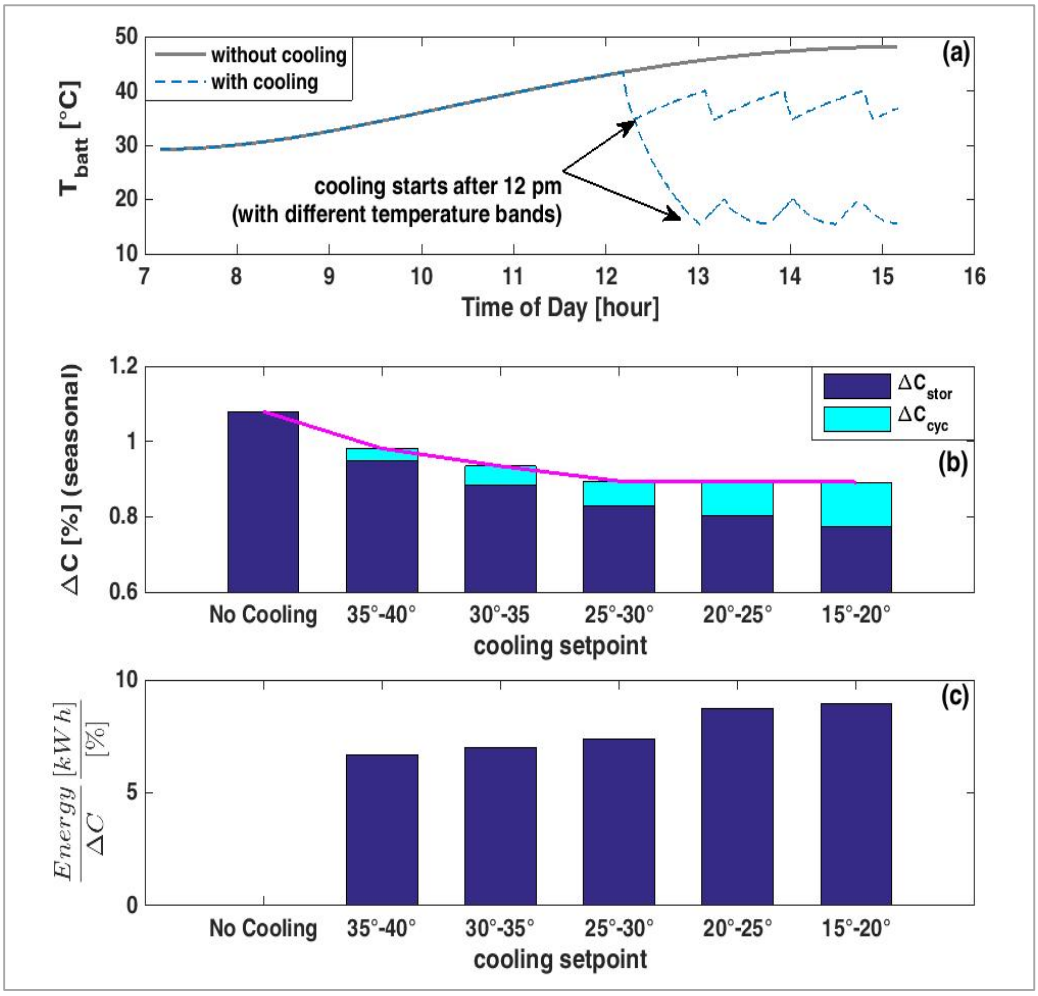

Figure 7-10. Key-off cooling after 12 pm (a) temperature profile (b) summer capacity loss, (c) daily energy requirement of key-off cooling for 1% reduction in seasonal capacity loss

As an alternative strategy, key-off cooling can be enabled for the duration of Day Park, aiming at maintaining the battery below certain temperature limits. This strategy was also investigated with different temperature bands and the results are shown in Figure 7-11. Maintaining the battery within lower temperature bands requires the cooling system to operate more, as Figure 7-11(a) shows. This may be infeasible in practice but was considered acceptable here as the aim was to determine the maximum benefit of (key-off) cooling. Figure 7-11(b) suggests that by maintaining a low battery temperature, a significant reduction in the total capacity loss can be achieved. Keeping the temperature below 25°C results in a significant cycling capacity loss, as the cooling system should frequently operate, while requiring a disproportionately higher energy, as Figure 7-11(c) suggests. It is also worth noting that the efficiency of cooling reduces as the ambient heat load increases. This can be inferred from Figure 7-11(a) which shows that the

temperature band of 5°C-20°C can be maintained before 12 pm, but not afterwards (the cooling system remains continuously on as the lower limit is not met).

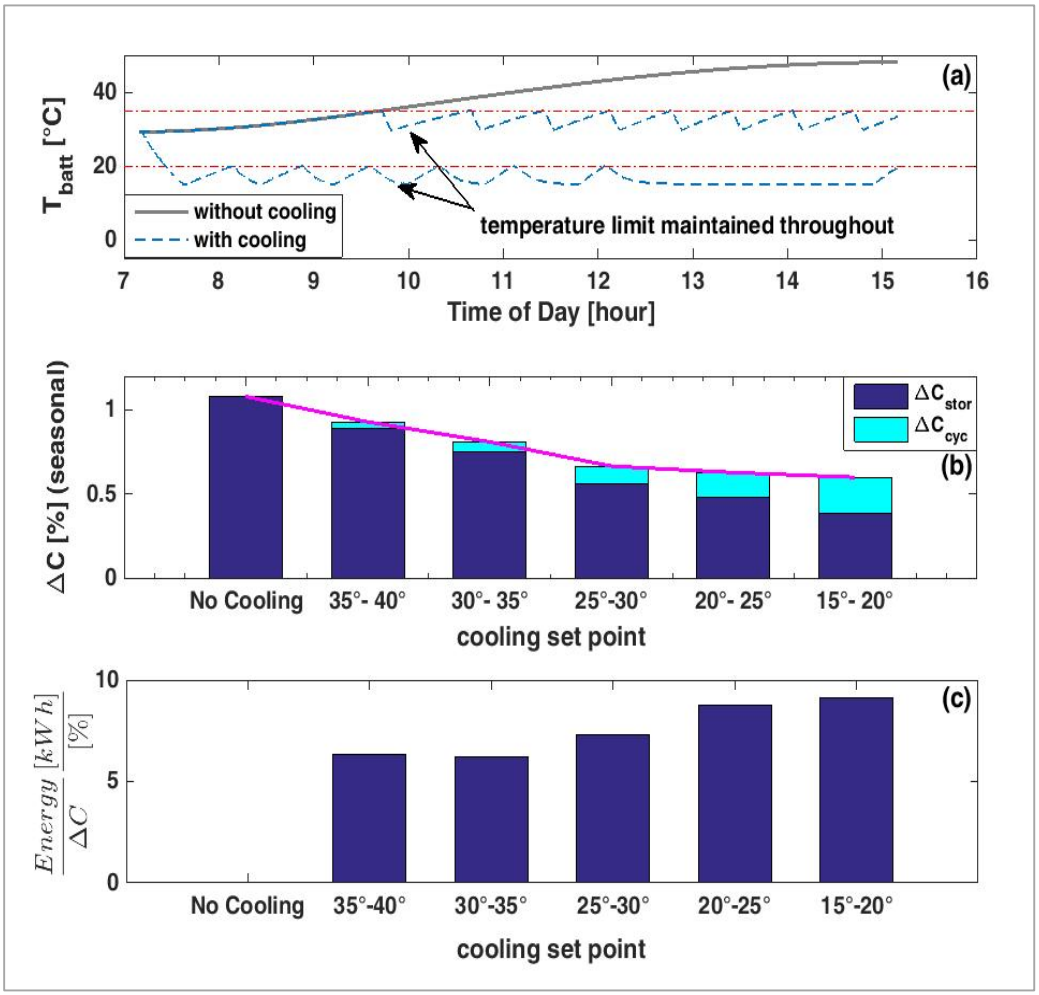

Figure 7-11. Key-off cooling of battery enabled for the duration of Day Park (a) temperature profile (b) summer capacity loss (c) daily energy requirement of key-off cooling to achieve 1% reduction in capacity loss per season

7.3.1.3 Pre-Cooling

Key-off cooling can be briefly applied to precool the battery for the following trip. As discussed in Chapter 4, precooling can help avoid the negative effect of key-on cooling on thermal comfort, while also eliminating battery overheating and its negative effect on the vehicle's electric traction capability. To investigate precooling, Trip 2 of the duty cycle was simulated with the cabin initially at 60°C but with three different initial battery temperatures of 46°C, 25°C and 15°C. Figure 7-12 shows the profiles of cabin temperature, vent temperature and battery temperature. It can be seen that precooling the battery shifts its key-on cooling

load, which allows more cooling power to be allocated to AC, thus leading to lower cabin and vent temperatures. When the battery is pre-cooled to 25°C, key-on cooling is only activated after 230 seconds into the trip. When key-on cooling initiates, the vent and cabin temperatures rise due to lower available cooling power. Pre-cooling to 15°C completely eliminates the key-on cooling load.

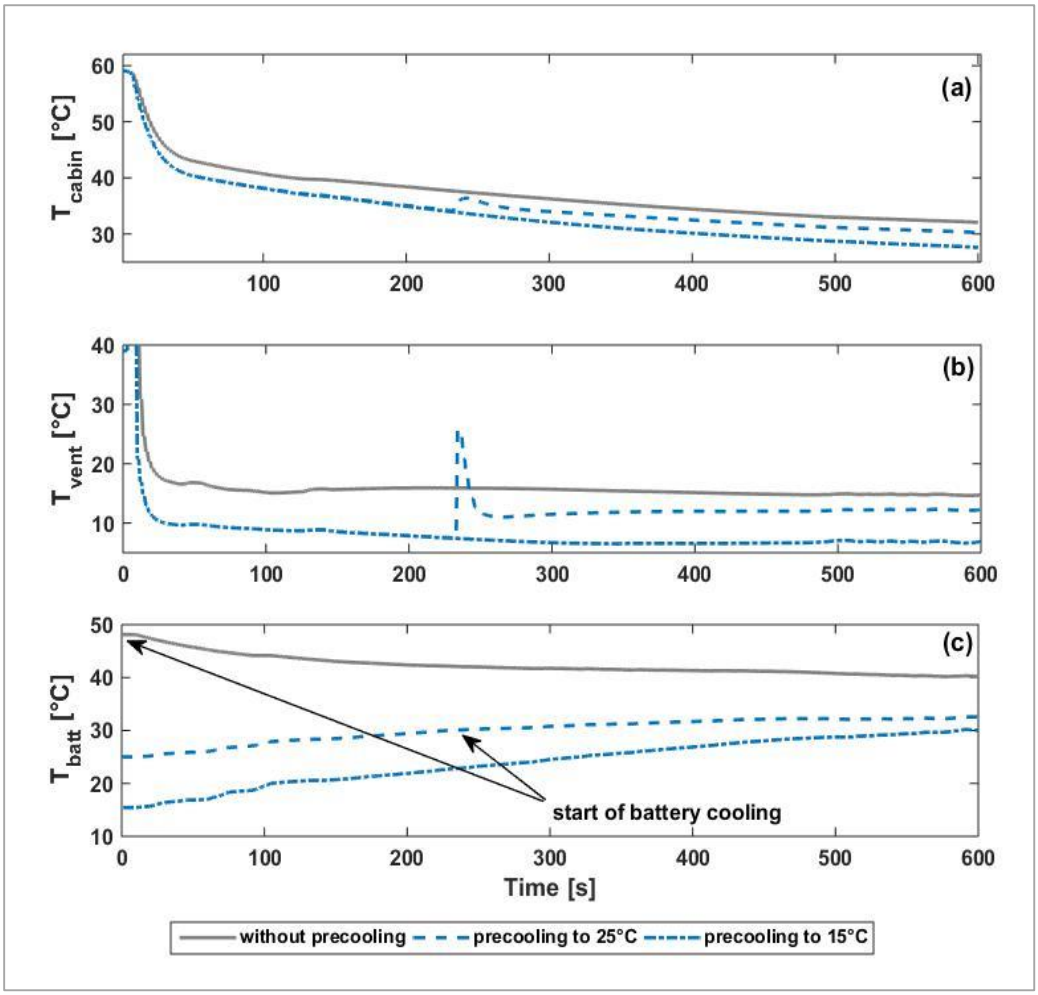

Figure 7-12. Effect of pre-cooling the battery on thermal comfort. Figure shows temperature of (a) cabin (b) vent air and (c) battery

Figure 7-13 compares the profile of engine torque in Trip 2 of the duty cycle with and without a pre-cooled battery. Precooling has eliminated the need for operating hybrid mode over the first 100 seconds of the drive cycle.

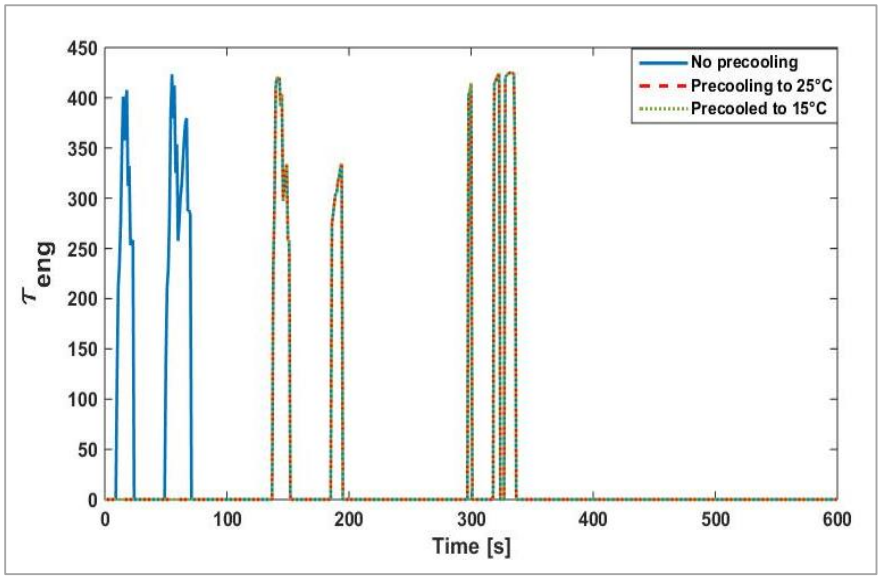

Figure 7-13. Effect of pre-cooling the battery in Day Park on torque of engine in Trip 2

It is worth noting that eliminating the unwanted hybrid operation does not require an intense precooling; Figure 7-13 shows that the engine torque profile is identical for precooling to 25°C and 15°C. In fact, for the conditions considered here, precooling the battery below 44°C[19] was sufficient to achieve similar result, although intense precooling benefits the thermal comfort.

Figure 7-14 compares the effect of various pre-cooling degrees on the discomfort index and fuel consumption in Trip 2, as well as the energy required from the battery for every 1°C precooling. Precooling to 15°C is sufficient to achieve a discomfort index of zero. The energy efficiency of pre-cooling decreases significantly with lower temperature set points.

[19] This was determined based on trial of different set points

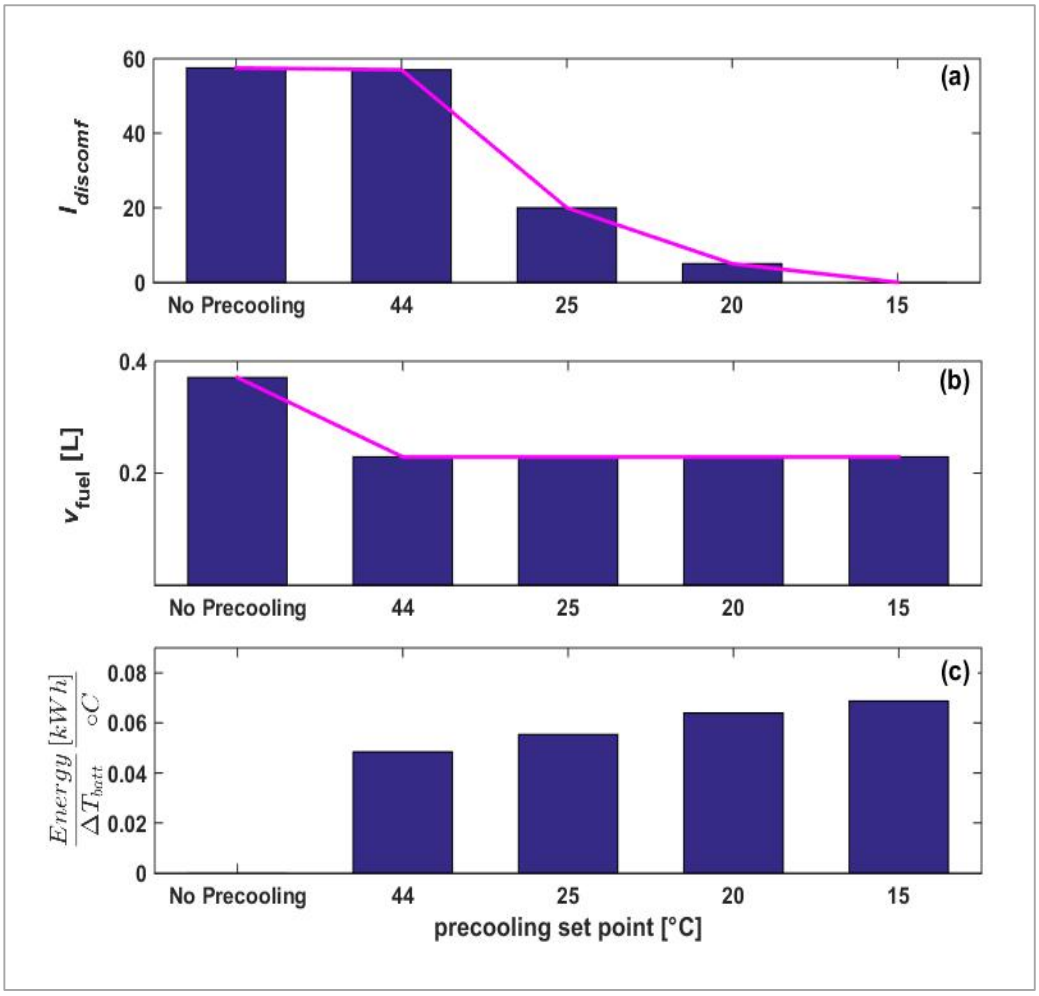

Figure 7-14. Effect of pre-cooling the battery on (a) discomfort index, (b) fuel consumption over Trip 2 of the duty cycle (c) energy requirement per degree of pre-cooling for various pre-cooling set points

It is worth emphasising the importance of the assumed drive cycle for controlling precooling. The battery charge that can be allocated to precooling without increasing the fuel consumption depends on the amount of excess charge which depends on the drive cycle (for given climate conditions). In addition, the effectiveness of precooling varies with the aggressiveness of the drive cycle, as the drive cycle affects the internal heat generation of the battery. The higher the heat generation, the lower the degree of precooling that is necessary, both for eliminating key-on cooling, and for preventing the battery from overheating during the trip. None of the drive cycles chosen here demonstrate the latter.

Other than the effect of various key-off cooling strategies on the performance attributes of the vehicle in Day Park and Trip 2, the energy allocated to key-off

cooling affects the battery in Night Park. This is because the capacity loss of the battery is a function of SoC, and energy throughput, as well as the temperature. Discharging the battery in Day Park to support key-off cooling will likely result in the battery being stored at a lower SoC in Day Park, but increases the throughput energy required to re-charge the battery. Therefore, in assessing the benefit of key-off cooling for battery lifetime, the complete duty cycle of the vehicle should be considered.

7.3.2 Partial charging

When the battery has some excess charge over the assumed duty cycle, as is the case for the duty cycle in Phoenix summer and US06 trips, partial charging can be considered. The excess charge can increase the storage capacity loss in Day Park and Night Park, so partial charging can be beneficial to the battery lifetime. To investigate this, the duty cycle was simulated with the battery initially charged to 55% SoC, rather than full charging (95% SoC) and the phase-by-phase capacity losses were compared. The result is shown in Figure 7-10. It can be seen that partial charging has enabled significant reductions in the (storage) capacity loss, both in Day Park and Night Park. At the same time, partial charging has led to a small increase in the (cycling) capacity loss in Trip 1 and Trip 2. This is because with a lower SoC (lower voltage), the battery current will be higher for an identical power, and this increases cycling ageing. It is worth noting that lower SoC can potentially reduce the storage component of capacity loss in the trips, but this effect is negligible within the context of this research given the short lengths of the trips compared to Day Park and Night Park.

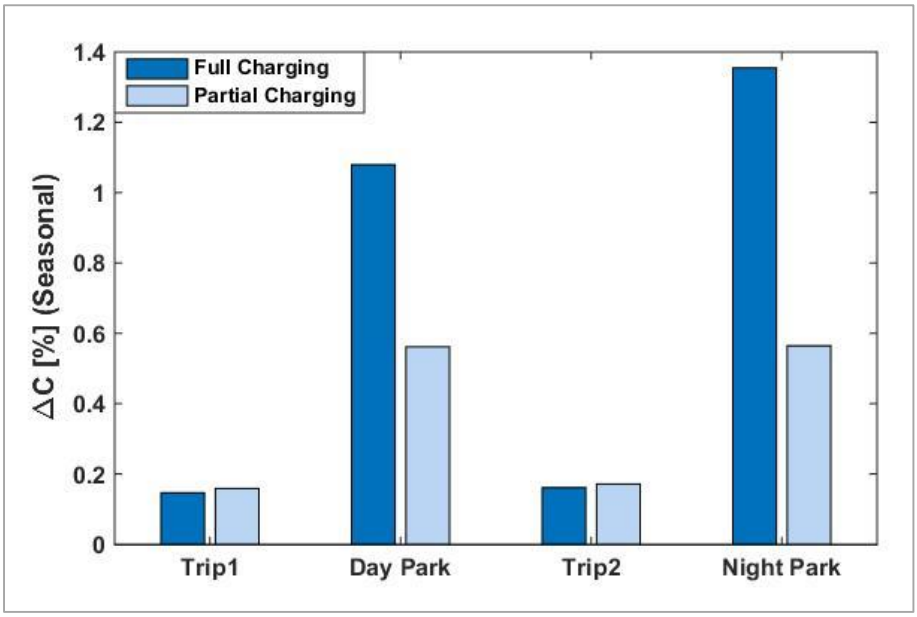

Figure 7-15 . Effect of partial charging of the battery on its capacity loss in Phoenix summer climate with US06 drive cycle

The above analysis shows that even the vehicle is only plugged-in once per day (as is assumed here), partial charging can improve battery lifetime. The effectiveness partial charging will vary from one duty cycle to another given its reliance on excess battery charge. Since partial charging can eliminate the ability to perform key-off cooling without needing extra fuel consumption, its importance relative to key-off cooling should be considered to maximise the benefits for the vehicle.

7.3.3 Summary

The applicability of key-off cooling for reducing the impact of hot climate conditions on battery lifetime was discussed. Different approaches for applying key-off cooling were attempted and compared based on their effectiveness in reducing the battery capacity loss during Day Park and the associated energy requirement. The results showed that maintaining a low battery temperature in Day Park through key-off cooling can reduce the storage capacity loss, although selecting very low temperature set points can be inefficient and lead to disproportionately high cycling capacity loss.

It was further shown that partial charging can potentially improve the battery lifetime, even when the vehicle is only plugged in once per day. Partial charging relies on the amount of available excess charge, so its benefits for the battery and its importance relative to key-off cooling can vary from one duty cycle to another.

CHAPTER 8 DEFINING KEY-OFF COOLING AS AN OPTIMAL CONTROL PROBLEM

Introduction

In this chapter, key-off cooling is defined as an optimal control problem. In Section 8.1 a mathematical definition is developed for the optimal control problem and the assumptions considered for solving the problem with DP are discussed. In Section 8.2 the problem is solved for the vehicle operating in the climate conditions of Phoenix summer based on a set of carefully selected initial and final conditions, and the factors affecting the solution are analysed. The discussions are summarised in Section 8.3.

8.1 Optimal control of key-off cooling for reducing Day Park capacity loss

Recall that the following notation was employed in Section 6.4 for the capacity loss of the battery:

$$\Delta C = \Delta C_{stor} + \Delta C_{cyc} = \Delta C(x_b, n). \tag{8-1}$$

In Day Park, the battery is not cycled, unless key-off cooling is applied. Given the interpretation of the key-off cooling flag discussed in Section 7.3, the number of charge-discharge cycles in Day Park is related to the key-off cooling flag (u). Therefore, n, in equation (8-1), is

$$\begin{cases} n = 0 & if\ u = 0 \\ n > 0 & if\ u = 1 \end{cases}, \tag{8-2}$$

and equation (8-1) can be re-written for capacity loss in Day Park ($[\Delta C]_{DPrk}$) as

$$[\Delta C]_{DPrk} = \left[\Delta C_{stor} + \Delta C_{cyc}\right]_{DPrk} = \Delta C(x_b, u). \tag{8-3}$$

Dividing the duration of Day Park into N intervals of Δt seconds, the optimal control of key-off cooling can be determined by minimising a cost function of the following form

$$J = h_N + \sum_{k=0}^{N-1} \Delta C_k\,(x_{bk}, u_k). \tag{8-4}$$

In the above equation, the first term on the right hand side in referred to as the terminal cost, while the second term is the arc cost. Also, x_{bk} and u_k denote the battery state and the key-off cooling flag at the interval $[t_{trp1} + k\Delta t\ , t_{trp1}+(k+1)\Delta t)$, while the k^{th} term of J, (J_k) denotes the corresponding capacity loss. The solution of the optimal control problem is equivalent to finding the trajectory of key-off cooling flag that minimises the cost function, that is

$$\min_{u^*} J = \min\left(h_N + \sum_{k=0}^{N-1} \Delta C_k\,(x_{bk}, u_k)\right). \tag{8-5}$$

In equation (8-5), $u^*$is a piecewise constant function that changes only at instances $k\Delta t$. Solving the above problem with DP includes evaluating the arc cost term on a grid of the system states. For controlling key-off cooling in Day Park, the state vector of the vehicle includes the temperature and the SoC of the battery as well as the cabin temperature:

$$x_v = \begin{bmatrix} T_{cabin} \\ T_{batt} \\ \zeta \end{bmatrix}, \tag{8-6}$$

Therefore, a three-dimensional state grid was formed by discretizing x_v as shown in Figure 8-1.

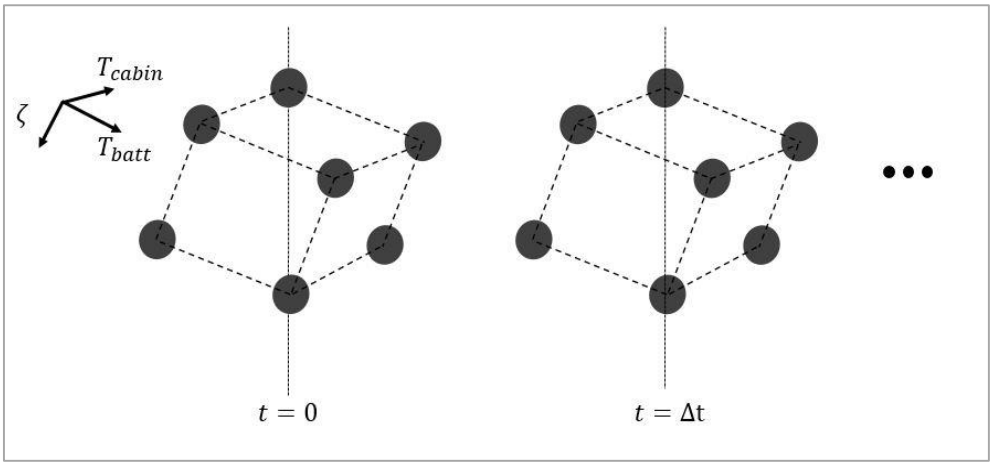

Figure 8-1. Structure of the state grid used with the DP algorithm

Based on the extreme limits of operation observed from the simulation results in Sections 7.2 and 7.3 the following bounds were considered for the states to accommodate all plausible scenarios:

$$\begin{bmatrix} 22°C \\ 20°C \\ 5\,\% \end{bmatrix} \leq x_v = \begin{bmatrix} T_{cabin} \\ T_{batt} \\ \zeta \end{bmatrix} \leq \begin{bmatrix} 62°C \\ 50°C \\ 80\% \end{bmatrix} \tag{8-7}$$

To form the state grid, cabin and battery temperatures were discretised in steps of two and one degrees, respectively, while ζ was discretised in steps of two per cent. With regards to discretisation in time, based on the sensitivity analysis presented in Appendix 2, the duration of Day Park was divided into 120 four-minute intervals ($\Delta t = 240\ s$) . Hence, the battery cooling flag changes once every four minutes.

With the above assumptions for the state grid, the computation time required for calculating the arc-cost term of equation (8-5) for every time interval is in the order of $O(88800s)$, amounting to a total computation time in the order of $O(10656000s)$ for the entire grid. The computation effort can be reduced by limiting the calculations to the reachable states, i.e. the states that can be attained given the inputs and the boundary conditions of the problem. As an example, consider the profile of battery temperature during Day Park in Phoenix summer when no key-off cooling is applied, as shown in Figure 8-2. At any point in time, this profile defines the highest possible value that the battery temperature can assume (since the heat flow to the battery is representative of the highest possible

scenario and no cooling is applied). Therefore, while it is potentially possible to reach the values marked in black (reachable states) through cooling, the battery temperature cannot reach the values marked in red (unreachable states). Similarly, unreachable battery SoC and cabin temperature states can be defined based on the simulation of extreme scenarios. Censoring the unreachable sections of the state grid reduces the computation time of arc-cost, making it manageable with a typical workstation.

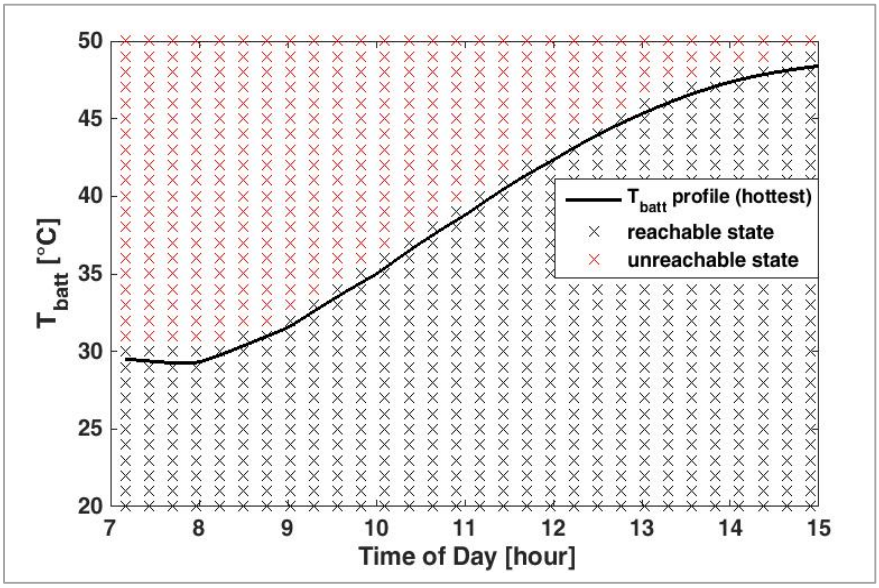

Figure 8-2. Reachable and unreachable battery temperature states. The state values are marked at steps of 4× Δt for clarity.

8.2 Solution for arbitrary initial and final conditions

Different definitions of the terminal cost, h_N in equation (8-5), can be considered to arrive at different variations of the problem. In this section, the problem is solved, only focusing on Day Park. Figure 8-3 compares the scope of the problem considered here with the baseline simulations in Chapter 7. For this initial investigation, h_N in equation (8-5) was defined as a constraint on the final SoC as

$$h_N = \begin{cases} 0 & if\ \zeta_N \geq 40\% \\ \infty & if\ \zeta_N < 40\% \end{cases} . \tag{8-8}$$

Since the battery is not charged during Day Park, the final SoC is the minimum SoC (i.e. $\zeta_N = \zeta_{min}$). Based on the baseline simulation results in Sections 7.1 and

7.2 for the duty cycle with US06 trips, the following initial conditions was assumed for the vehicle in Day Park:

$$x_{v,0} = \begin{bmatrix} T_{cabin,0} \\ T_{batt,0} \\ \zeta_0 \end{bmatrix} = \begin{bmatrix} 22°C \\ 30°C \\ 75\% \end{bmatrix}. \tag{8-9}$$

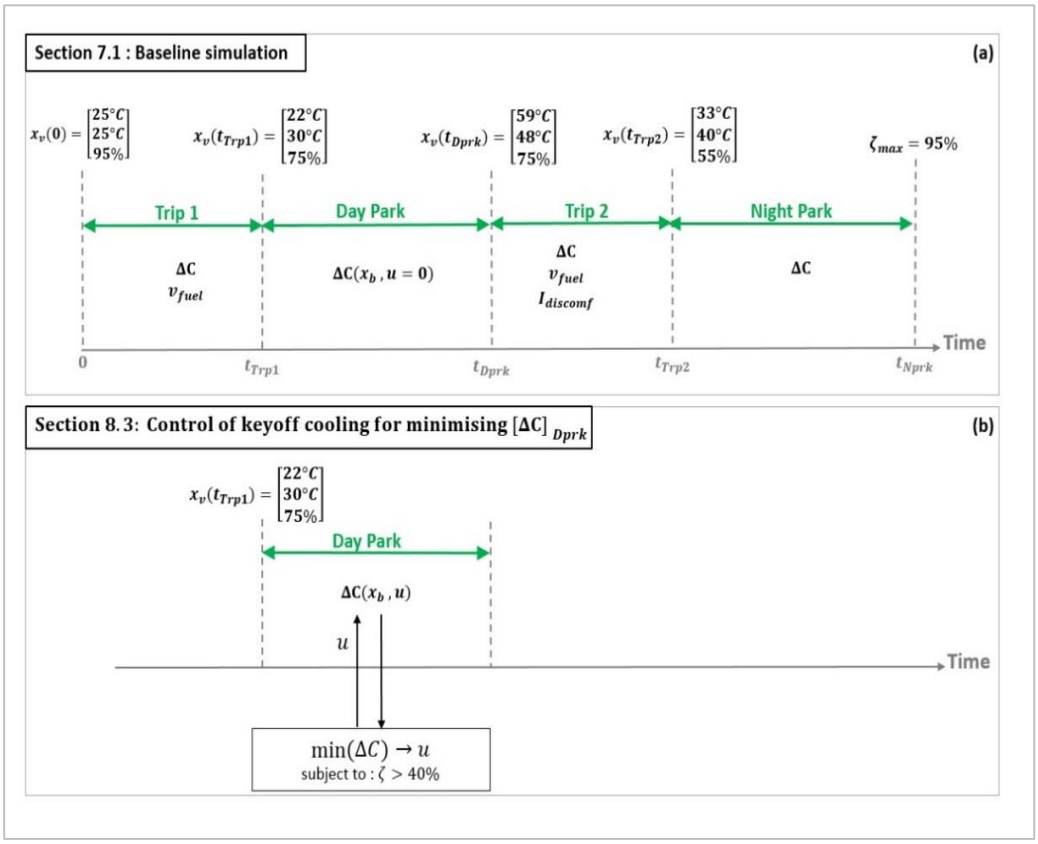

Figure 8-3. The scope of the analyses (a) in Chapter 7, (b) in this chapter. The vehicle state values shown are related to the duty cycle with US06 trips.

Solving (8-5) with (8-8) and (8-9) leads to the solution shown in Figure 8-4. The behaviour of the optimisation algorithm can be better understood considering that that the results shown in Figure 8-4 are governed by the following factors:

- Abundance of charge: since 35% of battery charge can be used, cooling can be intensely applied.

- Benefit of lower SoC: key-off cooling discharges the battery and reduces the capacity loss.

- Benefit of low battery temperature: maintaining a low battery temperature minimises the capacity loss.

- Higher effectiveness and higher efficiency of cooling earlier, compared to later, in the day: since the heat gains from the ambient environment and the cabin increase with time, cooling gradually becomes less effective and less efficient. Therefore, earlier cooling is preferred.

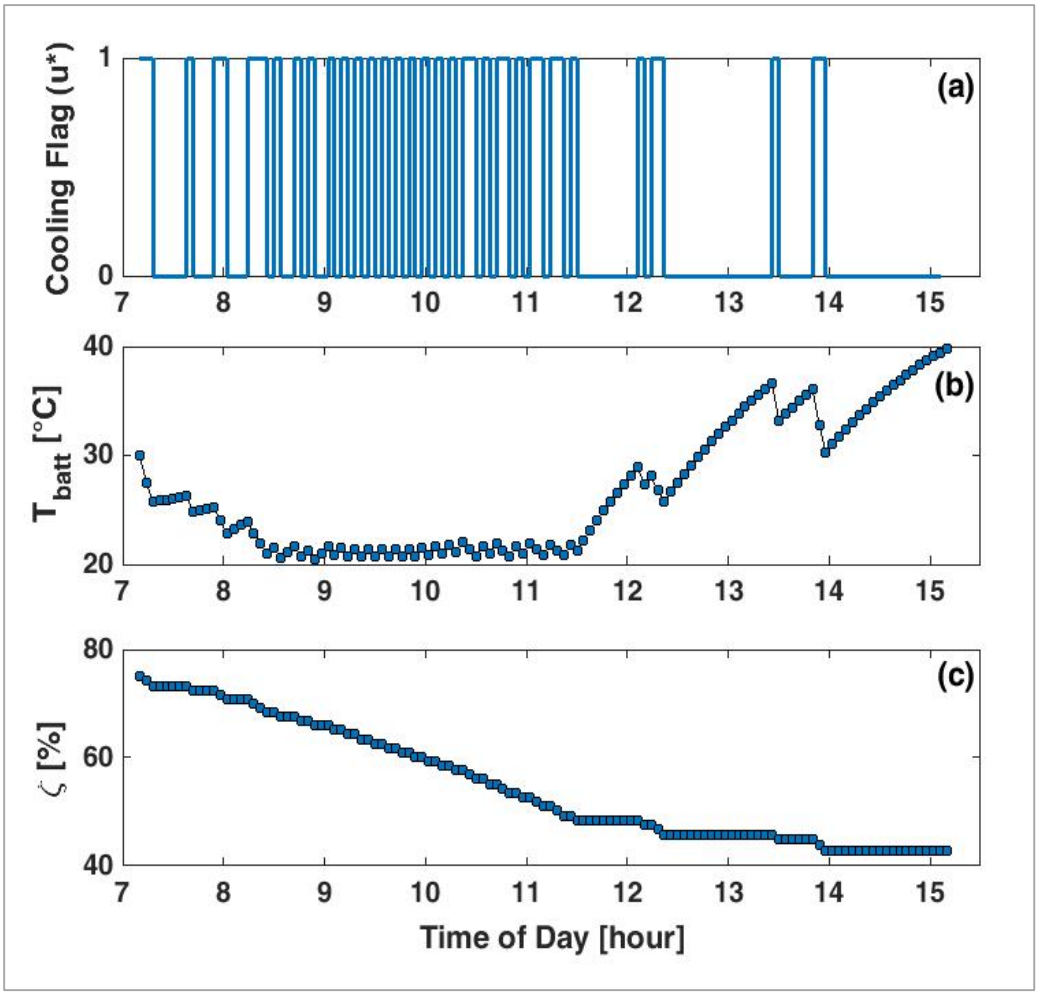

Figure 8-4. Optimum trajectory of (a) cooling flag, (b) battery temperature, and (c) SoC

The impact of controlling key-off cooling as above on the battery can be inferred from Table 8-1. It can be seen that key-off cooling reduces the seasonal storage capacity loss from 1.07% to 0.40%, whilst leading to a seasonal cycling capacity loss of 0.14%.

Table 8-1. Effect of optimised key-off cooling on the battery (in Day Park)

	Without cooling	**With cooling**
$\bar{\zeta}$ **[%]**	74.6	58.8
$\overline{T_{batt}}$ **[°C]**	39.0	27.8
Cycle count (per season)	0	26.7
Storage ΔC **[%]** ***(per season)***	1.07	0.40
Cycling ΔC **[%]** ***(per season)***	0	0.14

To show the significance of the above factors and illustrate the behaviour of the optimisation algorithm further, the effect of the initial SoC and limited charge availability on the solution of equation (8-5) are discussed in Sections 8.2.1 and 8.2.2

8.2.1 Effect of the initial SoC

To investigate the effect of the initial SoC on the solution of equation (8-5), three scenarios with different initial SoC levels, and availability of up to 25% of the SoC for key-off cooling were considered, as described in Table 8-2.

Table 8-2. Scenarios for investigating the effect of SoC on optimal key-off cooling

Scenario	ζ_0	ζ_{min}
1	75%	≥50%
2	60%	≥35%
3	50%	≥25%

In Figure 8-5(a), the optimal trajectories of the battery temperature for the scenarios of Table 8-2 is shown. In Figure 8-5(b), the resulting SoC trajectories are overlaid on the profile of storage capacity loss at 25°C. Comparing the temperature trajectories with the relevant SoC trajectory and the capacity loss profiles shows the impact of the remaining SoC on the control decisions, indicating the tendency to quickly discharge the battery below 50% SoC where capacity loss is lower. For example, in the scenario 2, which starts with 60% SoC, cooling is applied intensely until the SoC falls below 50%, after which point, the intensity of cooling reduces and cooling events are distributed more evenly. When less benefits

can be achieved through early discharge of the battery, cooling is distributed more evenly over time, as seen in scenario 3 with initial SoC of 50%, as well as in scenario 1 where the SoC is limited to the range of 75%-50%. Still, in the latter scenario, the algorithm seeks to avoid storage close to 60% SoC where the highest capacity loss occurs, so when the SoC nears this level (at approximately 11 am) cooling intensifies to accelerate discharge. The above analysis confirms that both the battery temperature and SoC have an important impact on the solutions of equation (8-5).

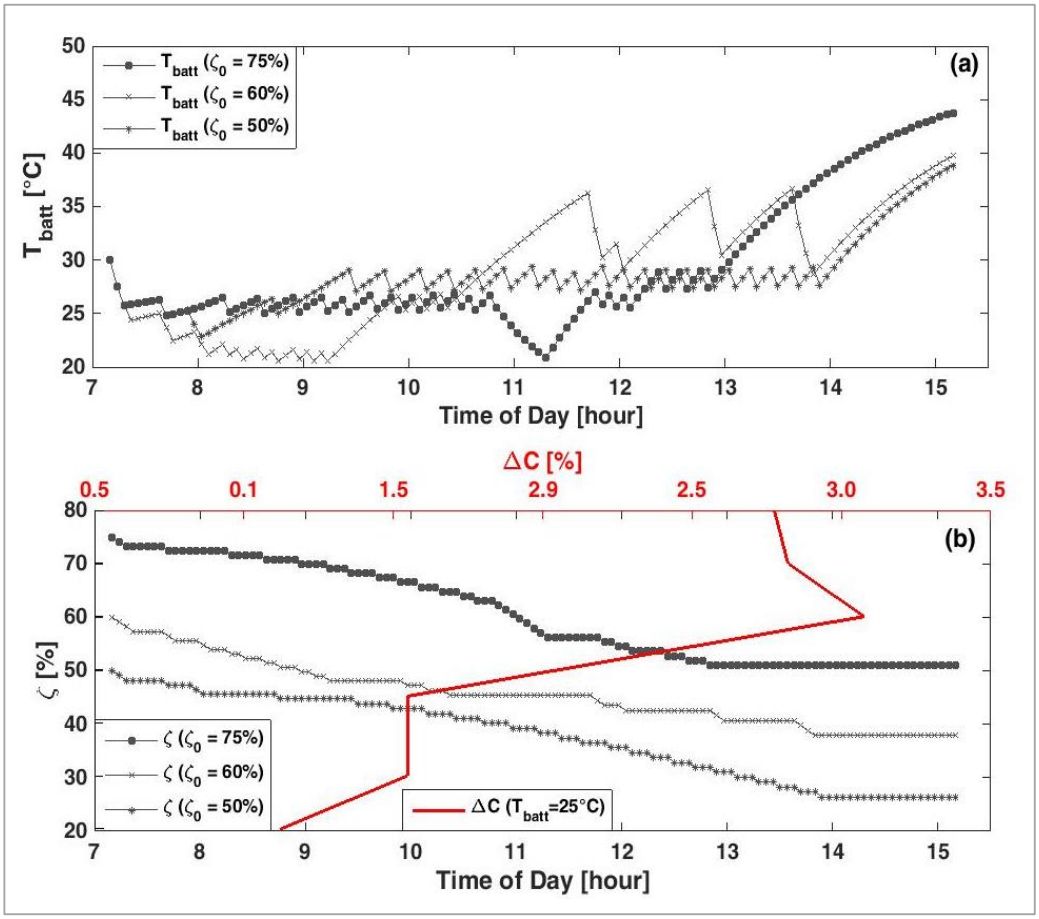

Figure 8-5. Effect of SoC on optimal control of key-off cooling (a) battery temperature trajectory, (b) SoC trajectory

8.2.2 Effect of charge limitation

In the solutions discussed so far, wide limits were set on SoC to enable sufficient cooling events and expose the behaviour of the optimisation algorithm. Nevertheless, a more plausible scenario is when only a significantly smaller amount of charge is available to key-off cooling. To investigate this, the scenarios

listed in Table 8-3 were considered in which only 5% or 10% of the battery SoC is allocated to key-off cooling; and the initial SoC is set at 75% or 50%.

Table 8-3. Scenarios for investigating the effect of charge limitation on key-off cooling strategy

Scenario	ζ_0	ζ_{min}
4	75%	≥70%
5	75%	≥65%
6	50%	≥45%
7	50%	≥40%

Figure 8-6 shows the temperature trajectories obtained through solving equation (8-5) for the scenarios defined in Table 8-3. When only 5% SoC is available (Figure 8-6(a) and Figure 8-6(c)), limited cooling is applied just before 12 noon. On the other hand, when 10% of SoC can be used (Figure 8-6(b) and Figure 8-6(d)) more cooling is applied around 12 pm, supplemented by further cooling early in the morning. Also, compared to Figure 8-6(d), in Figure 8-6(b) less cooling is applied early in the morning to avoid approaching the high capacity loss region of 60% SoC, as expected from the results presented in Section 8.2.1.

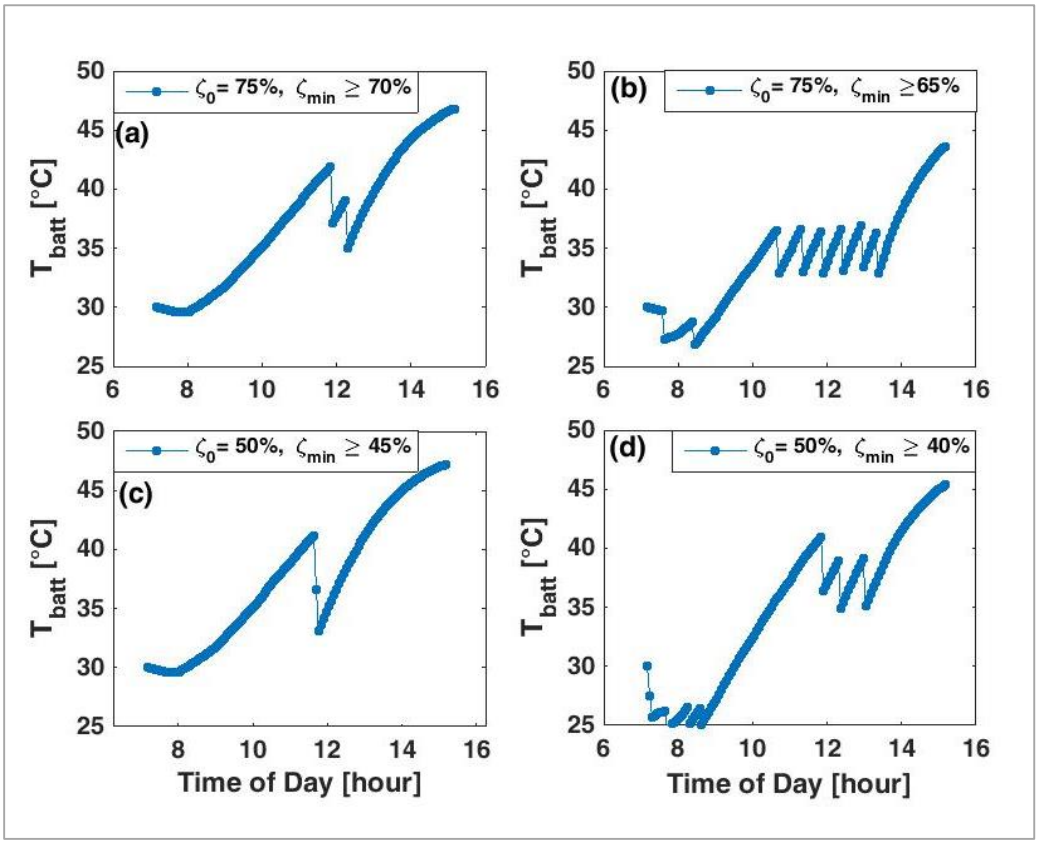

Figure 8-6. Battery temperature trajectory with optimal key-off cooling in scenarios with limited available charge. (a)-(d) refer to scenarios 4 – 7 defined in Table 8-3, respectively.

Table 8-4 compares the implications of applying cooling as above for the battery. Even limited cooling reduces the storage capacity loss of the battery (without having a noticeable effect on cycling capacity loss, as expected) although such reductions are more noticeable with more cooling. Notably, the effectiveness of key-off cooling is more pronounced when the battery is at a lower SoC. Due to penalties set on the boundaries of the DP state gird, the available charge window is not completely used for key-off cooling. This affects all solutions equally, therefore it does not undermine the validity of the above comparative analysis.

Table 8-4. Effect of optimised key-off cooling on the battery in scenarios with critical charge

Scenario		Figure	$\overline{T_{batt}}$ [°C]	$T_{batt,max}$ [°C]	$\Delta\zeta$ [%]	ΔC Storage† [%]	ΔC Cycling† [%]	Relative ΔC reduction [%]
$\zeta_0 = 75\%$, No cooling		NA	39.0	48.4	0	1.07	0.00	NA
4	**$\zeta_0 = 75\%$, $\zeta_{min} \geq 70\%$**	Figure 8-6(a)	37.4	46.8	2.5	1.00	0.00	6%*
5	**$\zeta_0 = 75\%$, $\zeta_{min} \geq 65\%$**	Figure 8-6(b)	34.0	43.6	7	0.84	0.04	18%*
$\zeta_0 = 50\%$, No cooling		NA	39.1	48.4	0	0.73	0.00	NA
6	**$\zeta_0 = 50\%$, $\zeta_{min} \geq 45\%$**	Figure 8-6(c)	37.4	47.2	2.5	0.65	0.00	9%**
7	**$\zeta_0 = 50\%$, $\zeta_{min} \geq 40\%$**	Figure 8-6(d)	34.8	45.3	7	0.46	0.04	32%**

† represents per season ΔC
* *with respect to* $\zeta_0 = 75\%$ and no cooling
** *with respect to* $\zeta_0 = 50\%$ and no cooling

Figure 8-6 suggests that when limited charge is available, cooling in midday is preferred over cooling in early morning. To investigate this, two additional scenarios were defined, as in Table 8-5. Here, the initial battery temperature is set to 35°C and 40°C, and the minimum SoC limit is reduced to 68% so more charge can be made available for key-off cooling compared to scenarios 4 and 6 above.

Table 8-5. Scenarios for investigating the effect of initial on key-off cooling strategy

Condition	$T_{batt,0}$	ζ_0	ζ_{min}
8	35°	75%	≥68%
9	40°	75%	≥68%

Figure 8-7 shows the result of solving equation (8-5) for scenarios 8 and 9. Even when the initial temperature is as high as 35°C, cooling at midday is preferred to cooling in early morning, and the battery is left to slowly cool down in low temperature ambient. However, when the battery is initially at 40°C, after-run cooling is applied for 1 time interval, consuming approximately 1% of the available SoC. Inevitably, less cooling is applied later in the day.

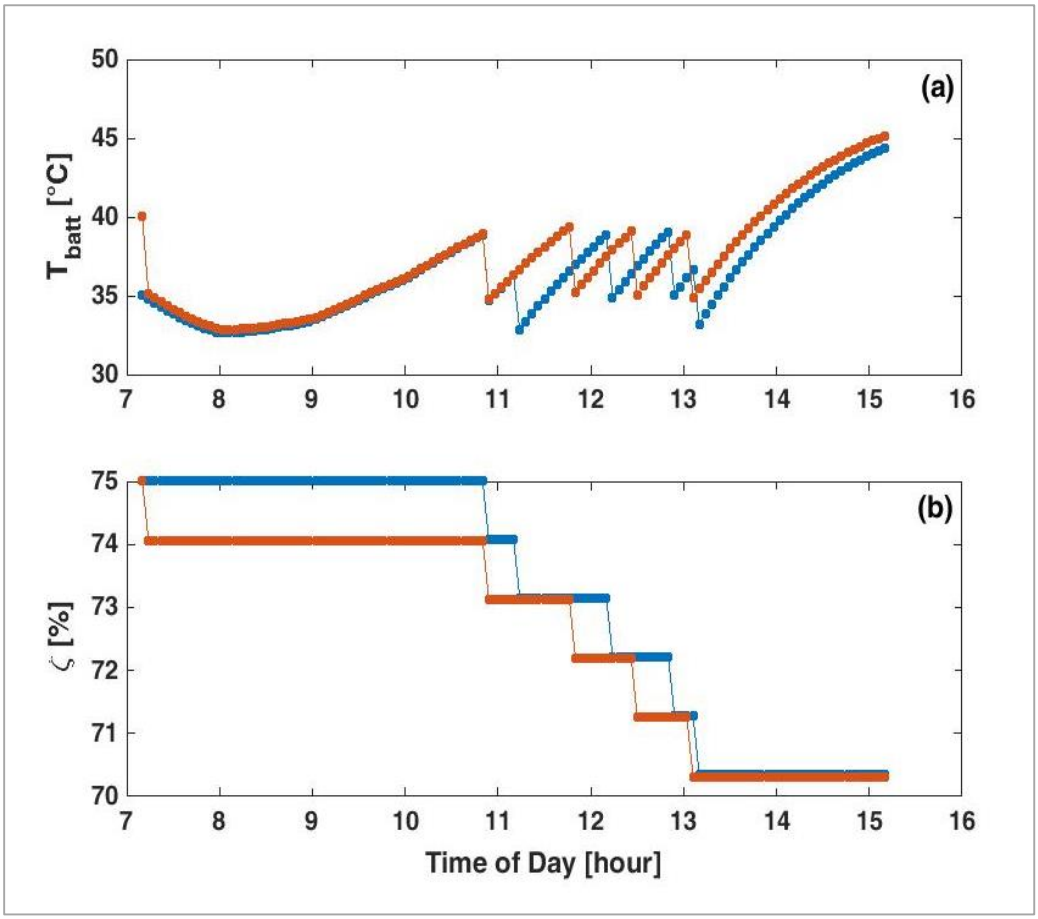

Figure 8-7. Effect of initial temperature on suitability of after-run cooling strategy. (a) temperature trajectory, (b) SoC trajectory. ***Annotation- blue: scenario 8, red: scenario 9***

8.2.3 Discussion

Analysing the solutions of scenarios 1-9 confirmed that

1. The SoC-dependent component of capacity loss has a noticeable effect on the solution of problem described by equation (8-5). When SoC is high, applying key-off cooling to discharge the battery early in the morning is preferred over maintaining a low temperature throughout Day Park

2. Even a limited key-off cooling is beneficial for reducing the capacity loss of the battery. Cooling the battery at midday is preferred to after-run cooling unless the initial temperature of the battery is very high.

The scenarios discussed above reveal the behaviour of the optimisation algorithm under a variety of battery temperature and SoC boundary conditions. In the following chapter, the boundary conditions rising from the daily duty cycle of the vehicle are considered in controlling key-off cooling.

It can be inferred from the scenarios discussed above that unless through solving an optimal control problem, controlling key-off cooling is not trivial. None of the simple control strategies defined for key-off cooling in Section 7.3.1 resembles the results achieved through optimisation in this chapter.

8.3 Summary

In this chapter, key-off cooling of the PHEV battery was defined as an optimal control problem based on minimising the battery capacity loss. The minimisation problem was solved with DP, considering Day Park in isolation. A variety of boundary condition were considered and the effectiveness of optimal control of key-off cooling was proved. Also, the effect of factors such as initial temperature and remaining SoC on the behaviour of the optimisation algorithm were analysed.

CHAPTER 9 OPTIMAL CONTROL OF KEY-OFF COOLING IN VIEW OF THE DUTY CYCLEV

Introduction

In this chapter, the optimal control of key-off cooling is discussed in the context of the PHEV daily duty cycle. In Section 9.1, the formulation of the optimal control problem proposed in Chapter 8 is expanded to include all three performance attributes of the vehicle, i.e. fuel economy, battery lifetime and thermal comfort, throughout the complete duty cycle. Seven scenarios are defined for controlling key-off cooling, based on considering individual and combinations of the performance attributes. The optimal control problem is solved in Sections 9.3 and 9.4, for the duty cycles comprising of US06 and NEDCx2 trips, respectively. In each case, the effect of the assumed scenario on control of key-off cooling is discussed. Section 9.5 discusses the applicability of the optimal control problem to the duty cycles with WLTC and Artemis trips. The discussions are summarised in Section 9.6.

9.1 Formulating the control of key-off cooling in view of the vehicle duty cycle

As discussed in Section 7.3, in addition to reducing the capacity loss of the battery in Day Park, key-off cooling affects the fuel consumption, the capacity loss, and the thermal discomfort in the subsequent phases of the vehicle duty cycle. Therefore, in controlling key-off cooling, the following three objectives are considered in this research with respect to the complete duty cycle:

1. minimising fuel consumption (i.e. improving fuel economy);

2. minimising capacity loss (i.e. improving battery lifetime);
3. minimising the discomfort index (i.e. improving thermal comfort).

The above objectives are combined as a minimisation of the following form

$$\min J = \min\left(\lambda_1 v_{fuel} + \lambda_2 \Delta C + \lambda_3 I_{discomf}\right), \tag{9-1}$$

where $\lambda = \{\lambda_1, \lambda_2, \lambda_3\}$ is the relative weighting of cost terms, i.e. the fuel consumption, the capacity loss, and the thermal discomfort. The daily values of the cost terms depend, among other factors, on how the vehicle (i.e. the powertrain, the AC and the battery cooling subsystems) is controlled during the two trips. Nevertheless, since the focus here is on key-off control, equation (9-1) can be solved assuming that the key-on control strategies of the vehicle are already optimised, that is, all subsystems are optimally controlled during the trips, for any initial conditions (of the relevant trip).

The above assumption enables an expansion of the terms of equation (9-1) as a function of vehicle states. v_{fuel} in equation (9-1), which is the total fuel consumption over the two trips, can be expanded as follows, considering that the operation of the vehicle in Trip 1 is independent of the key-off cooling strategy in Day Park, therefore

$$\begin{aligned} v_{fuel} = \left[v_{fuel}\right]_{Trp1} + \left[v_{fuel}\right]_{Trp2} &= \left[v_{fuel}\right]_{Trp1} + \\ &\left[v_{fuel}\left(x_v(t_{Dprk})\right)\right]_{Trp2}. \end{aligned} \tag{9-2}$$

where $\left[v_{fuel}\right]_{Trp1}$ and $\left[v_{fuel}\right]_{Trp2}$ denote the total fuel consumed in Trip 1 and Trip 2, respectively, while $x_v(t_{Dprk})$ is the state of the vehicle at the end of Day Park ($t = t_{Dprk}$). ΔC in equation (9-1) can be expanded in a similar manner. The capacity loss in Trip 2 depends on the vehicle state at the end of Day Park, $x_v(t_{Dprk})$. The capacity loss in Night Park is a function of the battery SoC after Trip 2, $\zeta(t_{Trp2})$ given that the battery temperature is controlled by plugged-in cooling and considering that the just-in-time charging strategy (to 95% SoC) is applied. Therefore,

$$\Delta C = [\Delta C]_{Trp1} + [\Delta C(x_b, u)]_{Dprk} + \left[\Delta C\left(x_v(t_{Dprk})\right)\right]_{Trp2} + \left[\Delta C\left(\zeta(t_{Trp2})\right)\right]_{Nprk}, \quad (9\text{-}3)$$

in which the capacity loss in Day Park is expressed as in equation (8-3).

The assumption made about the key-on control strategies follows that $\zeta(t_{Trp2})$ only depends on the state of the vehicle at the end of Day Park, $x_v(t_{Dprk})$. Therefore, equation (9-3) can be re-written as

$$\Delta C = [\Delta C]_{Trp1} + [\Delta C(x_b, u)]_{Dprk} + \left[\Delta C\left(x_v(t_{Dprk})\right)\right]_{Trp2} + \left[\Delta C\left(x_v(t_{Dprk})\right)\right]_{Nprk}. \quad (9\text{-}4)$$

Similarly, the discomfort index which is only defined for Trip 2 depends on the state of the vehicle at the end of Day Park:

$$I_{discomf} = I_{discomf}\left(x_v(t_{Dprk})\right). \quad (9\text{-}5)$$

The minimisation of the cost function of equation (9-1) can be reformulated in form of equation (8-5) as

$$\min_{u^*} J = \min\left(\lambda_1 \sum_{k=0}^{N-1} \Delta C_k\,(x_{bk}, u_k) + h_N\right) \quad (9\text{-}6)$$

where the terminal cost, h_N is derived from equations (9-2), (9-4), and (9-5) as

$$h_N = \lambda_1 \left[v_{fuel}\left(x_v(t_{Dprk})\right)\right]_{Trp2} + \lambda_2 \left[\Delta C\left(x_v(t_{Dprk})\right)\right]_{Trp2} + \lambda_2 \left[\Delta C\left(x_v(t_{Dprk})\right)\right]_{Nprk} + \lambda_3\, I_{discomf}\left(x_v(t_{Dprk})\right). \quad (9\text{-}7)$$

Since the fuel consumption and the capacity loss of Trip 1 are constant (i.e. they are independent of the key-off cooling control) they have been omitted from equation (9-6).

Figure 9-1 shows the scope of the analyses in this chapter compared to those in Chapter 7 and 8. The figure also shows the propagation of duty cycle information for solving the minimisation in equation (9-6).

Solving the minimisation defined in equation (9-6) with DP requires *a priori* knowledge of the terminal cost h_N, resulting from each value of $x_v(t_{Dprk})$ within the state grid of the DP. In other words, the effect of $x_v(t_{Dprk})$ on Trip 2 and Night Park should be evaluated in advance. To achieve this, Trip 2 and Night Park were simulated using all possible values of $x_v(t_{Dprk})$ as the initial state. The terms of the terminal cost related to each phase were then evaluated and mapped onto $x(t_{Dprk})$.

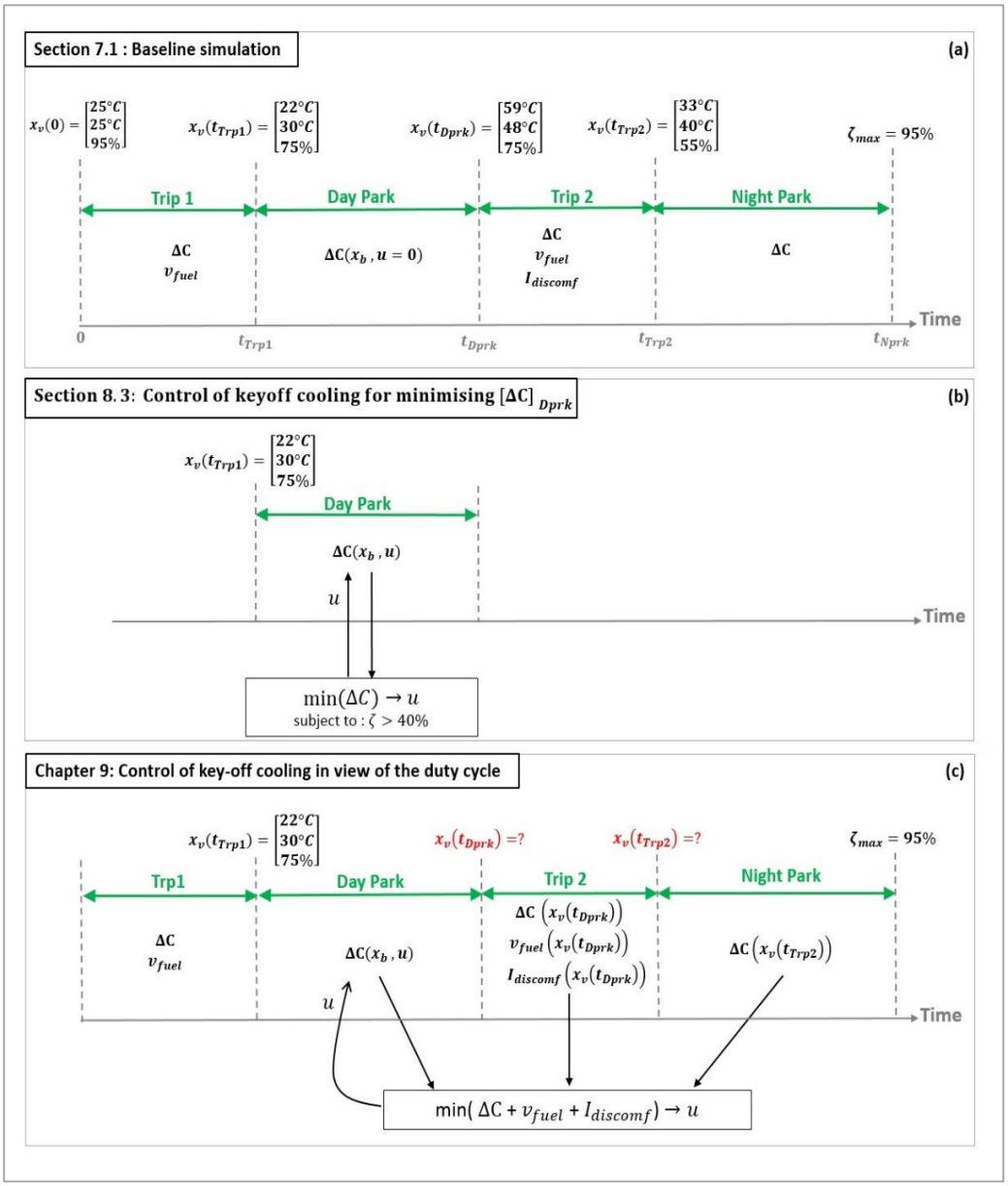

Figure 9-1. The scope of the analyses in (a) Chapter 7, (b) Chapter 8, and (c) in this chapter. The vehicle state values shown are related to the duty cycle with US06 trips.

As an example, Figure 9-2 shows the maps of the fuel consumption, the capacity loss and the discomfort index for the duty cycle with US06 trips. These maps are for a cabin temperature of 60°C at the start of Trip 2. Similar maps can be developed for alternative cabin temperatures and alternative drive cycles. In Figure 9-2(a), the fuel consumption in Trip 2 has been mapped on battery temperature and SoC at the end of Day Park. With a non-zero minimum, the fuel consumption increases as the initial SoC reduces below 50% (due to entering CS operating

mode) or as battery temperature increases above 45°C (due to reduced electric traction capability).

In Figure 9-2(b), capacity loss in Trip 2 has been mapped on battery temperature and SoC at the end of Day Park. This map shows that in the SoC range of approximately 20%-80%, capacity loss decreases with any increase in SoC (due to higher voltage and consequently lower charge throughput). In the same SoC range, capacity loss increases as the initial temperature increases above 20°C, but when the temperature at the end of Day Park exceeds 45°C, the capacity loss is significantly reduced due to reduced electric traction capability in Trip 2. Below 20% SoC, the capacity loss map has a noisy pattern since any small change in SoC or temperature can change the supervisory rules triggered in Trip 2, leading to different current throughput and temperature.

Figure 9-2(c) shows the discomfort index map on battery temperature and SoC at the end of Day Park. Discomfort is high when the battery is initially hot, and low for low battery temperature, while showing little sensitivity to variations in SoC. The variation of the discomfort index with temperature exhibits three distinct slopes. Between 20°C and 30°C, the discomfort index in most sensitive to temperature since the lower limit of this range represents the scenarios in which battery cooling is not initiated or is initiated very late in the trip, while its higher limit represents the scenarios in which battery cooling is activated from the start of the trip. Between 30°C and 45°C, battery cooling is activated from the start of the trip and higher temperature only extends the duration of cooling. Above 45°C, the power of the battery is limited and the vehicle starts the trip in hybrid mode, so the discomfort index is less sensitive to temperature.

In Figure 9-2(d), capacity loss in Night Park has been mapped on battery temperature and SoC at the end of Day Park. This is possible given that the battery temperature in Night Park is controlled by plugged-in cooling and that battery SoC in Night Park depends on the SoC at the end of Day Park for the assumed control strategy. The shape of this map is driven by the dataset used in propagating the ageing model. When the SoC is approximately in the range of 20%-60% or 70%-

80%, the dominant factor that affects the capacity loss in Night Park is the storage SoC. In the range of 20%-40%, the battery will be fully depleted by the start of Night Park, leading to a low capacity loss (due to low storage capacity loss). From 40% to 60% SoC, capacity loss increases since the battery will be stored at a higher SoC throughout Night Park. In the SoC range of 60%-70%, the effect of charge throughput (related to recharging the battery) is dominant, therefore the capacity loss decreases with any increase in SoC. Above 70%, the battery will be discharged and stored at SoC regions that cause significantly high storage capacity loss. In this range, the higher the SoC, the closer the final SoC will be to 60%, therefore the capacity loss increases with SoC.

In developing Night Park capacity loss map seen in Figure 9-2(d), battery charging was assumed to start at the same time (approximately 1.5 hour before the following Trip 1), irrespective of the charge remaining in the battery after Trip 2. This means that when the battery is fully depleted, the just-in-time charging strategy is accurately observed, but when more charge is left in the battery (full charging takes less time), charging starts earlier than required for just-in-time charging.

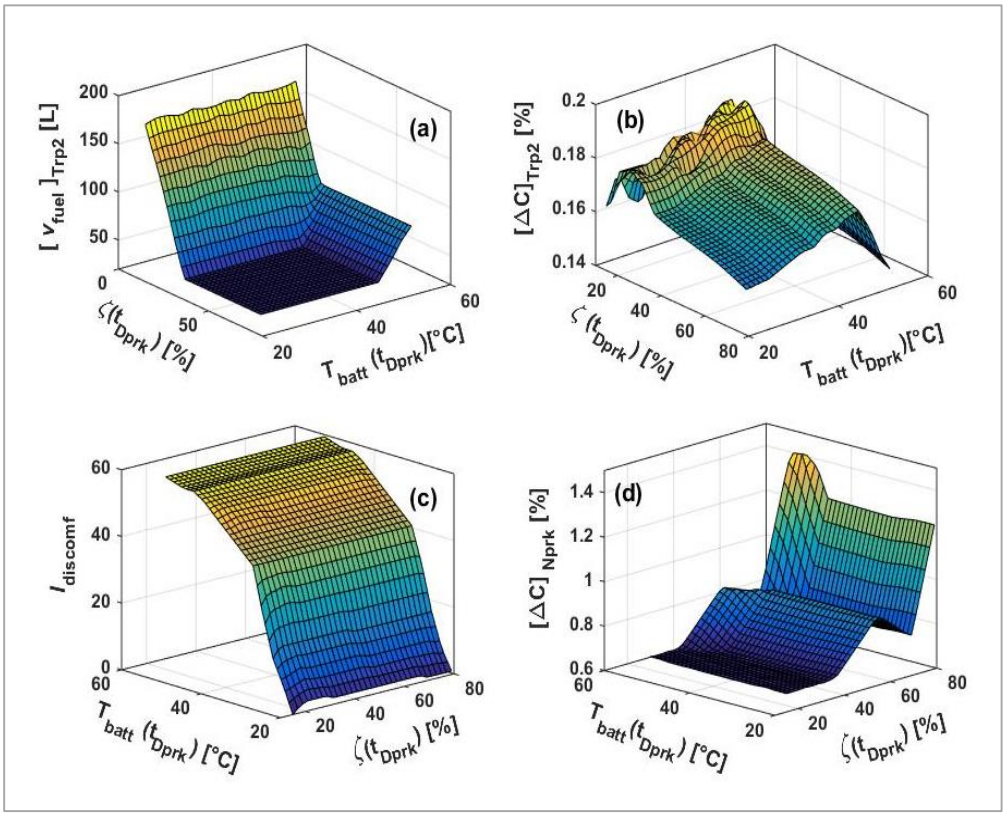

Figure 9-2. Maps of the terminal cost terms on $x_v(t_{Dprk})$ (a) fuel consumption in Trip 2, (b) capacity loss in Trip 2, (c) discomfort index (d) capacity loss in Night Park. The maps displayed are related to $T_{cabin}(t_{Dprk}) = 60°C$. Fuel consumption and capacity loss maps represent seasonal values. Note that the axes of (c) and (d) are rotate 90 degrees for higher clarity.

The terminal cost maps were used to propagate equation (9-7). Once h_N was calculated, equation (9-6) was solved with DP, as carried out in Chapter 8 for equation (8-5).

9.2 Scenarios for controlling key-off cooling

In Sections 9.3 and 9.4 the solutions of the minimisation defined by equation (9-6) is discussed for the duty cycles with US06 and NEDCx2 trips. To facilitate the discussions, the problem is solved for the seven scenarios defined in Table 9-1. Scenarios 9-I to 9-VI are designed to analyse the effect of considering one or two of the objectives (performance attributes) on the optimal control of key-off cooling, so extreme weights are assigned to the cost terms. In scenario 9-VII where all three objectives are included simultaneously, the weighting can be tuned based on the preference of the designer to enable a trade-off between the objectives.

Here, by solving the minimisation problem for scenarios 9-I to 9-VII and for a number of randomly selected weightings, the objective space of the minimisation is constructed, from which an appropriate solution for scenario 9-VII is chosen. The weighting leading to the chosen solution is also quoted.

Table 9-1. Scenarios for optimisation of key-off cooling

Scenario	Attribute			Weighting $\boldsymbol{\lambda = \{\lambda_1, \lambda_2, \lambda_3\}}$
	Fuel Economy	**Battery Lifetime**	**Thermal Comfort**	
9-I	✓	✗	✗	$\lambda = \{1, 0, 0\}$
9-II	✗	✓	✗	$\lambda = \{0, 1, 0\}$
9-III	✓	✓	✗	$\lambda = \{0.5, 0.5, 0\}$
9-IV	✗	✗	✓	$\lambda = \{0, 0, 1\}$
9-V	✓	✗	✓	$\lambda = \{0.5,0,0.5\}$
9-VI	✗	✓	✓	$\lambda = \{0,0.5,0.5\}$
9-VII	✓	✓	✓	To be defined *

* solution chosen after constructing the objective space

9.3 Solution for the duty cycle with US06 trips

In this section, the minimisation defined by equation (9-6) is solved for the duty cycle with US06 trips and the scenarios defined in Table 9-1. Initially, in Sections 9.3.1 to 9.3.7, the solution of each scenario is qualitatively analysed and compared with the relevant baseline results (discussed in Section 7.2). Section 9.3.8 provides further analysis of the solutions. For reference, the key features of baseline results are shown in Figure 9-3. Briefly, the daily profile of battery temperature in Figure 9-3(a) shows that the temperature reaches approximately 48°C in Day Park. The daily profile of battery SoC in Figure 9-3(b) shows that the battery is stored at approximately 74% SoC in Day Park and 54% SoC in Night Park. The profile of engine torque in Trip 2 shown in Figure 9-3(c) indicates that the vehicle enters hybrid mode within the first 100 seconds of the trip (due to high temperature of the battery). Finally, the profile of cabin temperature in Trip 2 shown in Figure 9-3(d) suggests that the PHEV cabin cools down at a slower rate compared to the equivalent CV.

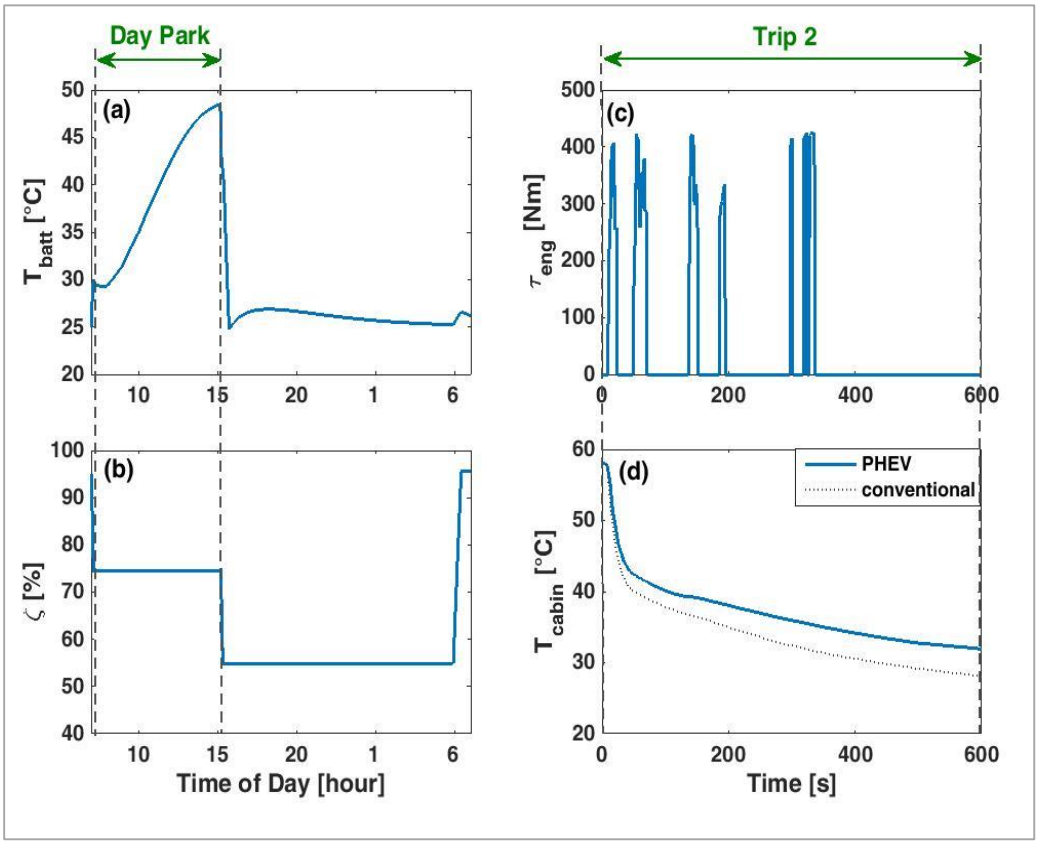

Figure 9-3. Result of baseline scenario for duty cycle in Phoenix summer with US06 trips

9.3.1 Scenario 9-I: Control of key-off cooling for improving fuel economy

When fuel economy is the only attribute of interest, key-off cooling can be controlled by applying a weighting of $\lambda = \{1, 0, 0\}$ to solve equation (9-6). The results are shown in Figure 9-4. The daily profile of the temperature and the SoC of the battery, are shown in Figure 9-4(a), and Figure 9-4(b), respectively. It can be seen that the battery temperature in Day Park is allowed to rise, and key-off cooling is limited to cooling the battery to approximately 42°C prior to Trip 2, which requires approximately 1% of battery SoC. Figure 9-4(c) compares the resulting profile of engine torque in Trip 2 with the baseline scenario. Pre-cooling the battery has enhanced the electric traction capability in Trip 2, as the engine has not started at the beginning of the trip. Figure 9-4(d), compares the resulting profile of cabin temperature with the baseline scenario and that of the equivalent CV. The limited key-off cooling has not affected the thermal comfort, as the cabin cools down at a similar rate to the baseline scenario.

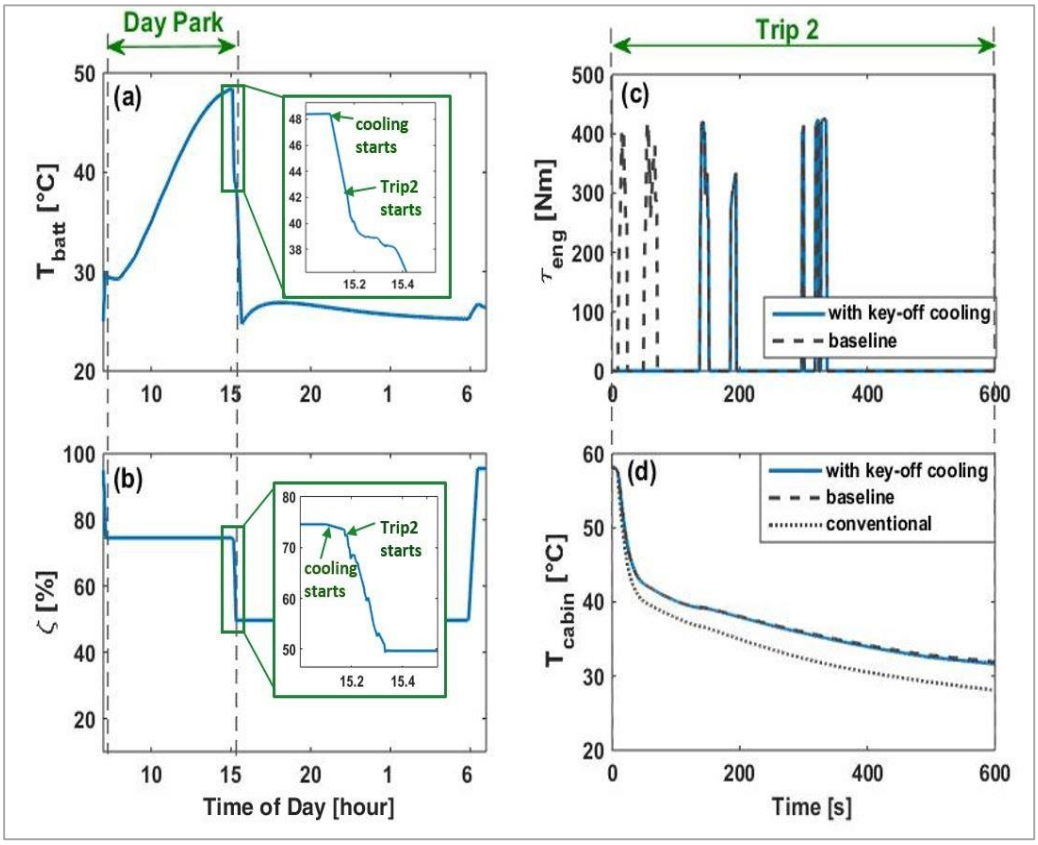

Figure 9-4. Solution of equation (9-6) with US06 trips and $\lambda = \{1, 0, 0\}$. (a) daily battery temperature, (b) daily SoC, (c) engine torque in Trip 2, and (d) cabin temperature in Trip 2

9.3.2 Scenario 9-II: Control of key-off cooling for improving battery lifetime

When battery lifetime is the only attribute of interest, key-off cooling can be controlled by solving (9-6) with $\lambda = \{0, 1, 0\}$ weighting. Figure 9-5 shows the results. The battery temperature profile in Day Park, as seen in Figure 9-5(a), resembles the trends seen previously in Figure 8-4, although more energy is allocated here to key-off cooling (48% of SoC, according to Figure 9-5(b), depleting the battery to approximately 27%) given that no constraint is set on minimum SoC. In addition, towards the end of Day Park, the battery temperature has been maintained lower than it was in Figure 8-4, given that higher temperatures lead to higher capacity loss in Trip 2, as can be inferred from the map of capacity loss in Trip 2 shown in Figure 9-2(b).

Applying key-off battery cooling as above affects the vehicle in Trip 2. Figure 9-5(c), which compares the engine torque in Trip 2 with the baseline, shows that

while the vehicle has been able to operate in EV mode at the start of the trip due to the lower initial battery temperature, it is forced to operate in CS mode later in the trip due to lower charge. This indicates a trade-off between fuel consumption and capacity loss.

In addition, comparing the cabin temperature in Trip 2 with the baseline scenario and the equivalent CV in Figure 9-5(d) indicates that the cabin has cooled down at a similar rate to the CV equivalent in the first 200 seconds of the trip. This is because the lower initial battery temperature has shifted the battery cooling load. This suggests a lower overall thermal discomfort index, and improved thermal comfort, compared to the baseline scenario.

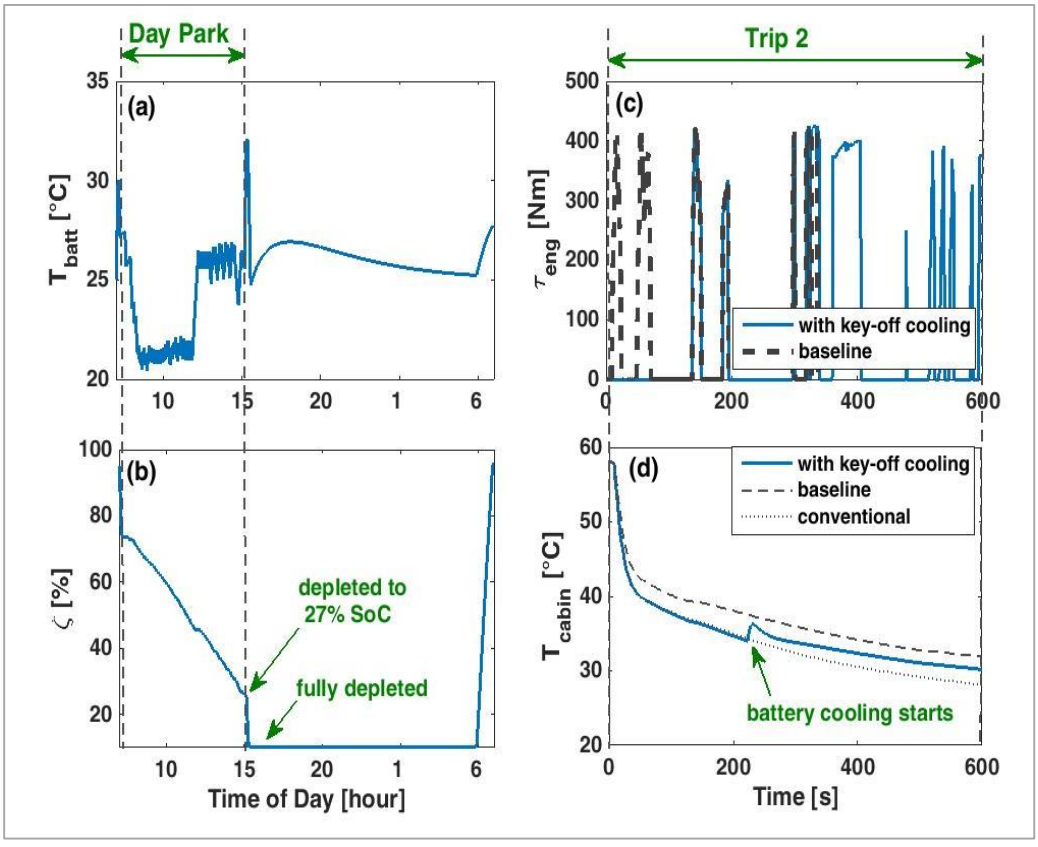

Figure 9-5. Solution of equation (9-6) with US06 trips and $\lambda = \{0, 1, 0\}$. (a) daily battery temperature, (b) daily SoC, (c) engine torque in Trip 2, and (d) cabin temperature in Trip 2

It is worth noting that the application of key-off cooling leads to lower SoC in Night Park compared to the baseline case (compare Figure 9-5(b) and Figure 9-3(b)), but recharging the battery to 95% SoC requires more charge throughput. Therefore, it can be expected that key-off cooling will lead to less storage and

higher cycling capacity loss in Night Park. Figure 9-2(d) implies that the reduction in storage capacity loss generally outweighs any increase in cycling capacity loss, at least for the duty cycle under consideration. Nevertheless, consideration of the complete daily duty cycle for controlling key-off cooling, as proposed here, ensures that the benefits of key-off cooling are not negated in the subsequent parts of the duty cycle.

9.3.3 Scenario 9-III: Control of key-off cooling based on the trade-off between fuel economy and battery lifetime

When fuel economy and battery lifetime are both of importance, key-off cooling can be controlled by solving (9-6) with $\lambda = \{0.5, 0.5, 0\}$ weighting. The results are shown in Figure 9-6. Here, although key-off cooling is applied to maintain a low battery temperature in Day Park, the allocated energy is limited to the excess battery charge to avoid unwanted CS operation in Trip 2. Therefore, the battery is warmer in this scenario compared to scenario 9-II (in Figure 9-6(a) the temperature is allowed to rise to approximately 35°C towards the end of Day Park while in Figure 9-5(a) the temperature is maintained close to 25°C). Figure 9-6(b) shows that the battery is fully depleted by the end of Trip 2. Figure 9-6(c) suggests that the electric traction capability of the vehicle in Trip 2 has improved by key-off cooling. No significant improvement in cabin temperature over the baseline is expected, as Figure 9-6(d) indicates.

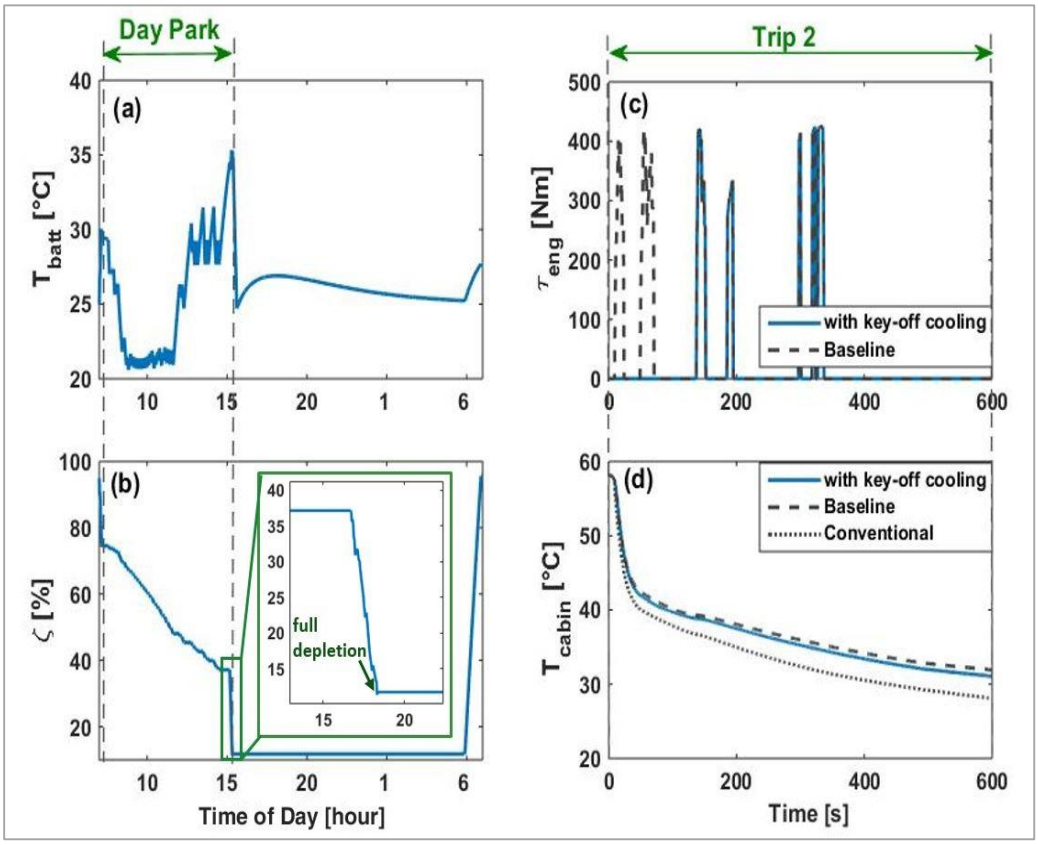

Figure 9-6. Solution of equation (9-6) with US06 trips and λ={0.5,0.5,0}. (a) daily battery temperature, (b) daily SoC, (c) engine torque in Trip 2, and (d) cabin temperature in Trip 2

9.3.4 Scenario 9-IV: Control of key-off cooling for improving thermal comfort

When thermal comfort is the only attribute of interest, key-off cooling of the battery can be controlled by applying a weighting of $\lambda = \{0, 0, 1\}$ to solve equation (9-6). This leads to the results shown in Figure 9-7. As Figure 9-7(a) shows, key-off cooling has been limited to pre-cooling for Trip 2. Here, cooling starts well in advance of the trip, maintaining the battery at approximately 21°C. This consumes approximately 20% of the SoC, as Figure 9-7(b) suggests. Figure 9-7(d) shows that battery cooling in Trip 2 has been shifted by approximately 400 seconds due to pre-cooling. In other words, the thermal discomfort index of the initial 6.6 minutes of the trip is zero, implying that the thermal discomfort has reduced considerably compared to the baseline. In addition, as a by-product of pre-cooling, the electric traction capability of the vehicle in trip2 has been maximized, as Figure 9-7(c) indicates. It is worth noting that this solution in not unique, as further key-

off cooling can be applied, even at the expense of increased fuel consumption in Trip 2, and still finish Day Park with a similar battery temperature.

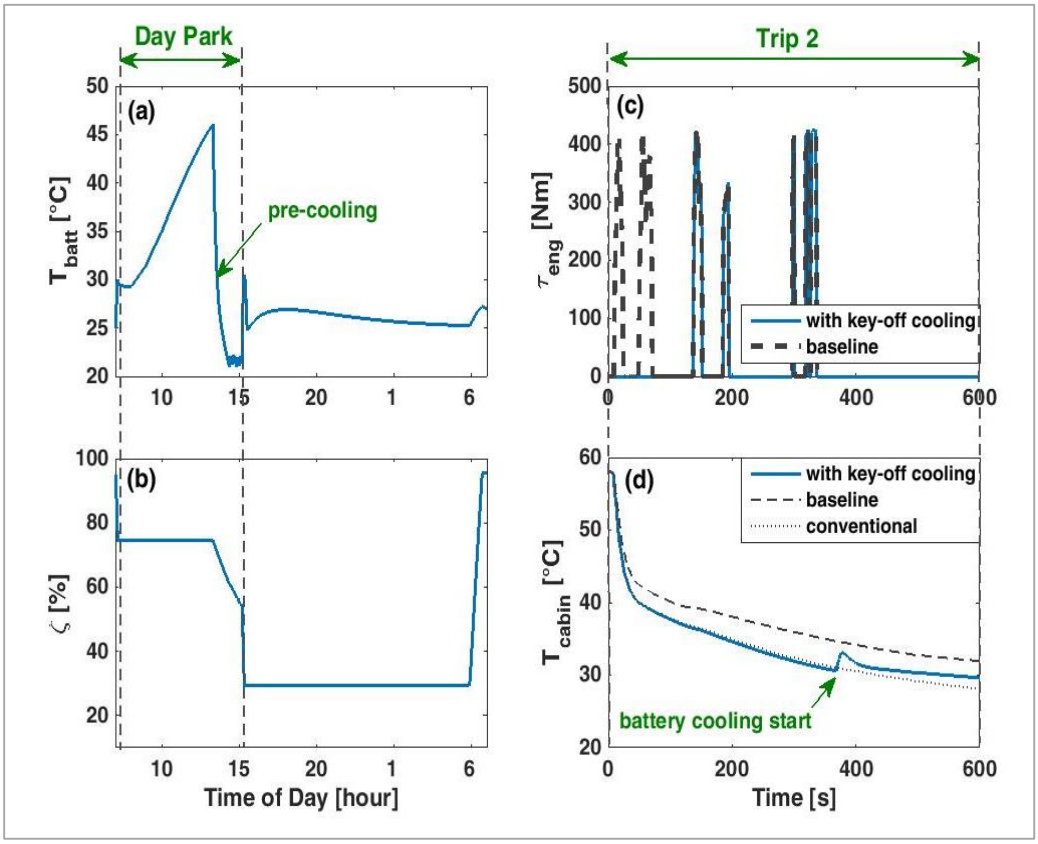

Figure 9-7. Solution of equation (9-6) with US06 trips and λ={0,0,1}. (a) daily battery temperature, (b) daily SoC, (c) engine torque in Trip 2, and (d) cabin temperature in Trip 2

9.3.5 Scenario 9-V: Control of key-off cooling for improving fuel economy and thermal comfort

The similarity between the engine torque profiles achieved in scenarios 9-I and 9-IV (Figure 9-4 and Figure 9-7), indicates that there is no trade-off between fuel economy and thermal comfort over the duty cycle with US06 trips. In other words, the excess charge of the battery is sufficient to support the pre-cooling required for improving thermal comfort (to 21°C), without leading to extra fuel consumption in Trip 2. Besides, it is clear that pre-cooling based on thermal comfort consideration is more than sufficient for eliminating the effect of battery overheating on the electric traction capability of the vehicle and improving the fuel economy. Therefore, when improving fuel economy and thermal comfort are both considered, Figure 9-7 remains a possible solution. Here, as in the case of scenario

9-IV, further key-off cooling can be applied, so the solutions are not unique. However, in spite of scenario 9-IV, the charge that can be allocated to key-off cooling will be limited by the excess charge of the battery, to prevent increased fuel consumption in Trip 2.

9.3.6 Scenario 9-VI: Control of key-off cooling for improving battery lifetime and thermal comfort

When both battery lifetime and thermal comfort are important, key-off cooling can be controlled by solving equation (9-6) with a $\lambda = \{0, 0.5, 0.5\}$ weighting. This leads to the results shown in Figure 9-8, where key-off cooling is aimed at both maintaining a low battery temperature throughout Day Park to reduce capacity loss, and pre-cooling the battery for Trip 2 to reduce thermal discomfort. Comparing Figure 9-8(a) and Figure 9-5(a) suggests that in order to enable pre-cooling, less cooling has been applied in the afternoon hours, hence the battery temperature reaches approximately 33°C before pre-cooling to 21°C. Figure 9-8(c) shows that while the vehicle has been able to start Trip 2 in EV mode as a result of key-off cooling, it is forced to operate in CS mode towards the end of the trip. Figure 9-8(d) shows that pre-cooling has shifted the cooling load of the battery in Trip 2 by approximately 400 seconds (as in the case of scenario IV).

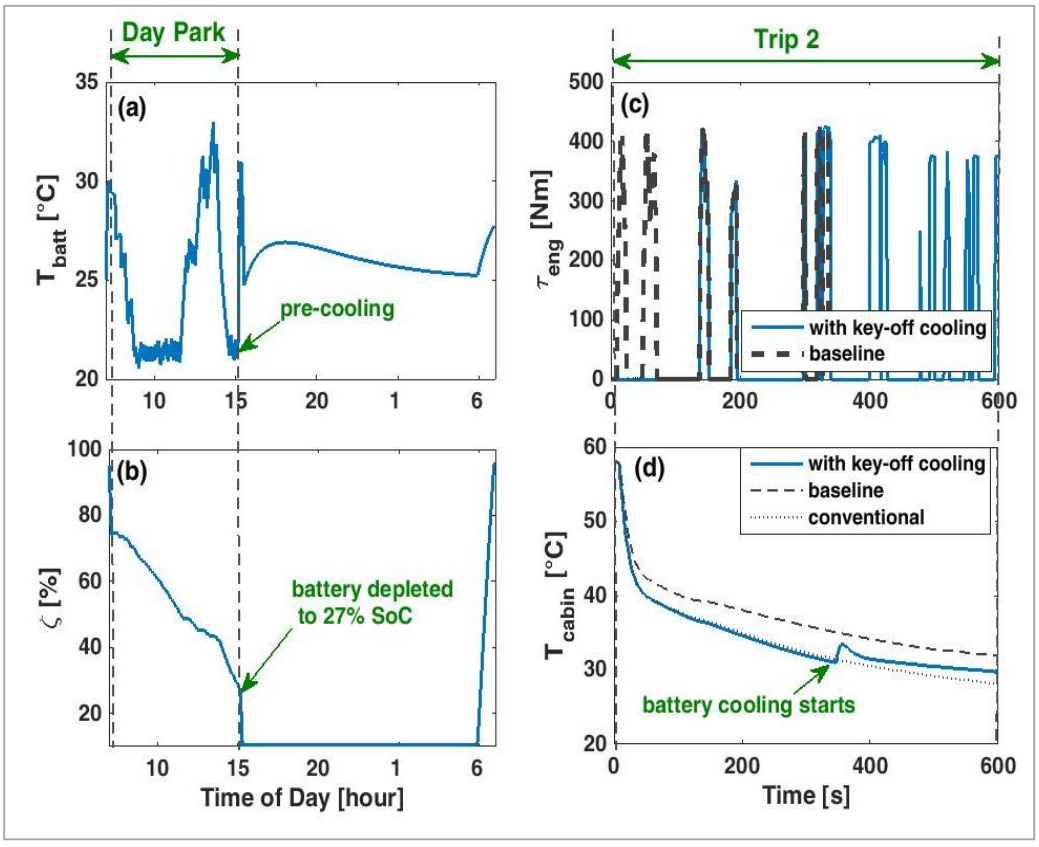

Figure 9-8. Solution of equation (9-6) with US06 trips and λ={0,0.5,0.5}. (a) daily battery temperature, (b) daily SoC, (c) engine torque in Trip 2, and (d) cabin temperature in Trip 2

9.3.7 Scenario 9-VII: Control of key-off cooling based on a trade-off between fuel economy, battery life, and thermal comfort

The previous scenarios illustrated the effect of prioritising different objectives on the control of key-off cooling. In Figure 9-9 the cost space (or objective space) of the minimisation problem is projected on the planes of cost term pairs (the $v_{fuel} - I_{discomf}$ plane is not shown as there is no trade-off between fuel economy and thermal comfort). This figure is achieved by simulating the model with random key-off cooling flag inputs, as well as by solving equation (9-6) with various weightings of the objectives. The solutions of the scenarios 9-I to 9-VI are marked on the figure. The dotted lines specify the (normalized) minimum achievable values of the objective terms, while the dashed lines approximate the pareto front that highlights the trade-off between the cost pairs. The following observations can be made:

- Pre-cooling the battery in scenario 9-I has reduced the fuel consumption to its lower limit, while slightly reducing the capacity loss and thermal discomfort compared to the baseline. Note that the non-zero minimum value of fuel consumption reflects the need for using the engine in the high power demanding parts of the US06.

- The intense key-off cooling applied in scenario 9-II leads to a significant reduction in the capacity loss compared to the baseline, but leads to a high fuel consumption. The thermal discomfort has also noticeably reduced.

- In scenario 9-III, where key-off cooling is limited by the excess battery charge, the capacity loss is still considerably reduced, while the fuel consumption is minimised. Since key-off cooling reduces the maximum temperature of the battery, it also reduces the thermal discomfort to some extent. As Figure 9-9(a) shows, the solutions of scenarios 9-II and 9-III lie on the pareto front of the $v_{fuel} - \Delta C$ plane.

- The intense pre-cooling applied in scenario 9-IV minimises the thermal discomfort. It also prevents any effect of battery overheating on the electric traction capability of the vehicle which minimises the fuel consumption. The reductions in the capacity loss are however small, given that no further key-off cooling is applied to avoid high temperature.

- In scenario 9-VI, the key-off cooling applied to maintain a low temperature throughout Day Park in addition to pre-cooling for Trip 2 reduces the capacity loss and the discomfort index significantly, but leads to a high fuel consumption. The solutions of scenarios 9-II, 9-IV and 9-VI lie on the pareto front of the $\Delta C - I_{discomf}$ plane.

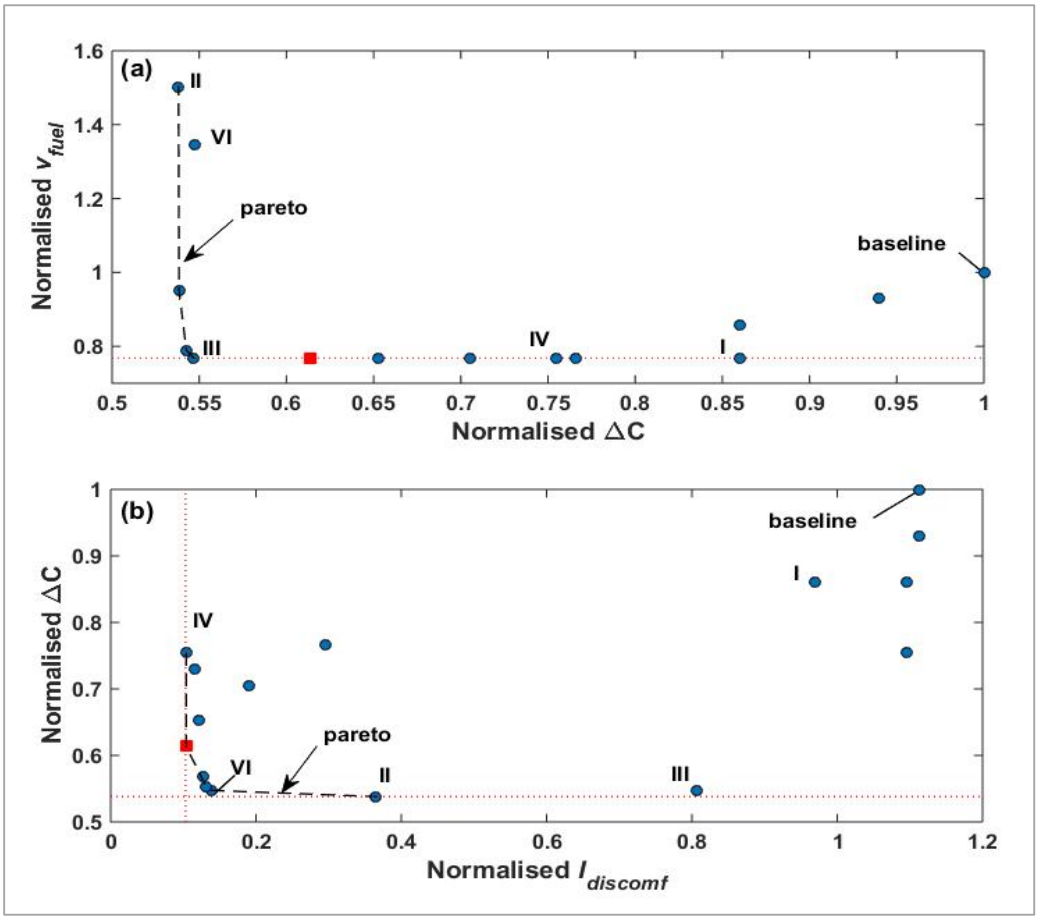

Figure 9-9. Objective planes of equation (9-6) with US06 trips and (a) $\lambda_3 = 0$ and (b) $\lambda_1 = 0$. The dotted lines indicate the achievable boundary of the objective planes. The dahsed lines approximate the pareto front. The red square marks the solution achieved with $\lambda = \{0.33, 0.33, 0.33\}$.

A good solution for equation (9-6) is marked by red squares in Figure 9-9 and corresponds to minimum fuel consumption as well as significant reductions in both the capacity loss and the discomfort index (it lies on the pareto front of the $\Delta C - I_{discomf}$ plane). This solution, which is plotted in Figure 9-10, is achieved by solving equation (9-6) with $\lambda = \{0.33, 0.33, 0.33\}$. It can be seen that the battery has been maintained at a low temperature in Day Park, and is pre-cooled for Trip 2. Comparing the profile of the battery temperature in Figure 9-10(a) and Figure 9-8(b) suggests that the intensity of key-off cooling is lower, and pre-cooling is delayed until just before Trip 2. Figure 9-10(b) shows that more than 41% of SoC is reserved for Trip 2. Applying key-off cooling in this manner has enhanced both the electric traction capability and thermal comfort attribute, as Figure 9-10(c) and Figure 9-10(d) indicate.

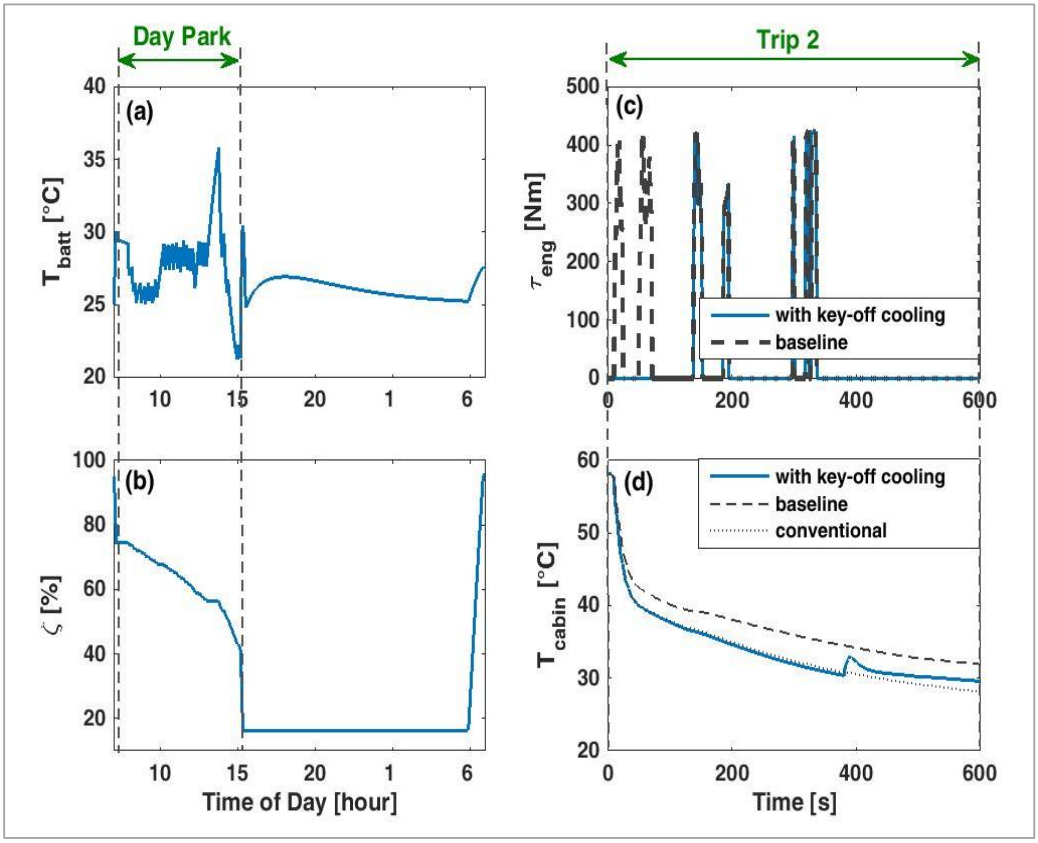

Figure 9-10. Result of optimising key-off cooling of the battery for λ={0.33,0.0.33,0.0.33}. (a) daily battery temperature, (b) daily SoC, (c) engine torque in Trip 2, and (d) cabin temperature in Trip 2

9.3.8 Discussion

Table 9-2 summarises the results of the different solutions of (9-6) discussed in sections 9.3.1 to 9.3.7. The evolution of the capacity loss, the fuel consumption and the thermal discomfort are consistent with the weightings applied. These results confirm the benefit of key-off cooling for the battery lifetime. In addition, the following observations can be made from these results:

- The limited pre-cooling applied in scenario 9-I has led to a 23% reduction in the seasonal fuel consumption by enhancing the electric traction capability of the vehicle. However, this limited pre-cooling has a negligible impact on battery lifetime and thermal comfort

- The result of scenario 9-II indicates that regardless of the impact on fuel consumption, key-off cooling has the potential for improving the battery lifetime by 2.2 years.

- The result of scenario 9-III indicates that even when key-off cooling is limited by the availability of excess battery charge, it can improve the battery lifetime from 6.3 years to 8.3 years.

- The result of scenario 9-IV shows the effectiveness of pre-cooling significantly in reducing the thermal discomfort. Even when pre-cooling is limited by the availability of excess battery charge, significant reductions in the discomfort index can be achieved (as inferred from the result of scenario 9-V).

- The result of scenario 9-VI show that when the fuel consumption is not constrained, key-off cooling can enable significant improvement in battery lifetime and thermal comfort.

- The result of scenario 9-VII shows the optimal control of key-off cooling can simultaneously improve the battery lifetime from 6.3 years to 8 years, reduce the thermal discomfort from 57 to 6, and reduce the seasonal fuel consumption from 108 L to 83 L.

It is worth noting that in scenarios 9-II and 9-III, the Day Park capacity loss reduced to 0.47%, and 0.48% respectively, which is much lower than the lowest capacity loss observed without optimising key-off cooling in Section 7.3.1. This shows the importance of approaching key-off cooling as an optimal control problem.

Another important observation from Table 9-2 is the correlation between the average battery temperature in Day Park and capacity loss in Night Park, across different solutions. Therefore, an indirect benefit of using the battery charge to perform key-off cooling is lower capacity loss in Night Park. Application of key-off cooling increases the cycling component of the capacity loss in Night Park, since the battery needs to receive more charge to compensate for the spent energy. Therefore, the reduction achieved in Night Park capacity loss is due to lower storage capacity loss enabled by lower storage SoC (temperature variation in Night Park is negligible since plugged-in cooling is assumed). Hence, a significant part of the improvements achieved in battery lifetime through key-off cooling is enabled by the resulting lower SoC of the battery in Night Park. The above observation indicates that an opportunity exists for achieving further improvements in battery lifetime through partial charging.

Table 9-2. Summary of results for different solutions of equation (9-6) for the duty cycle with US06 trip

Scenario	Solution	$[\bar{T}_{batt}]_{Dprk}$ [°C]	$[T_{batt,max}]_{Dprk}$ [°C]	$T_{batt}(t_{Dprk})$ [°C]	$\zeta(t_{Dprk})$ [%]	$[\Delta C]_{Dprk}$ [%]	$[\Delta C]_{Trp2}$ [%]	$[\Delta C]_{Nprk}$ [%]	EoL [years]*	v_{fuel} [L]	$I_{discomf}$ [-]
Baseline	--	39.0	48.4	48.4	74.6	1.07	0.16	1.36	6.3	108.5	57
9-I	**Min v_{fuel}:** $\boldsymbol{\lambda} = \{\mathbf{1}, \mathbf{0}, \mathbf{0}\}$	39.0	48.4	42.2	73.6	1.06	0.17	0.98	6.8	83.4	56
9-II	**Min ΔC:** $\boldsymbol{\lambda} = \{\mathbf{0}, \mathbf{1}, \mathbf{0}\}$	23.8	29.5	25.5	25	0.47	0.18	0.68	8.5	163.0	21
9-III	**Min v_{fuel} + ΔC:** $\boldsymbol{\lambda} = \{\mathbf{0.5}, \mathbf{0.5}, \mathbf{0}\}$	25.4	34.5	34.5	37.2	0.48	0.18	0.70	8.3	83.4	46
9-IV	**Min $I_{discomf}$:** $\boldsymbol{\lambda} = \{\mathbf{0}, \mathbf{0}, \mathbf{1}\}$	33.7	46.0	21.0	54.1	0.87	0.16	0.90	7.3	83.4	5
9-V	**Min v_{fuel} + $I_{discomf}$:** $\boldsymbol{\lambda} = \{\mathbf{0.5}, \mathbf{0}, \mathbf{0.5}\}$	33.7	46.0	21.0	54.1	0.87	0.16	0.90	7.3	83.4	5
9-VI	**Min ΔC + $I_{discomf}$:** $\boldsymbol{\lambda} = \{\mathbf{0}, \mathbf{0.5}, \mathbf{0.5}\}$	24.6	33.0	22.1	27.6	0.50	0.18	0.69	8.4	145.9	8
9-VII	**Min v_{fuel} + ΔC + $I_{discomf}$:** $\boldsymbol{\lambda} = \{\mathbf{0.33}, \mathbf{0.33}, \mathbf{0.33}\}$	27.7	35.8	21.3	41.4	0.62	0.17	0.75	8.0	83.4	6

**Assumes the capacity loss in winter is equal to the baseline scenario*

9.4 Solution for the duty cycle with NEDCx2 trips

In this section, the solution of the optimal control problem defined in Section 9.1 is discussed for the duty cycle with NEDCx2 trips. The scenarios defined in Table 9-1 are considered. For reference, the key features of the relevant baseline results discussed in Section 0 are shown in Figure 9-11.

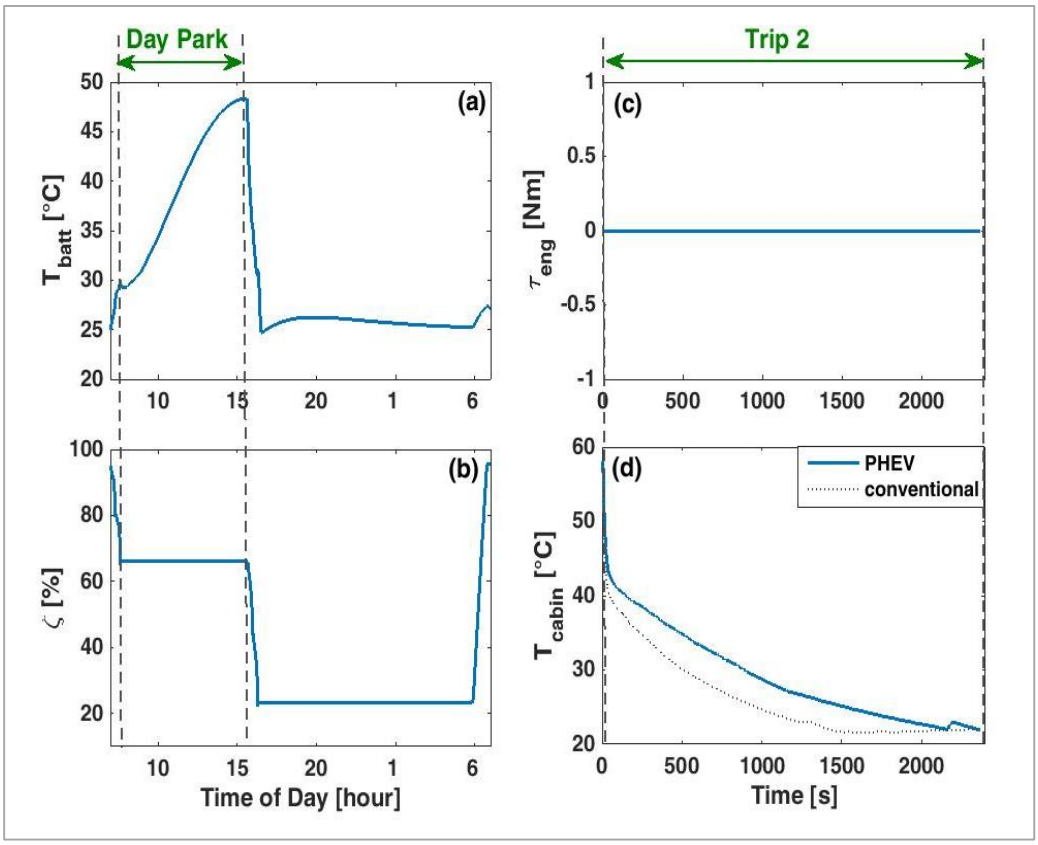

Figure 9-11. PHEV simulation results assuming baseline control strategies and operation in Phoenix summer with two daily trips on the NEDCx2

Since in duty cycle with NEDCx2 trips the temperature of the battery in Day Park does not directly lead to extra fuel consumption in trip 2, control of key-off cooling based on fuel economy alone (scenario 9-I) does not have a unique solution. However, key-off cooling can be aimed at mitigating the effect of the high battery temperature on other performance attributes, i.e. the battery lifetime and thermal comfort. The solutions of scenarios 9-II to 9-VI for this duty cycle are qualitatively similar to the solutions of the corresponding scenarios for the duty cycle with US06

trips discussed in Section 9.3. A complete explanation of these solutions are provided in Appendix 3. The main features of the solutions are as follows:

- In scenario 9-II, key-off cooling is applied to maintain a low battery temperature at the expense of high fuel consumption in Trip 2;

- In scenario 9-III, key-off cooling is applied to maintain a low battery temperature but it is limited by the excess battery charge;

- In scenario 9-IV, the battery is pre-cooled for Trip 2 is pre-cooled to the vicinity of 20°C before Trip 2 at the expense of high fuel consumption in Trip 2;

- In scenario 9-V, the battery is pre-cooled for Trip 2 but the energy allocated to pre-cooling is limited by the excess battery charge;

- In scenario 9-VI, a low battery temperature is maintained throughout Day Park while the battery is pre-cooled to the vicinity of 20°C before Trip 2.

The solutions of scenarios 9-II to 9-VI are marked on Figure 9-12 which shows the projection of the objective space of equation (9-6) onto the planes of the cost term pairs. The figure is achieved by simulating the model with random key-off cooling flag inputs, as well as by solving equation (9-6) with various weightings of the cost terms. The dotted lines specify the achievable boundaries, while the dashed lines approximate the pareto fronts that highlight the trade-off between the objectives.

Figure 9-12(a) shows that applying an intense key-off cooling in scenario 9-II leads to a significant reduction in the capacity loss compared to the baseline scenario, although this results in a high fuel consumption. A lower, but still considerable, reduction in capacity loss can be achieved without consuming fuel if key-off cooling is controlled as in scenario 9-III. The solutions of scenarios 9-II and 9-III lie on the pareto front which highlights the trade-off between lower capacity loss and lower fuel consumption.

Figure 9-12(b) illustrates the trade-off between minimising the thermal discomfort and minimising the fuel consumption. As the figure shows, pre-cooling in scenarios 9-IV and 9-V reduces the discomfort index compared to the baseline. The solution of scenario 9-IV lies on the pareto front and corresponds to the minimum discomfort index and the lowest fuel consumption required to achieve it. In scenario 9-V, the discomfort index is not minimised as pre-cooling was limited by the available excess charge.

Figure 9-12(b) also shows that the solution of scenario 9-V is 'suboptimal' (it does not lie on the pareto front). This suggests that more accurate tuning of the weightings of the objective terms (instead of λ=$\{0.5,0,0.5\}$) can improve the solution. Nevertheless, the current result sufficiently illustrates the limiting effect of the fuel consumption on reducing thermal discomfort.

Figure 9-12(c) shows that both the capacity loss and the discomfort index have been significantly reduced in scenario 9-VI. The pareto front is 'approximately vertical' along ΔC and 'approximately horizontal' along $I_{discomf}$, indicating that the trade-off between capacity loss and thermal discomfort is small when fuel consumption is not considered.

When all three objectives are of importance, one way of controlling key-off cooling is to limit the charge allocated to cooling to the available excess charge and prioritise battery lifetime over thermal comfort. The red squares in Figure 9-12 mark one such solution which is related to solving equation (9-6) with $\lambda = \{0.005, 0.8,0.195\}$. It can be seen that this solution corresponds to significant reductions in the capacity loss and the thermal discomfort without any negative effect on the fuel consumption. This solution is plotted in Figure 9-13. A part of the available excess charge is allocated to cooling around midday to avoid a high battery temperature, while further cooling is applied to pre-cooling the battery for Trip 2.

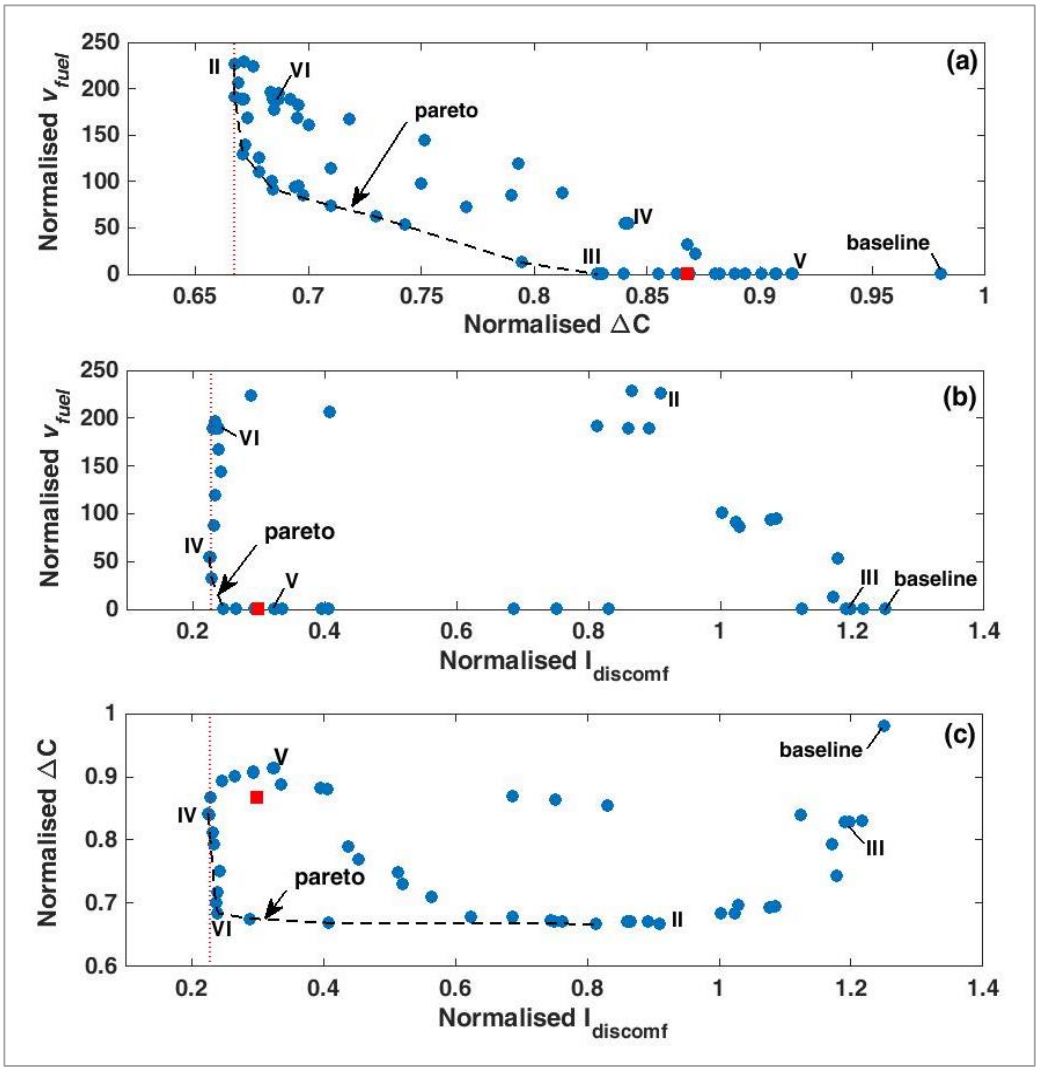

Figure 9-12 Objective planes of (9-6) NEDCx2 trips and (a) $\lambda_3 = 0$, (b) $\lambda_2 = 0$, and (c) $\lambda_3 = 0$.

Annotations: the dotted lines indicate the achievable boundary of the objective space. The red square marks the solution of (9-6) achieved with $\lambda = \{0.005, 0.8, 0.195\}$.

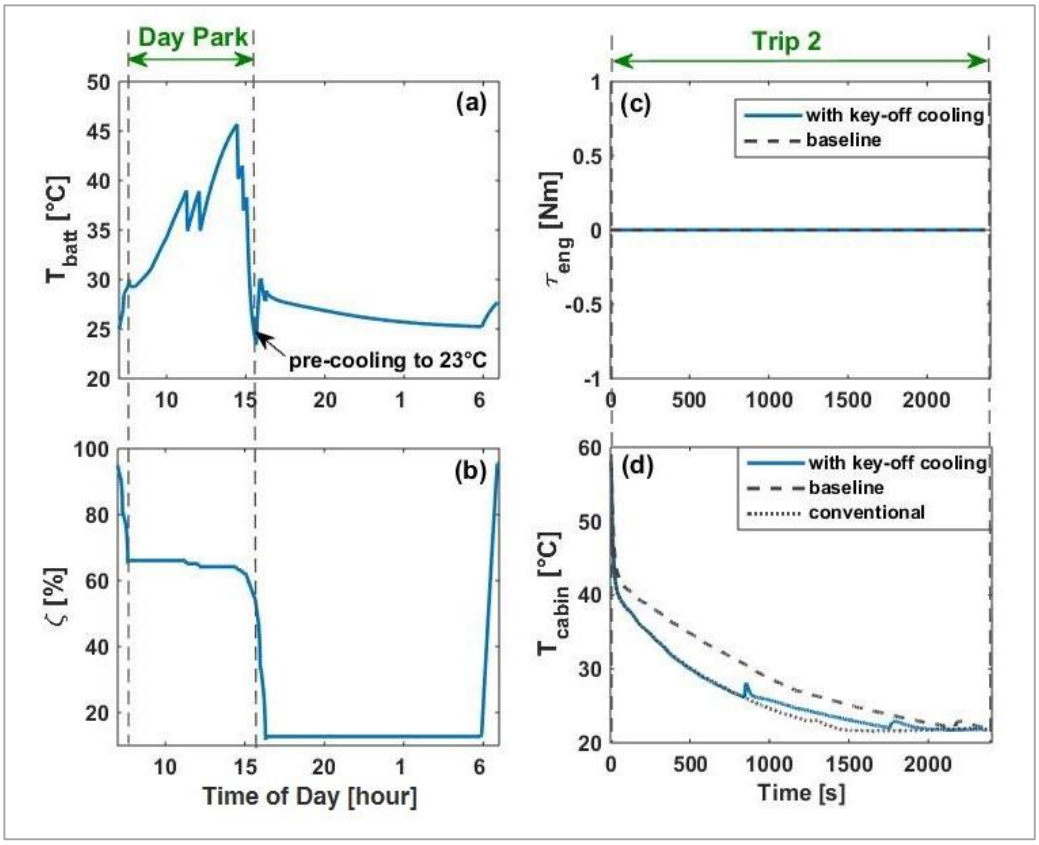

Figure 9-13. Solution of equation (9-6) with NEDCx2 trips and λ= {0.2, 0.7, 0.1}. (a) daily battery temperature, (b) daily SoC, (c) engine torque in Trip 2, and (d) cabin temperature in Trip 2

Table 9-3 summarises the key aspects of the solutions of equation (9-6) for scenarios 9-II to 9-VII. The results of the baseline scenario are included in table for reference. The evolution of the capacity loss, the fuel consumption and the thermal discomfort are consistent with the weightings applied. The following observations can be made from these results:

- The result of scenario 9-II indicates that regardless of the impact on fuel consumption, key-off cooling has the potential for improving the battery lifetime by 1.6 years.

- The result of scenario 9-III indicates that even when key-off cooling is limited by the availability of excess battery charge, it can significantly improve the battery lifetime.

- The result of scenario 9-IV indicates that pre-cooling the battery significantly reduces the thermal discomfort compared to the baseline scenario.

- In scenario 9-VII, although the energy available for key-off cooling was limited to the amount of the excess battery charge, controlling key-off cooling through solving equation (9-6) has led to noticeable benefits. Compared to the baseline scenario, the battery lifetime has improved from 7.2 years to 7.8 years, while the thermal discomfort index has reduced from 579 to 138.

In addition, comparing the solutions of scenario 9-VII for the duty cycles with NEDCx2 trips (Figure 9-13) and for the duty cycles with US06 trips (Figure 9-10) shows that the control of key-off cooling has been adapted to the lower excess charge on the duty cycle with NEDCx2 trips. This adaption has maximised the benefit of key-off cooling. Clearly, more improvements in battery lifetime and thermal comfort can be achieved with higher excess charge or with more fuel consumption. Nevertheless, it is evident from the results presented above that solving equation (9-6) produces the best possible key-off cooling strategy for the considered duty cycle

Table 9-3. Summary of results for different solutions of equation (9-6) for the duty cycle with NEDCx2 trips

Scenario	Solution	$[\overline{T}_{batt}]_{Dprk}$ [°C]	$[T_{batt,max}]_{Dprk}$ [°C]	$T_{batt}(t_{Dprk})$ [°C]	$\zeta(t_{Dprk})$ [%]	$[\Delta C]_{Dprk}$ [%]	$[\Delta C]_{Trp2}$ [%]	$[\Delta C]_{Nprk}$ [%]	EoL [years]*	v_{fuel} [L]	$I_{discomf}$ [-]
Baseline	--	39.7	48.3	48.3	66.1	1.09	0.25	0.80	7.2	0.0	579
9-I	Min v_{fuel}: $\lambda = \{1,0,0\}$	--	--	--	--	--	--	--	--	--	--
9-II	Min ΔC: $\lambda = \{0,1,0\}$	25.1	34.5	34.5	24.4	0.44	0.27	0.67	8.8	226.1	419
9-III	Min $v_{fuel} + \Delta C$: $\lambda = \{0.5,0.5,0\}$	33.6	45.5	45.5	56.2	0.82	0.26	0.69	8.0	0.0	549
9-IV	Min $I_{discomf}$: $\lambda = \{0,0,1\}$	34.3	46.5	21.4	45.2	0.88	0.23	0.68	7.9	54.9	104
9-V	Min $v_{fuel} + I_{discomf}$: $\lambda = \{0.5,0,0.5\}$	38.1	48.1	23.9	57.0	1.01	0.24	0.72	7.5	0.0	149
9-VI	Min $\Delta C + I_{discomf}$: $\lambda = \{0,0.5,0.5\}$	27.2	36.5	21.9	27.7	0.49	0.26	0.67	8.7	189.1	111
9-VII	Min $v_{fuel} + \Delta C + I_{discomf}$: $\lambda = \{0.005,0.8,0.195\}$	35.9	45.7	23.4	54.2	0.93	0.24	0.69	7.8	0	138

** Assumes the capacity loss in winter is equal to the baseline scenario*

9.5 Applicability of key-off cooling to other drive cycles

As the baseline simulation results in Section 7.2 indicated, the battery will be left with no excess charge if the daily trips of the vehicle are on either the WLTC or the Artemis. Therefore, when these drive cycles are assumed, any application of key-off battery cooling will compromise the fuel economy of the vehicle. Consequently, scenarios 9-I, 9-III and 9-V are not applicable to such circumstances. Where this compromise can be justified, i.e. when battery lifetime and thermal comfort attributes take priority over fuel economy, applying key-off cooling by solving equation (9-6) produces the optimum results. This is evident considering that assigning low weighting to fuel consumption in equation (9-6) eliminates the significance of the drive cycle. Therefore, the solutions of scenario 9-II, 9-IV, 9-VI, and 9-VII are qualitatively similar to the solutions achieved in previous sections for the duty cycles with US06 and NEDCx2 trips, so, they will not be shown here in the interest of brevity.

Understanding the effectiveness of key-off cooling for improving battery lifetime and thermal comfort when the duty cycle includes WLTC or Artemis trips will be illuminating. To achieve this, the key aspects of the solutions of equation (9-6) for scenario 9-II (best achievable battery lifetime, $\lambda = \{0,1,0\}$) and scenario 9-IV (best achievable thermal comfort, $\lambda = \{0,0,1\}$) for these duty cycles are given in Table 9-4 to Table 9-6.

Table 9-4 compares the battery lifetime between the baseline scenario and scenario 9-II for different drive cycle assumptions. It can be seen that in all cases key-off cooling can improve the battery lifetime, although the improvements vary from 35% in case of US06 trips to only 8% in case of Artemis trips. There are two main reasons behind this variability. First, since some of the improvement in battery lifetime enabled by key-off cooling is due to reduction of SoC, the benefit of key-off cooling is lower when the battery is stored at a lower SoC in Day Park. With Artemis trips, the battery is left with approximately 33% SoC in Day Park (compared to 75% with US06 trips), so key-off cooling can enable little benefit

through depleting the battery. Second, when the battery is stored at low SoC levels, its sensitivity to elevated temperatures is lower, therefore, so is the benefit of key-off cooling. So the trips that leave the battery at lower SoC reduce the potential benefit of cooling for battery lifetime.

Table 9-4. Effect of trip drive cycle on the effectiveness of key-off battery cooling for improving battery lifetime

Drive Cycle	Baseline EoL [years]	Scenario 9-II EoL [years]	Improvement [%]
WLTC	7.3	8.8	20
US06	6.3	8.5	35
Artemis	7.4	8.0	8
NEDCx2	7.2	8.8	22

Table 9-5 gives more details about the battery temperature and SoC in Day Park for solutions of scenario 9-II with different trip assumptions. Comparing the average and maximum values of battery temperature suggests that key-off cooling has been applied less for the case of Artemis trips.

Table 9-5. Comparison of battery temperature and SoC in Day Park for scenarios 9-II with different drive cycle assumptions

Drive Cycle	Scenario	$\bar{T}_{batt}$ [°C]	$T_{batt,max}$ [°C]	$T_{batt,final}$ [°C]	Initial ζ [%]	$\Delta\zeta$ [%]
WLTC	**9-II:** $\boldsymbol{\lambda = \{0, 1, 0\}}$	26.2	37.4	33.7	58	0.37
Artemis	**9-II:** $\boldsymbol{\lambda = \{0, 1, 0\}}$	31.3	39.3	39.3	33	0.16
US06	**9-II:** $\boldsymbol{\lambda = \{0, 1, 0\}}$	23.8	29.5	25.5	75	0.50
NEDCx2	**9-II:** $\boldsymbol{\lambda = \{0, 1, 0\}}$	25.1	34.5	34.5	66	0.42

Given the variation in their duration, the effect of the drive cycles on the benefit of key-off cooling (pre-cooling) for thermal comfort in Trip 2 cannot be compared based on $I_{discomf}$. Instead, this comparison can be based on the duration of time for which the battery cooling load in Trip 2 can be shifted by pre-cooling (duration of time for which $I_{discomf}$ remains zero in Trip 2). These durations are shown in Table 9-6 for scenario 9-IV with different drive cycle assumptions. In all cases,

the battery is pre-cooled to approximately 21°C. In case of the US06, pre-cooling shifts the cooling load of the battery by 6.4 minutes as seen in Section 9.3.4, while in the case of NEDCx2, WLTC and the Artemis, the cooling loads are shifted by 16.7 minutes, 13.5 minutes and 10.7 minutes, respectively. Since these durations are shorter than the length of the respective drive cycle, they are not affected by it and can therefore be compared. The dominant factor that leads to the above variation is the difference in the battery internal heat generation over different drive cycles. The internal heat generation is highest over the US06 (as seen in Table 6-6), so pre-cooling the battery is least effective over this drive cycle. Pre-cooling is most effective when with NEDCx2 trips which is the mildest drive cycle. Other drive cycles can be compared in a similar manner.

Table 9-6. Effect of trip drive cycle on the effectiveness of battery pre-cooling for improving thermal comfort

Drive Cycle	Duration of zero $I_{discomf}$ [min]
WLTC	13.5
US06	6.4
Artemis	10.7
NEDCx2	16.7

9.6 Summary

In this chapter, the problem of optimal control of key-off battery cooling was explored for the complete vehicle duty cycles with US06 and NEDCx2 trips, given the available excess battery charge on these duty cycles. In each case, different scenarios were considered to analyse the effect of prioritising individual and combinations of the objectives on the solution of the optimal control problem. This analysis illustrated the significance of defining key-off cooling as an optimal control problem in view of complete vehicle duty cycles, as proposed in this work. The battery has no excess charge for the duty cycles with WLTC and Artemis trips,

so these duty cycles were not included in the analysis. However, the effectiveness of key-off cooling for improving the battery lifetime and thermal comfort attributes was compared for all duty cycles.

It was shown that key-off cooling can improve the battery lifetime, although the potential for improvement was shown to depend on the assumed duty cycle. Over the duty cycles with US06 and NEDCx2 trips, key-off cooling improved the battery lifetime by more than 35% (from 6.3 years to 8.5 years) and 22% (from 7.2 years to 8.8 years), respectively. Key-off cooling was also shown to noticeably improve the battery lifetime over the duty cycle with WLTC trips (20% improvement was achieved), while the improvement was limited to 8% over the duty cycle with Artemis trips. This variation in the effectiveness of key-off cooling in improving battery lifetime was primarily associated to the effect of storage SoC on the sensitivity of the battery to elevated temperature.

Key-off cooling was also shown to reduce the thermal discomfort during Trip 2, as it enables pre-cooling of the battery for Trip 2, thus postponing key-on cooling in the trip. It was shown however that the potential for reducing the thermal discomfort through pre-cooling depends on the assumed duty cycle, as the internal heat generation of the battery can negate the benefits of pre-cooling. Pre-cooling was shown to be most effective on the duty cycle with NEDCx2 trips, where a thermal discomfort index of zero was maintained for the initial 13.5 minutes of Trip 2. On the duty cycle with US06 trips, pre-cooling is least effective as it can only postpone key-on cooling in Trip 2 by approximately 6.5 minutes. Thus the effectiveness of pre-cooling seems to depend on the aggressiveness of the drive cycle.

It was shown that for the duty cycle with US06 trips, key-off cooling improves the fuel economy by ensuring that the battery is not overheated at the start of Trip 2. Generally, the battery charge that can be allocated to key-off cooling without compromising the fuel economy of the vehicle depends on the duty cycle.

Over the duty cycle with US06 trips which leaves more than 30% excess battery charge, the optimal control of key-off cooling can simultaneously improve the battery lifetime from 6.3 years to 8 years, reduce the thermal discomfort from 57 to 6, and reduce the seasonal fuel consumption from 108 L to 83 L.

Over the duty cycle with NEDCx2 trips, the battery has more than 10% excess charge. The solutions of scenario 9-II, 9-IV and 9-VI for this duty cycle were qualitatively similar to the solution of the corresponding scenarios for the duty cycle with US06 trips. It was shown that through optimal control of key-off cooling, this charge can be used to either improve the battery lifetime from 7.3 years to 8 years, or reduce the thermal discomfort index from 579 to 111. It was also shown that optimal control enabled trade-off solutions, including one in which the battery lifetime was improved to 7.8 years and the thermal discomfort index was reduced to 138.

When the duty cycle leaves the battery with no excess charge, the solutions of scenario 9-II, 9-IV and 9-VI will be qualitatively similar to the solutions achieved for the duty cycles that have excess battery charge. This is because the zero weighting assigned to the fuel consumption in these scenarios eliminates the significance of the drive cycle. When fuel consumption is included in the optimisation cost function (scenarios 9-III, 9-V and 9-VII), key-off cooling will not be applied to avoid extra fuel consumption, hence the solution will be identical to the corresponding baseline scenario.

The analyses presented in this chapter illustrates that irrespective of the vehicle duty cycle, the method proposed for controlling the key-off cooling produces the optimum results. For all duty cycles, the solution of the optimisation problem is consistent with the vehicle performance attributes included in the optimisation, and any trade-off between the performance attributes can be explained. Where key-off cooling has the potential for improving a performance attribute, the proposed method guarantees maximum improvement.

CHAPTER 10 INTEGRATING KEY-OFF COOLING WITH PARTIAL CHARGING

Introduction

As discussed in Chapter 3, when the vehicle duty cycle leaves the battery with excess charge, partial charging can help maintain a lower battery SoC throughout the day; potentially improving the battery lifetime. In Chapter 9, the battery was assumed to be charged fully, every day. In this chapter, optimised partial charging is considered in addition to key-off cooling. Since the ability to perform key-off cooling depends on the available battery charge, optimisation of key-off cooling and partial charging are integrated to maximise their benefit for the battery. Therefore, in Section 10.1, the formulation developed in Chapter 9 for optimal control of key-off cooling is expanded by integrating partial charging. An algorithm is developed that determines the optimum combination of key-off cooling and partial charging strategy based on the duty cycle. Four scenarios are then considered for solving the problem, based on the relevant combinations of the vehicle performance attributes. The problem is then solved for the vehicle duty cycles with US06 and NEDCx2 trips, in Sections 10.2 and 10.3, respectively. The duty cycles with WLTC and Artemis trips that leave no excess battery charge are not discussed in this chapter as they are not suitable for partial charging. The discussions are summarised in Section 10.4.

10.1 Integrated control of partial charging and key-off cooling

Partial charging is concerned with controlling the maximum SoC (ζ_{max}) to which the battery is charged in Night Park, considering the requirements of the vehicle duty cycle. Assuming that the duty cycle starts at $t = 0$, the vehicle starts and ends its duty cycle with ζ_{max}, that is:

$$\zeta_{max} = \zeta(t = 0) = \zeta(t = t_{NPrk}). \quad (10\text{-}1)$$

The capacity loss in Day Park is a function of battery temperature and SoC, which are affected by both key-off cooling and partial charging. In addition, partial charging affects the energy available to perform key-off cooling in Day Park. Therefore, in order to ensure maximum benefit for the battery, key-off cooling and partial charging should be jointly optimised. As in the case of optimising key-off cooling alone, this can be achieved through solving a minimisation of the following form

$$\min J = \min\left(\lambda_1 v_{fuel} + \lambda_2 \Delta C + \lambda_3 I_{discomf}\right). \quad (10\text{-}2)$$

The above minimisation should be solved in view of the complete duty cycle. The method used to achieve this is outlined below and shown in Figure 10-1 which also compares the scope of the analyses in this chapter with those in Chapters 8 and 9.

J in equation (10-2) can be expanded as

$$\begin{aligned} J = {} & \lambda_1 \left[v_{fuel}\right]_{trp1} + \lambda_2 \left[\Delta C\right]_{trp1} \\ & + \lambda_2 \left[\Delta C\right]_{Dprk} \\ & + \lambda_1 \left[v_{fuel}\right]_{trp2} + \lambda_2 \left[\Delta C\right]_{trp2} + \lambda_3 I_{discomf} \\ & + \lambda_2 \left[\Delta C\right]_{Nprk}. \end{aligned} \quad (10\text{-}3)$$

Among the terms of (10-3), fuel consumption and capacity loss in Trip 1 are only affected by ζ_{max}:

$$\left[v_{fuel}, \Delta C\right]_{Trp1} \propto \zeta_{max}. \quad (10\text{-}4)$$

Other terms of (10-3) are affected both by the level of charge and the control of key-off cooling.

In combining partial charging and key-off cooling, the control of partial charging takes precedence over the control of key-off cooling. In other words, when key-off cooling is being applied, the level of battery charge at the start (and the end) of the duty cycle is known (so is the charge remaining in the battery at the start of

Day Park). Therefore, the terms of (10-3) that are related to Trip 2 and Night Park constitute the terminal cost for the problem of optimal key-off cooling control. As a result, partial charging and key-off cooling can be optimised through solving the following minimisation

$$\min_{u^*,\zeta^*_{max}} J = \min\left(\lambda_1[v_{fuel}]_{Trp1} + \lambda_2[\Delta C]_{Trp1} + \lambda_2\sum_{k=0}^{N-1}\Delta C_k\,(x_{bk},u_k) + h_N\right), \tag{10-5}$$

where ζ^*_{max} denotes the optimum level of (maximum) charge. The term h_N has a similar form to equation (9-7) but here, the cycling component of the capacity loss in Night Park is a function of level of charge

$$[\Delta C]_{Nprk} = \left[\Delta C_{stor}\left(x_v(t_{Dprk})\right)\right] + \left[\Delta C_{cyc}\left(\zeta_{max},\ x_v(t_{Dprk})\right)\right], \tag{10-6}$$

leading to

$$\begin{aligned} h_N = {} & \lambda_1\left[v_{fuel}\left(x_v(t_{Dprk})\right)\right]_{Trp2} + \lambda_2\left[\Delta C\left(x_v(t_{Dprk})\right)\right]_{Trp2} + \\ & \lambda_3\, I_{discomf}\left(x_v(t_{Dprk})\right) + \lambda_2\left[\Delta C_{stor}\left(x_v(t_{Dprk})\right)\right] + \\ & \lambda_2\left[\Delta C_{cyc}\left(\zeta_{max}, x_v(t_{Dprk})\right)\right]. \end{aligned} \tag{10-7}$$

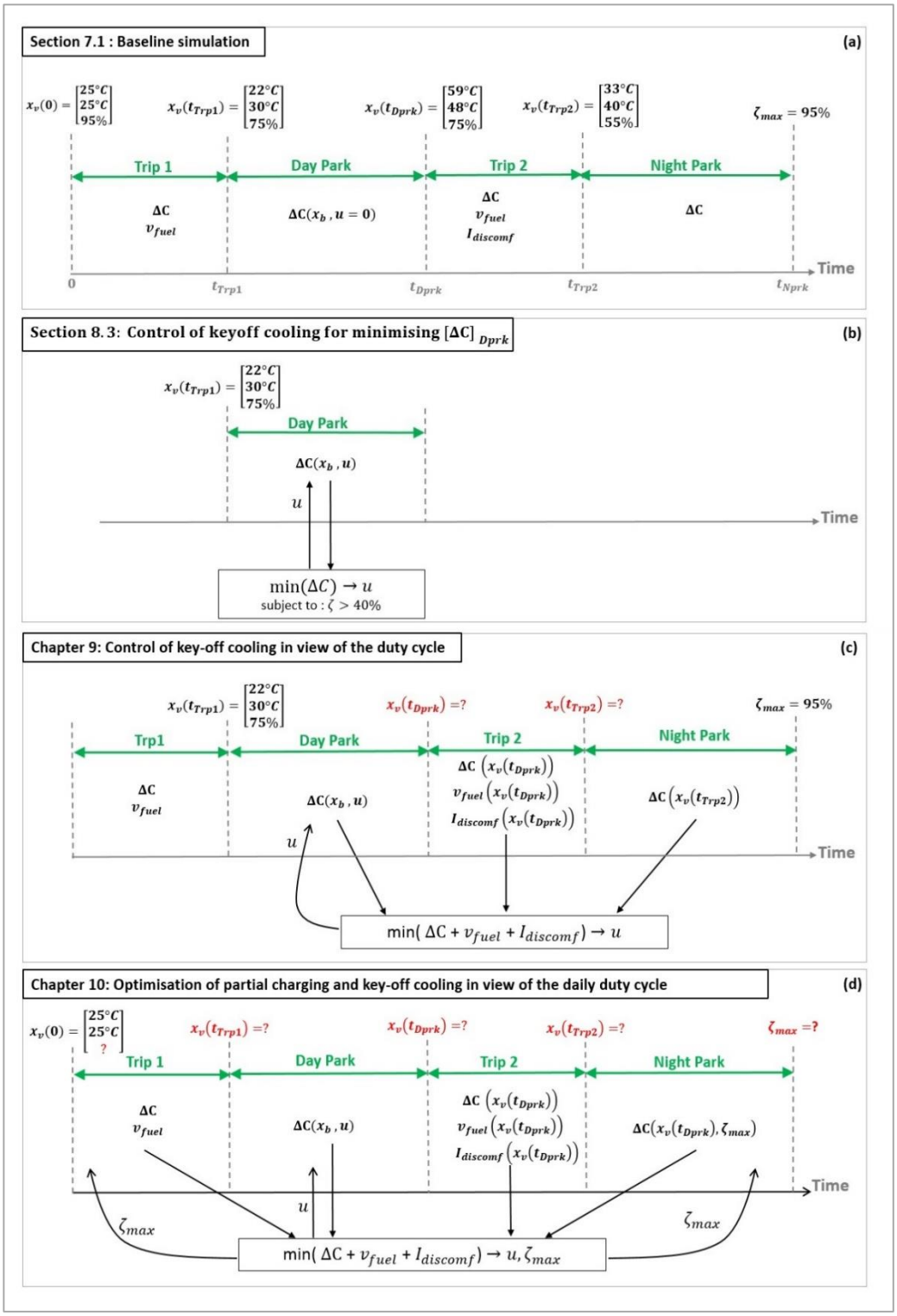

Figure 10-1. The scope of the analyses in (a) Chapter 7, (b) Chapter 8, (c) Chapter 9, and (d) this chapter. The vehicle state values shown are related to the duty cycle with US06 trips.

For every choice of ζ_{max}, the minimisation defined by equation (10-5) reduces to the optimisation of key-off cooling in Day Park defined by equations (9-6) and

(9-7), which can be solved as explained in Chapter 9. Therefore, by iterating over ζ_{max}, the combination of the level of charge and key-off cooling that solves equation (10-5) can be determined. This requires a single calculation of the 'arc term' of equation (10-5) since calculation of it is independent of the initial conditions. However, in every iteration, the forward solution of DP should be evaluated based on the initial and terminal conditions relevant to the iteration.

To find ζ^*_{max}, the design space of ζ_{max} can be searched exhaustively, or an optimisation algorithm with a strong search method can be used to accelerate the process. Here, the Simulated Annealing (SA) algorithm is used for searching the design space of ζ_{max}, while in every iteration (i.e. every choice of ζ_{max}), DP is used to solve optimisation of key-off cooling in Day Park defined by equations (9-6) as achieved previously in Chapter 9. The process of combining the SA and DP solutions, which is illustrated in Figure 10-2, includes the following steps:

Step 1: capacity loss in Day Park is evaluated throughout the state grid defined in Section 8.1 with different cooling flag, to determine the arc term in equation (8-5), i.e. the term $\sum_{k=0}^{N} \Delta C_k\ (x_{bk},\ u_k)$,

Step 2: Trip 2 is simulated from all possible $x_v(t_{Dprk})$ as initial conditions. Fuel consumption, capacity loss and discomfort index of Trip 2 are mapped to $x_v(t_{Dprk})$, as done previously in Section 9.1. Also, all possible states of the vehicle at the end of Trip 2, $x_v(t_{trp2})$, are determined.

Step 3: a value is chosen for ζ_{max} (SA algorithm search)

Step 4-1: with initial SoC equal to ζ_{max} and assuming the vehicle temperature is 25°C, Trip 1 is simulated to calculate the associated fuel consumption and capacity loss, i.e. $\left[v_{fuel}, \Delta C\right]_{Trp1}$. Also the state of the vehicle at the end of Trip 1, i.e. $x_v(t_{Trp1})$ is determined,

Step 4-2: knowing ζ_{max}, Night Park is simulated with initial conditions determined from simulating Trip 2 in step 2, charging the battery to ζ_{max}. The just-in-time charging strategy is applied. $[\Delta C]_{Nprk}$ is calculated.

Step 5: h_N in equation (10-7) is evaluated from results of step 4-2 and step 2,

Step 6: from the terminal cost h_N and the arc cost of key-off cooling (given by step 1), key-off cooling is optimised knowing the initial state of the vehicle in Day Park ($x_v(t_{Trp1})$ determined in step 4-1) and the remaining battery charge. This step is equivalent to solving (9-6) by DP for the current ζ_{max}

Step 7: from the result of steps 6 and 4-1, equation (10-5) is evaluated.

Steps 3 to 7 are then repeated until u^* and ζ^*_{max} are found.

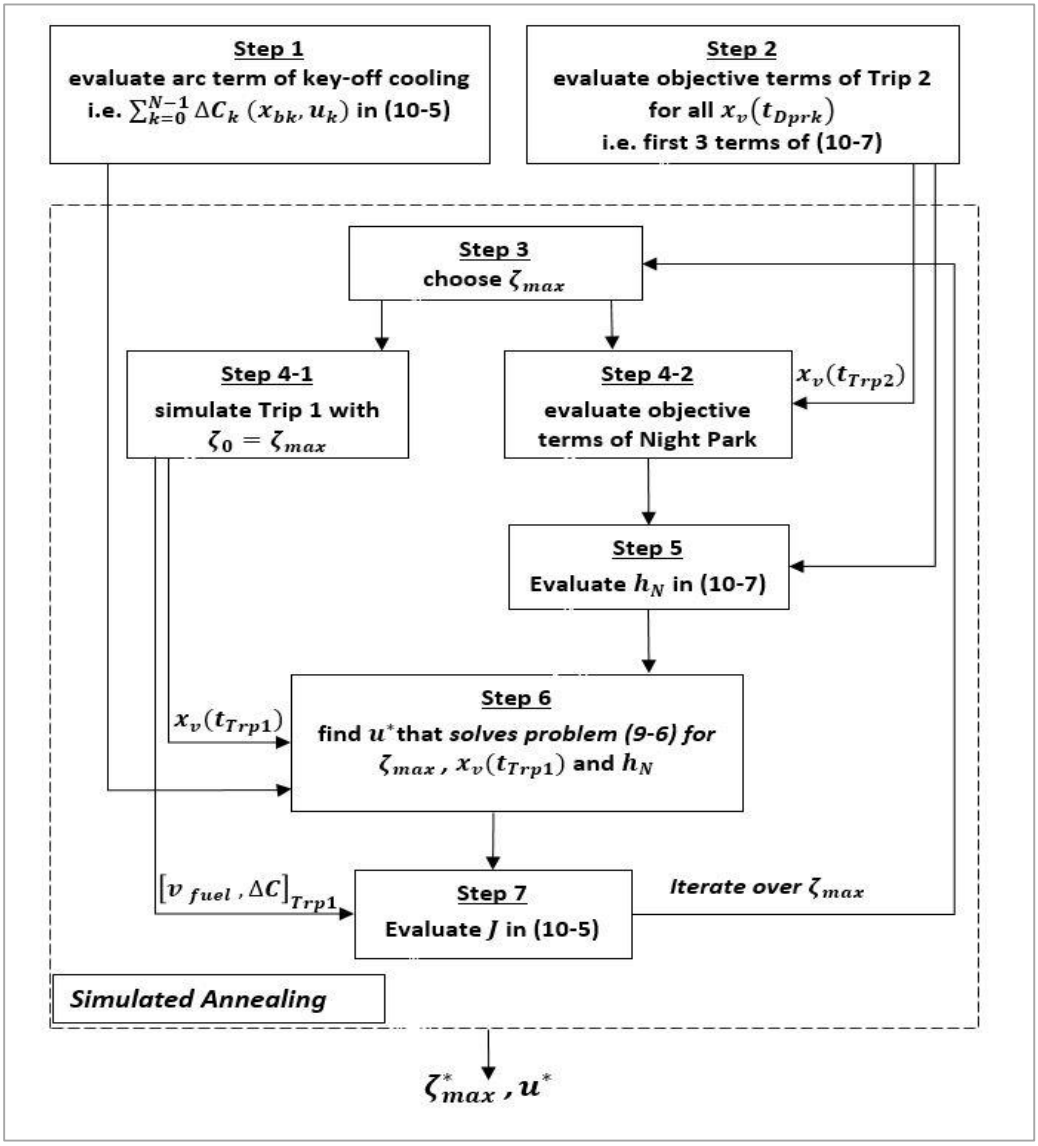

Figure 10-2. Flow chart of the process used for solving equation (10-5)

The SA algorithm is initialised at the default ζ_{max} value of 95%. Also, to achieve rapid convergence, the level of charge constrained is between 40% and 95% SoC ($40\% \leq \zeta_{max} \leq 95\%$). This assumption also ensures that the operating mode of the vehicle in Trip 1 is not affected by partial charging.

The solution of the above problem is discussed in Sections 10.2 and 10.3 for the scenarios defined in Table 10-1. These scenarios correspond to those previously defined in Chapter 9 (Table 9-1) for controlling key-off cooling. Since partial charging is aimed at improving battery lifetime, only the scenarios that include battery lifetime within the cost function are relevant. For scenario 10-VII in which all three objectives are included, the weighting can be tuned based on the preference of the designer to enable a trade-off between the objectives. Here, by solving the minimisation problem for the other scenarios defined in Table 10-1 and for a number of randomly selected weightings, the objective space of the minimisation is constructed, from which an appropriate solution for scenario 10-VII is chosen. The weighting leading to the chosen solution is also quoted.

Table 10-1. Scenarios for integration of partial charging and key-off cooling

Scenario	Attribute			Weighting $\boldsymbol{\lambda = \{\lambda_1, \lambda_2, \lambda_3\}}$
	Fuel Economy	Battery Lifetime	Thermal Comfort	
10-II	✗	✓	✗	$\lambda = \{0, 1, 0\}$
10-III	✓	✓	✗	$\lambda = \{0.5, 0.5, 0\}$
10-VI	✗	✓	✓	$\lambda = \{0,0.5,0.5\}$
10-VII	✓	✓	✓	To be defined

10.2 Solution for the duty cycle with US06 Trips

In this section, the problem defined in Section 10.1 is solved for the duty cycle with US06 trips. In Sections 10.2.1 to 10.2.4, the solutions of the scenarios defined in Table 10-1 are qualitatively analysed while Section 10.2.5 provides more detailed analysis of the solutions.

10.2.1 Scenario 10-II: Control of partial charging and key-off cooling for improving battery lifetime

Consider the scenario in which battery lifetime is the only attribute of interest in controlling partial charging and key-off cooling. In this scenario a weighting of $\lambda = \{0, 1, 0\}$ is applied to (10-5).

Figure 10-3 shows the progress of the SA algorithm. The algorithm converges to $\zeta_{max} = 41\%$ after 77 iterations. Figure 10-3(a) shows the values of ζ_{max} for each iteration, which suggests that the search space is thoroughly sampled. Figure 10-3(b) shows the best achieved value of normalised J which is first attained in the 23rd iteration (the iterations continue until the convergence criteria of the algorithm are met). Given that zero weights have been assigned to fuel consumption and thermal discomfort ($\lambda = \{0, 1, 0\}$), the value of J represents the normalised total capacity loss. Therefore, Figure 10-3(b) implies that partial charging reduces the capacity loss, as expected.

For every chosen ζ_{max}, the algorithm determines the key-off cooling control that reduces, as much as possible, the total capacity loss in Day Park and subsequent parts of the duty cycle (other performance attributes are not included). Iterations continue until the combination of partial charge and key-off cooling control that minimise J are found. For iterations 1, 15, 26, 37, and 44 (with respective ζ_{max} of 95%, 81%, 70%, 51%, and 41%,) the breakdown of normalized components of J are compared with the baseline scenario (full charging and no key-off cooling) in Figure 10-3(c). Also, Figure 10-3(d) gives the histogram of battery temperature in Day Park for these iterations and the baseline. Note that iterations 44 and 23 are equivalent.

In iteration 1, the battery is fully charged, therefore the results are similar to those achieved in Section 9.3.2 (shown in Figure 9-5). The histogram of battery temperature in Day Park in Figure 10-3(d) indicates that key-off cooling has mostly maintained the battery below 30°C. Figure 10-3(c) shows that the change in the performance attributes are consistent with the descriptions given in Section 9.3.2, i.e. the capacity loss in Day Park and Night Park decreases, the discomfort

in Trip 2 reduces, and the fuel consumption in Trip 2 increases compared to the baseline.

In the iterations in which the battery is only partially charged (iterations 15, 26, 37, and 44), less energy is available for key-off cooling, therefore, the temperature histogram in Figure 10-3(d) shows higher temperature during Day Park. Even when the battery is partially charged, key-off cooling is still applied as much as possible, given that reducing capacity loss is the only objective. Hence, in iteration 15, fuel consumption significantly increases in Trip 2 compared to iteration 1. Also, thermal discomfort increases in Trip 2 consistent with higher battery temperature in Day Park. Similar trends can be observed for iteration 26.

In iteration 37, despite less key-off cooling and consequently higher temperature compared to iteration 1 (see the temperature histogram in Figure 10-3(d)), Day Park capacity loss is lower, due to lower SoC. In addition, since the combination of key-off cooling and driving the trips completely deplete the battery in all iterations (as discussed previously in Section 9.3.2 and shown in Figure 9-5), the capacity loss in Night Park decreases as the level of charge decreases, due to less cycling.

As Figure 10-3(a) shows, the algorithm sweeps through a wide range of solutions, covering all meaningful combinations of partial charging and key-off cooling. The convergence of the solution to $\zeta_{max}^{*} = 41\%$ (which enables limited key-off cooling compared to scenario 9-II in Section 9.3.2) suggests that maintaining a low SoC throughout the day is more beneficial to the battery than maintaining a low temperature.

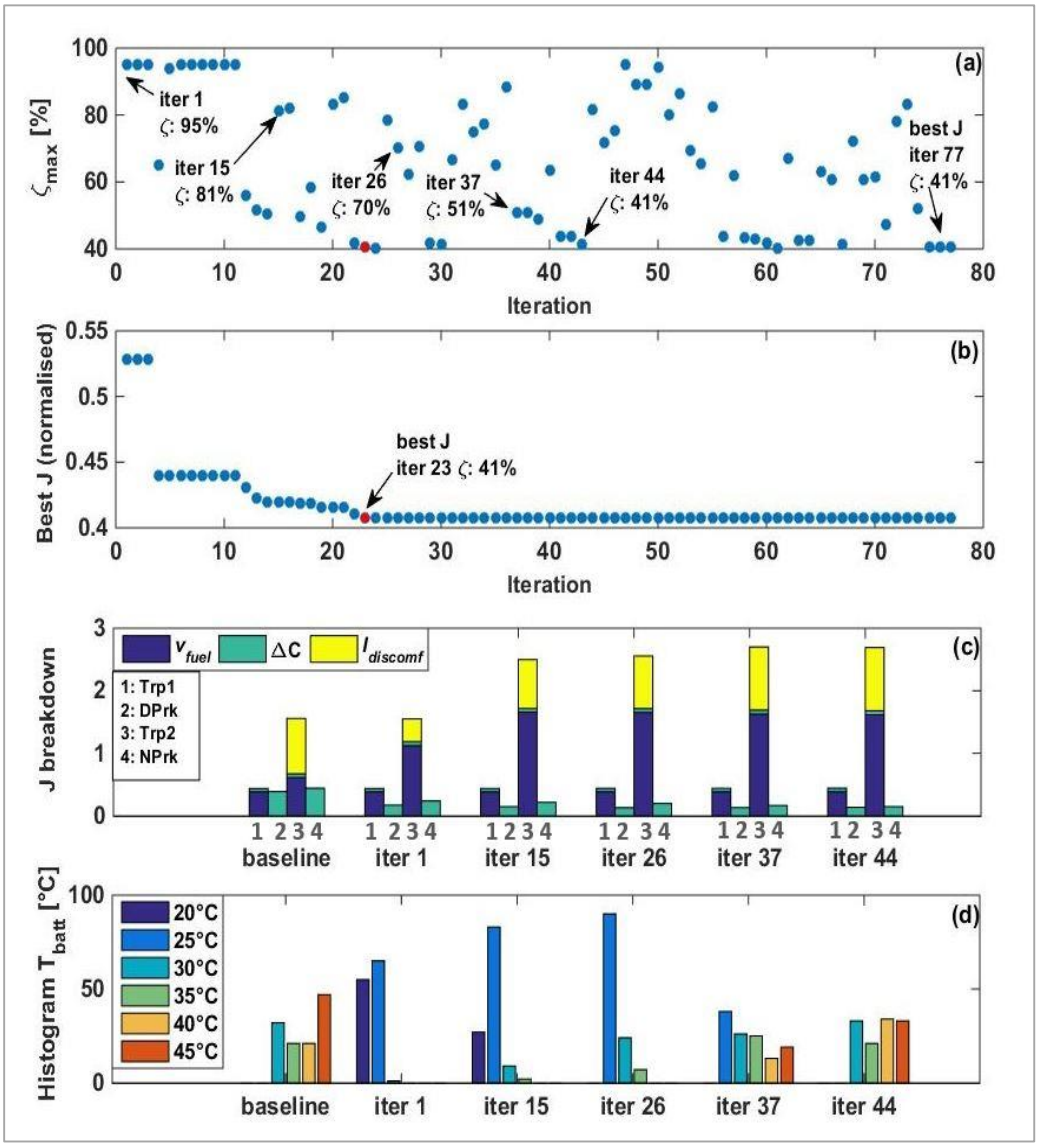

Figure 10-3. Progress of the integrated partial charging and key-off cooling optimisation- The figure is relate to $\lambda = \{0, 1, 0\}$. (a) ζ_{max} in iterations of the algorithm, (b) function value for each iteration (c) phase-by-phase breakdown of cost terms for 6 important iterations, and (d) histogram of battery temperature in Day Park,

In Figure 10-4, the model is simulated with the optimum level of charge and key-off cooling (these results are equivalent to iterations 77 and 44 in Figure 10-3). Figure 10-4(a) shows that key-off cooling is only applied at about midday (for two time intervals or 8 minutes), slightly reducing the mean and maximum temperature of the battery in Day Park, compared to the baseline case. According to Figure 10-4(b), charging the battery to 41% SoC leaves the battery with approximately 18% SoC in Day Park. 2% of the remaining SoC is allocated to key-off cooling while the rest is used in Trip 2, leaving the battery fully depleted in Night Park. Figure 10-4(c) shows the lack of sufficient battery charge forces the vehicle to

operate in CS mode in a significant part of Trip 2. Figure 10-4(d) shows that the effect of key-off battery cooling on cabin temperature in Trip 2 has been negligible.

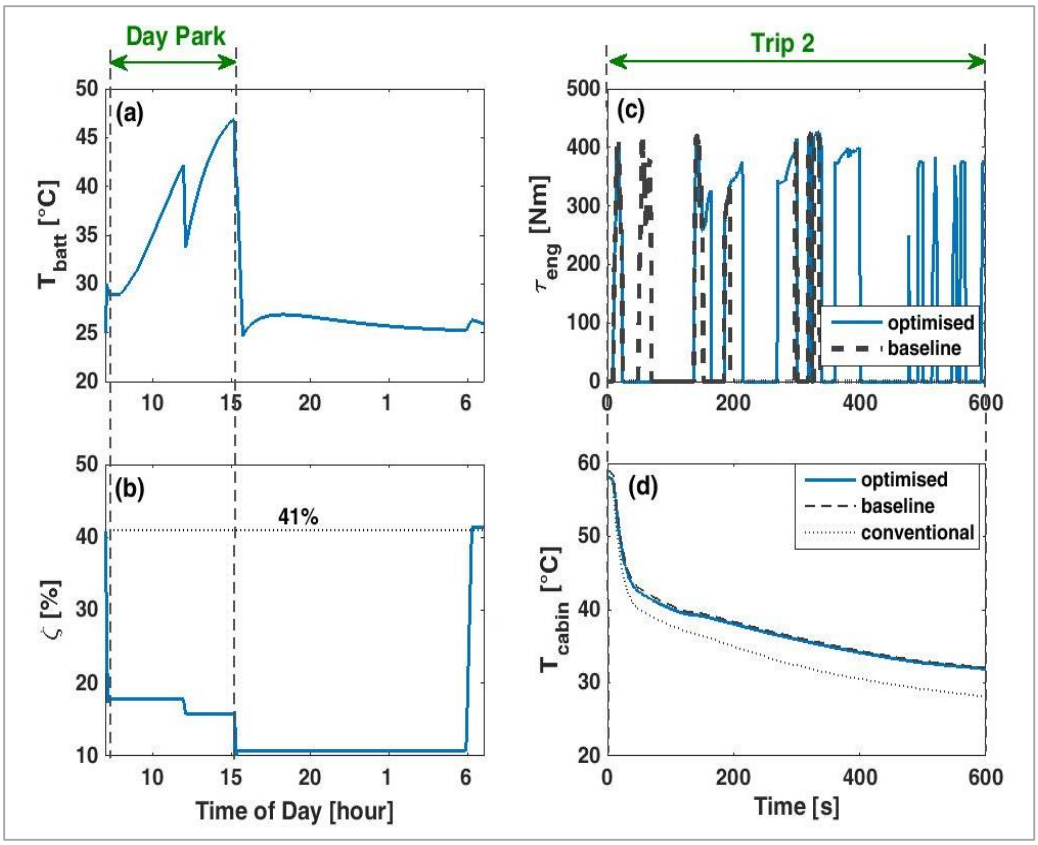

Figure 10-4. Solution of equation (10-5) for the duty cycle with US06 trips and λ={0,1,0}. (a) daily battery temperature, (b) daily SoC , (c) engine torque in Trip 2, and (d) cabin temperature in Trip 2

10.2.2 Scenario 10-III: Control of partial charging and key-off cooling based on the trade-off between fuel economy and battery lifetime

Figure 10-5 shows the result of solving equation (10-5) with λ={0.5,0.5,0}, which enables consideration of the fuel economy and the battery lifetime. To avoid any impact on fuel consumption, the window of partial charging should be limited to the excess charge of the battery for the considered duty cycle. In other words, the battery should be at least charged to approximately 59%, for the duty cycle with US06 trips.

Compared to scenario 10-II, the battery is charged more, to approximately 68%. This level of charge is not only sufficient to minimise fuel consumption in Trip 2, it also enables key-off cooling, for which approximately 9% of battery SoC is used. As a result, the battery temperature is maintained below 40°C in Day Park, suggesting reduced capacity loss, while improving the electric traction in Trip 2. Since the battery temperature is allowed to rise before the start of Trip 2, improvements in the cabin temperature are negligible.

The importance of key-off cooling can be realised from this solution. Whilst charging the battery to 59% SoC was sufficient to minimise the fuel consumption (as can be inferred from the result of scenario 9-II in Section 9.3.2) the battery is charged 9% more to support key-off cooling, rather than charging it as little as possible.

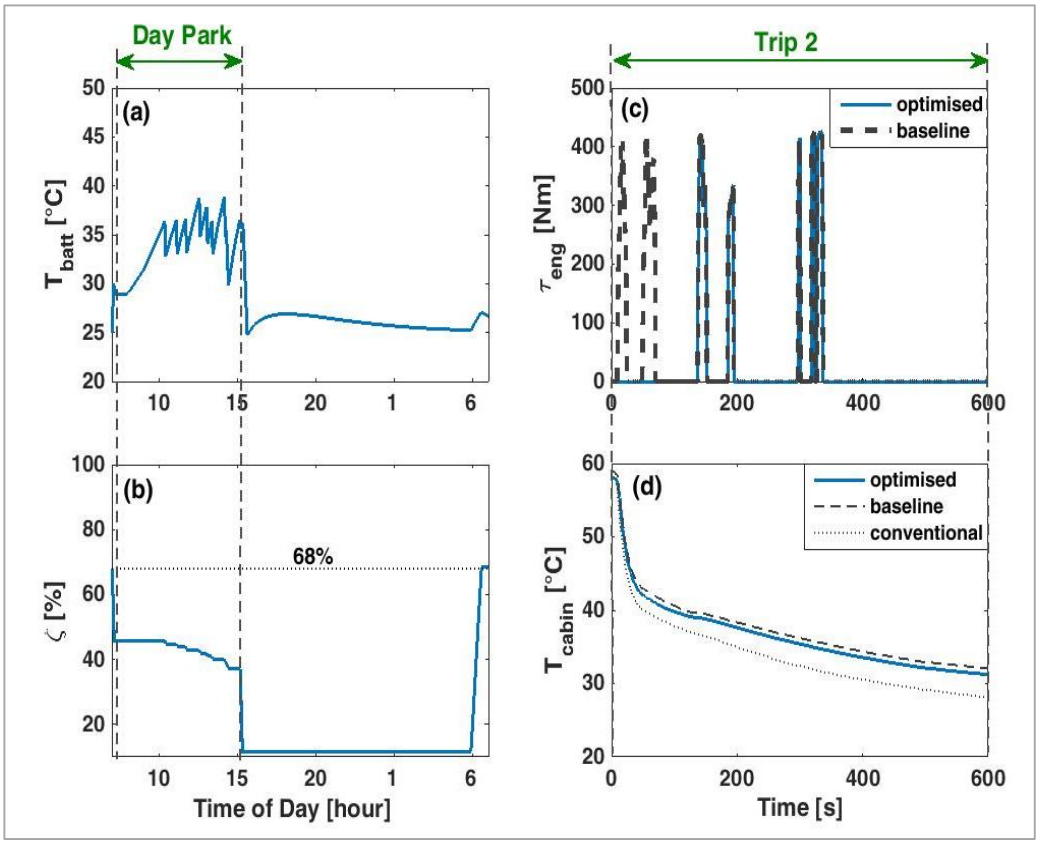

Figure 10-5. Solution of equation (10-5) for the duty cycle with US06 trips and λ={0.5,0.5,0}. (a) daily battery temperature, (b) daily SoC , (c) engine torque in Trip 2, and (d) cabin temperature in Trip 2

10.2.3 Scenario 10-VI: Control of partial charging and key-off cooling based on battery lifetime and thermal comfort

Considering thermal comfort in addition to battery lifetime in solving equation (10-5) leads to different results. Figure 10-6 shows the results for the scenario when these objectives are equally weighted $\lambda = \{0, 0.5, 0.5$. Here, the battery has been charged to approximately 56%. This has enabled pre-cooling the battery for Trip 2 which has consumed approximately 15% of the battery charge. Pre-cooling has helped the cabin to cool at same rate as in the conventional vehicle for 400 seconds. The vehicle operates in EV mode in the first 100 seconds of Trip 2, since the battery is pre-cooled and its SoC is at 18% before the start of the trip (approximately 5% above the threshold of CS operation). This has been preferred over further reduction of the initial battery charge, or allocation of this extra charge to key-off cooling and maintaining a lower battery temperature in Day Park.

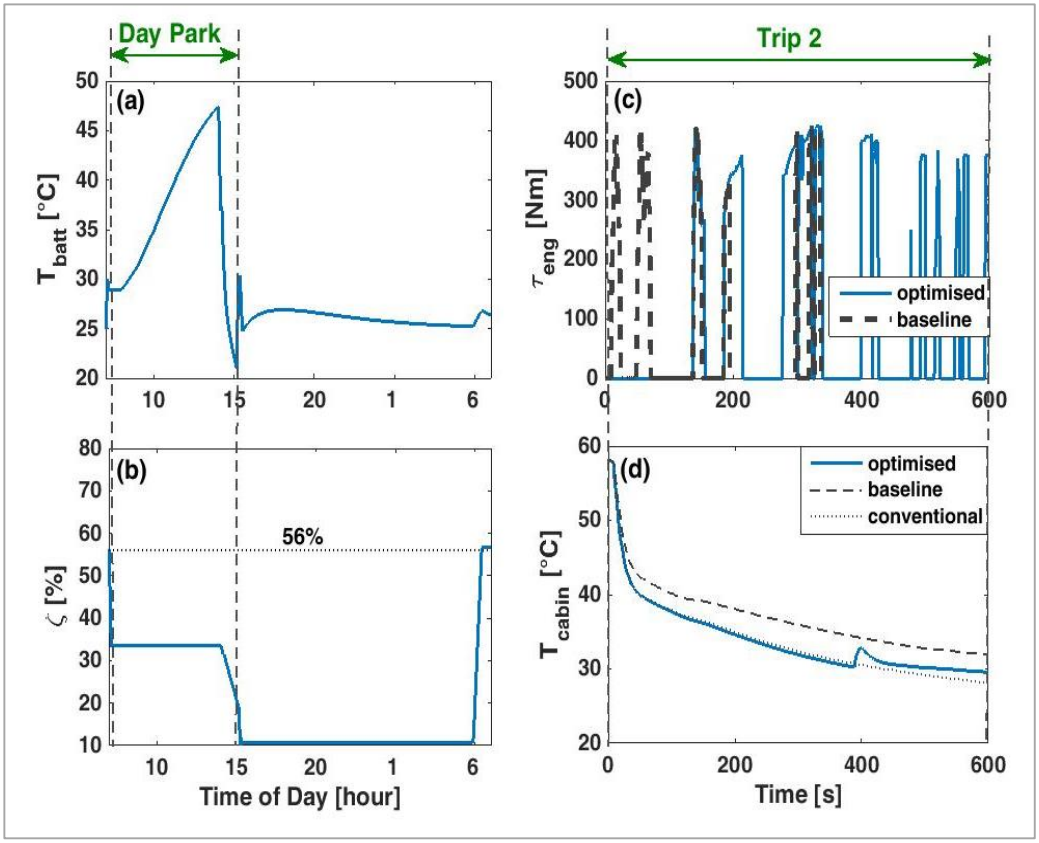

Figure 10-6. Solution of equation (10-5) for the duty cycle with US06 trips and λ={0,0.5,0.5}. (a) daily battery temperature, (b) daily SoC , (c) engine torque in Trip 2, and (d) cabin temperature in Trip 2

10.2.4 Scenario 10-VII: Control of partial charging and key-off cooling based on fuel economy, battery lifetime and thermal comfort

In Figure 10-7 the objective space of equation (10-5) is projected onto the planes of the cost term pairs. This figure is achieved by simulating the model with random charge level and key-off cooling flag inputs, as well as by solving equation (10-5) with various weightings of the cost terms. The dotted lines specify the achievable boundaries, while the dashed lines approximate the pareto fronts that highlight the trade-off between the objectives. The solutions of the scenarios discussed above as well as the equivalent key-off cooling optimisation scenarios discussed Chapter 9 are marked on the figure.

Comparing Figure 10-7 with Figure 9-9 shows that partial charging has extended the boundaries of the objective space towards lower capacity loss. Therefore, the solutions of the partial charging scenarios lie on the left, and below, the equivalent full-charge scenarios, in Figure 10-7(a), and Figure 10-7(b), respectively.

The solution of scenario 10-II corresponds to minimum capacity loss while the solution of scenario 10-III corresponds to the lowest capacity loss that can be achieved without compromising the fuel economy. Comparing these solutions with the equivalent full-charge scenarios (9-II and 9-III respectively) shows that partial charging enables significant reductions in capacity loss.

In Figure 10-7(a), the points that lie on the boundary line correspond to the solutions in which the battery charge is enough for supporting the vehicle in both trips, as well as for sufficient key-off cooling and avoiding an overheated battery. These include the solutions of scenarios 9-I, 9-III and 10-III. Moving from the solution of scenario 9-III to the solution of scenario 10-III, the battery maximum charge level decreases from 95% to 68%. The points that lie within the rectangle in Figure 10-7(a) represent the scenarios in which the vehicle operates in CS mode in a significant part of Trip 2, either as a result of an intense key-off cooling, or due to very low level of charge. The height of this rectangle is equivalent to the impact of battery overheating on fuel consumption in Trip 2 (the points that lie on

the lower edge represent the scenarios in which the battery is not overheated at the start of the trip).

In Figure 10-7(b), the points that lie on the right hand boundary represent the solutions with limited or no key-off cooling, so the battery temperature at the start of Trip 2 is similar to the baseline scenario and the discomfort is high. The points adjacent to the left hand boundary line represent the solution in which the battery is pre-cooled (to approximately 21°C) for Trip 2, therefore the discomfort is minimised. The variability in capacity along this line is due to different charge levels. The points adjacent to the right hand boundary line in Figure 10-7(b) represent the solutions in which the battery is relatively hot before the start of Trip 2, therefore the discomfort is high. Still in all these solutions some level of key-off cooling is applied and the battery temperature is less than the baseline scenario (see Figure 9-9(b)).

When all three objectives are of importance, one way of controlling key-off cooling is to limit the charge allocated to cooling to the available excess charge and prioritise battery lifetime over thermal comfort. The red squares in Figure 10-7 mark one such solution which is achieved by solving equation (10-5) with $\lambda = \{0.2,0.5,0.3\}$. The figure shows that the capacity loss and the discomfort index are reduced in this solution, compared to solution of scenario 9-VII while the fuel consumption is unaffected.

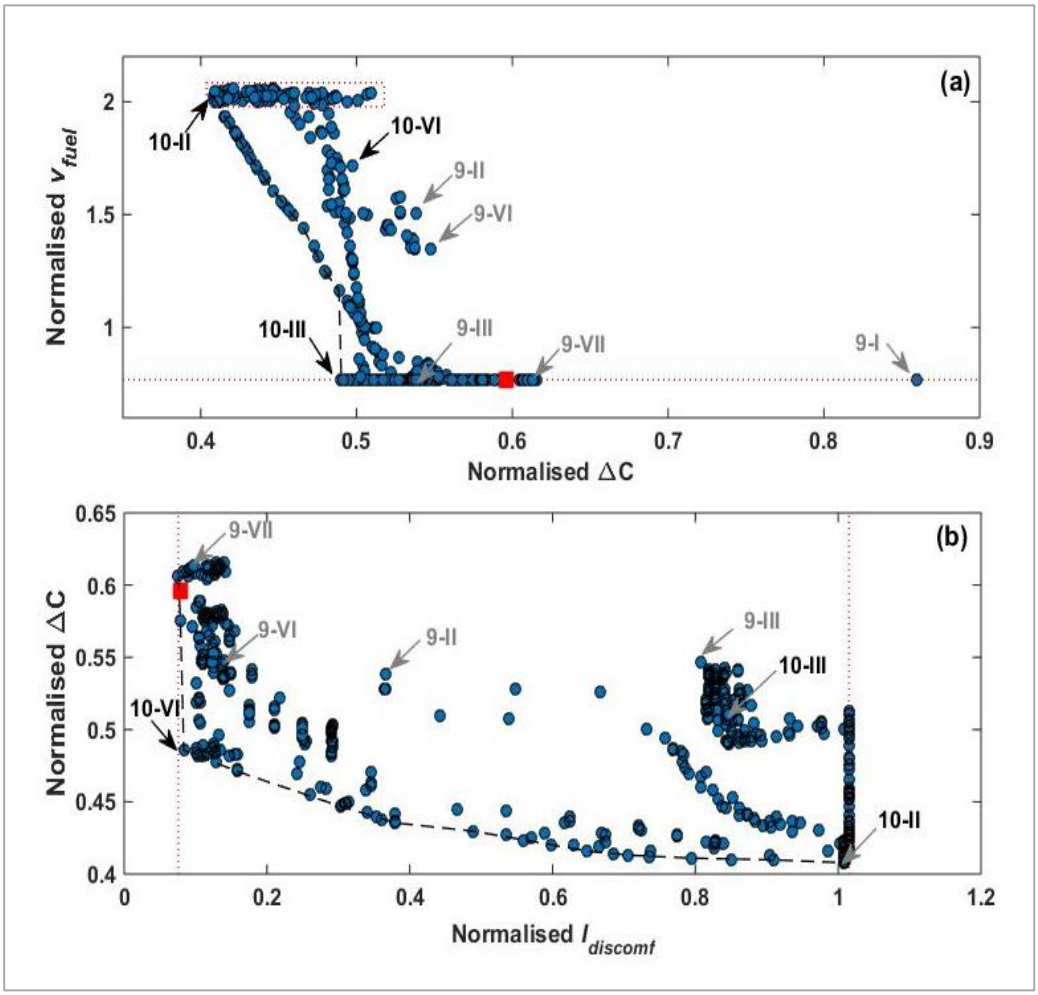

Figure 10-7. Objective planes of equation (10-5) with US06 trips and (a) $\lambda_3 = 0$ and (b) $\lambda_1 = 0$ The dotted lines indicate the achievable boundary of the objective planes. The dahsed lines approximate the pareto front. The red square marks the solution achieved with $\boldsymbol{\lambda} = \{0.2, 0.5, 0.3\}$.

This solution is plotted in Figure 10-8. It can be seen that the battery is charged to 89%. This is sufficient for supporting the operation of the vehicle in the two daily trips, and at the same time for supporting key-off cooling, which has been applied to maintain a relatively low battery temperature throughout Day Park, as well as to pre-cool the battery to 21°C for Trip 2. Note that the battery is fully depleted by the end of Trip 2.

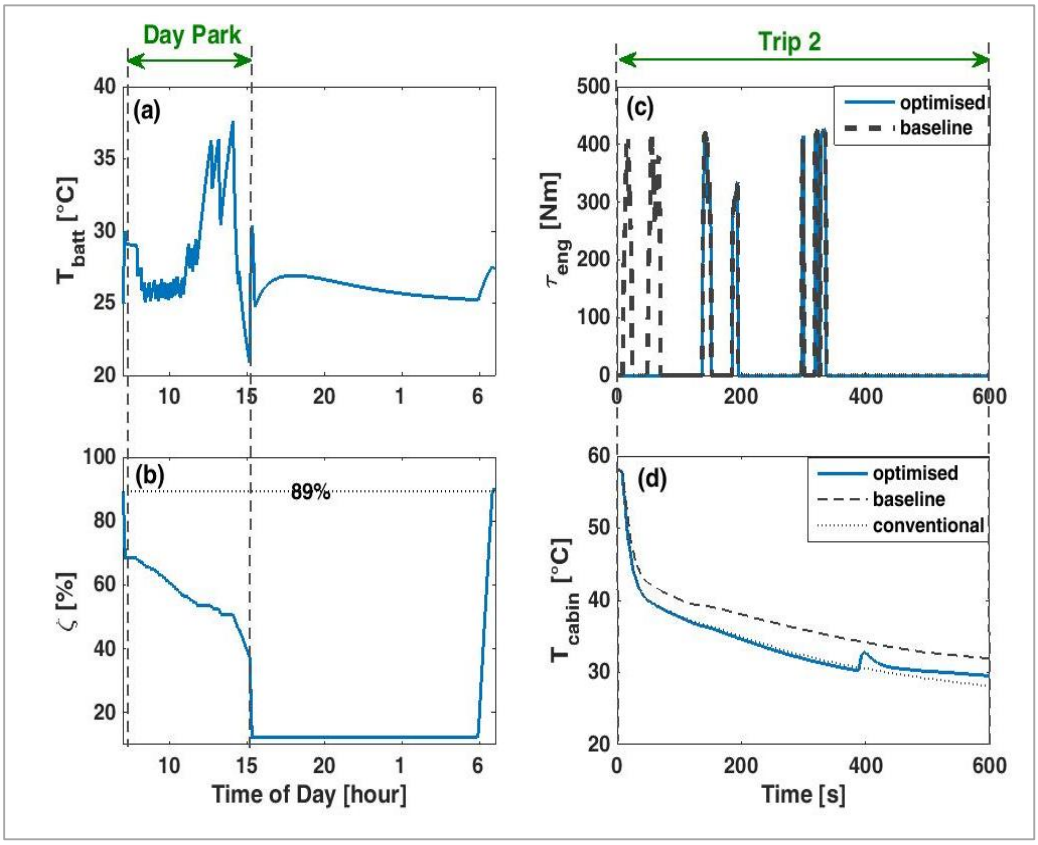

Figure 10-8. Solution of equation (10-5) for the duty cycle with US06 and λ={0.2,0.5,0.3}. (a) daily battery temperature, (b) daily SoC, (c) engine torque in Trip 2, and (d) cabin temperature in Trip 2

10.2.5 Discussion

Table 10-2 summarises the key features of the results discussed above and compares them with the results of the corresponding key-off cooling optimisation scenarios in Chapter 9. The general trend that can be observed is that integrating partial charging and key-off cooling leads to noticeable improvements in battery lifetime (without compromising other performance attributes of the vehicle, as expected).

- Comparing scenarios 9-II and 10-II shows that partial charging significantly reduces the (SoC related storage) capacity loss, both in Day Park and Night Park, leading to battery lifetime improvement by approximately 1 year.

- Comparing the scenarios 9-III and 10-III shows that partial charging has led to a noticeable improvement in battery lifetime, mainly by reducing the (SoC related storage) capacity loss in Night Park. Battery lifetime in scenario 10-III is even longer that in scenario 9-II, further confirming the benefit of combining partial charging and key-off cooling compared to key-off cooling alone.

- The effect of partial charging on the capacity loss in Night Park is also evident from comparing the results of scenario 9-VI and 10-VI. Partial charging leads to a reduction in capacity loss (in Night Park) that outweighs the adverse effect of high temperature in Day Park.

- Comparing the discomfort indices of scenario 9-VI and 10-VI shows that a slightly lower discomfort index has been achieved in scenario 10-VI. This is because key-off cooling in scenario 10-VI is primarily aimed at pre-cooling the battery for Trip 2 (as seen in Figure 10-6), leading to a slightly lower battery temperature just before the trip and subsequently leads to a lower discomfort index.

- It can be seen that the fuel consumption and the thermal discomfort in scenario 10-VII are similar to those achieved in scenario 9-VII, but partial charging has helped improve the battery lifetime from 8 years to 8.2 years.

Table 10-2. Summary of results for different solutions of equation (10-5) for the duty cycle with US06 trips

Solution	Scenario	ζ_{max} [%]	$[\bar{T}_{batt}]_{Dprk}$ [°C]	$[T_{batt,max}]_{Dprk}$ [°C]	$T_{batt}(t_{Dprk})$ [°C]	$\zeta(t_{Dprk})$ [%]	$[\Delta C]_{Dprk}$ [%]	$[\Delta C]_{Trp2}$ [%]	$[\Delta C]_{Nprk}$ [%]	EoL * [years]	v_{fuel} [L]	$I_{discomf}$ [-]
Baseline	--	Full**	39.0	48.4	48.4	74.6	1.07	0.16	1.36	6.3	108.5	57
Min ΔC: $\boldsymbol{\lambda} = \{\mathbf{0}, \mathbf{1}, \mathbf{0}\}$	9-II	Full**	23.8	29.5	25.5	25.0	0.47	0.18	0.68	8.5	163.0	21
	10-II	41	37.2	46.9	46.9	15.7	0.37	0.18	0.44	9.4	219.9	58
Min v_{fuel} + ΔC: $\boldsymbol{\lambda} = \{\mathbf{0.5}, \mathbf{0.5}, \mathbf{0}\}$	9-III	Full**	25.4	34.5	34.5	37.2	0.48	0.18	0.70	8.3	83.4	46
	10-III	68	33.7	38.8	36.4	37.1	0.47	0.18	0.57	8.8	83.4	49
Min ΔC + $I_{discomf}$: $\boldsymbol{\lambda} = \{\mathbf{0}, \mathbf{0.5}, \mathbf{0.5}\}$	9-VI	Full**	24.6	33.0	22.1	27.6	0.50	0.18	0.69	8.4	145.9	8
	10-VI	56	36.0	47.4	21.0	18.9	0.53	0.18	0.51	8.8	201.9	5
Min v_{fuel} + ΔC + $I_{discomf}$: $\boldsymbol{\lambda} = \{\mathbf{0.33}, \mathbf{0.33}, \mathbf{0.33}\}$	9-VII	Full**	27.7	35.8	21.3	41.4	0.62	0.17	0.75	8.0	83.4	6
$\boldsymbol{\lambda} = \{\mathbf{0.2}, \mathbf{0.5}, \mathbf{0.3}\}$	10-VII	89	28.7	37.6	20.9	37.5	0.61	0.17	0.70	8.2	83.4	5

** Assumes the capacity loss in winter is equal to the baseline scenario (see Section 7.2.1)*

** $\zeta_{max} = 95\%$

10.3 Solution for the duty cycle with NEDCx2 trips

In this section, the solutions of equation (10-5) are discussed for the duty cycle with NEDCx2 trips. For this duty cycle, the lower bound of the level of charge is set to 45% ($45\% \leq \zeta_{max} \leq 95\%$) to ensure that the operating mode of the vehicle in Trip 1 is not affected by partial charging.

The solutions of scenarios 10-II, 10-III and 10-VI for this duty cycle are qualitatively similar to the solutions of the corresponding scenarios for the duty cycle with US06 trips discussed in 10.2. A complete explanation of these solutions are provided in Appendix 3. The main features of the solutions are as follows:

- In scenario 10-II, the battery is charged to the minimum limit. This eliminates the possibility of considerable key-off cooling and forces the vehicle to operate in CS mode throughput Trip 2. This leads to full charging in this instance.

- In scenario 10-III, the battery is sufficiently charged to support the energy requirement of the trips in EV mode, as well as a limited key-off cooling.

- In scenario 10-VI, the battery is charged more than the minimum limit to enable key-off cooling throughout Day Park. The battery is also pre-cooled for Trip 2 to the vicinity of 20°C. The vehicle is forced to operate in CS mode for most of Trip 2.

The solutions of scenarios 10-II, 10-III and 10-VI are marked on Figure 10-9 which shows the projection of the objective space of equation (10-5) on the planes of cost term pairs. This figure is achieved by simulating the model with random charge level and key-off cooling flag inputs, as well as by solving equation (10-5) with various weightings of the cost terms. The dotted lines specify the achievable boundaries, while the dashed lines approximate the pareto fronts that highlight the trade-off between the objectives. The solutions of the scenarios discussed above and the corresponding key-off cooling optimisation scenarios in Chapter 9 are marked on the figure. Comparing Figure 10-9 and Figure 9-12 shows that partial

charging has extended the boundaries of the objective space towards lower capacity loss.

The solution of scenario 10-II shows the effectiveness of partial charging in reducing the capacity loss, compared to intense key-off cooling which was applied in scenario 9-II. As expected, the capacity loss is minimized in this solution, at the expense of high fuel consumption and thermal discomfort. The solution of scenario 10-III (which is similar to the solution of 9-III) corresponds to the minimum capacity loss that can be achieved without compromising the fuel economy. Also, in scenario 10-VI, lower capacity loss has been achieved compared to scenario 9-VI.

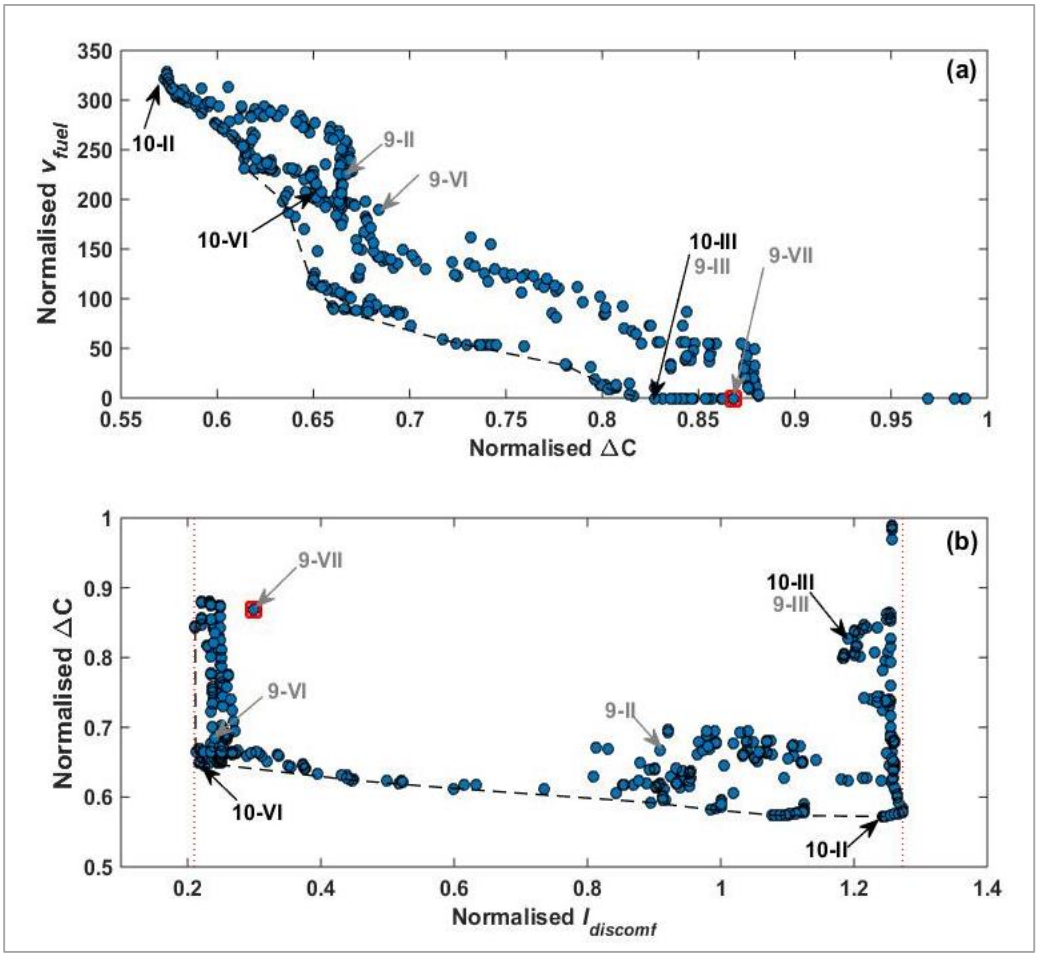

Figure 10-9. Objective planes of equation (10-5) with NEDCx2 trips and (a) $\lambda_3 = 0$ and (b) $\lambda_1 = 0$. *Annotations- The dotted lines indicate the achievable boundary of the objective planes. The dahsed lines approximate the pareto front. The red square marks the solution achieved with $\boldsymbol{\lambda} = \{0.005, 0.8, 0.195\}$.*

In Figure 10-9(a), the points between the solutions of scenarios 10-III and 9-VII correspond to a fully charged battery. The variation in capacity loss between these points are due to the trade-off between the minimization of capacity loss and the minimization of thermal discomfort. In scenario 10-III the entire excess battery charge is used to maintain a low battery temperature throughout Day Park, leaving no charge for pre-cooling. In scenario 9-VII, the excess charge was distributed between maintaining a low battery temperature throughout Day Park as well as pre-cooling. Therefore, any solution of equation (10-5) in which all three performance attributes are considered, leads to a fully charged battery, and falls among these points, unless a compromise on fuel economy is acceptable. Thus, scenarios 10-VII and 9-VII lead to identical solutions. As an example, Figure 10-10 shows the solution of equation (10-5), with $\lambda = \{0.005, 0.8, 0.195\}$, which is identical to the solution achieved in Section 9.4.

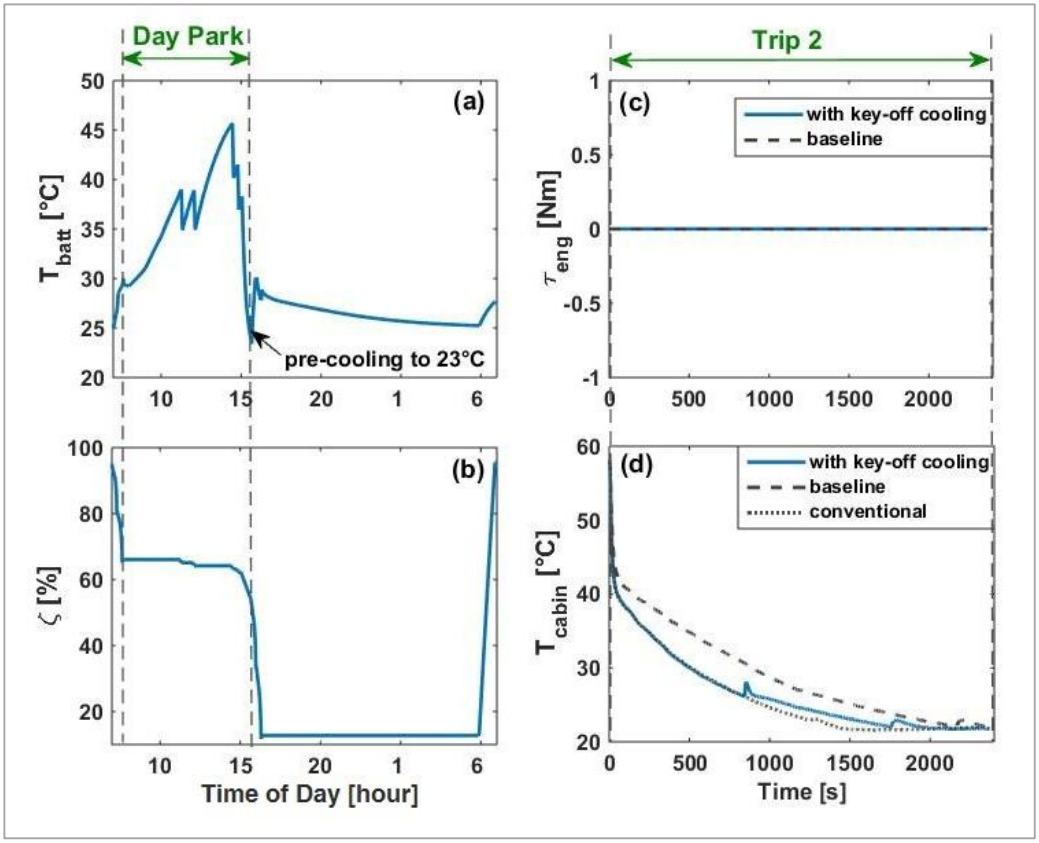

Figure 10-10. Solution of equation (10-5) for the duty cycle with US06 and $\lambda = \{0.005, 0.8, 0.195\}$. (a) daily battery temperature, (b) daily SoC, (c) engine torque in Trip 2, and (d) cabin temperature in Trip 2

Table 10-3 summarises the key features of the results and compares them with the results of the corresponding key-off cooling optimisation scenarios in Chapter 9. The following observations can be made:

- Partial charging enables significant reductions in the SoC related capacity loss, both in Day Park and Night Park. Compared to scenario 9-II where applying an intense key-off cooling increased the battery lifetime by 1.6 years, partial charging (and no key-off cooling) in scenario 10-II increased the battery lifetime by 2.3 years. This shows that when they are not constrained by other considerations, partial charging is more effective than key-off cooling in reducing the capacity loss. In other words, the capacity loss reductions enabled by maintaining a low SoC throughout the day outweigh the negative impact of high battery temperature in Day Park.

- In scenarios 10-III and 10-VII, optimisation of partial charging converges to $\zeta_{max} = 95\%$ (full charge). Therefore, in these scenarios, key-off cooling is controlled as in scenarios 9-III and 9-VII, respectively, leading to similar performance attributes.

- In scenario 10-III, the battery should be charged to at least 85% to meet the energy requirements of the trips, therefore the opportunity for partial charging is limited. Comparing the result of scenarios 10-III and 10-II indicates that when the opportunity for partial charging is limited, it is more beneficial to charge the battery fully and apply key-off cooling to maintain the lowest possible battery temperature, rather than maintaining the lowest possible SoC.

- Charging the battery to 78% in scenario 10-VI has improved the battery lifetime compared to scenario 9-VI. This improvement has been achieved as a result of lower capacity loss in Day Park and Night Park, in spite of reduced key-off cooling and subsequently higher battery temperature in Day Park.

Table 10-3. Summary of results for different solutions of equation (10-5) for the duty cycle with NEDCx2 trips

Solution	Scenario	ζ_{max} [%]	$[\bar{T}_{batt}]_{Dprk}$ [°C]	$[T_{batt,max}]_{Dprk}$ [°C]	$T_{batt}(t_{Dprk})$ [°C]	$\zeta(t_{Dprk})$ [%]	$[\Delta C]_{Dprk}$ [%]	$[\Delta C]_{Trp2}$ [%]	$[\Delta C]_{Nprk}$ [%]	EoL * [years]	v_{fuel} [L]	$I_{discomf}$ [-]
Baseline	--	Full**	39.7	48.3	48.3	66.1	1.09	0.25	0.80	7.2	0.0	579
Min ΔC: $\boldsymbol{\lambda} = \{\mathbf{0}, \mathbf{1}, \mathbf{0}\}$	9-II	Full**	25.1	34.5	34.5	24.3	0.44	0.27	0.67	8.8	226.1	419
	10-II	45	39.7	48.3	48.3	13.4	0.37	0.33	0.45	9.5	321.4	573
Min v_{fuel} + ΔC: $\boldsymbol{\lambda} = \{\mathbf{0.5}, \mathbf{0.5}, \mathbf{0}\}$	9-III	Full**	33.6	45.5	45.5	56.1	0.82	0.26	0.69	8.0	0.0	549
	10-III	95	33.6	45.5	45.5	56.1	0.82	0.26	0.69	8.0	0.0	549
Min ΔC + $I_{discomf}$: $\boldsymbol{\lambda} = \{\mathbf{0}, \mathbf{0.5}, \mathbf{0.5}\}$	9-VI	Full**	27.2	36.5	21.9	27.7	0.49	0.26	0.67	8.7	189.1	111
	10-VI	78	31.8	38.8	21.9	25.6	0.47	0.26	0.60	8.9	206.2	111
Min v_{fuel} + ΔC + $I_{discomf}$: $\boldsymbol{\lambda} = \{\mathbf{0.005}, \mathbf{0.8}, \mathbf{0.195}\}$	9-VII	Full**	35.9	45.7	23.4	0.54	0.93	0.24	0.69	7.8	0	138
	10-VII	95	35.9	45.7	23.4	0.54	0.93	0.24	0.69	7.8	0	138

** Assumes the capacity loss in winter is equal to the baseline scenario*

** $\zeta_{max} = 95\%$

10.4 Summary

In this chapter, the problem of integrated control of partial charging and key-off cooling was defined and solved for complete vehicle duty cycles with US06 and NEDCx2 trips. For each duty cycle, different scenarios were considered to analyse the effect of prioritising individual and combinations of the objectives on the solution. These analyses confirmed that integrating partial charging and key-off cooling can have significant benefits, although the benefits vary from one duty cycle to another. In addition, the following key observations were made:

- Comparing the difference between the solutions of scenarios 10-II and 10-VI for the two duty cycles discussed in this chapter is revealing. The duty cycles had similar solutions in scenario 10-II in that partial charging was preferred over key-off cooling and the battery charge was maintained close to the minimum limit. However, including thermal comfort (scenario 10-VI) led to completely different results for the two duty cycles. On the duty cycle with US06 trips, the battery was charged more to allow pre-cooling. On the duty cycle with NEDCx2 trips, the charge was increased to allow significant cooling throughout Day Park, as well as pre-cooling. This once again indicates that the relative importance of key-off cooling and partial charging for battery lifetime depends on the SoC window available for partial charging.

- In scenario 10-II where the battery lifetime was the only attribute of interest, partial charging converged to SoC levels near the minimum limit. In the duty cycle with US06 trips, the combination of 41% charging and a limited key-off cooling improved the battery lifetime by 3.1 years (from 6.3 years in the baseline scenario to 9.4 years). In the duty cycle with NEDCx2 trips, the battery lifetime was improved by 2.3 years (from 7.2 years in the baseline scenario to 9.5 years) just by charging the battery as little as possible (45% SoC).

- In scenario 10-III where the window of partial charging was limited by the excess charge, the battery was charged to 68% on the duty cycle with US06

trips, which provided approximately 9% charge for key-off cooling. Combining key-off cooling and partial charging improved the battery lifetime by 2.5 years, compared to key-off cooling alone which improved the battery lifetime by 2.3 years. On the duty cycle with NEDCx2 trips, partial charging was not applied, and the excess charge (approximately 10%) was allocated to key-off cooling. This suggests that key-off cooling is more beneficial than a limited partial charging.

- In scenario 10-VI where battery lifetime and thermal comfort were considered, the battery was charged more than the minimum limit to allow pre-cooling. On the duty cycle with NEDCx2 trips, extra charge was allowed and cooling was also applied throughout Day Park. The results indicate that on the duty cycle with US06 trips, lower charge was preferred to extra cooling.

- The limited excess battery charge over the duty cycle with NEDCx2 trips means that considering all three performance attributes in scenario 10-VII does not leave any room for partial charging. So scenario 10-VII and 9-VII led to identical performance for this duty cycle. On the other hand, higher excess charge on the duty cycle with US06 trips allowed partial charging, even in scenario 10-VII. Combining partial charging and key-off cooling on this duty cycle improved the battery lifetime to 8.2 years, compared to the 8 years achieved with key-off cooling alone, while enabling similar improvements in thermal comfort and fuel economy.

CHAPTER 11 DISCUSSION

Introduction

In this chapter, further discussion on the methodologies presented in Chapters 9 and 10 are presented. In Section 11.1, the generality of the proposed methodologies and their applicability to alternative duty cycles and vehicle-level assumptions are discussed in Section 11.1. In Section 11.3, important considerations about realisation of the proposed methodologies are outlined. The limitations of the research are discussed in Section 11.3. In Section 11.4, the areas that require further work are highlighted.

11.1 Generality of the proposed methodologies

The duty cycles considered in this research were designed to expose the challenges of operation in hot climate conditions for PHEVs, and the ultimate effectiveness of key-off cooling and partial charging in avoiding these challenges. The 8-hour Day Park of the work-commute usage case and the hot climate conditions of Phoenix enabled consideration of extreme (hot soak) conditions. Considering a range of scenarios for solving the control problem proved that the behaviour of the optimisation algorithm and the trade-off between different performance attributes can be explained. Using different drive cycles enabled considering the variation in excess battery charge, as well as considering the impact of drive cycle aggressiveness on the effectiveness of key-off cooling and partial charging. Nevertheless, the proposed methods are expected to be equally applicable to alternative duty cycles, as well as alternative vehicle-level assumptions.

11.1.1 Applicability to alternative duty cycles

Some important alternatives to the duty cycles for which the optimisation problem was solved will be those that have milder climate conditions, alternative Day Park durations, and more trips per day. In the following sections, the key considerations

about applying the proposed method under each alternative assumption will be discussed. In each case, every other aspect of the duty cycle is assumed to be consistent with those outlined in Section 7.1.

11.1.1.1 Milder climate conditions:

Applying the proposed methods to control key-off cooling and partial charging in milder climate conditions is straightforward. To achieve this, it will be sufficient to change the climate conditions input to the model and evaluating equation (9-6) or (10-5) for the new climate conditions, following the same process outlined in Chapters 9 and 10. It is important to note that for with any change to the climate conditions, two sets of time consuming calculations should be repeated:

1. The terminal cost terms h_N should be re-evaluated for their new climate conditions. Therefore Trip 2 and Night Park should be simulated with the new climate conditions to generate new maps for h_N, as explained in Section 9.1.

2. The arc cost terms $\sum_{k=0}^{N-1} \Delta C_k\ (x_{bk}, u_k)$ should be reevaluated for the new climate conditions in Day Park.

Also, as with the duty cycles studied previously, Trip 1 should be simulated with the new climate conditions, either once, when solving equation (9-6), or at every iteration, when solving equation (10-5).
Highlighting a few points about the anticipated results in milder climate conditions is necessary:

- In milder climate conditions the battery and the cabin experience lower temperatures in Day Park. Also, cooling will be less energy demanding, given the lower heat flow to the battery and the higher efficiency of the refrigeration circuit. Therefore, the AC and battery cooling loads will be lower and the battery will have more excess charge when the trips are on the US06, and NEDCx2. Even when the trips are on the WLTC, the battery will likely have some excess charge.

- In milder climate conditions, it will be unlikely for the battery to overheat due to the heat gain from the ambient environment alone. Therefore, the electric traction capability of the vehicle will be unaffected irrespective of the assumed drive cycle, making key-off pre-cooling unnecessary as far as the fuel economy attribute is concerned.

- Lower battery temperature reduces the need for key-off cooling as far as the battery lifetime is concerned. However, if maintaining the battery at an even lower temperature is beneficial, key-off cooling will be applied accordingly. Since cooling is more effective in milder climate conditions, less energy is required from the battery, making the cycling capacity loss even less significant.

- Key-off pre-cooling will continue to benefit the thermal comfort in Trip 2 by reducing the need for key-on cooling. Also, with the cabin at a lower temperature at the start of Trip 2, lower AC loads in Trip 2 can reduce the internal heat generation of the battery, increasing the effectiveness of pre-cooling.

- The higher excess charge in mild climate conditions increases the opportunity for partial charging. Also, since the battery will be more likely to have excess charge, the applicability of partial charging will include the duty cycles with WLTC trips, as well as those with US06 and NEDCx2 trips. The lower battery temperature in Day Park will reduce the impact of partial charging on the storage capacity loss in this phase, although noticeable battery lifetime improvements can still be realised.

11.1.1.2 Alternative Day Park durations

The proposed methods can be also applied when the duty cycle of the vehicle includes a shorter or longer Day Park. Changing the duration of Day Park affects the ambient conditions to which the vehicle is exposed after Trip 1, as well as changing the duration of Night Park. Therefore, as in the case of changing the climate conditions, the h_N and $\sum_{k=0}^{N} \Delta C_k$ terms of equations (9-6) or (10-5) should

be re-evaluated. Changing the duration of Day Park also affects the size of the state grid of the DP algorithm, therefore affecting the number of calculations and the time required to evaluate $\sum_{k=0}^{N} \Delta C_k$.

Varying the duration of Day Park can affect the benefits of key-off cooling and partial charging in a similar manner to milder climate conditions:

- With a shorter Day Park, the total heat absorbed from the ambient reduces, leading to lower cabin and battery temperatures throughout Day Park. The lower battery temperature and the shorter duration of Day Park reduce the importance of key-off cooling as far as the battery lifetime is concerned. Lower heat absorption from the ambient means that the battery might not overheat in Day Park, so pre-cooling might not benefit the fuel economy. Even in such conditions, pre-cooling will reduce the need for key-on cooling in Trip 2 and improves the thermal comfort. Also, with a shorter Day Park, Trip 2 starts earlier. With a sufficiently early start of Trip 2, the vehicle will be exposed to milder ambient conditions during the trip.

- A long Day Park extends the exposure of the battery to high temperature, increasing the benefit of key-off cooling for the battery lifetime. Also, a longer Day Park will delay Trip 2. A sufficient delay will allow the hot vehicle to reject heat to the ambient environment during the cooler hours of the day, therefore the battery and the cabin will be at a lower temperature by the start of Trip 2. This reduces the benefit of pre-cooling for eliminating battery overheating, although the pre-cooling will still benefit thermal comfort.

- A sufficiently shorter or a longer Day Park leads to higher excess battery charge, due to the lower battery and cabin temperatures at the start of Trip 2, and the milder ambient conditions during the trip. Therefore, the opportunity for key-off cooling and partial charging without affecting the fuel consumption can increase.

11.1.1.3 More trips per day

Applying the proposed method to duty cycles with more trips per day requires some minor modifications to the implementation of the algorithms. Every additional trip will be accompanied by an additional park phase. So with three trips, the order of the duty cycles phases will become: Trip1 – Park 1 – Trip 2 – Park 2 – Trip3 – Night Park.

The relative importance of key-off cooling in Park 1 and Park 2 depends on their timing. For example, when Park 1 is short and spans early morning hours, or when Park 2 only spans late afternoon hours, applying key-off cooling in the respective phase becomes less beneficial. When this is the case, the key-off cooling control problem can be solved for the other park phase only. To solve the problem with DP, an implementation similar to the one proposed in Chapter 9 will be required:

$$\min_{u^*} J = \min \left(\lambda_1 \sum_{k=0}^{N-1} \Delta C_k \left(x_{bk}, u_k\right) + h_N \right), \tag{11-1}$$

in which N, i.e. the number of 4-minute time intervals in the assumed park phase, will be fewer than the 120 intervals that was previously considered for the 8-hour Day Park.

When solving the problem for Park 1, the terminal cost in equation (11-1) will include the subsequent phases of the duty cycle as:

$$\begin{aligned} h_N = h_{N1} = {} & \lambda_1 \left[v_{fuel}(\cdot)\right]_{Trip\,2} + \lambda_2 \left[\Delta C\,(\cdot)\right]_{Trip\,2} \\ & + \lambda_3 \left[I_{discomf}(\cdot)\right]_{Trip\,2} \\ & + \lambda_2 \left[\Delta C(\cdot)\right]_{Park\,2} \\ & + \lambda_1 \left[v_{fuel}(\cdot)\right]_{Trip\,3} + \lambda_2 \left[\Delta C\,(\cdot)\right]_{Trip\,3} \\ & + \lambda_2 \left[\Delta C(\cdot)\right]_{Park\,3}. \end{aligned} \tag{11-2}$$

In writing equation (11-2), the discomfort index is only defined for Trip 2. Also, it is assumed that if the control algorithms of the vehicle are unaffected by how key-off cooling is applied, the fuel consumption, the capacity loss and the

discomfort index can be expressed as functions of the vehicle state at the end of Park 1, $x_v(t_{Park\,1})$. To solve equation (11-1), the duty cycle should be simulated from Trip 2 to Night Park, to create maps of h_N onto $x_v(t_{Park\,1})$, and the arc-cost term should be evaluated for Park 1, as explained in Chapters 8 and 9.

When solving equation (11-1) for Park 2, the terminal cost will be of the form:

$$h_N = h_{N2} = \lambda_1 \left[v_{fuel}(\cdot)\right]_{Trip\,3} + \lambda_2 \left[\Delta C\,(\cdot)\right]_{Trip\,3} + \lambda_3 \left[I_{discomf}(\cdot)\right]_{trip\,3} + \lambda_2 \left[\Delta C(\cdot)\right]_{NPrk}. \tag{11-3}$$

in which the fuel consumption, the capacity loss and the discomfort index are functions of the vehicle state at the end of Park 2, i.e. $x_v(t_{Park\,2})$.

If key-off cooling in both Park 1 and Park 2 is required, the DP problem should be solved for each one individually. However, the general implementation of the problem will be similar to when key-off cooling is considered in one park phase. Briefly, the process will include solving equation (11-1) for Park 2, as explained above, but for all possible initialisations (of Park 2). From these results, the minimum value of the cost function $[J^*]_{Park2}$ will be mapped onto the vehicle states at the start of Park 2. Since the control algorithms of the vehicle in Trip 2 are not affected by key-off cooling, $[J^*]_{Park2}$ can be mapped onto the vehicle states at the end of Park 1, i.e. $x_v(t_{Park\,1})$. To solve the problem for Park 1, these maps, which can be denoted as $\left[J^*(x_v(t_{park\,1})\right]_{Park2}$, will be used to propagate the maps of the terminal cost term in equation (11-1) as:

$$h_N = h_{N1} = \lambda_1 \left[v_{fuel}(\cdot)\right]_{Trip\,2} + \lambda_2 \left[\Delta C\,(\cdot)\right]_{Trip\,2} + \lambda_3 \left[I_{discomf}(\cdot)\right]_{Trip\,2} + \left[J^*(x_v(t_{park\,1})\right]_{Park2}. \tag{11-4}$$

Once the optimal key-off cooling trajectory is defined for Park 1, the true initial vehicle state in park 2 will be known, so the optimal key-off cooling trajectory in Park 2 will be also identified.

In all of the above cases, implementation of the partial charging problem follows the same process, although at each iteration of the SA algorithm, the capacity loss related to Night Park in equation (11-3) will be a function of the chosen level of charge.

General considerations about the benefits of key-off cooling and partial charging for duty cycles with three or more trips will be similar to those mentioned about shorter or longer Day Park durations, so they will not be repeated in the interest of brevity.

11.1.2 Applicability to alternative vehicle specifications

The proposed methods can be applied to all PHEVs, independent of the size of the battery or other powertrain components. The applicability of the methods is also independent of the architecture of the powertrain (series, parallel hybrid, etc.), and the control algorithms of the vehicle.

The analyses within the present research only focused on proving the benefits of key-off cooling (and partial charging) for PHEVs. Nevertheless, it is clear that comparable benefits will be achieved if these functions are enabled in BEVs, given the similarities in the behaviour of the battery of PHEVs and BEVs, and the generality of the assumptions of this research. In implementing the optimal control problems for BEVs, battery lifetime and thermal comfort will be still applicable, and can be represented by capacity loss and discomfort index in the cost functions. However, instead of fuel economy, a measure for the ability of the vehicle in meeting its drive cycle should be represented in the cost functions. For example, a cost function of the following form can be applied instead of equations (9-1) and (10-2):

$$J = \min\left(\lambda_1(\Delta a + \ \Delta \mathrm{d}) + \lambda_2\, \Delta C + \lambda_3\, I_{discomf}\right), \tag{11-5}$$

in which Δa is the difference between the achieved acceleration and the acceleration demand of the drive cycle. The term Δd is the difference between the achieved distance and the distance covered by the drive cycle. These terms allow for considering any impact of battery overheating on the vehicle's electric traction capability, as well as any impact of applying key-off cooling or partial charging on the AER. The process for solving the optimal control problems will be similar to those described in Chapters 9 and 10.

11.2 Realisation of the method

The method of controlling key-off cooling and partial charging in this research assumes *a priori* knowledge of the complete vehicle duty cycle, including the hourly climate conditions, the recharging strategy of the battery, and the timing and the drive cycle of the trips. This assumption served an important objective of this research; determining the ultimate benefit of applying key-off cooling and partial charging. Although such *a priori* knowledge is not available in real-life, realisation of the methods can be still possible considering that:

1. The main significance of different drive cycles for the methods proposed here is creating the necessary boundary conditions. That is, the battery charge required for meeting an assumed drive cycle determines the window of charge that is available for key-off cooling or partial charging. This level of information about trips of the vehicle can be extracted from historical data, especially with the work-commute usage case in which the trips are frequently repeated.

2. Current trends towards developing 'smart and connected' vehicles suggests that future vehicle will benefit from internet access [65]. This provides access to the driver's diary, information about the availability of parking spaces and charger at the destination, and the weather forecast. Therefore, in the near future,

vehicle energy management algorithms can benefit from advanced knowledge of the timing of the trips, opportunity for plugging-in the vehicle, and the climate conditions to which the vehicle will be exposed.

Therefore, the critical information about the duty cycle of the vehicle can be determined and used to optimise the relevant control strategies, prior to the start of the duty cycle. This points to the potential for realising optimal control techniques, such as the ones proposed in this work, on production vehicles in near future.

11.3 Limitations of the research

The main limitations of this research include neglecting the electric energy consumption, neglecting the effect of temperature on battery voltage, and using relatively simplified battery ageing calculations.

11.3.1 Neglecting the electric energy consumed for key-off cooling

In practice, the electric energy allocated to key-off cooling incurs costs, as well as creating extra energy demands, that should be supported by the electricity grid. Therefore, in a comprehensive formulation of the control problem, the electric energy consumption should be included in the cost function. This was however neglected in the current research. As a result, subject to fuel consumption and cycling capacity loss considerations, the entire (remaining) battery charge was generally used for key-off cooling, as the charge could be replenished 'for free' later in the duty cycle. Although less representative, this simpler cost function was preferred in this research, because:

1. Considering the electric energy consumption within the optimisation will inevitably lead to a more conservative application of key-off cooling, which defies the objective of determining the ultimate benefit of the strategy. Therefore, neglecting the electric energy consumption is consistent with the interests of this research.

2. The price and the abundance of electricity varies significantly from one country to another, depending on the source of the energy as well as the transportation and storage infrastructure [267]. Therefore, including the electric energy consumption within the optimization reduces the generality of the subsequent analyses. It is worth noting that the price and the abundance of fuel also varies between different locations. However, the direct correlation between fuel consumption and emissions makes minimization of fuel consumption in PHEVs worthwhile, independent of the location.

3. By reducing the capacity loss of the battery, key-off cooling increases the scope of second-life application of the battery within the electricity grid. Previous studies have shown various revenue streams for this application, including reduced network reinforcement costs [268], and improved control over generation of electricity from renewable source [269]. This suggests that the extra cost and electricity grid load that result from key-off cooling in the short term can be potentially compensated for in the long term.

11.3.2 Neglecting the effect of temperature on battery voltage

In practice, the open-circuit voltage of typical battery cells varies with temperature, so cooling can reduce the deliverable energy of the battery. This can affect the optimum battery pre-cooling strategy. The battery model that was developed for the purpose of this research neglects the effect of temperature on the open-circuit voltage of the cells, making intense pre-cooling generally preferable. In the range of 20°C–40°C, which is approximately the range in which the battery operates in this research, the effect of temperature on the open-circuit voltage is negligible [261,262], but for a more accurate analysis of the benefits of pre-cooling, this effect should be included in the model. Nevertheless, this will not affect the implementation of the proposed methods.

11.3.3 Simple battery ageing calculation

Another limitation of this research stems from battery ageing calculations. Most importantly, the capacity loss of the cells was accepted as the only measure of their

ageing, ignoring the resistance increase. In practice, however, the capacity loss and the resistance growth of the battery cells are of equal concerns to PEVs, and should be both considered in controlling key-off cooling and partial charging. In addition, key-off cooling and partial charging can have a significant effect on the DoD of the battery, while also affecting its C-rate to some extent. Both of these factors contribute to the capacity loss (and the resistance growth) of the battery, but were neglected in this research.

The proposed methods could benefit from more accurate ageing calculations. However, this will not affect the implementation of the optimal control problem, nor will it affect the general form of the cost functions.

11.4 Future work

Additional work in the following areas can complement this research:

1. Key-off pre-cooling of the cabin

As mentioned in Chapter 2, to improve thermal comfort, cabin precooling is applied in some CVs. In xEVs, plugged-in cabin pre-cooling has been proposed for a similar purpose, as well as for reducing the AC loads. Having considered key-off battery cooling, incorporating the option of key-off cabin pre-cooling will be an appropriate improvement to the method proposed in this work. This will result in a strong trade-off between battery lifetime and thermal comfort when limited battery charge should be divided between maintaining a low battery temperature and precooling the cabin.

2. Optimal control of key-on battery cooling

In this research, rather than pre-defined temperature set points, a set of criteria such as battery ageing were used in controlling key-off cooling. Therefore, key-off cooling was applied only when necessary. Extending this approach to key-on cooling can be beneficial. For example, key-on cooling can be controlled based on ageing and safety criteria. In this way, when the battery warms up during a trip, in

the absence of severe ageing and safety concerns, cooling can be delayed, ideally until the vehicle is plugged-in again. This method can enhance the energy efficiency and thermal comfort by reducing the need for key-on cooling and maximising the benefits of battery precooling.

3. Considering more realistic climate conditions

In this research, the variability in the climate conditions between different days of the year was simplified to enable a straightforward process for developing and assessing the proposed numerical methodologies. To improve the accuracy of the analyses, stochastic climate conditions can be implemented in the model. The proposed methodology can be applied and the results can be analysed as demonstrated in this thesis.

CHAPTER 12 CONCLUSIONS

Introduction

This chapter highlights the key contributions to knowledge and conclusion of this research.

12.1 Contributions to knowledge

12.1.1 Optimal control of key-off cooling

This research, for the first time, proposed the application of key-off battery cooling in PEVs and developed an underpinning methodology for optimal control of key-off cooling in a PHEV.

In the existing state of the art strategy, in order to avoid high battery temperatures in hot climate conditions, battery cooling is applied when the vehicle is driven (key-on cooling) as well as when the vehicle is plugged in (plugged-in cooling) [32,40]. The present research showed that the existing strategy is insufficient as very high battery temperatures can be experienced if the vehicle is parked and not plugged-in (key-off) and this leads to poor battery lifetime, passengers' thermal comfort, and fuel economy. Therefore, compared to the state of the art, a more comprehensive strategy was proposed in which key-on cooling and plugged-in cooling were combined with key-off cooling.

Key-off cooling was approached as an optimal control problem, both to contain any negative effect on fuel economy (or AER), and to maximise its benefits for battery lifetime and passengers' thermal comfort attributes. The problem was formulated as a minimisation of the weighted sum of the fuel consumption, the battery capacity loss, and the thermal discomfort index over the 24-hour duty cycle. Relying on *a priori* knowledge of the duty cycle, this formulation enables trade-offs between fuel economy, battery lifetime, and thermal comfort attributes, which was especially important when limited battery charge was available for key-

off cooling. Consideration of the passengers' thermal comfort in the control of battery cooling was proposed in this research for the first time.

12.1.2 Integration of partial charging and key-off cooling

Optimised partial charging has been proposed previously as a method for maintaining a low battery SoC throughout the duty cycle of the vehicle to improve the battery lifetime [40,42,45]. However, previous research has not considered the benefits of partial charging relative to the benefits of maintaining a low temperature through cooling. In other words, even when plugged-in cooling was applied, optimisation of partial charging was considered independently, without optimising cooling [40]. This is however a significant shortcoming as improving the battery lifetime by (plugged-in or key-off) cooling is generally preferable to improving it by partial charging given that cooling can benefit additional performance attributes, and that it is robust to uncertainty in knowledge of the usage case in that it does not generally risk the ability to achieve an early trip.

In this research, for the first time, a methodology was developed for determining the optimum combination of the level of charge and (key-off) cooling that best serves the battery lifetime. Other performance attributes (i.e. fuel economy and thermal comfort) were also accounted for through minimizing the weighted sum of fuel consumption, the battery capacity loss, and thermal discomfort index, as proposed initially for controlling key-off cooling. Solving the optimisation problem for various duty cycles showed the benefits of the proposed approach compared to applying key-off cooling only or partial charging only.

12.1.3 General observations from the analyses presented in this thesis

12.1.3.1 Observations related to key-off cooling

To investigate the benefits of key-off cooling, a PHEV was simulated over 24-hour duty cycles representing a work commute usage scenario with two trips (Trip 1 and Trip 2) and two park phases (Day Park and Night Park). The vehicle was plugged in once per day in Night Park so optimal control of key-off cooling in Day

Park was required. A range of drive cycles were assumed for the trips to account for the variation in the 'excess' battery charge which could be used for key-off cooling. Overall, the benefits of key-off cooling are considerable. The importance of defining key-off cooling as an optimal control problem and the significance of the proposed formulation is evident from the results. With optimal control, the efficiency of cooling is accounted for, any cycling capacity loss that may result from cooling is considered, the relative importance of the affected attributes is observed, and the limits of the available charge are carefully maintained. Therefore, optimal control enhances the benefits of key-off cooling. In addition, the following key observations are made from the results presented in Chapter 9:

- Regardless of the drive cycle of the trips, key-off cooling improved battery lifetime and thermal comfort. Key-off cooling reduced the high storage capacity loss that would have otherwise resulted from high temperature in Day Park, without leading to disproportionately high cycling capacity loss. Also, (key-off) precooling reduced the negative impact of key-on cooling on thermal comfort in Trip 2 of the duty cycle by shifting the key-on cooling loads towards the end of the trip.

- Key-off cooling, through enabling precooling the battery below its overheating threshold, can improve the fuel economy by maximising the electric traction capability of the vehicle. However, when the drive cycle has a mild (low power demand) start, the effect of battery overheating on the available electric torque is not exposed, so key-off cooling does not improve the fuel economy.

- The effectiveness of (key-off) precooling for improving the thermal comfort varies with the aggressiveness of the drive cycle. More aggressive drive cycles increase the internal heat generation of the battery in Trip 2, which reduces the effectiveness of precooling.

- The energy (i.e. the battery charge) that can be used for key-off cooling depends on the importance of the fuel economy compared to the battery lifetime and

thermal comfort attributes. If fuel economy is less important than battery lifetime or thermal comfort, key-off cooling can be applied up to the limit of full battery depletion. This can force the vehicle to operate in CS mode over a part or the entirety of Trip 2, compromising the fuel economy. Therefore, generally, a trade-off exists between fuel economy on the one side, and battery lifetime or thermal comfort on the other side.

- When fuel economy is of high importance, i.e. when a compromise on fuel economy is unacceptable, the key-off cooling should be bounded by the excess battery charge. For similar climate conditions, the excess charge is governed by the drive cycle of the trips. When the battery has no excess charge over the assumed duty cycle, there is not an opportunity to perform key-off cooling without compromising fuel consumption. When the battery is left with a high excess charge, key-off cooling can be applied intensely, without affecting the fuel consumption, and significant improvements in battery lifetime and thermal comfort is found.

- A trade-off also exists between battery lifetime and thermal comfort. Therefore, even when abundant battery charge is available for key-off cooling, the key-off cooling strategy that maximises battery lifetime does not necessarily maximise thermal comfort, and vice versa.

- Even with a limited excess charge, noticeable improvements in battery lifetime and thermal comfort can be possible, especially if key-off cooling is optimally controlled.

12.1.3.2 General observations related to integration of partial charging and key-off cooling

The following general observations are made from the results presented in Chapter 10:

- Irrespective of its effect on the fuel economy, partial charging can always be considered as a means for improving the battery lifetime. Generally, partial

charging benefits battery lifetime more than key-off cooling benefits it. Therefore, if compromising the fuel economy is allowed, the optimisation of partial charging and key-off cooling converges to minimum charge and no key-off cooling.

- When compromising the fuel economy is not acceptable, that is, when the window of partial charging is limited by the excess battery charge, the benefit of partial charging for battery lifetime becomes comparable with key-off cooling. In the ideal case that the excess battery charge is sufficiently high, the highest battery lifetime can be achieved if key-off cooling and partial charging are combined. When the excess charge is low, full charging is preferred to enable key-off cooling and reduce the temperature as much as possible. For example, the simulation results in Chapter 10 (for the duty cycle with NEDCx2 trips) showed that when the battery had only 10% excess charge, it was fully charged so that key-off cooling could be applied.

12.2 Conclusions

The analyses presented within this thesis support the following key conclusions:

1. The new methodology proposed for controlling key-off cooling maximizes the effectiveness of key-off cooling for any duty cycle and vehicle type. The proposed methodology also enables prioritizing one or more of the affected performance attributes when limited battery charge is available for key-off cooling.

2. Integration of partial charging and key-off cooling enables further improvements in battery lifetime compared to the improvements enabled by each partial charging or key-off individually.

3. Key-off cooling improves the battery lifetime through reducing the battery temperature, while also improving the thermal comfort through reducing the

need for key-on cooling. In addition, key-off cooling maximizes the electric traction capability of the vehicle.

4. The methodology proposed for integrated optimisation of partial charging and key-off cooling maximizes the battery lifetime for any duty cycle and vehicle type. The proposed methodology also enables improvements in the attributes of thermal comfort and electric traction capability (fuel economy in PHEVs) while allowing prioritization of these attributes for optimum use of the available battery charge.

REFERENCES

[1] M. Qiancheng, NASA GISS: Science Briefs: Greenhouse Gases: Refining the Role of Carbon Dioxide, (1998). https://www.giss.nasa.gov (accessed December 4, 2017).

[2] S.K. Mahapatra, K.C. Ratha, Paris Climate Accord: Miles to Go, J. Int. Dev. 29 (2017) 147–154.

[3] E. Lin, K. Jiang, X. Hu, J. Zuo, M. Li, H. Ju, Climate Change Mitigation and Adaptation: Technology and Policy Options, in: Clim. Environ. Chang. China 1951–2012, Springer, 2016: pp. 107–127.

[4] International Energy Agency (IEA), World Energy Outlook 2017, (2017). https://www.iea.org/weo2017/ (accessed December 4, 2017).

[5] The European Commission, A European Strategy for Low-Emission Mobility, (2016). http://eur-lex.europa.eu/resource.html?uri=cellar:e44d3c21-531e-11e6-89bd-01aa75ed71a1.0002.02/DOC_1&format=PDF.

[6] Y. Chen, K. Hu, J. Zhao, G. Li, J. Johnson, J. Zietsman, In-use energy and CO2 emissions impact of a plug-in hybrid and battery electric vehicle based on real-world driving, Int. J. Environ. Sci. Technol. (2017) 1–8.

[7] O. Egbue, S. Long, Barriers to widespread adoption of electric vehicles: An analysis of consumer attitudes and perceptions, Energy Policy. 48 (2012) 717–729. doi:10.1016/j.enpol.2012.06.009.

[8] B.G. Pollet, I. Staffell, J.L. Shang, Current status of hybrid, battery and fuel cell electric vehicles: From electrochemistry to market prospects, Electrochim. Acta. 84 (2012) 235–249. doi:10.1016/j.electacta.2012.03.172.

[9] J. Neubauer, E. Wood, The impact of range anxiety and home, workplace, and public charging infrastructure on simulated battery electric vehicle lifetime utility, J. Power Sources. 257 (2014) 12–20. doi:10.1016/j.jpowsour.2014.01.075.

[10] A. Cooper, K. Schefter, Plug-in Electric Vehicle Sales Forecast Through 2025 and the Charging Infrastructure Required, 2017.

[11] M.F. M. Sabri, K.A. Danapalasingam, M.F. Rahmat, A review on hybrid electric vehicles architecture and energy management strategies, Renew. Sustain. Energy Rev. 53 (2016) 1433–1442. doi:10.1016/j.rser.2015.09.036.

[12] The European Commission, Reducing Emissions from Transport, (2016). https://ec.europa.eu/clima/policies/transport_en (accessed December 20, 2017).

[13] B. Sen, M. Noori, O. Tatari, Will Corporate Average Fuel Economy (CAFE) Standard help? Modeling CAFE's impact on market share of electric vehicles, Energy Policy. 109 (2017) 279–287. doi:10.1016/j.enpol.2017.07.008.

[14] US Department of Energy, Find Electric Vehicle Models, (2017). https://energy.gov/eere/electricvehicles/find-electric-vehicle-models (accessed December 4, 2017).

[15] State of the Plug-in Electric Vehicle Market, Electrification Coalition, 2013. http://www.pwc.com/en_GX/gx/automotive/industry-publications-and-thought-leadership/assets/pwc-ec-state-of-pev-market-final.pdf.

[16] US Department of Energy, Global Plug-in Light Vehicle Sales Increased by About 80% in 2015, (2016). https://energy.gov/eere/vehicles/fact-918-march-28-2016-global-plug-light-vehicle-sales-increased-about-80-2015 (accessed December 4, 2017).

[17] P. Cazzola, M. Gorner, Global EV Outlook 2017: Two million and counting, n.d. doi:10.1787/9789264278882-en.

[18] UK Department for Transport, Air quality plan for nitrogen dioxide (NO2) in UK, (2017). https://www.gov.uk/government/publications/air-quality-plan-for-nitrogen-dioxide-no2-in-uk-2017 (accessed December 4, 2017).

[19] A. Zubaryeva, C. Thiel, Paving the way to electrified road transport Publicly funded research , development and demonstration projects on electric and plug-in vehicles in Europe, Eur. Com. Jt. Res. Cent. (2013) 5–

12. doi:10.2790/85057.

[20] A. Eddahech, O. Briat, J.M. Vinassa, Performance comparison of four lithium-ion battery technologies under calendar aging, Energy. 84 (2015) 542–550.

[21] W. Waag, S. Käbitz, D.U. Sauer, Experimental investigation of the lithium-ion battery impedance characteristic at various conditions and aging states and its influence on the application, Appl. Therm. Eng. 102 (2013) 885–897.

[22] J. Neubauer, A. Pesaran, C. Bae, R. Elder, B. Cunningham, Updating United States Advanced Battery Consortium and Department of Energy battery technology targets for battery electric vehicles, J. Power Sources. 271 (2014) 614–621. doi:10.1016/j.jpowsour.2014.06.043.

[23] B. Scrosati, J. Garche, Lithium batteries: Status, prospects and future, J. Power Sources. 195 (2010) 2419–2430. doi:10.1016/j.jpowsour.2009.11.048.

[24] L. Lu, X. Han, J. Li, J. Hua, M. Ouyang, A review on the key issues for lithium-ion battery management in electric vehicles, J. Power Sources. 226 (2013) 272–288. doi:10.1016/j.jpowsour.2012.10.060.

[25] T. Yuksel, J.J. Michalek, J. Michalek, Evaluation of the Effects of Thermal Management on Battery Life in Plug-in Hybrid Electric Vehicles, in: Proc. Batter. Congr., Carnegie Mellon University, Ann Arbor, MI, USA, 2012.

[26] C. Zhang, F. Yan, C. Du, J. Kang, R. Turkson, Evaluating the Degradation Mechanism and State of Health of LiFePO4 Lithium-Ion Batteries in Real-World Plug-in Hybrid Electric Vehicles Application for Different Ageing Paths, Energies. 10 (2017) 110. doi:10.3390/en10010110.

[27] T. Guan, S. Sun, Y. Gao, C. Du, P. Zuo, Y. Cui, et al., The effect of elevated temperature on the accelerated aging of LiCoO 2 /mesocarbon microbeads batteries, Appl. Energy. 177 (2016) 1–10. doi:10.1016/j.apenergy.2016.05.101.

[28] A. Barré, B. Deguilhem, S. Grolleau, M. Gérard, F. Suard, D. Riu, A review on lithium-ion battery ageing mechanisms and estimations for automotive

applications, J. Power Sources. 241 (2013) 680–689. doi:10.1016/j.jpowsour.2013.05.040.

[29] I. Bloom, B.W. Cole, J.J. Sohn, S.A. Jones, E.G. Polzin, V.S. Battaglia, et al., An accelerated calendar and cycle life study of Li-ion cells, J. Power Sources. 101 (2001) 238–247. doi:10.1016/S0378-7753(01)00783-2.

[30] J. Schmalstieg, S. Kabitz, M. Ecker, D.U. Sauer, A holistic aging model for Li(NiMnCo)O2 based 18650 lithium-ion batteries, J. Power Sources. 257 (2014) 325–334. doi:10.1016/j.jpowsour.2014.02.012.

[31] Y. Shi, K. Smith, E. Wood, A. Pesaran, A multi-node thermal system model for lithium-ion battery packs, Am. Control Conf. 2015–July (2015) 723–727.

[32] J. Neubauer, E. Wood, Thru-life impacts of driver aggression, climate, cabin thermal management, and battery thermal management on battery electric vehicle utility, J. Power Sources. 259 (2014) 262–275. doi:10.1016/j.jpowsour.2014.02.083.

[33] Q. Wang, B. Jiang, B. Li, Y. Yan, A critical review of thermal management models and solutions of lithium-ion batteries for the development of pure electric vehicles, Renew. Sustain. Energy Rev. 64 (2016) 106–128. doi:10.1016/j.rser.2016.05.033.

[34] Z. Rao, S. Wang, A review of power battery thermal energy management, Renew. Sustain. Energy Rev. 15 (2011) 4554–4571. doi:10.1016/j.rser.2011.07.096.

[35] K. Smith, M. Earleywine, E. Wood, J. Neubauer, A. Pesaran, Comparison of Plug-In Hybrid Electric Vehicle Battery Life Across Geographies and Drive Cycles, in: SAE Tech. Pap., 2012. doi:10.4271/2012-01-0666.

[36] M. Shirk, J. Wishart, Effects of Electric Vehicle Fast Charging on Battery Life and Vehicle Performance, in: SAE Tech. Pap., 2015. doi:10.4271/2015-01-1190.

[37] R.A. Barnitt, A.D. Brooker, L. Ramroth, J. Rugh, K.A. Smith, Analysis of Off-Board Powered Thermal Preconditioning in Electric Drive Vehicles, in: World Batter. Hybrid Fuel Cell Electr. Veh. Symp. Exhib., Shenzhen,

China, 2010.

[38] J.A. Rugh, A. Pesaran, K. Smith, Electric Vehicle Battery Thermal Issues and Thermal Management Techniques, in: SAE Altern. Refrig. Syst. Effic. Symp., Scottsdale, AZ,USA, 2011.

[39] A. Pesaran, S. Santhanagopalan, G.-H. Kim, Addressing the Impact of Temperature Extremes on Large Format Li-Ion Batteries for Vehicle Applications, in: Int. Batter. Semin., Ft. Lauderdale, Florida, 2013.

[40] J.S. Neubauer, E. Wood, Will Your Battery Survive a World With Fast Chargers ?, in: SAE Tech. Pap., 2015.

[41] O. Gross, S. Clark, Optimizing Electric Vehicle Battery Life through Battery Thermal Management, SAE Int. J. Engines. 4 (2011) 2011-01–1370. doi:10.4271/2011-01-1370.

[42] A. Hoke, A. Brissette, D. Maksimovic, D. Kelly, A. Pratt, Maximizing lithium ion vehicle battery life through optimized partial charging, IEEE Innov. Smart Grid Technol. Conf. ISGT. (2013) 1–5. doi:10.1109/ISGT.2013.6497818.

[43] J. Neubauer, A. Brooker, E. Wood, Sensitivity of plug-in hybrid electric vehicle economics to drive patterns, electric range, energy management, and charge strategies, J. Power Sources. 236 (2013) 357–364. doi:10.1016/j.jpowsour.2012.07.055.

[44] S. Bashash, S.J. Moura, J.C. Forman, H.K. Fathy, Plug-in hybrid electric vehicle charge pattern optimization for energy cost and battery longevity, J. Power Sources. 196 (2011) 541–549.

[45] A. Hoke, A. Brissette, K. Smith, A. Pratt, D. Maksimovic, Accounting for Lithium-Ion Battery Degradation in Electric Vehicle Charging Optimization, IEEE J. Emerg. Sel. Top. Power Electron. PP (2014) 1–1. doi:10.1109/JESTPE.2014.2315961.

[46] P. Miller, XEV market trend and prospect, 2012 IEEE Veh. Power Propuls. Conf. VPPC 2012. (2012) 1095–1099. doi:10.1109/VPPC.2012.6422499.

[47] K. Çağatay Bayindir, M.A. Gözüküçük, A. Teke, A comprehensive overview of hybrid electric vehicle: Powertrain configurations, powertrain

control techniques and electronic control units, Energy Convers. Manag. 52 (2011) 1305–1313. doi:10.1016/j.enconman.2010.09.028.

[48] R. Giral-Castillón, L. Martínez-Salamero, Conventional Cars, in: Handb. Automot. Power Electron. Mot. Drives, CRC press, 2005.

[49] M. Eshani, Y. Gao, S.E. Gay, A. Emadi, Modern electric, hybrid electric and fuel cell vehicles, CRC press, 2010. doi:10.1201/9781420037739.

[50] S.F. Tie, C.W. Tan, A review of energy sources and energy management system in electric vehicles, Renew. Sustain. Energy Rev. 20 (2013) 82–102. doi:10.1016/j.rser.2012.11.077.

[51] O. Bitsche, G. Gutmann, Systems for hybrid cars, J. Power Sources. 127 (2004) 8–15. doi:10.1016/j.jpowsour.2003.09.003.

[52] C. Mi, M.A. Masrur, Hybrid electric vehicles: principles and applications with practical perspectives, John Wiley & Sons, 2017.

[53] F. Herrmann, F. Rothfuss, Introduction to hybrid electric vehicles, battery electric vehicles, and off-road electric vehicles, in: Adv. Batter. Technol. Electr. Veh., Elsevier Ltd., 2015: pp. 3–16. doi:http://dx.doi.org/10.1016/B978-1-78242-377-5.00001-7.

[54] A. Elgowainy, A. Burnham, M. Wang, Well-to-wheels energy use and greenhouse gas emissions of plug-in hybrid electric vehicles, SAE Int. J. Fuels Lubr. 2 (2009) 627–644. doi:10.4271/2009-01-1309.

[55] S. Amjad, S. Neelakrishnan, R. Rudramoorthy, Review of design considerations and technological challenges for successful development and deployment of plug-in hybrid electric vehicles, Renew. Sustain. Energy Rev. 14 (2010) 1104–1110. doi:10.1016/j.rser.2009.11.001.

[56] N. Jackson, Technology Roadmap, (2011) 1–16.

[57] International Energy Agency (IEA), Technology roadmap: Electric and plug-in hybrid electric vehicles, Int. Energy Agency, Tech. Rep. (2011) 52. doi:10.1109/IEMBS.2004.1403974.

[58] M. Melaina, B. Bush, J. Eichman, E. Wood, D. Stright, V. Krishnan, et al., National Economic Value Assessment of Plug-In Electric Vehicles:

Volume I, Golden, CO, USA, 2016.

[59] M. Ehsani, Y. Gao, Hybrid Drivetrains, in: Handb. Automot. Power Electron. Mot. Drives, CRC press, 2005.

[60] S.S. Williamson, Electric and Plug-in Hybrid Electric Vehicle Drive Train Topologies, in: Energy Manag. Strateg. Electr. Plug-in Hybrid Electr. Veh., Springer, 2013: pp. 7–14. doi:10.1007/978-1-4614-7711-2.

[61] Z. Song, H. Hofmann, J. Li, X. Han, X. Zhang, M. Ouyang, A comparison study of different semi-active hybrid energy storage system topologies for electric vehicles, J. Power Sources. 274 (2015) 400–411. doi:10.1016/j.jpowsour.2014.10.061.

[62] Y. Liu, J. Li, M. Ye, D. Qin, Y. Zhang, Z. Lei, Optimal energy management strategy for a plug-in hybrid electric vehicle based on road grade information, Energies. 10 (2017). doi:10.3390/en10040412.

[63] N. Rotering, M. Ilic, Optimal charge control of plug-in hybrid electric vehicles in deregulated electricity markets, IEEE Trans. Power Syst. 26 (2011) 1021–1029. doi:10.1109/TPWRS.2010.2086083.

[64] A.A. Malikopoulos, Supervisory Power Management Control Algorithms for Hybrid Electric Vehicles: A Survey, in: IEEE Trans. Intell. Transp. Syst., 2014.

[65] A. Mola, Automotive Industry Trends: IoT Connected Smart Cars & Vehicles, (2016). http://uk.businessinsider.com/internet-of-things-connected-smart-cars-2016-10.

[66] A. Pesaran, Battery Requirements for Plug-In Hybrid Electric Vehicles – Analysis and Rationale, in: Electr. Veh. Symp., Anaheim, CA, USA, 2007: p. 26.

[67] T.G. Choi, MODELING , SIZING AND CONTROL OF PLUG-IN LIGHT DUTY FUEL CELL HYBRID ELECTRIC VEHICLE, Ohio State, 2008.

[68] L. Tang, G. Rizzoni, S. Onori, Energy Management Strategy for HEVs Including Battery Life Optimization, IEEE Trans. Transp. Electrif. 1 (2015) 211–222. doi:10.1109/TTE.2015.2471180.

[69] S. Stockar, V. Marano, M. Canova, G. Rizzoni, L. Guzzella, Energy-optimal control of plug-in hybrid electric vehicles for real-world driving cycles, Veh. Technol. IEEE Trans. 60 (2011) 2949–2962.

[70] M. Pourabdollah, N. Murgovski, A. Grauers, B. Egardt, Optimal sizing of a parallel PHEV powertrain, IEEE Trans. Veh. Technol. 62 (2013) 2469–2480. doi:10.1109/TVT.2013.2240326.

[71] V. Madanipour, M. Montazeri-Gh, M. Mahmoodi-k, Multi-objective component sizing of plug-in hybrid electric vehicle for optimal energy management, Clean Technol. Environ. Policy. 18 (2016) 1189–1202. doi:10.1007/s10098-016-1115-1.

[72] N. Kandasamy, S. Whelan, Numerical Investigations of Vehicle Climate Control Strategies Impact on Plug-In Electrical Vehicle Battery Range, (2017). doi:10.4271/2017-01-0190.

[73] J. Neubauer, E. Wood, Accounting for the Variation of Driver Aggression in the Simulation of Conventional and Advanced Vehicles Preprint, in: SAE Tech. Pap., 2013. doi:10.4271/2013-01-1453.

[74] H. Lohse-Busch, M. Duoba, E. Rask, K. Stutenberg, V. Gowri, L. Slezak, et al., Ambient Temperature (20°F, 72°F and 95°F) Impact on Fuel and Energy Consumption for Several Conventional Vehicles, Hybrid and Plug-In Hybrid Electric Vehicles and Battery Electric Vehicle, in: SAE Tech. Pap., 2013. doi:10.4271/2013-01-1462.

[75] Midterm Evaluation of Light-Duty Vehicle Greenhouse Gas Emission Standards and Corporate Average Fuel Economy Standards for Model Years 2022-2025, U.S. Environmental Protection Agancy, 2016. doi:420d16900.

[76] Regulation 101 of the Economic Commission for Europe of the United Nations, Off. J. Eur. Union-EUR-Lex. 55 (2012) 1–67.

[77] Environmental Protection Agency and Deprartment of Transportation, 2017 and Later Model Year Light-Duty Vehicle Greenhouse Gas Emissions and Corporate Average Fuel Economy Standards; Final Rule, Fed. Regist. 77 (2012). https://www.epa.gov/regulations-emissions-vehicles-and-

engines/final-rule-model-year-2017-and-later-light-duty-vehicle.

[78] O. of T. and A.Q. US Environmental Protection Agancy, fueleconomy.gov, (n.d.). fueleconomy.gov (accessed November 7, 2017).

[79] J. Gonder, A. Simpson, Measuring and Reporting Fuel Economy of Plug-In Hybrid Electric Vehicles, WEVA. 1 (2007) 134–141.

[80] Environmental Protection Agency and Deprartment of Transportation, Test Procedures for Electric Vehicles and Plug-in Hybrids -Final Rule 2013, (2013) 5-. https://www.epa.gov/emission-standards-reference-guide/epa-federal-test-procedure-ftp.

[81] R. Garcia-valle, F. Marra, State of the Art on Different Types of Electric Vehicles, in: Electr. Veh. Integr. into Mod. Power Networks, Springer Science & Business Media, 2013. doi:10.1007/978-1-4614-0134-6.

[82] C. Toepfer, SAE electric vehicle conductive charge coupler, SAE J1772, Soc. Automot. Eng. (2009).

[83] Idaho National Laboratory (INL), Plugged In: How Americans Charge Their Electric Vehicles, 2015.

[84] Y. Cao, S. Tang, C. Li, P. Zhang, Y. Tan, Z. Zhang, et al., An optimized EV charging model considering TOU price and SOC curve, IEEE Trans. Smart Grid. 3 (2012) 388–393. doi:10.1109/TSG.2011.2159630.

[85] C. Guenther, B. Schott, W. Hennings, P. Waldowski, M.A. Danzer, Model-based investigation of electric vehicle battery aging by means of vehicle-to-grid scenario simulations, J. Power Sources. 239 (2013) 604–610. doi:10.1016/j.jpowsour.2013.02.041.

[86] Batteries for Electric Cars: Challenges, Opportunities, and the Outlook to 2020, The Boston Consulting Group, 2010.

[87] D. Doughty, E.P. Roth, A General Discussion of Li Ion Battery Safety, Electrochem. Soc. Interface. (2012) 37–44. doi:10.1021/cm901452z.

[88] B. Nykvist, M. Nilsson, Rapidly falling costs of battery packs for electric vehicles, Nat. Clim. Chang. 5 (2015) 329–332.

[89] Battery Warranty Periods for Model Year 2016 Electric and Plug-in Hybrid

Vehicles, US Dep. Energy. (2016). https://energy.gov/eere/vehicles/fact-913-february-22-2016-most-common-warranty-plug-vehicle-batteries-8-years100000 (accessed November 8, 2017).

[90] Crude Oil Prices - 70 Year Historical Chart, (n.d.). http://www.macrotrends.net/1369/crude-oil-price-history-chart (accessed November 8, 2017).

[91] Z. Lin, Optimizing and Diversifying the Electric Range of Plug-in Hybrid Electric Vehicles for U.S. Drivers, SAE Int. J. Altern. Powertrains. 5 (2012) 180–194. doi:10.4271/2012-01-0817.

[92] T. Johnson, A. Joshi, Review of Vehicle Engine Efficiency and Emissions, SAE Tech. Pap. (2017). doi:10.4271/2017-01-0907.

[93] S.S. Williamson, EV and PHEV Battery Technologies, in: Energy Manag. Strateg. Electr. Plug-in Hybrid Electr. Veh., Springer, New York, NY, USA, 2013: pp. 65–90. doi:10.1007/978-1-4614-7711-2.

[94] C. Linse, R. Kuhn, Design of high-voltage battery packs for electric vehicles, in: Adv. Batter. Technol. Electr. Veh., Elsevier Ltd., 2015: pp. 245–263. doi:http://dx.doi.org/10.1016/B978-1-78242-377-5.00010-8.

[95] V. Etacheri, R. Marom, R. Elazari, G. Salitra, Challenges in the development of advanced Li-ion batteries: a review, Energy Environ. Sci. 4 (2011) 3243–3262. doi:10.1039/c1ee01598b.

[96] J. Axsen, A. Burke, K. Kurani, Batteries for Plug-in Hybrid Electric Vehicles (PHEVs): Goals and the State of Technology circa 2008, Inst. Transp. Stud. Univ. Calif. Davis. 155 (2008).

[97] J. Cherry, Battery Durability in Electrified Vehicle Applications : A Review of Degradation Mechanisms and Durability Testing Prepared for Environmental Protection Agency, 2015.

[98] T.D. Finley, Battery Degradation Modeling For Vehicle Applications, Waterloo, 2014.

[99] B. Scrosati, K.M. Abraham, W.A. van Schalkwijk, J. Hassoun, Lithium batteries: advanced technologies and applications, John Wiley & Sons, 2013.

[100] H. Lee, M. Yanilmaz, O. Toprakci, K. Fu, X. Zhang, A review of recent developments in membrane separators for rechargeable lithium-ion batteries, Energy Environ. Sci. 7 (2014) 3857–3886. doi:10.1039/C4EE01432D.

[101] M. Ehsani, Y. Gao, A. Emadi, Chapter 12:Peaking Power Sources and Energy Storages, in: Mod. Electr. Hybrid Electr. Fuel Cell Veh. Fundam. Theory, Des., CRC press, 2010: pp. 384–388.

[102] K. Young, C. Wang, L.Y. Wang, K. Strunz, Electric Vehicle Battery Technologies, in: Electr. Veh. Integr. into Mod. Power Networks, Springer, New York, NY, USA, 2013. doi:10.1007/978-1-4614-0134-6.

[103] A. Hauser, R. Kuhn, Cell balancing, battery state estimation, and safety aspects of battery management systems for electric vehicles, in: Adv. Batter. Technol. Electr. Veh., Elsevier Ltd., 2015: pp. 283–326. doi:http://dx.doi.org/10.1016/B978-1-78242-377-5.00010-8.

[104] B. Stiaszny, J.C. Ziegler, E.E. Krauß, M. Zhang, J.P. Schmidt, E. Ivers-Tiffée, Electrochemical characterization and post-mortem analysis of aged LiMn 2O4-NMC/graphite lithium ion batteries part I: Cycling aging, J. Power Sources. 258 (2014) 61–75. doi:10.1016/j.jpowsour.2014.02.019.

[105] R.B. Wright, C.G. Motloch, J.R. Belt, J.P. Christophersen, C.D. Ho, R.A. Richardson, et al., Calendar- and cycle-life studies of advanced technology development program generation 1 lithium-ion batteries, J. Power Sources. 110 (2002) 445–470. doi:10.1016/S0378-7753(02)00210-0.

[106] S.F. Schuster, T. Bach, E. Fleder, J. M??ller, M. Brand, G. Sextl, et al., Nonlinear aging characteristics of lithium-ion cells under different operational conditions, J. Energy Storage. 1 (2015) 44–53. doi:10.1016/j.est.2015.05.003.

[107] T. Waldmann, M. Wilka, M. Kasper, M. Fleischhammer, M. Wohlfahrt-Mehrens, Temperature dependent ageing mechanisms in Lithium-ion batteries - A Post-Mortem study, J. Power Sources. 262 (2014) 129–135. doi:10.1016/j.jpowsour.2014.03.112.

[108] M. Broussely, P. Biensan, F. Bonhomme, P. Blanchard, S. Herreyre, K.

Nechev, et al., Main aging mechanisms in Li ion batteries, J. Power Sources. 146 (2005) 90–96. doi:10.1016/j.jpowsour.2005.03.172.

[109] M. Ecker, J.B. Gerschler, J. Vogel, S. Käbitz, F. Hust, P. Dechent, et al., Development of a lifetime prediction model for lithium-ion batteries based on extended accelerated aging test data, J. Power Sources. 215 (2012) 248–257. doi:10.1016/j.jpowsour.2012.05.012.

[110] M. Ecker, N. Nieto, S. Käbitz, J. Schmalstieg, H. Blanke, A. Warnecke, et al., Calendar and cycle life study of Li(NiMnCo)O2-based 18650 lithium-ion batteries, J. Power Sources. 248 (2014) 839–851. doi:10.1016/j.jpowsour.2013.09.143.

[111] C. Delacourt, M. Safari, Mathematical Modeling of Aging of Li-Ion Batteries, in: Phys. Multiscale Model. Numer. Simul. Electrochem. Devices Energy Convers. Storage, 2016: pp. 151–160.

[112] M.A. Danzer, V. Liebau, F. Maglia, Chapter 14: Aging of lithium-ion batteries for electric vehicles, in: Adv. Batter. Technol. Electr. Veh., Elsevier Ltd., 2015: pp. 359–387. doi:10.1016/B978-1-78242-377-5.00014-5.

[113] R. V. Bugga, M.C. Smart, L. Whitcanack, Storage Characteristics of Lithium-Ion Cells, 25 (2010) 297–306. doi:10.1149/1.3393865.

[114] S. Grolleau, A. Delaille, H. Gualous, P. Gyan, R. Revel, J. Bernard, et al., Calendar aging of commercial graphite/LiFePO4 cell - Predicting capacity fade under time dependent storage conditions, J. Power Sources. 255 (2014) 450–458. doi:10.1016/j.jpowsour.2013.11.098.

[115] K. Amine, C.H. Chen, J. Liu, M. Hammond, A. Jansen, D. Dees, et al., Factors responsible for impedance rise in high power lithium ion batteries, J. Power Sources. 97–98 (2001) 684–687. doi:10.1016/S0378-7753(01)00701-7.

[116] M.C. Smart, K.B. Chin, L.D. Whitcanack, B. V Ratnakumar, a L. November, Storage Characteristics of Li-Ion Batteries, (2006).

[117] J. Belt, V. Utgikar, I. Bloom, Calendar and PHEV cycle life aging of high-energy, lithium-ion cells containing blended spinel and layered-oxide

cathodes, J. Power Sources. 196 (2011) 10213–10221. doi:10.1016/j.jpowsour.2011.08.067.

[118] S.S. Choi, H.S. Lim, Factors that affect cycle-life and possible degradation mechanisms of a Li-ion cell based on LiCoO2, J. Power Sources. 111 (2002) 130–136. doi:10.1016/S0378-7753(02)00305-1.

[119] M. Fleischhammer, T. Waldmann, G. Bisle, B.I. Hogg, M. Wohlfahrt-Mehrens, Interaction of cyclic ageing at high-rate and low temperatures and safety in lithium-ion batteries, J. Power Sources. 274 (2015) 432–439. doi:10.1016/j.jpowsour.2014.08.135.

[120] J. Wang, P. Liu, J. Hicks-Garner, E. Sherman, S. Soukiazian, M. Verbrugge, et al., Cycle-life model for graphite-LiFePO4 cells, J. Power Sources. 196 (2011) 3942–3948. doi:10.1016/j.jpowsour.2010.11.134.

[121] X. Han, M. Ouyang, L. Lu, J. Li, Y. Zheng, Z. Li, A comparative study of commercial lithium ion battery cycle life in electrical vehicle: Aging mechanism identification, J. Power Sources. 251 (2014) 38–54. doi:10.1016/j.jpowsour.2013.11.029.

[122] E. Wood, M. Alexander, T.H. Bradley, Investigation of battery end-of-life conditions for plug-in hybrid electric vehicles, J. Power Sources. 196 (2011) 5147–5154. doi:10.1016/j.jpowsour.2011.02.025.

[123] J.R. Belt, C.D. Ho, C.G. Motloch, T.J. Miller, T.Q. Duong, A capacity and power fade study of Li-ion cells during life cycle testing, J. Power Sources. 123 (2003) 241–246. doi:10.1016/S0378-7753(03)00537-8.

[124] K.G. Gallagher, P.A. Nelson, S. Ahmed, D.W. Dees, Battery Testing , Analysis and Design, 2013.

[125] A. Barai, K. Uddin, W.D. Widanage, A. McGordon, P. Jennings, A study of the influence of measurement timescale on internal resistance characterisation methodologies for lithium-ion cells, Sci. Rep. 8 (2018) 21. doi:10.1038/s41598-017-18424-5.

[126] P. Keil, A. Jossen, Aging of Lithium-Ion Batteries in Electric Vehicles : Impact of Regenerative Braking, in: EVS28 Int. Electr. Veh. Symp. Exhib., Kintex, Korea, 2015: pp. 1–11. doi:10.13140/RG.2.1.3485.2320.

[127] K. Uddin, T. Jackson, W.D. Widanage, G. Chouchelamane, P.A. Jennings, J. Marco, On the possibility of extending the lifetime of lithium-ion batteries through optimal V2G facilitated by an integrated vehicle and smart-grid system, Energy. (2017). doi:10.1016/j.energy.2017.04.116.

[128] S. Watanabe, M. Kinoshita, T. Hosokawa, K. Morigaki, K. Nakura, Capacity fading of LiAlyNi1-x-yCoxO 2 cathode for lithium-ion batteries during accelerated calendar and cycle life tests (effect of depth of discharge in charge-discharge cycling on the suppression of the micro-crack generation of LiAlyNi 1-x-yCoxO2 parti, J. Power Sources. 260 (2014) 50–56. doi:10.1016/j.jpowsour.2014.02.103.

[129] Electric Vehicle Battery Test Procedures - Rev. 2, 2001. doi:DOE/ID-10597.

[130] J. Neubauer, A. Pesaran, The ability of battery second use strategies to impact plug-in electric vehicle prices and serve utility energy storage applications, J. Power Sources. 196 (2011) 10351–10358. doi:10.1016/j.jpowsour.2011.06.053.

[131] S. Watanabe, M. Kinoshita, K. Nakura, Capacity fade of LiNi(1−x−y)CoxAlyO2 cathode for lithium-ion batteries during accelerated calendar and cycle life test. I. Comparison analysis between LiNi(1−x−y)CoxAlyO2 and LiCoO2 cathodes in cylindrical lithium-ion cells during long term storage test, J. Power Sources. 247 (2014) 412–422. doi:10.1016/j.jpowsour.2013.08.079.

[132] A. Santos, N. McGuckin, H.Y. Nakamoto, D. Gray, S. Liss, Summary of Travel Trends : 2009 National Household Travel Survey, U.S. Department of Transportation, Federal Highway Adminstration, Washinton DC, USA, 2011. nhts.ornl.gov/2009/pub/stt.pdf.

[133] J. Hall, T. Lin, G. Brown, P. Biensan, F. Bonhomme, Decay Processes and Life Predictions for Lithium Ion Satellite Cells, in: 4th Int. Energy Convers. Eng. Conf. Exhib., American Institute of Aeronautics and Astronautics, Reston, Virigina, 2006. doi:10.2514/6.2006-4078.

[134] Electrek, Tesla Model S battery pack data shows very little capacity loss

over high mileage, (n.d.). https://electrek.co/2016/06/06/tesla-model-s-battery-pack-data-degradation/ (accessed October 1, 2016).

[135] M. Kane, Tesla Model S Battery Degradation Data, (2014). http://insideevs.com/tesla-model-s-battery-degradation-data/ (accessed October 1, 2016).

[136] V. Marano, S. Onori, Y. Guezennec, G. Rizzoni, N. Madella, Lithium-ion batteries life estimation for plug-in hybrid electric vehicles, in: Veh. Power Propuls. Conf. 2009. VPPC'09. IEEE, IEEE, 2009: pp. 536–543.

[137] C. Huber, R. Kuhn, Thermal management of batteries for electric vehicles, in: Adv. Batter. Technol. Electr. Veh., Elsevier Ltd., 2015: pp. 327–358. doi:10.1016/B978-1-78242-377-5.00013-3.

[138] L. Lefebvre, Smart Battery Thermal Management for PHEV Efficiency, Oil Gas Sci. Technol. 68 (2013) 149–164. doi:10.2516/ogst/2012076.

[139] R. Srinivasan, A. Carson Baisden, B.G. Carkhuff, M.H. Butler, The five modes of heat generation in a Li-ion cell under discharge, J. Power Sources. 262 (2014) 93–103. doi:10.1016/j.jpowsour.2014.03.062.

[140] A.A. Pesaran, Battery thermal models for hybrid vehicle simulations, J. Power Sources. 110 (2002) 377–382.

[141] Z. Song, H. Hofmann, J. Li, J. Hou, X. Zhang, M. Ouyang, The optimization of a hybrid energy storage system at subzero temperatures: Energy management strategy design and battery heating requirement analysis, Appl. Energy. 159 (2015) 576–588. doi:10.1016/j.apenergy.2015.08.120.

[142] A. Tourani, P. White, P. Ivey, Analysis of electric and thermal behaviour of lithium-ion cells in realistic driving cycles, J. Power Sources. 268 (2014) 301–314. doi:10.1016/j.jpowsour.2014.06.010.

[143] K. Buford, J. Williams, M. Simonini, Determining most energy efficient cooling control strategy of a rechargeable energy storage system, SAE Technical Paper, 2011.

[144] E. Hosseinzadeh, A. Barai, J. Marco, P. Jennings, A Comparative Study on Different Cooling Strategies for Lithium-Ion Battery Cells, in: Eur. Batter. Hybrid Fuel Cell Electr. Veh. Congr., Geneva, Switzerland, 2017: pp. 1–9.

[145] M. Khan, M. Swierczynski, S. Kær, Towards an Ultimate Battery Thermal Management System: A Review, Batteries. 3 (2017) 9. doi:10.3390/batteries3010009.

[146] A.A. Pesaran, Battery Thermal Management in EV and HEVs: Issues and Solutions, Batter. Man. 43 (2001) 34–49.

[147] S. Daly, Automotive air conditioning and climate control systems, Butterworth-Heinemann, 2011.

[148] D. Nagel, R. Trapp, Comfortable vehicle air conditioning, ATZ Worldw. 107 (2005) 16–18. doi:10.1007/BF03224794.

[149] M.S. Oh, J.H. Ahn, D.W. Kim, D.S. Jang, Y. Kim, Thermal comfort and energy saving in a vehicle compartment using a localized air-conditioning system, Appl. Energy. 133 (2014) 14–21. doi:10.1016/j.apenergy.2014.07.089.

[150] X. Zeng, G. Major, T. Hirao, M. Sekita, Automotive A/C system integrated with electrically controlled variable capacity scroll compressor and fuzzy logic refrigerant flow management, Training. 2014 (2001) 3–31.

[151] H. Khayyam, Adaptive intelligent control of vehicle air conditioning system, Appl. Therm. Eng. 51 (2013) 1154–1161.

[152] M. Arndt, M. Sauer, Spectroscopic carbon dioxide sensor for automotive applications, Proc. IEEE Sensors, 2004. (2004) 252–255. doi:10.1109/ICSENS.2004.1426149.

[153] M.H. Dane, N.R. Miller, A.G. Alleyne, C.W. Bullard, P.S. Hrnjak, Investigation of Control Strategies for Reducing Mobile Air Conditioning Power Consumption, Air Conditioning and Refrigeration Center. College of Engineering. University of Illinois at Urbana-Champaign., 2002.

[154] R.E. Sonntag, C. Borgnakke, G.J. Van Wylen, S. Van Wyk, Fundamentals of thermodynamics, Wiley New York, 1998.

[155] A. Kusiak, M. Li, Reheat optimization of the variable-air-volume box, Energy. 35 (2010) 1997–2005.

[156] K. Bennion, M. Thornton, Integrated Vehicle Thermal Management for

Advanced Vehicle Propulsion Technologies Preprint, (2010).

[157] K. Umezu, H. Noyama, Air-conditioning system for electric vehicles (i-MiEV), in: SAE Automot. Altern. Refrig. Syst. Symp., 2010.

[158] A. Eilemann, H. Kampf, Comfort-management, SAE Technical Paper, 2001.

[159] R.E. Sonntag, C. Borgnakke, G.J. Van Wylen, Fundamentals of thermodynamics, 2009.

[160] M. Fritz, F. Gauterin, M. Frey, E. Wohlfarth, R. Oberfell, An Approach to Develop Energy Efficient Operation Strategies and Derivation of Requirements for Vehicle Subsystems Using the Vehicle Air Conditioning System as an Example, in: SAE Tech. Pap., 2007: pp. 2–26.

[161] J. Rugh, V. Hovland, S.O. Andersen, Significant Fuel Savings and Emission Reductions by Improving Vehicle Air Conditioning, Mob. Air Cond. Summit, Washington, DC. (2004).

[162] H. Khayyam, J. Abawajy, R.N. Jazar, Intelligent energy management control of vehicle air conditioning system coupled with engine, Appl. Therm. Eng. 48 (2012) 211–224.

[163] D. Leducq, J. Guilpart, G. Trystram, Non-linear predictive control of a vapour compression cycle, Int. J. Refrig. 29 (2006) 761–772.

[164] M. Razi, M. Farrokhi, M.H. Saeidi, A.R.F. Khorasani, Neuro-predictive control for automotive air conditioning system, in: Eng. Intell. Syst. 2006 IEEE Int. Conf., IEEE, 2006: pp. 1–6.

[165] B. Torregrosa-Jaime, J. Payá, J. Corberan, Design of Efficient Air-Conditioning Systems for Electric Vehicles, SAE Int. J. Altern. Powertrains. 2 (2013) 2013-01–0864. doi:10.4271/2013-01-0864.

[166] B.P. Rasmussen, A.G. Alleyne, Dynamic modeling and advanced control of air conditioning and refrigeration systems, Air Conditioning and Refrigeration Center. College of Engineering. University of Illinois at Urbana-Champaign., 2006.

[167] O. Ekren, S. Sahin, Y. Isler, Comparison of different controllers for variable

speed compressor and electronic expansion valve, Int. J. Refrig. 33 (2010) 1161–1168.

[168] ANSI/ASHRAE, ASHRAE 55-2013: Thermal Environmental Conditions for Human Occupancy, (2013). doi:ISSN 1041-2336.

[169] P.O. Fanger, Thermal comfort. Analysis and applications in environmental engineering., Copenhagen: Danish Technical Press., 1970.

[170] ANSI/ASHRAE, Thermal environmental conditions for human occupancy (ANSI/ASHRAE standard 55–2013), (n.d.).

[171] R. De Dear, G.S. Brager, Developing an Adaptive Model of Thermal Comfort and Preference, ASHRAE Trans. 104 (1998).

[172] P. Xu, P. Haves, M.A. Piette, L. Zagreus, Demand Shifting With Thermal Mass in Large Commercial Buildings: Field Tests, Simulation and Audits, Lawrence Berkeley Natl. Lab. (2005). http://escholarship.org/uc/item/14j2n3b3 (accessed February 22, 2015).

[173] D. Huang, E. Öker, S.-L. Yang, Ö. Arici, A Dynamic Computer-Aided Engineering Model for Automobile Climate Control System Simulation and Application Part II : Passenger Compartment Simulation and Applications, in: SAE Tech. Pap., 1999. doi:10.4271/1999-01-1196.

[174] J.G. Ingersoll, T.G. Kalman, L.M. Maxwell, R.J. Niemiec, Automobile passenger compartment thermal comfort model - Part II : human thermal comfort calculation, SAE Tech. Pap. - Int. Congr. Expo. 920266 (1992). doi:10.4271/920266.

[175] M.A. Jeffers, L. Chaney, J.P. Rugh, Climate Control Load Reduction Strategies for Electric Drive Vehicles in Warm Weather, (2015) 21–23. doi:10.4271/2015-01-0355.Copyright.

[176] Y. Farzaneh, A.A. Tootoonchi, Controlling automobile thermal comfort using optimized fuzzy controller, Appl. Therm. Eng. 28 (2008) 1906–1917.

[177] T. Kataoka, Y. Nakamura, Prediction of thermal sensation based on simulation of temperature distribution in a vehicle cabin, Heat Transf. Res. 30 (2001) 195–212.

[178] R.Z. Freire, G.H.C. Oliveira, N. Mendes, Predictive controllers for thermal comfort optimization and energy savings, Energy Build. 40 (2008) 1353–1365. doi:10.1016/j.enbuild.2007.12.007.

[179] P. Morales-vald, Analyzing the Effects of Comfort Relaxation on Energy Demand Flexibility of Buildings : A Multiobjective Optimization Approach, Energy Build. 1 (2014) 1–24. doi:10.1016/j.enbuild.2014.09.040.

[180] J.A. Wright, H.A. Loosemore, R. Farmani, Optimization of building thermal design and control by multi-criterion genetic algorithm, Energy Build. 34 (2002) 959–972.

[181] H. Zhang, L. Dai, G. Xu, Y. Li, W. Chen, W.-Q. Tao, Studies of air-flow and temperature fields inside a passenger compartment for improving thermal comfort and saving energy. Part I: Test/numerical model and validation, Appl. Therm. Eng. 29 (2009) 2022–2027.

[182] O. Kaynakli, E. Pulat, M. Kilic, Thermal comfort during heating and cooling periods in an automobile, Heat Mass Transf. Und Stoffuebertragung. 41 (2005) 449–458.

[183] A. Fujita, J. Kanemaru, H. Nakagawa, Y. Ozeki, Numerical simulation method to predict the thermal environment inside a car cabin, JSAE Rev. 22 (2001) 39–47.

[184] J. Rugh, Integrated Numerical Modeling Process for Evaluating Automobile Climate Control Systems, in: Proc. Futur. Car Congr. Arlington, VA, Citeseer, 2002.

[185] J. Ling, V. Aute, Y. Hwang, R. Radermacher, A New Computational Tool for Automotive Cabin Air Temperature Simulation, SAE Int. J. Passeng. Cars - Mech. Syst. 6 (2013) 841–846. doi:10.4271/2013-01-0868.

[186] World climate data, (n.d.). http://www.weatherbase.com/ (accessed September 20, 2017).

[187] US Climate Data: Arizona, (n.d.). https://www.usclimatedata.com/climate/arizona/united-states/3172 (accessed September 20, 2017).

[188] R.B. Farrington, R. Anderson, D.M. Blake, S.D. Burch, M.R. Cuddy, M.A. Keyser, et al., Challenges and potential solutions for reducing climate control loads in conventional and hybrid electric vehicles, Natl. Renew. Energy Lab. Golden, CO, USA, Download from Www. Ott. Doe. Gov/coolcar/pubs. Html. (1999).

[189] Jaguar-LandRover, Engineering Test Procedure : Air Conditioning Evaluation- Solar Soak, (2009).

[190] D. Türler, D. Hopkins, H. Goudey, Reducing vehicle auxiliary loads using advanced thermal insulation and window technologies, SAE Technical Paper, 2003.

[191] S. Sen, M. Selokar, Numerical Simulation and Validation of Cabin Aiming and Cool-Down of a Passenger Car, SAE Int. J. Passeng. Cars - Mech. Syst. 9 (2016) 2016-01–0251. doi:10.4271/2016-01-0251.

[192] J. Rugh, R. Farrington, National Renewable Energy Laboratory: Vehicle ancillary load reduction project close-out report, 2008.

[193] M. Parrino, R. Carnino, G. Romitelli, M. Dongiovanni, A. Mannoni, Investigation of Pre-Cooling Effectiveness in Vehicle Cabin Cool-Down, in: SAE Tech. Pap., 2004. doi:10.4271/2004-01-1380.

[194] L. Huang, T. Han, Validation of 3-D Passenger Compartment Hot Soak and Cool-Down Analysis for Virtual Thermal Comfort Engineering, SAE Tech. Pap. (2002) 10.

[195] J.P. Rugh, Integrated Vehicle Thermal Management–Combining Fluid Loops in Electric Drive Vehicles, (2013).

[196] S. Hausberger, W. Stadlhofer, K. Martin, R. Vermeulen, S. Bleunaus, Z. Samaras, et al., MAC test procedure to be used in a pilot phase; Test procedure V1.11, November 5th 2010, Off. J. United Nations Econ. Comm. Eur. 21 (2010). http://www.unece.org/fileadmin/DAM/trans/doc/2011/wp29grpe/ECE-TRANS-WP29-GRPE-61-inf21e.pdf.

[197] M. Sengupta, A. Habte, P. Gotseff, A. Weekley, A. Lopez, M. Anderberg, et al., National Solar Radiation Data Base, (n.d.).

http://rredc.nrel.gov/solar/old_data/nsrdb (accessed November 5, 2015).

[198] U.S. Climate Data, (n.d.). http://www.usclimatedata.com/ (accessed September 20, 2017).

[199] E. Wood, J. Neubauer, a D. Brooker, J. Gonder, K. a Smith, Variability of battery wear in light duty plug-in electric vehicles subject to ambient temperature, battery size, and consumer usage, in: Electr. Veh. Symp., 2012: pp. 270–281.

[200] S. Shendge, P. Tilekar, S. Dahiya, S.H. Kapoor, Reduction of MAC Power Requirement in a Small Car, in: SAE Tech. Pap., SAE Technical Paper, 2010.

[201] F. Nielsen, S. Gullman, F. Wallin, Å. Uddheim, J.-O. Dalenbäck, Measurement of Energy Used for Vehicle Interior Climate, SAE Int. J. Passeng. Cars - Mech. Syst. 8 (2015) 2015-01–9116. doi:10.4271/2015-01-9116.

[202] G.G. Gao, Investigation of Climate Control Power Consumption in DTE Estimation for Electric Vehicles Power Usage of Climate Control, in: SAE Tech. Pap., SAE International, 2014. doi:10.4271/2014-01-0713.

[203] S. Sanaye, M. Dehghandokht, Thermal Modeling for Predication of Automobile Cabin Air Temperature, Int. J. Automot. Eng. 1 (2011) 13.

[204] V.H. Johnson, Fuel used for vehicle air conditioning: a state-by-state thermal comfort-based approach, in: SAE Tech. Pap., 2002: p. 1957.

[205] A. Yokoyama, T. Osaka, Y. Imanishi, S. Sekiya, Thermal Management System for Electric Vehicles, SAE Int. J. Mater. Manuf. 4 (2011) 2011-01–1336. doi:10.4271/2011-01-1336.

[206] R.B. Farrington, M. Cuddy, M. Keyser, J. Rugh, Opportunities to Reduce Air-Conditioning Loads Through Lower Cabin Soak Temperatures, in: Electr. Veh. Symp., National Renewable Energy Laboratory, 1999.

[207] R. Farrington, J. Rugh, Impact of vehicle air-conditioning on fuel economy, tailpipe emissions, and electric vehicle range, in: Earth Technol. Forum, 2000.

[208] J. Rugh, R. Howard, R. Farrington, M. Cuddy, D. Blake, Innovative techniques for decreasing advanced vehicle auxiliary loads, in: SAE Futur. Congr., 2000: pp. 1–1562.

[209] K.R. Kambly, T.H. Bradley, Estimating the HVAC energy consumption of plug-in electric vehicles, J. Power Sources. 259 (2014) 117–124. doi:10.1016/j.jpowsour.2014.02.033.

[210] E. Samadani, R. Fraser, M. Fowler, Evaluation of Air Conditioning Impact on the Electric Vehicle Range and Li-Ion Battery Life, in: SAE Tech., SAE Technical Paper, 2014.

[211] E. Samadani, M. Mastali, S. Farhad, R. Fraser, M. Flower, Li-ion battery performance and degradation in electric vehicles under different usage scenarios, Int. J. Energy Res. 40 (2016) 379–392. doi:10.1002/er.3378.

[212] S. Gasworth, T. Tankala, Effect of Glazing Thermal Conductivity on Cabin Soak Temperature, SAE Technical Paper, 2012.

[213] P. Letocart, Optically active glazing with overvoltage protection, (2009).

[214] J.P. Rugh, L. Chaney, J. Lustbader, Reduction in Vehicle Temperatures and Fuel Use from Cabin Ventilation , Solar-Reflective Paint , and a New Solar-Reflective Glazing, SAE Tecnhical Pap. 2007-01-1194. (2007) 1–8. doi:10.4271/2007-01-1194.

[215] M.Y. Chan, W.K. Chow, Car park ventilation system: Performance evaluation, Build. Environ. 39 (2004) 635–643. doi:10.1016/j.buildenv.2003.10.009.

[216] A. Bahman, E. Groll, T. Horton, J. Braun, Technologies to Improve the Performance of A / C Systems in Hot Climate Regions, (2014) 1–10.

[217] Y.F. Zhang, D.P. Wyon, L. Fang, A.K. Melikov, The influence of heated or cooled seats on the acceptable ambient temperature range., Ergonomics. 50 (2007) 586–600. doi:10.1080/00140130601154921.

[218] Z. Tian, J.A. Love, A field study of occupant thermal comfort and thermal environments with radiant slab cooling, Build. Environ. 43 (2008) 1658–1670. doi:10.1016/j.buildenv.2007.10.012.

[219] D. Roy, P. Petitjean, D. Clodic, K. El Khoury, Experimental Investigation of a Thermal Preconditioning of a Car cabin, SAE Tech. Pap. (2005). doi:10.4271/2005-01-2057.

[220] Z. Hu, G. Tan, Z. Li, H. Xu, W. Huang, Y. Ye, Solar Powered Vehicle Parking Ventilation System Pre-Cooling Analysis, SAE Tech. Pap. 2015–April (2015). doi:10.4271/2015-01-0367.

[221] Hybrid Committee, Use cases for communication between plug-in vehicles and the utility grid, SAE Int. Detroit, Michigan, Stand. J. 2836 (2010).

[222] Maximizing Electric Cars Range in Extreme Temperatures, U.S. Dep. Energy- Off. Energy Effic. Renew. Energy. (n.d.). https://energy.gov/eere/electricvehicles/maximizing-electric-cars-range-extreme-temperatures (accessed July 27, 2017).

[223] H. Khayyam, A.Z. Kouzani, E.J. Hu, Reducing energy consumption of vehicle air conditioning system by an energy management system, in: Intell. Veh. Symp. 2009 IEEE, IEEE, 2009: pp. 752–757.

[224] H. Khayyam, S. Nahavandi, E. Hu, A. Kouzani, A. Chonka, J. Abawajy, et al., Intelligent energy management control of vehicle air conditioning via look-ahead system, Appl. Therm. Eng. 31 (2011) 3147–3160.

[225] H. Khayyam, A.Z. Kouzani, E.J. Hu, S. Nahavandi, Coordinated energy management of vehicle air conditioning system, Appl. Therm. Eng. 31 (2011) 750–764.

[226] A. Gasparella, G. Pernigotto, F. Cappelletti, P. Romagnoni, P. Baggio, Analysis and modelling of window and glazing systems energy performance for a well insulated residential building, Energy Build. 43 (2011) 1030–1037. doi:10.1016/j.enbuild.2010.12.032.

[227] M.A. Aktacir, O. Büyükalaca, T. Yilmaz, A case study for influence of building thermal insulation on cooling load and air-conditioning system in the hot and humid regions, Appl. Energy. 87 (2010) 599–607. doi:10.1016/j.apenergy.2009.05.008.

[228] P. Xu, P. Haves, M.A. Piette, J. Braun, Peak demand reduction from pre-cooling with zone temperature reset in an office building, Lawrence

Berkeley Natl. Lab. (2004). http://escholarship.org/uc/item/1205612d (accessed January 11, 2015).

[229] J.E. Braun, Load Control Using Building Thermal Mass, J. Sol. Energy Eng. 125 (2003) 292. doi:10.1115/1.1592184.

[230] M. Johnson, IR reflective glass a "here-and-now" solution, SAE Int. (2009). http://articles.sae.org/6407/ (accessed December 20, 2017).

[231] I.L. Krüger, D. Limperich, G. Schmitz, Energy Consumption Of Battery Cooling In Hybrid Electric Vehicles, in: Int. Refrig. Air Cond. Conf., Lafayette, IN,USA, 2012.

[232] Y. Xing, E.W.M. Ma, K.L. Tsui, M. Pecht, Battery Management Systems in Electric and Hybrid Vehicles, Energies. 4 (2011) 1840–1857. doi:10.3390/en4111840.

[233] J. Ling, M. Eisele, H. Qiao, V. Aute, Y. Hwang, R. Radermacher, Transient Modeling and Validation of an Automotive Secondary Loop Air-Conditioning System, SAE Technical Paper, 2014.

[234] D. Chen, J. Jiang, G.H. Kim, C. Yang, A. Pesaran, Comparison of different cooling methods for lithium ion battery cells, Appl. Therm. Eng. 94 (2016) 846–854. doi:10.1016/j.applthermaleng.2015.10.015.

[235] A. Traussnig, L. Rover, H. Petutschnig, S. Steiner, P. Gruen, A Simulation Approach for Vehicle Life-Time Thermal Analysis Applied to a HEV Battery System, in: SAE Tech. Pap., 2016. doi:10.4271/2016-01-0201.Copyright.

[236] K. Smith, M. Earleywine, E. Wood, A. Pesaran, Battery Wear from Disparate Duty-Cycles : Opportunities for Electric-Drive Vehicle Battery Health Management, in: Am. Control Conf., 2012.

[237] T. Yuksel, S. Litster, V. Viswanathan, J.J. Michalek, Plug-in hybrid electric vehicle LiFePO4 battery life implications of thermal management, driving conditions, and regional climate, J. Power Sources. 338 (2017) 49–64. doi:10.1016/j.jpowsour.2016.10.104.

[238] C.S.N. Shiau, C. Samaras, R. Hauffe, J.J. Michalek, Impact of battery weight and charging patterns on the economic and environmental benefits

of plug-in hybrid vehicles, Energy Policy. 37 (2009) 2653–2663. doi:10.1016/j.enpol.2009.02.040.

[239] J. Lindgren, P.D. Lund, Effect of extreme temperatures on battery charging and performance of electric vehicles, J. Power Sources. 328 (2016) 37–45. doi:10.1016/j.jpowsour.2016.07.038.

[240] J. Quirós-Tortós, L.F. Ochoa, B. Lees, A statistical analysis of EV charging behavior in the UK, in: Innov. Smart Grid Technol. Lat. Am. (ISGT LATAM), 2015 IEEE PES, IEEE, Montevideo, Uruguay, 2015: pp. 445–449. doi:10.1109/ISGT-LA.2015.7381196.

[241] I.J. Fernández, C.F. Calvillo, A. Sánchez-Miralles, J. Boal, Capacity fade and aging models for electric batteries and optimal charging strategy for electric vehicles, Energy. 60 (2013) 35–43. doi:10.1016/j.energy.2013.07.068.

[242] A. Hoke, A. Brissette, D. Maksimović, A. Pratt, K. Smith, Electric vehicle charge optimization including effects of lithium-ion battery degradation, IEEE Veh. Power Propuls. Conf. VPPC. (2011). doi:10.1109/VPPC.2011.6043046.

[243] P. Mock, J. Kühlwein, U. Tietge, V. Franco, A. Bandivadekar, J. German, The WLTP: How a new test procedure for cars will affect fuel consumption values in the EU, (2014). doi:10.1016/j.enpol.2013.12.013i.

[244] M. Andre, The ARTEMIS European driving cycles for measuring car pollutant emissions, Sci. Total Environ. 334–335 (2004) 73–84. doi:10.1016/j.scitotenv.2004.04.070.

[245] H. Tummescheit, Design and Implementation of Object-Oriented Model Libraries using Modelica, Lund Institute of Technology, 2002.

[246] Modeon, Dymola AirConditioning Library, (n.d.). http://www.modelon.com/products/modelica-libraries/air-conditioning-library/ (accessed December 10, 2016).

[247] H. Tummescheit, J. Eborn, K. Prölss, Airconditioning–a Modelica library for dynamic simulation of AC systems, in: Model. Conf., 2005.

[248] S. Dw, W.K.H. Runvkrs, K. Zzz, R.U.J. Prgholfd, S. Kwpo, F. Ri, et al.,

Development of a Modelica Base Library for Modeling of Thermo-Hydraulic Systems, in: Model. Conf., 2000.

[249] T. Markel, A. Brooker, T. Hendricks, V. Johnson, K. Kelly, B. Kramer, et al., ADVISOR: A systems analysis tool for advanced vehicle modeling, J. Power Sources. 110 (2002) 255–266. doi:10.1016/S0378-7753(02)00189-1.

[250] A. Walker, A. McGordon, G. Hannis, A. Picarelli, J. Breddy, S. Carter, et al., A novel structure for comprehensive HEV powertrain modelling, IEEE Veh. Power Propuls. Conf. VPPC 2006. (2006) 1–5. doi:10.1109/VPPC.2006.364299.

[251] A. Abel, T. Blochwitz, A. Eichberger, Functional mock-up interface in mechatronic gearshift simulation for commercial vehicles, in: Model. Conf., 2012: pp. 775–780. doi:10.3384/ecp12076775.

[252] A. Nicolai, Co-Simulation of Modelica and Complex Models using High Performance Solvers, in: EnTool Symp., 2013.

[253] C. Zhang, J. Jiang, Y. Gao, W. Zhang, Q. Liu, X. Hu, Charging optimization in lithium-ion batteries based on temperature rise and charge time, Appl. Energy. 194 (2017) 569–577. doi:10.1016/j.apenergy.2016.10.059.

[254] T. Yuksel, J. Michalek, Development of a Simulation Model to Analyze the Effect of Thermal Management on Battery Life, SAE Tech. Pap. (2012). doi:10.4271/2012-01-0671.

[255] C. Rostiti, S. Stockar, M. Canova, A Rule-Based Control for Fuel-Efficient Automotive Air Conditioning Systems, in: SAE Int., 2015. doi:10.4271/2015-01-0366.Copyright.

[256] S. Kirkpatrick, C.D. Gelatt, M.P. Vecchi, Optimization by Simulated Annealing, Science (80-.). 220 (1983) 671–680. doi:10.1126/science.220.4598.671.

[257] O. Sigmund, On the usefulness of non-gradient approaches in topology optimization, Struct. Multidiscip. Optim. 43 (2011) 589–596. doi:10.1007/s00158-011-0638-7.

[258] T.D. Gillespie, Vehicle Dynamics, 1997.

[259] J. Reimpell, H. Stoll, J. Betzler, The automotive chassis: engineering principles, 2001. https://books.google.co.uk/books?hl=en&lr=&id=fuXf3wmahM8C&oi=fnd&pg=PP1&dq=automotive+chassis+reimpell&ots=pbCsLbtYLO&sig=0nFh1cJDRG6_MKSCm-Ddh878wE0 (accessed November 12, 2015).

[260] L. Guzzella, A. Sciarretta, Vehicle Propulsion Systems: Introduction to Modeling and Optimization, Springer, 2007.

[261] V.H. Johnson, A.A. Pesaran, T. Sack, Temperature-Dependent Battery Models for High-Power Lithium-lon Batteries, (2000). http://www.doe.gov/bridge.

[262] O. Erdinc, B. Vural, M. Uzunoglu, A dynamic lithium-ion battery model considering the effects of temperature and capacity fading, 2009 Int. Conf. Clean Electr. Power, ICCEP 2009. (2009) 383–386. doi:10.1109/ICCEP.2009.5212025.

[263] A. Rijnders, Mobile AirConditioning Test Procedure, 2012.

[264] F.P. Incropera, Fundamentals of heat and mass transfer, John Wiley & Sons, 2011.

[265] T. Sobota, Experimental prediction of heat transfer correlations in heat exchangers, in: Dev. Heat Transf., InTech, 2011.

[266] T. Kiss, L. Chaney, J. Meyer, A New Automotive Air Conditioning System Simulation Tool Developed in MATLAB/Simulink, SAE Int. J. Passeng. Cars-Mechanical Syst. 6 (2013) 826–840.

[267] Eurostat, Electricity production, consumption and market overview, (n.d.). http://ec.europa.eu/eurostat/statistics-explained/index.php/Electricity_production,_consumption_and_market_overview.

[268] D. Strickland, L. Chittock, D.A. Stone, M.P. Foster, B. Price, Estimation of transportation battery second life for use in electricity grid systems, IEEE Trans. Sustain. Energy. 5 (2014) 795–803. doi:10.1109/TSTE.2014.2303572.

[269] M.J. Knowles, A. Morris, Impact of Second Life Electric Vehicle Batteries

on the Viability of Renewable Energy Sources, Br. J. Appl. Sci. Technol. 4 (2014) 152–167. doi:10.9734/BJAST/2014/5632.

[270] M.A. Hannan, F.A. Azidin, A. Mohamed, Hybrid electric vehicles and their challenges: A review, Renew. Sustain. Energy Rev. 29 (2014) 135–150. doi:10.1016/j.rser.2013.08.097.

[271] C. Henry, Basal metabolic rate studies in humans: measurement and development of new equations, Public Health Nutr. 8 (2005) 1133–1152. doi:10.1079/PHN2005801.

[272] I. Edition, ASHRAE HANDBOOK FUNDAMENTALS, (2005).

[273] B. Lofton, Chevy Volt Battery System, (2015). https://www.evhangar.com/system/battery-systems/sys-batt-chevy-volt/ (accessed August 3, 2017).

[274] BMW i8, (2015). http://www.bmw.co.uk/en_GB/new-vehicles/bmw-i/i8/2013/introduction.html (accessed August 3, 2017).

Appendix 1 Additional model parameters

A1.1 Range Rover HEV model parameters

This section gives additional parameters used in developing the Range Rover HEV subsystem models, as described in Chapter 5. All parameters have been provided by the industry partner.

A1.1.1 Powetrain subsystem

Figure A1-1 shows the data used to propagate the rolling resistance lookup table in implementation of equation (5-1).

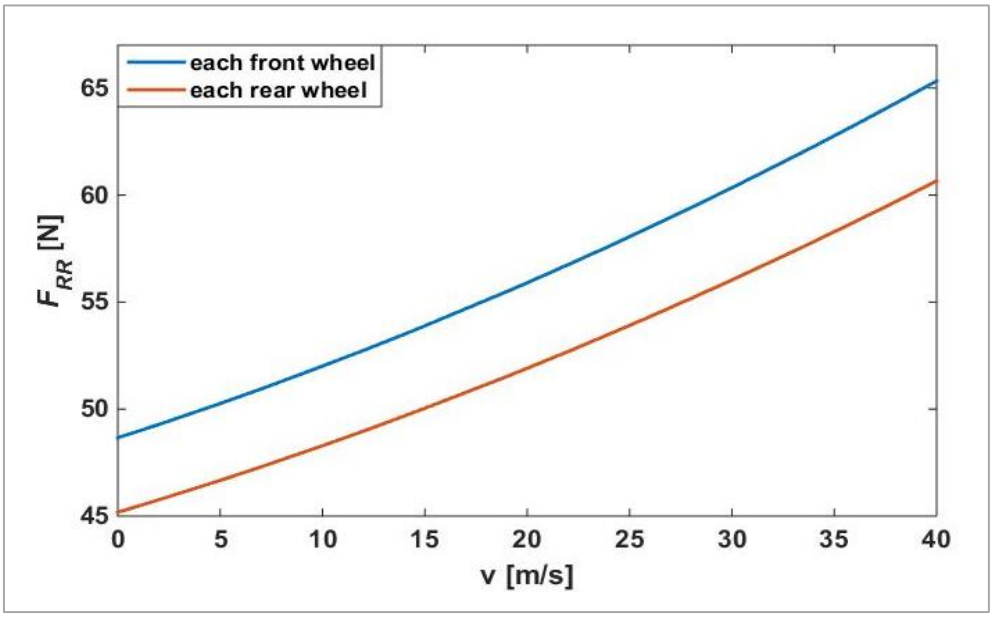

Figure A1-1. The rolling resistance force acting on each wheel

Figure A1-2 shows the losses of gear 1 of the gearbox as implemented in the powertrain model look-up tables. Similar losses were implemented for other gears of the gearbox and or the differential in implementation of equation (5-4).

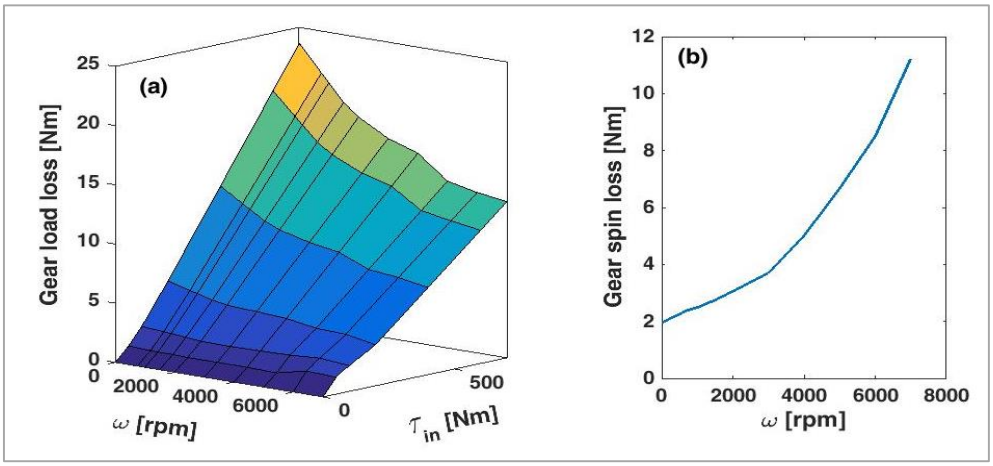

Figure A1-2. Gearbox losses (gear 1): (a) load loss, (b) spin loss

Figure A1-3 shows the shift maps of the gearbox, as implemented in the powertrain model.

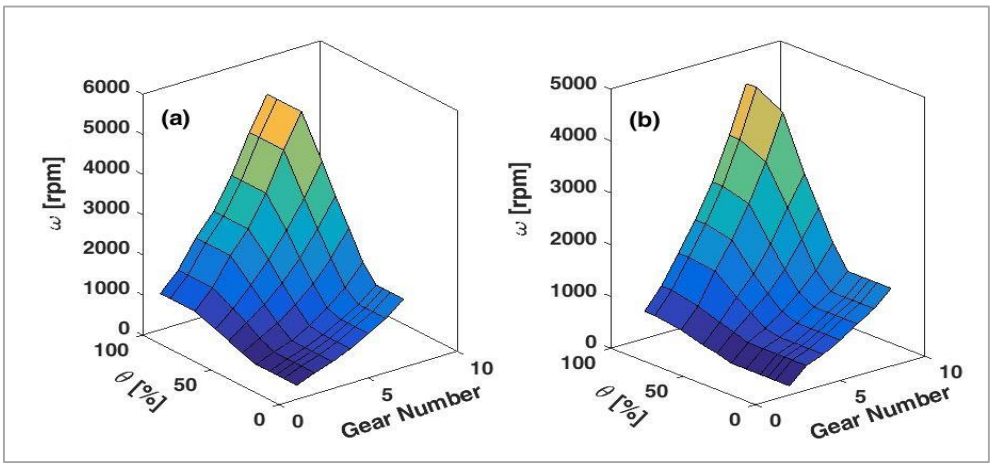

Figure A1-3. Gearbox shift maps: (a) upshift map, (b) downshift map

Figure A1-4 shows the torque capability (maximum torque) curves of the electric machine and the engine as used in the implementation of equation (5-5).

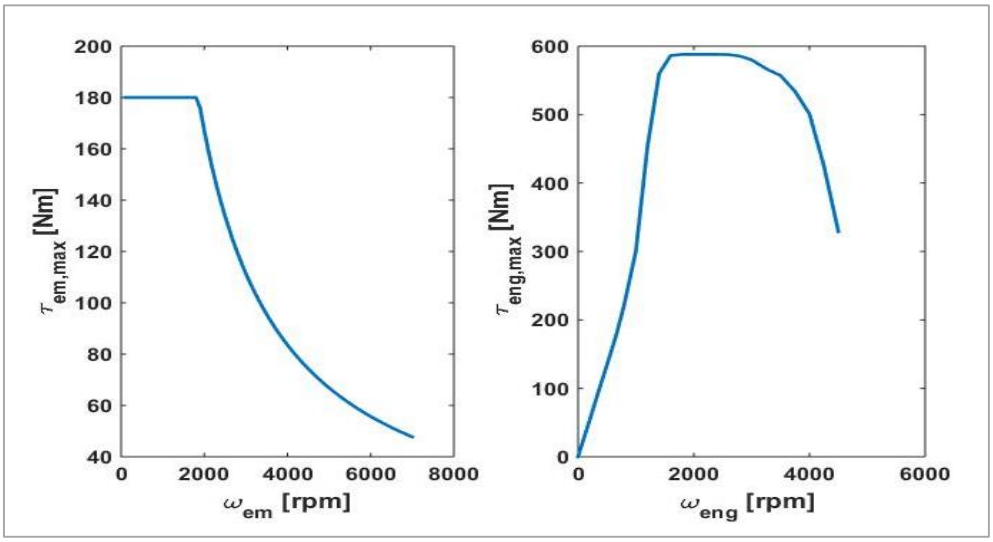

Figure A1-4. Maximum torque capabilities: (a) the electric machine (motoring), and (b) the engine

Figure A1-5 shows the efficiency map of the electric machine as used in the implementation of equation (5-7).

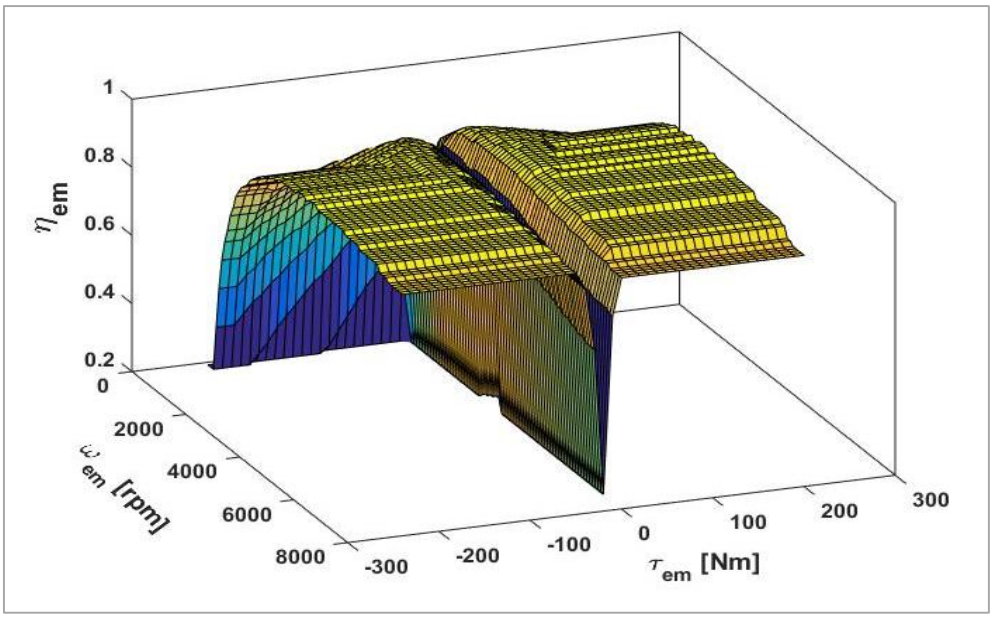

Figure A1-5. The efficiency map of the electric machine and the inverter of Range Rover HEV

Figure A1-6 shows the fuel flow map of the engine implemented in the powertrain model

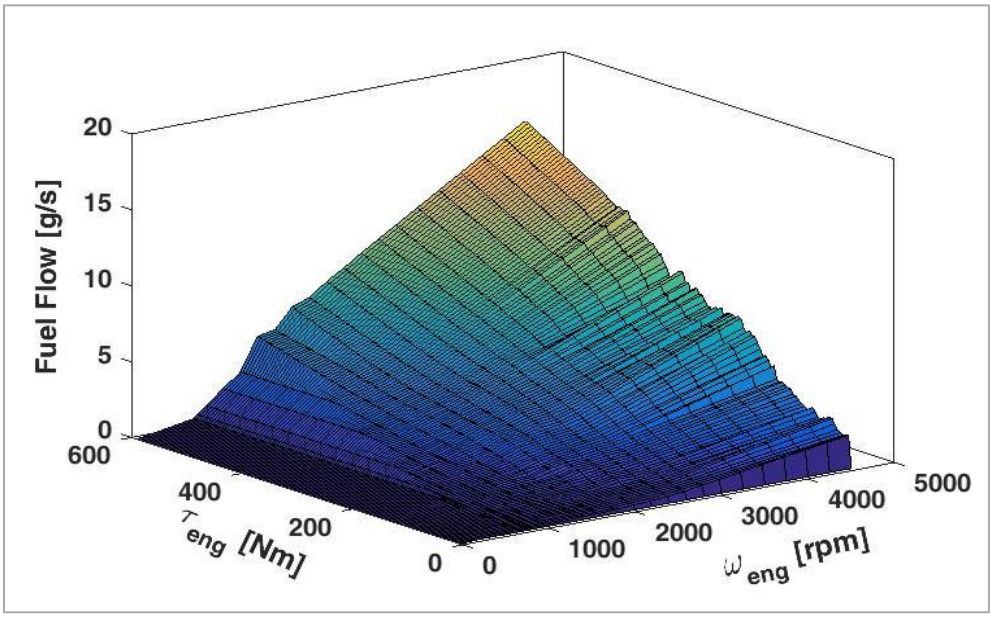

Figure A1-6. The engine fuel consumption map (oil temperature: 90°C)

Figure A1-7 shows the open circuit voltage and the internal resistance of the battery cells as used in the implementation of equation (5-8).

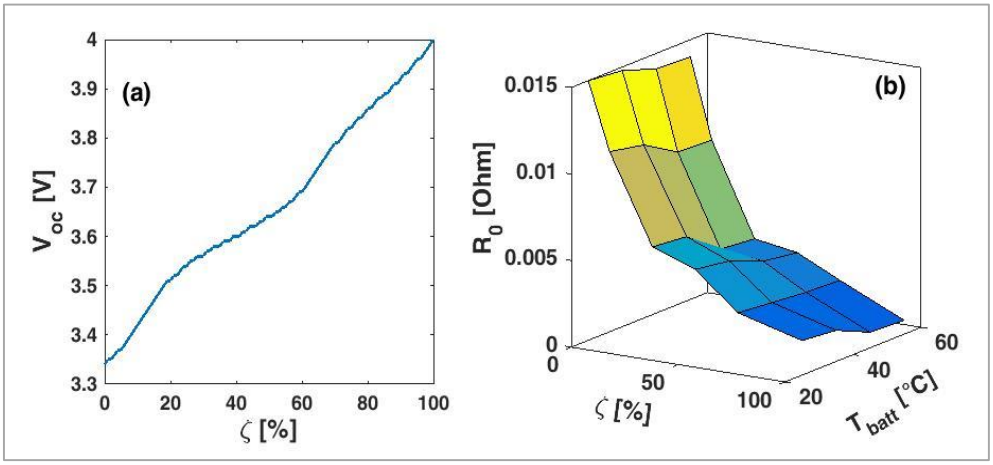

Figure A1-7. Cell parameters: (a) open-circuit voltage, (b) internal resistance

A1.1.2 AC subsystem

Table A1-1 shows the geometric specifications of the condenser used to parameterise the condenser model, as explained in Section 5.5.2.1

Table A1-1. Condenser geometry specifications

	Parameter Name	Value
Core Geometry 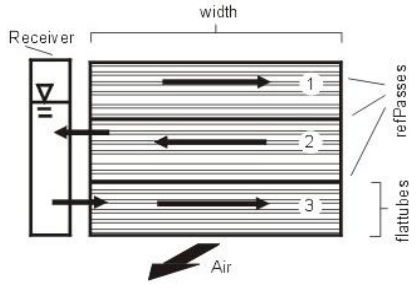	core material	Aluminium
	number of refrigerant Passes	6
	number of flat tubes in each pass	{14,11,10,8,4,4}
	number of passes before receiver	5
	core depth	16 mm
	core Width	593 mm
Flat Tubes Geometry 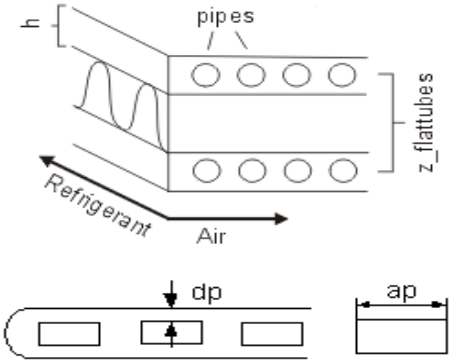	flat tube material	Aluminium with zinc coating
	height of tubes *(h)*	1.9 mm
	centre to centre distance of tubes	11.178 mm
	number of pipes in each tube	7
	wall thickness of flat tubes (*dp*)	0.38 mm
	shape of pipe cross section	rectangular
	length of pipe cross section (*ap*)	1.57 mm
Fin Geometry 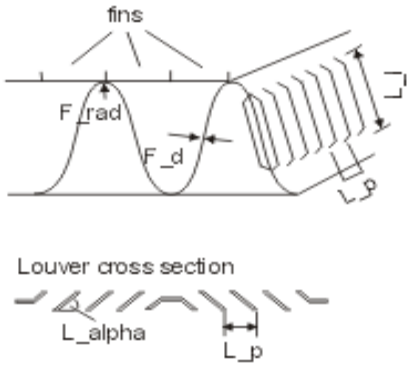	number of fins per 10 cm length of flat tube	92
	length of louver (*L_I*)	1 mm
	pitch of louver (*L_p*)	1mm
	thickness of fins *(F_d)*	0.1 mm
	louvre angle (*L_alpha*)	27 degrees

Figure A1-8 shows the compressor efficiency maps used in implementation of equations (5-23) and (5-24).

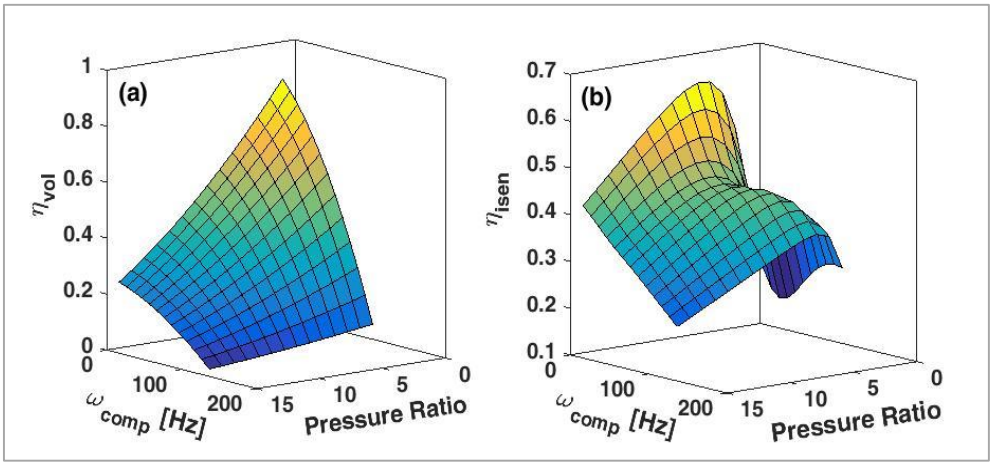

Figure A1-8. Compressor efficiency maps (a) volumetric efficiency, (b) isentropic efficiency

A1.2 The PHEV model parameters

A1.2.1 The powertrain subsystem

A1-9 shows the efficiency map of the 75kW electric machine used in developing the PHEV model, as discussed in Section 6.1.

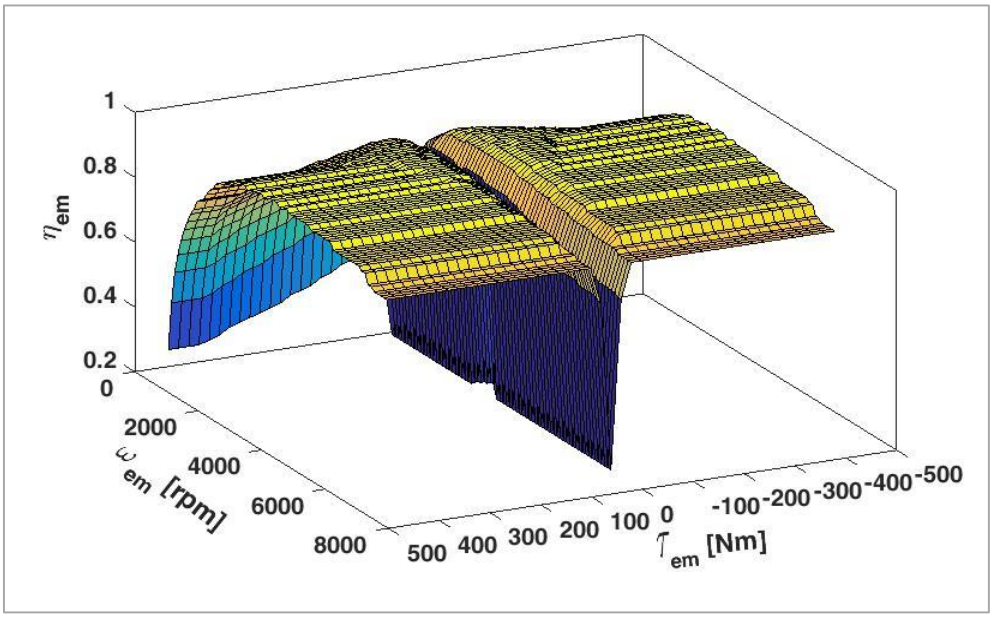

Figure A1-9. The efficiency map of the PHEV electric machine and the inverter

A1.3 Chevy Volt and BMW i8 parameters

Table A1-2 gives the parameters used to estimate the internal heat generation of the battery of Chevy Volt and BMW i8 in Section

Table A1-2. Parameters used to estimate the heat generation in the battery of Chevy Volt and BMW8 in Section 6.1.2.1

Vehicle	Specification										Source
	Mass [kg]	Frontal Area [m^2]	Drag	Battery Capacity [kWh]	Battery Voltage [V]	Battery architecture	Number of cells	Tyoe of cells	Cell Resistance (nominal) [Ohm]		
Chevy Volt	1801	2.2	0.28	16.5	370	3P-96S	288	NMC-LMO	3.2		[273]
BMW i8	1565	2.11	0.26	7.1	355	1P- 96S	96	NMC	5		[75,274]

Appendix 2 Considerations related to the formulation of the optimal control problem in chapter 8

A2.1 Choosing the time interval for control of key-off cooling

As explained in Section 8.1, in solving (8-5) with DP, the duration of Day Park was divided to 120 four-minute intervals. The choice of interval lengths for solving the DP has been based on maximising the effectiveness of key-off cooling. To study the impact of the interval length, optimal control of key-off cooling in the final 2 hours of Day Park was considered and the minimisation described by (8-5) was solved with four interval lengths of 480s, 360s, 240s, and 120s, from the initial condition of $x_{v,0} = [\,51°C, 40°C, 75\%]'$ and with SoC constraint of $\zeta_{min} \geq 40\%$. Figure A2-1(a) compares the capacity losses resulted from optimal key-off cooling with different interval lengths, as well as the capacity loss without key-off cooling. It can be seen that capacity loss exhibits a small sensitivity to the length of intervals below 240 seconds. Still, as Figure A2-1(b) shows for the case of the 240 and 120-second-long intervals, the temperature (and consequently SoC) trajectory resulting from smaller interval lengths can be different. Nevertheless, as far as the effectiveness of key-off cooling is concerned, 240-second-long intervals were considered sufficiently small for solving (8-5).

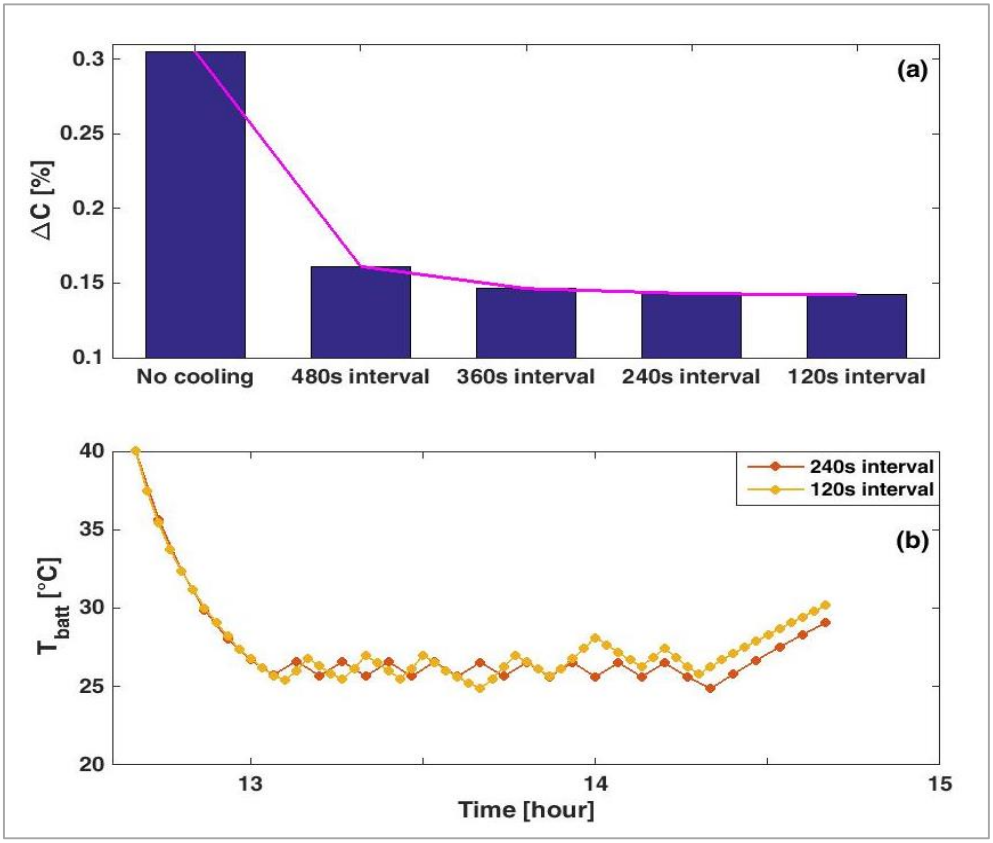

Figure A2-1. Sensitivity of the effectiveness of key-off cooling strategy to time interval length (a) comparison of capacity loss with different interval lengths (b) comparison of battery temperture profiles with 240 seconds and 120 seconds intervals. Data is related to simulating the final 2 hours of day park with $x_{v,0} = [\,51°C, 40°C, 75\%]'$ and $\zeta_{min} \geq 40\%$

A2.2 Choosing the states represented in the DP state grid

Based on the thermal diagram shown in Figure 5-8, the battery is thermally coupled to all elements of the cabin including, its air, glass, wall and interiors. Therefore, the temperature of these elements affect the battery temperature and are the states of the system for the key-off cooling control problem defined in Chapter 8. However, as explained in Section 8.1, in forming the DP state grid for solving the equation (8-5), only the cabin (air) temperature was included in the state grid (in addition to the SoC and the temperature of the battery). This decision was based on the observation that the sensitivity of the temperature of cabin elements to the control inputs (key-off cooling flag) are limited. To illustrate this, the temperature profile of the battery as well as that of the cabin components for the two conditions of 'no key-off cooling' (baseline) and an 'intense key-off cooling' are plotted in

Figure A2-2. It can be seen that when a low battery temperature is maintained, the temperatures of the cabin components are lower than the baseline due to the heat rejected to the battery. Still, the heat gain from the ambient has the dominant effect on the cabin.

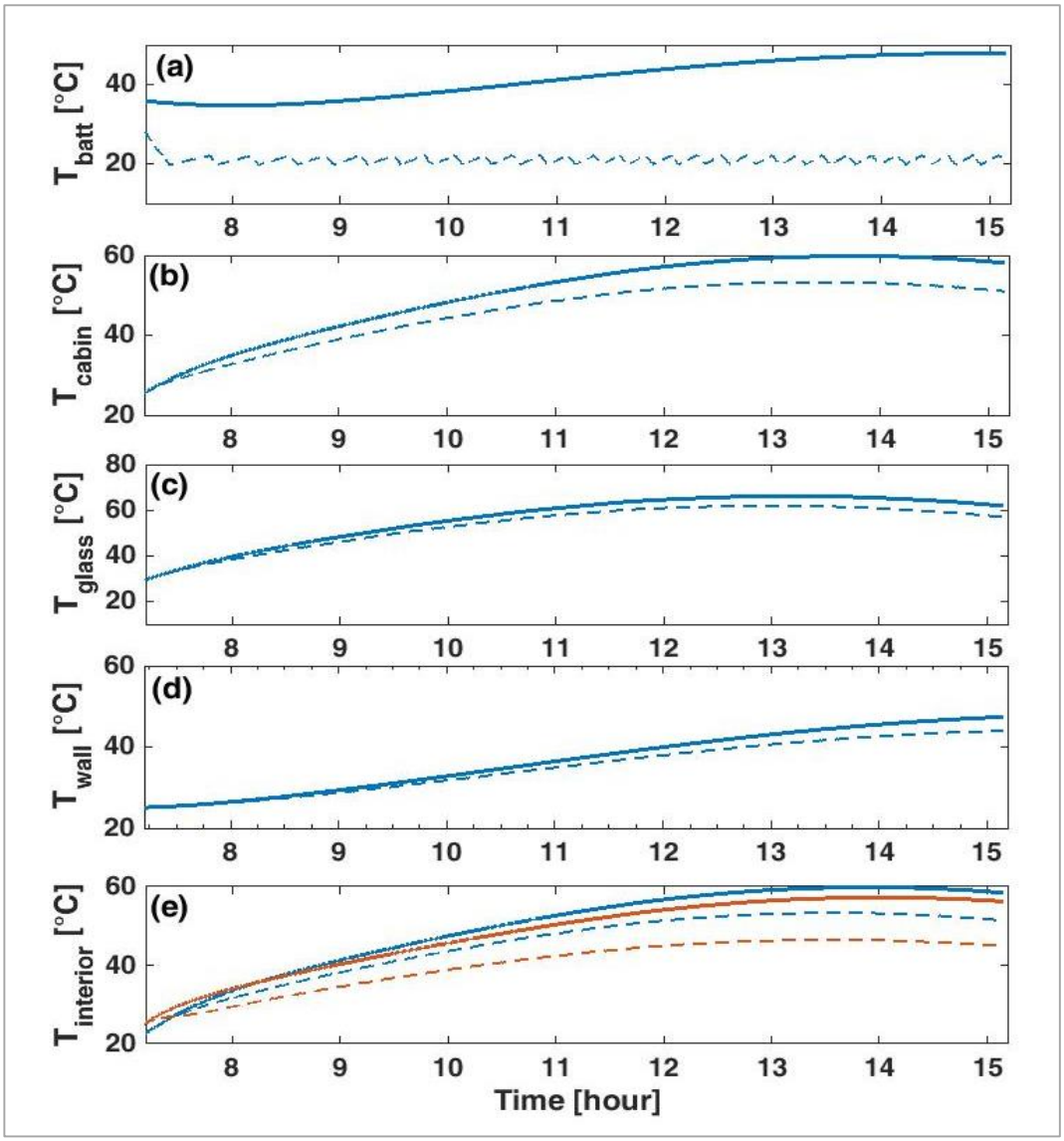

Figure A2-2 The effect of cooling the battery (in Day Park) on the temperature of cabin components. ***Annotations: the continuous lines are related to the case of no cooling while the broken lines represent the case of intense cooling. In (d), the blue and red lines represent the temperature of the upper and lower interior of the cabin, respectively***

The temperature profiles in Figure A2-2 represent the highest and the lowest temperatures that battery and each of the cabin components can assume in Day Park. Therefore, instead forming a higher-order state grid for solving equation (8-5), for any cabin (air) temperature, the temperature of remaining cabin

components were estimated by interpolation between their highest and lowest temperatures.

Appendix 3 Qualitative analysis of the optimisation results for the duty cycle with NEDCx2 trips

A3.1 Optimal control of key-off cooling

In this section, the solution of the optimal control problem defined by equations (9-6) and (9-7) are presented for the scenarios 9-II to 9-VI as defined in Table 9-1. For reference, Figure A3-1 shows the baseline results.

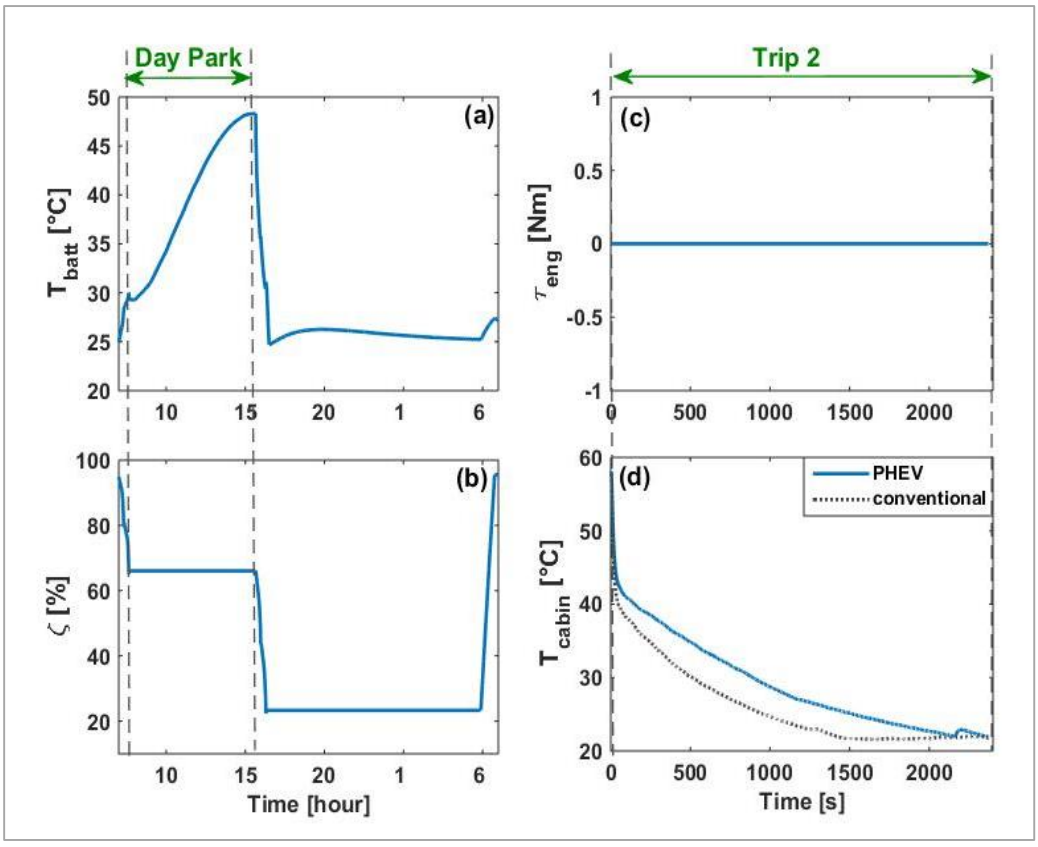

Figure A3-1. PHEV simulation results assuming baseline control strategies and operation in Phoenix summer with two daily trips on the NEDCx2

Scenario 9-II: Control of key-off cooling for improving battery lifetime

Figure A3-2 shows the solution of scenario 9-II, which is qualitatively similar to the results presented in Section 9.2.2. Here, a low battery temperature is maintained throughout Day Park through key-off cooling which uses approximately 40% of the battery charge. The vehicle is forced to operate in CS mode in the second half of Trip 2, implying a significant fuel consumption compared to the baseline scenario. The battery temperature rises to approximately 35°C before the start of Trip 2, therefore the cabin temperature in Trip 2 is only slightly lower than that in the baseline scenario.

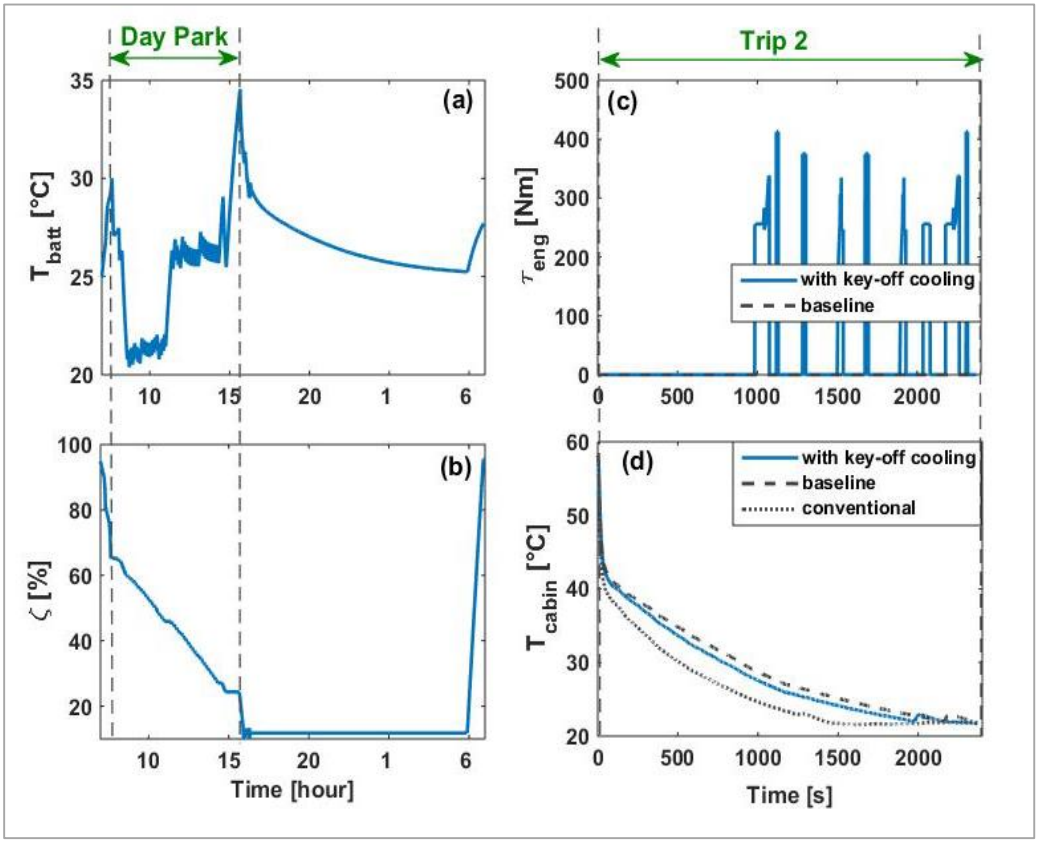

Figure A3-2. Solution of equation (9-6) with NEDCx2 trips and $\boldsymbol{\lambda = \{0, 1, 0\}}$. (a) daily battery temperature, (b) daily SoC, (c) engine torque in Trip 2, and (d) cabin temperature in Trip 2

A3.1.1 Scenario 9-III: Control of key-off cooling based on the trade-off between fuel economy and battery lifetime

When fuel economy and battery lifetime are both of importance, one plausible solution is to limit key-off cooling to the available excess battery charge. Figure

A3-3 shows the result of solving equation (9-6) with λ={0.5,0.5,0}. Here, compared to scenario 9-II, battery temperature is higher in Day Park, as expected, but the vehicle operates in EV mode in Trip 2. Since the battery temperature is allowed to rise before the start of Trip 2, improvements in the cabin temperature are negligible

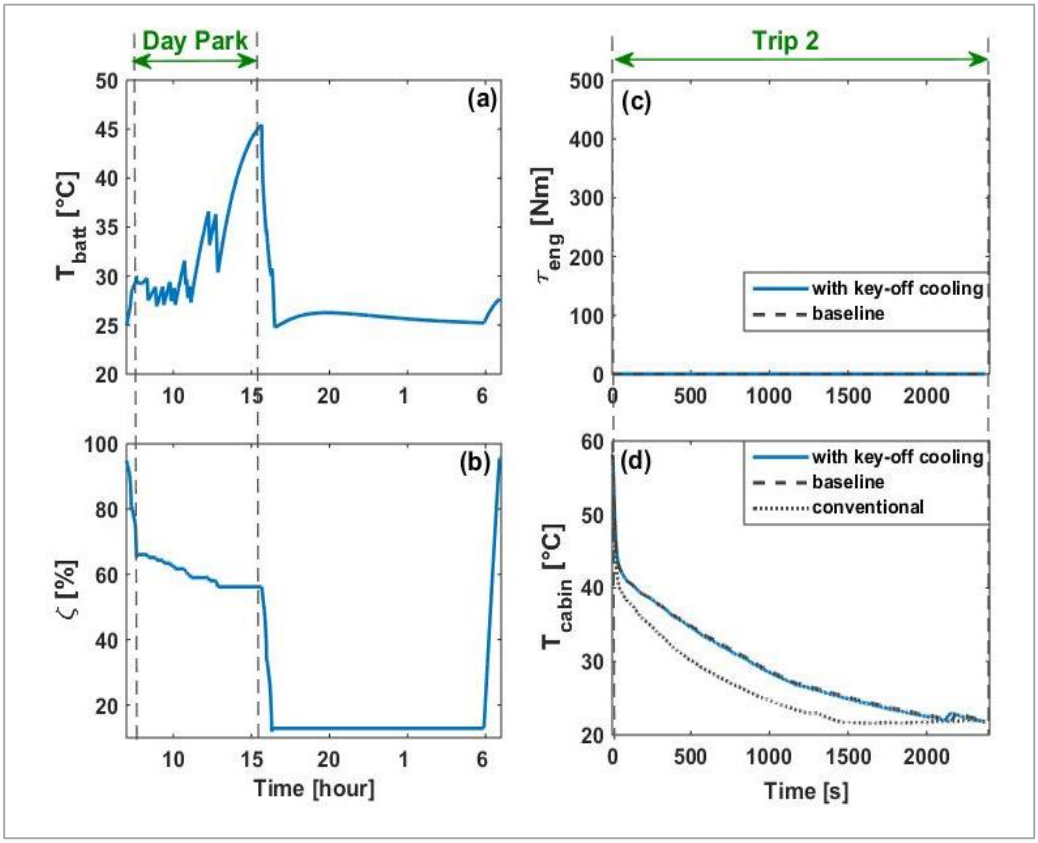

Figure A3-3. Solution of equation (9-6) with NEDCx2 trips and λ={0.5,0.5,0}. (a) daily battery temperature, (b) daily SoC, (c) engine torque in Trip 2, and (d) cabin temperature in Trip 2

A3.1.2 Scenario 9-IV: Control of key-off cooling for improving thermal comfort

Figure A3-4 shows the solution of scenario 9-IV where key-off cooling is limited to pre-cooling for Trip 2. This solution is qualitatively similar to the solution presented in Section 9.3.4. It can be seen that pre-cooling starts well in advance of the trip, consuming approximately 20% of the battery charge to cool the battery and maintain it at approximately 21°C. Pre-cooling shifts the cooling load of the battery in Trip 2 by approximately 1000 seconds. This allows the cabin to cool

down at a similar rate to the equivalent CV. In other words, the discomfort index in the initial 16.7 minutes of Trip 2 is zero, suggesting a lower overall discomfort index and improved thermal comfort. However, the charge allocated to key-off cooling forces the vehicle to enter CS operating mode towards the end of Trip 2.

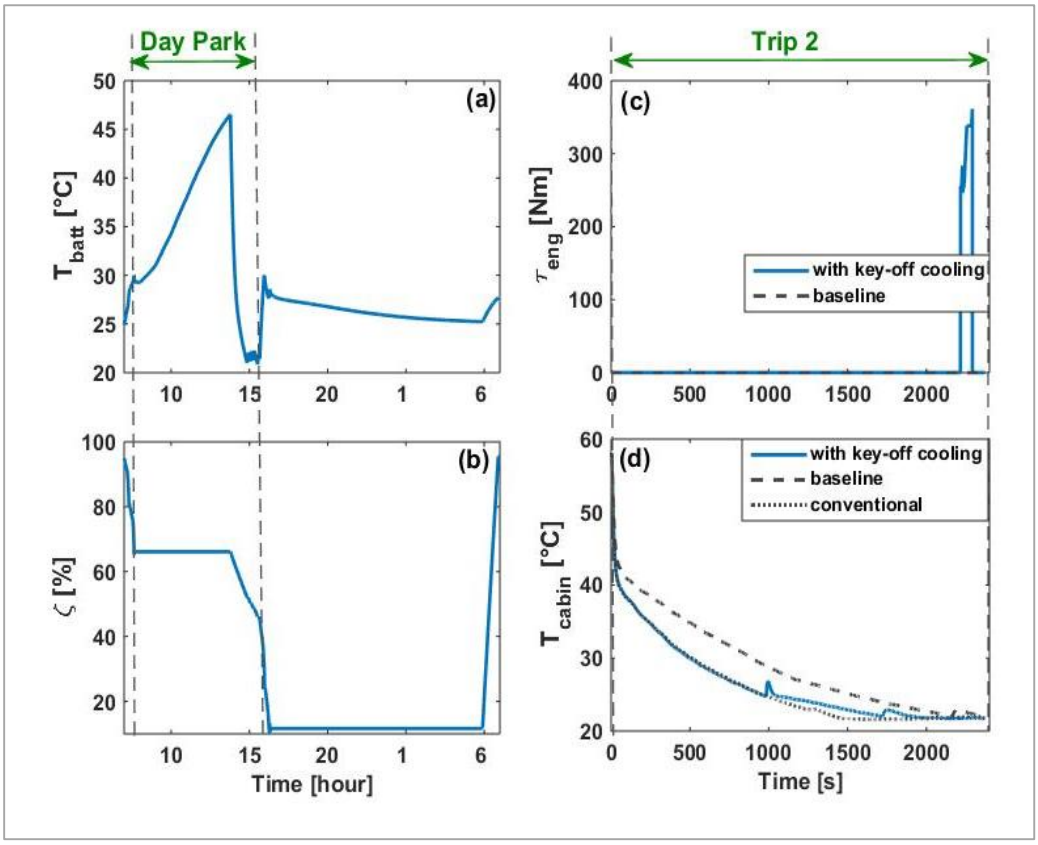

Figure A3-4. Solution of equation (9-6) with NEDCx2 trips and λ={0,0,1}. (a) daily battery temperature, (b) daily SoC, (c) engine torque in Trip 2, and (d) cabin temperature in Trip

A3.1.3 Scenario 9-V: Control of key-off cooling based on the trade-off between fuel economy and thermal comfort

When fuel economy and thermal comfort are both of importance, pre-cooling can be limited by the excess charge of the battery to avoid extra fuel consumption. Figure A3-5 shows the result of solving equation (9-6) with λ={0.5,0,0.5}. Here, pre-cooling starts just before the start of Trip 2. The battery is cooled to 24°C (compared to 21°C in scenario 9-IV), shifting its cooling load by approximately 750 seconds into Trip 2.

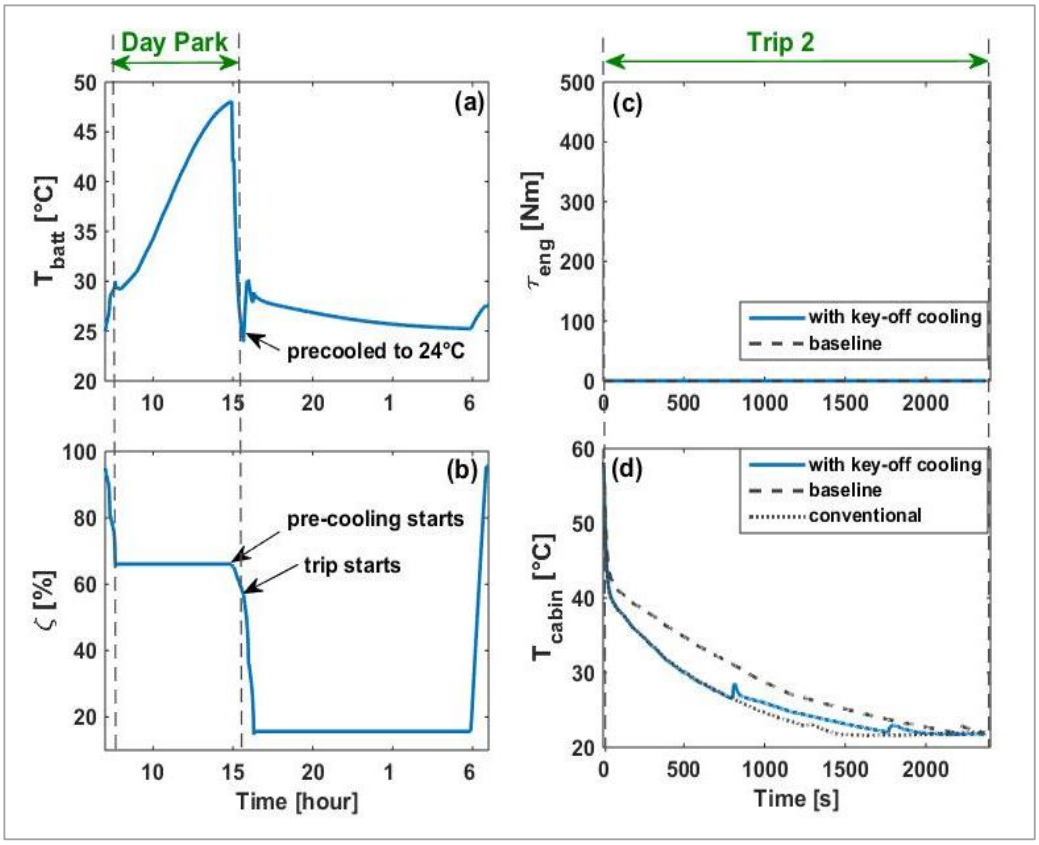

Figure A3-5. Solution of equation (9-6) with NEDCx2 trips and λ={0.5,0,0.5}. (a) daily battery temperature, (b) daily SoC, (c) engine torque in Trip 2, and (d) cabin temperature in Trip 2

A3.1.4 Scenario 9-VI: Control of key-off cooling for improving battery life and thermal comfort

When improving battery lifetime and thermal comfort are of equal importance, optimal control of key-off cooling leads to the results shown in Figure A3-6 which is qualitatively similar to the results presented in Section 9.3.6. It can be seen that approximately 40% of battery charge is allocated to key-off cooling, which is aimed at both maintaining a low battery temperature throughout Day Park and pre-cooling the battery for Trip 2. Compared to scenario 9-IV, the battery is generally warmer here throughout Day Park; pre-cooling starts just in time for Trip 2. As expected, application of key-off cooling has forced the vehicle to operate in CS mode in Trip 2.

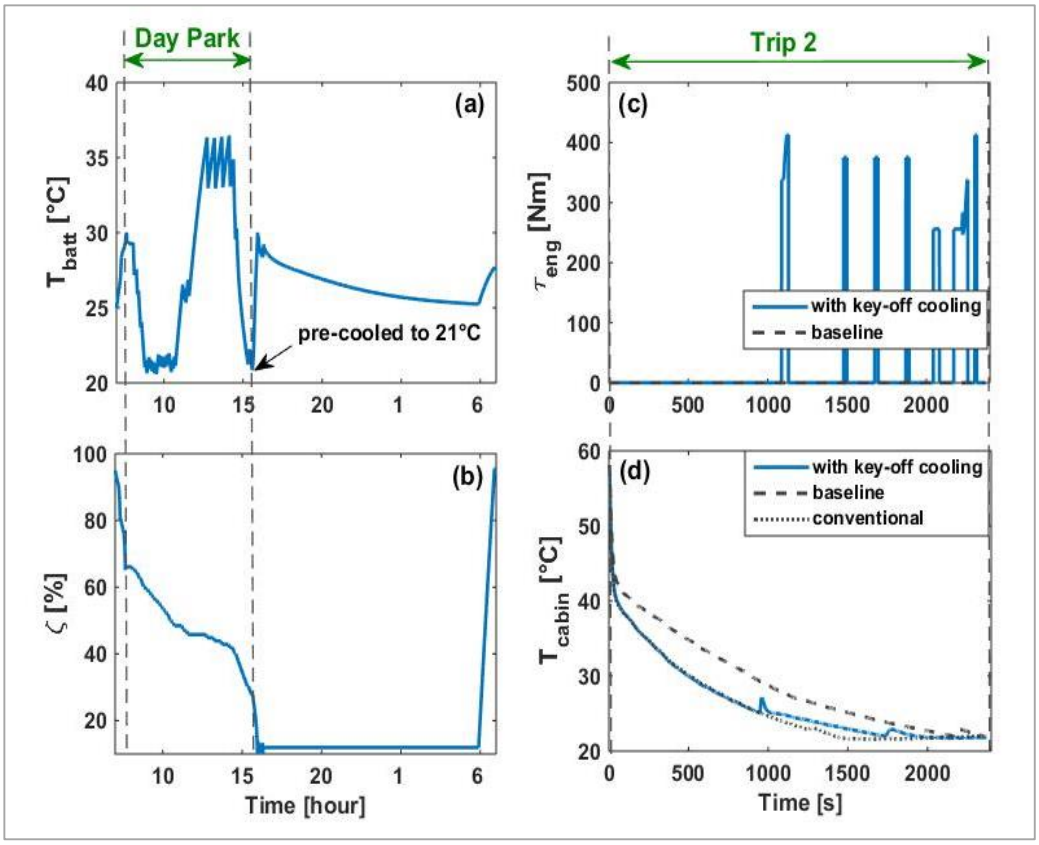

Figure A3-6. Solution of equation (9-6) with NEDCx2 trips and λ={0, 0.5, 0.5}. (a) daily battery temperature, (b) daily SoC, (c) engine torque in Trip 2, and (d) cabin temperature in Trip 2

A3.2 Integrated optimisation of partial charging and key-off cooling

In this section, the solutions of equation (10-5) for the duty cycle with NEDCx2 trips are discussed for scenarios 10-II, 10-III and 10-VI defined As explained in Section 10.3, the lower bound of the level of charge is set to 45% ($45\% \leq \zeta_{max} \leq 95\%$) for this duty cycle to ensure that the operating mode of the vehicle in Trip 1 is not affected by partial charging.

A3.2.1 Scenario 10-II: Control of partial charging and key-off cooling for improving battery lifetime

Figure A3-7 shows the solution of equation (10-5) when battery lifetime is the only attribute of interest (λ={0,1,0}).The battery is charged to 45%, which allows

maintaining a low SoC in Day Park and Night Park. However, this low level of charge disables key-off cooling and forces the vehicle to operate in CS mode in Trip 2. This solution is qualitatively similar to the solution achieved in Section 10.2.1.

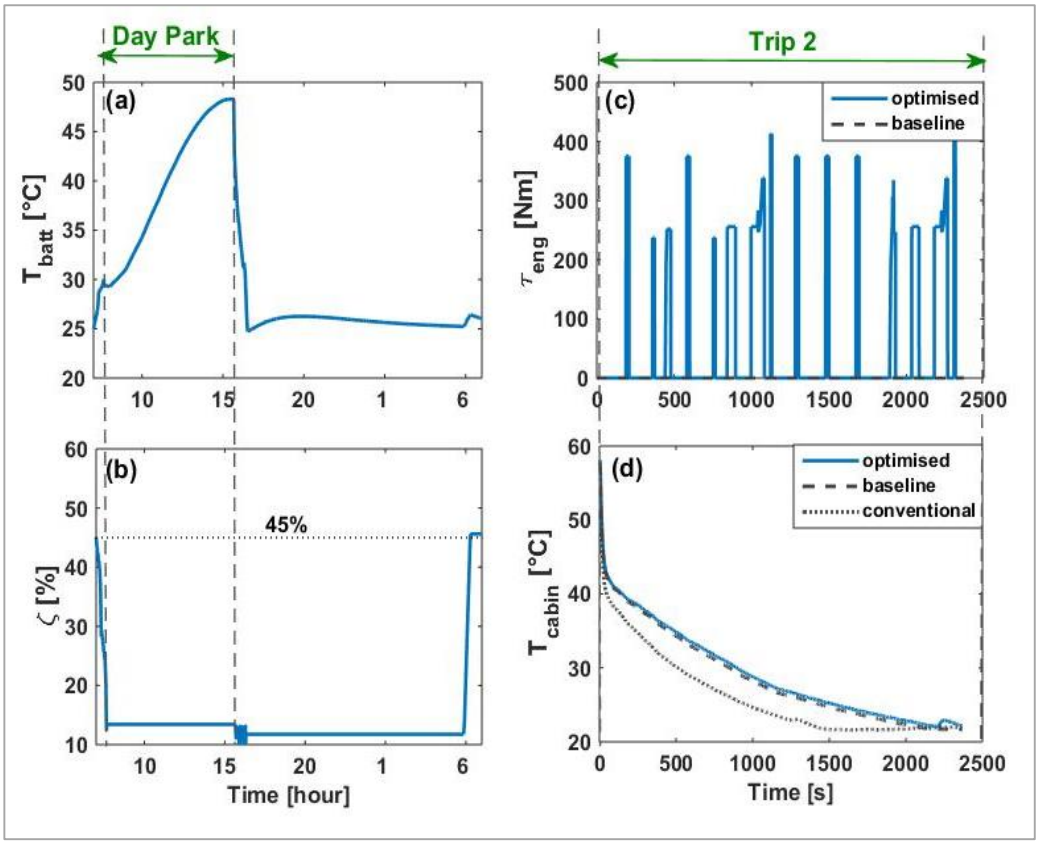

Figure A3-7. Solution of equation (10-5) for the duty cycle with NEDCx2 trips and λ={0,1,0}. (a) daily battery temperature, (b) daily SoC, (c) engine torque in Trip 2, and (d) cabin temperature in Trip 2

A3.2.2 Scenario 10-III: Control of partial charging and key-off cooling based on the trade-off between fuel economy and battery lifetime

Applying a weighting of λ={0.5,0.5,0} to solve equation (10-5) allows no compromise on fuel consumption (compared to the baseline). Therefore, to reduce the capacity loss, partial charging, key-off cooling or a combination of both can be applied within the limit of the excess battery charge (approximately 10%). Figure A3-8 shows that the battery is fully charged in this scenario (contrary to the solution achieved for the duty cycle with US06 trips in Section 10.2.2) so the results are similar to those shown in Figure A6.3 where key-off cooling was

considered for the fully charged battery. This suggests that key-off cooling is more beneficial than a limited partial charging.

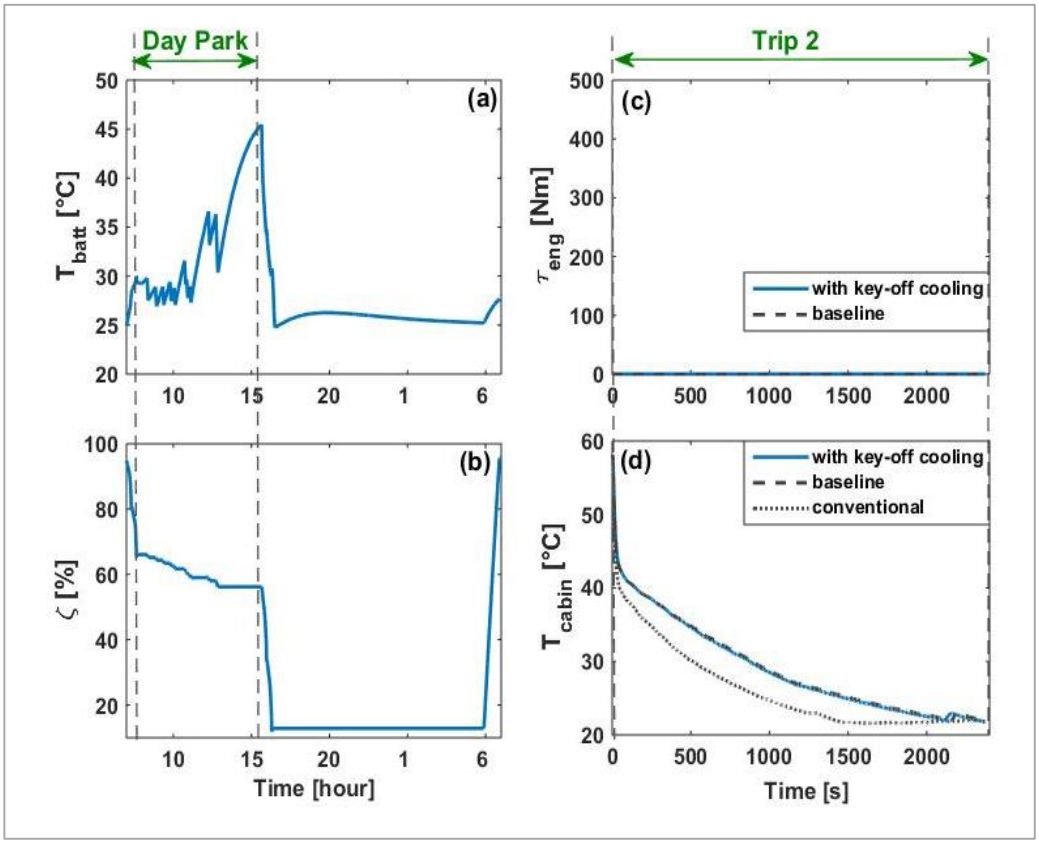

Figure A3-8. Solution of equation (10-5) for the duty cycle with NEDCx2 trips and λ={0.5,0.5,0}. (a) daily battery temperature, (b) daily SoC, (c) engine torque in Trip 2, and (d) cabin temperature in Trip 2

A3.2.3 Scenario 10-VI: Control of partial charging and key-off cooling based on battery lifetime and thermal comfort

Solving equation with λ= {0,0.5,0.5} to consider battery lifetime and thermal comfort leads to the results shown in Figure A3-9 where the battery is charged to 78%. Approximately 22% of this charge is allocated to key-off cooling, including the approximately 14% of charge that is allocated to pre-cool the battery (21°C) for Trip 2. At the start of Trip 2, 25% of the battery charge remains, which is used to drive the vehicle in CD mode in the first 1000 seconds of trip, while the vehicle is forced to operate in CS mode in the remainder of the trip. Also, pre-cooling the battery for Trip 2 allows the cabin to cool down as fast as the conventional vehicle

for 1000 seconds (16.7 minutes). At the end of Day Park, the battery has sufficient charge to support operation in CD mode for approximately 1000 seconds into Trip 2. This operation has been preferred over lower initial battery charge or more key-off cooling.

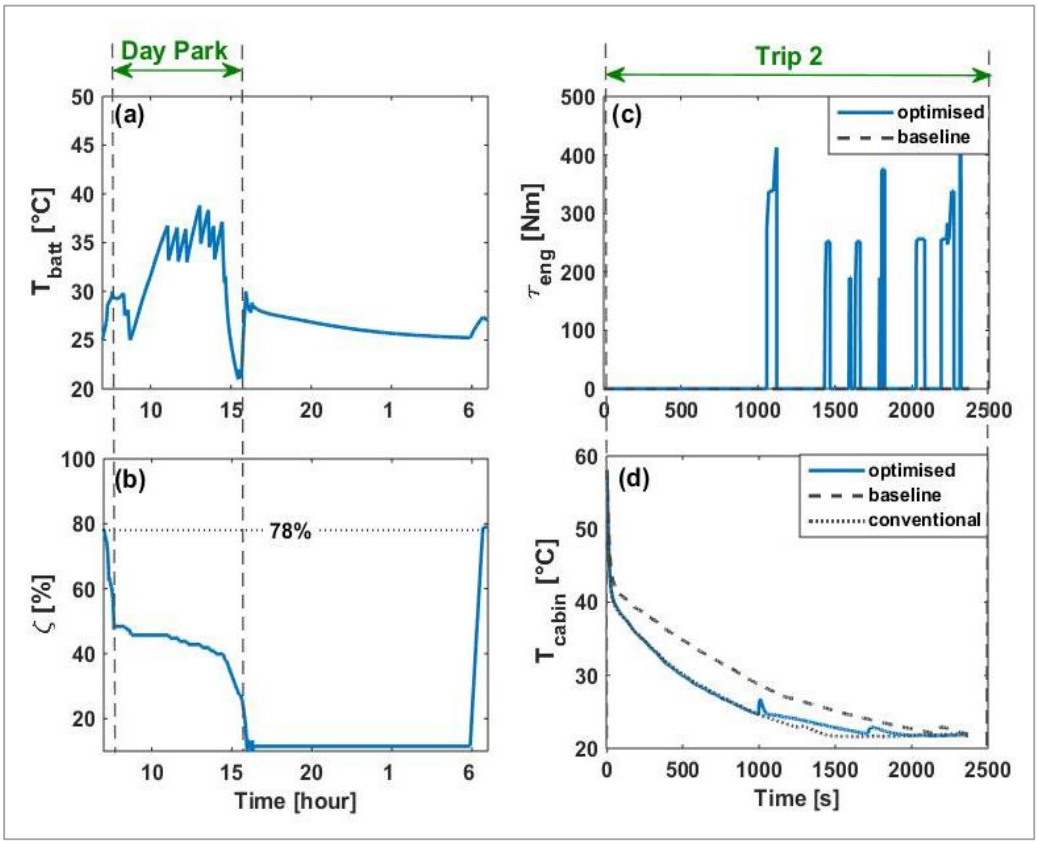

Figure A3-9. Solution of equation (10-5) for the duty cycle with NEDCx2 trips and λ={0,0.5,0.5}. (a) daily battery temperature, (b) daily SoC, (c) engine torque in Trip 2, and (d) cabin temperature in Trip 2

Appendix 4 Introduction to optimal control, Dynamic Programming, and Simulated Annealing

A4.1 The optimal control problem [1]

Consider a dynamic system

$$\dot{x}(t) = f(x(t), u(t), t), \tag{A4.1}$$

in which $x(t) \in R^n$ is the state vector, $u(t) \in R^m$ is the vector of control inputs, while t denotes time. A history of state vectors is referred to as a state trajectory and is denoted by x. A history of control vectors is called a control signal, or briefly a control, and is denoted by u.

The performance of the above system in the interval $[t_0, t_f]$ is evaluated by a cost function (also referred to as a performance measure) such as

$$J = h(x(t_f), t_f) + \int_{t_0}^{t_f} g(x(t), u(t), t)dt, \tag{A4.2}$$

where $h \in R$ and $g \in R$ are referred to as terminal and instantaneous costs. In the above formulation, t_f may be specified or left free, depending on the type of problem. Also x and u should each satisfy relevant constraints to be admissible. In other words, defining U as the set of all admissible control signals and X as the set of all admissible state trajectories, x and u satisfy the following condition

$$\begin{aligned} &u \in U \\ &x \in X. \end{aligned} \tag{A4.3}$$

Starting from the initial state $x(t_0) = x_0$, applying a control signal $u(t)$ causes the system to follow a certain state trajectory. The cost function assigns a unique real

number (cost) to each trajectory of the system. Formally, optimal control in the interval $[t_0, t_f]$ is concerned with finding an admissible control u^* which causes the above system to follow an admissible trajectory x^* that minimises the cost function. u^* is called an optimal control and x^* an optimal trajectory.

Minimising the cost function means that for all $u \in U$ that lead to $x \in X$ we have

$$J^* = \int_{t_0}^{t_f} g(x^*(t), u^*(t), t)dt + h(x^*(t_f), t_f) \leq \int_{t_0}^{t_f} g(x(t), u(t), t)dt + h(x(t_f), t_f) \quad \text{(A4.4)}$$

which states that an optimal control and its state trajectory cause the cost to have a global minimum. If a functional relationship of the form

$$u^*(t) = F(x(t), t) \quad \text{(A4.5)}$$

can be found for the optimal control at time t, the function F is called the optimal control policy (or strategy). Equation (A4.5) implies that the optimal control can be determined at any time t and for any admissible state at time t as a feedback of the state. In contrast, if the optimal control can be only determined as a function of time for a specific initial state, that is,

$$u^*(t) = E(x(t_0), t) \quad \text{(A4.6)}$$

then such optimal control is said to be in open loop form.

Optimal control problems can be categorised based on the form of the assumed cost function. When the aim is to transfer a system from an initial state to a specified target set S with a minimum expenditure of the control effort. For such problems, a cost function of the following form is used:

$$J = \int_{t_0}^{t_f} f(u(t))\, dt \quad \text{(A4.7)}$$

where f defines the expenditure of control effort based on the nature of the problem.

If the interval $[t_0, t_f]$ can be divided to N intervals of Δt seconds and the control input is assumed to be piece-wise constant (changing only at instances $k\Delta t$), the cost function (A4.7) can be written as:

$$J = h_N + \sum_{k=1}^{N} \int_{(k-1)\Delta t}^{\mathrm{k}\Delta t} g(x(t), u_k, t)dt\,, \tag{A4.8}$$

in which $h_N = h(x(t_f))$ is the terminal cost, g is referred toas a the arc cost, while the sum of the arc costs (the second term on the right hand side of the above equation) is referred to cost-to-go. For the problem defined by a cost function in form of (A4.8) , a control policy is defined as $\pi = \{\mu_1, \mu_2, \ldots \mu_{\mathrm{N}}\}$ in which μ_k maps the state $x_k = x(k\Delta t)$ to a control action $u_k = \mu_k(x_k)$. The optimal control policy $\pi^* = \{\mu_1^*, \mu_2^*, \ldots \mu_N^*\}$ gives u^* for any $x_0 = x(0)$.

A4.1.1 Solving the optimal control problem

The optimal control policy can be derived using the Pontryagin's Minimum Principle (PMP) or the method of Dynamic Programming (DP) [1,2]. PMP gives the necessary conditions of optimality and states that any optimal control policy, along with the optimal state trajectory must minimise a Hamiltonian function (a function of the instantaneous objective and constraints) at every instant in time. The mathematical significance of the PMP is that minimising the Hamiltonian of the problem is much easier than solving the original problem [3]. In practice, the PMP is used to generate the set of potential solutions. If the optimal control problem admits a unique solution that satisfies the necessary conditions, then the solution is globally optimal. PMP is especially applicable to energy management of charge-sustaining HEVs due to the uniqueness of the optimal solution [4,5]. DP is commonly used to numerically solve optimal control problems and has a more general applicability to xEVs [6-10]. More details about the DP method are provided in Section A4.2.

A4.1.2 Realisation of the control strategy in xEVs

Based on the information necessary to derive them, control strategies can be categorised as non-realisable and realisable [11,12]. Optimal control is only achievable with *a priori* knowledge of the operation of the system, which is not attainable in real-life for xEVs [13]. From this point of view, control strategies derived from DP and PMP are non-realisable [14]. In addition, a complete definition of the optimal control problem in multifaceted systems such as xEVs will lead to optimisation in high dimension spaces, which can be rather complex [12]. Therefore, significant simplification and abstraction is needed before optimal control techniques can be applied [15]. Nevertheless, solutions to such ideal problems are of interest as they reveal the ultimate limits of performance attributes of the vehicle, providing a benchmark for realizable control strategies [15-17].

Realizable control strategies only require knowledge of the time histories of the variables involved in the decision making process [12]. However, since these strategies are developed with the primary objective of 'realisability', they do not guarantee optimality [4]. Rule-based algorithms derived based on the designers' intuition, or more methodically, based on analysis of global solutions of the optimal control problem are currently the most common method of implementing control strategies in vehicles [18-21]. Some rule-based algorithms are developed offline for a range of scenarios (driving pattern, climate conditions, etc.) to accommodate a degree of real-time adaptability. Examples range from simple switching between different rule sets, to heuristic approaches such as neuro-fuzzy algorithms that can tailor rules to conditions encountered in real-time [22-25]. Methods such as Stochastic Dynamic Programming [26], Model Predictive Control [27], and some other methods inferred from PMP [28], have been proposed for realisable near-optimal control of xEVs.

A4.2 Introduction to Dynamic Programming [1]

Dynamic Programming (DP) is a numerical method for solving complex decision making problems through solving simpler sub-problems, and combining their

solutions to reach an overall solution. DP, which is the only technique capable of solving optimal control problems of any complexity (within the limits of computation), is based on Bellman's principle of optimality:

An optimal policy has the property that whatever the initial states and the initial control actions are, the remaining decisions must constitute an optimal policy with regards to the state resulting from initial decisions.

To explain the theory behind DP, consider a discretized description of the dynamic system in (A4.9)

$$x_{k+1} = f_k(x_k, u_k), \qquad k = 0,1, \dots N-1 \tag{A4.9}$$

where the index k indicates the time step such that $x_k = x(k\Delta t)$ and $u_k = u(k\Delta t)$, where Δt is the length of the time step.

A control policy of the system in (A4.9) is defined as $\pi = \{\mu_1, \mu_2, \dots \mu_{\mathrm{N}}\}$ in which μ_k maps the state x_k to a control decision u_k. The performance measure of this system is of the general form

$$J_\pi = h_N + \sum_{k=0}^{N-1} g_k(x_k, u_k) \tag{A4.10}$$

where h_N and g_k are the terminal and the instantaneous performance measures. The optimal control policy $\pi^* = \{\mu_1^*, \mu_2^*, \dots \mu_N^*\}$ produces the control actions that minimize the cost function (A4.10), that is

$$J^* = J_{\pi^*} = \min_\pi J_\pi. \tag{A4.11}$$

Consider the tail sub-problem of minimizing the cost-to-go from time step *i*, i.e. the total cost from time step i to time step N:

$$J_i = h_N + \sum_{k=i}^{N-1} g_k(x_k, u_k) \tag{A4.12}$$

which leads to the tail optimal policy $\{\mu_i^*, \mu_{i+1}^*, \dots \mu_{N-1}^*\}$, which is the last part of π^*. Bellman's principle of optimality states that the tail policy is optimal for the tail sub-problem. Therefore, to determine the optimal control policy, it is sufficient to calculate the optimal policy for the final time step μ_{N-1}^*, then move to the one-to-the-last time step and calculate the relevant optimal policy μ_{N-2}^* knowing μ_{N-1}^* and J_{N-1}^* from previous step, continuing to the first time step, and combining the solutions to arrive at π^*.

Computing the optimal policy for each time step requires trying all admissible control inputs at each admissible state. To make the computational procedure feasible, it is necessary to quantise the admissible states into a finite number of levels, forming a grid of quantised state values. Similarly, the control inputs should be quantised into a finite number of levels. For example, Figure A4.1 shows the computation process for a system with one state and one control input in which the state is quantized to i levels $(x_1, \dots x_i)$ and the control input to 2 levels (u_1, u_2). Note that the terminal cost h_N is calculated for all i states levels, and the two control levels are tried for all state levels in all previous time steps to calculate the respective arc cost (only shown for x_{i-1}). The boundaries of the state grid act as hard constraints, therefore a heavy penalty is assigned to any control input that leads to breach of the grid boundaries.

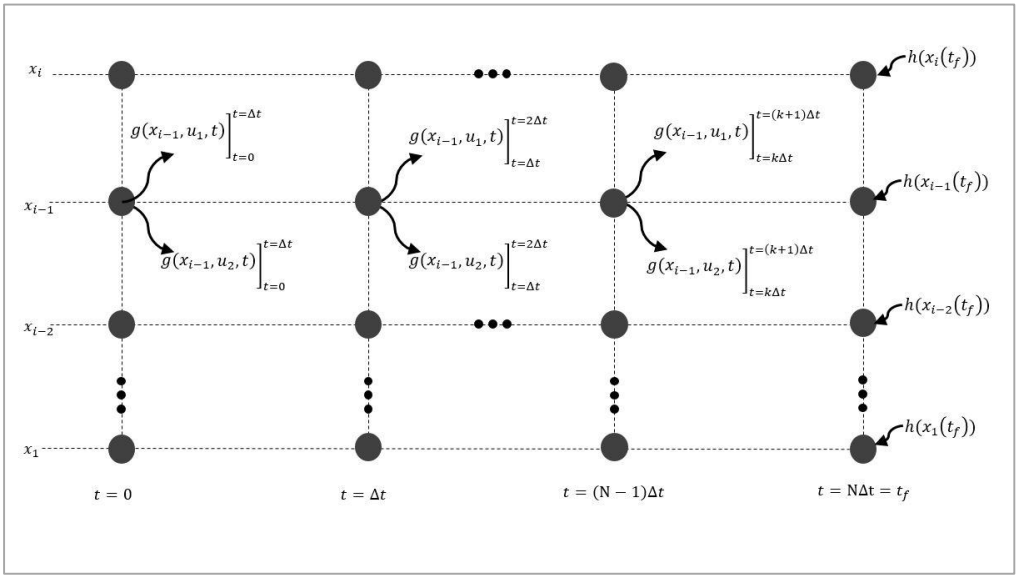

Figure A4-1. DP computational process of a system with one state quantised to *i* levels and one control input quantised to 2 levels.

It is worth noting that the computational effort of DP quickly increases with higher number of states, higher number of control inputs, finer quantization, or finer discretisation of time. For the system with one state and one control input that are quantised to i and two levels respectively, the computation effort over N time steps is $O(N \times i \times 2)$ time. Similarly, for a system with two states and two control inputs, quantizing the states to i levels and the control inputs to n levels leads to a computation effort of $O(N \times i^2 \times n^2)$. Therefore, computational feasibility is an important consideration in using DP.

A4.3 Introduction to the Simulated Annealing method [29]

The Simulated Annealing method (SA) is based on the simulation of thermal annealing of critically heated solids. Thermal Annealing is referred to as tempering certain alloys of metal, glass, or crystal by heating above its melting point, holding its temperature, and then cooling it very slowly until it solidifies into a perfect crystalline structure. When in molten state, the atoms in the metal move freely with respect to each other. However, the movements of atoms get restricted as the temperature is reduced. The defect-free crystal state corresponds to the global minimum energy configuration. The SA simulates the process of slow cooling of molten metal to achieve the minimum function value in a minimization problem.

The SA is a descent algorithm modified by random ascent moves in order to escape local minima. SA is basically composed of two stochastic processes: one process for the generation of solutions and the other for the acceptance of solutions. The cooling phenomenon of the molten metal is simulated by introducing a temperature-like parameter and controlling it using the concept of Boltzmann's probability distribution. The Boltzmann's probability distribution implies that the energy (E) of a system in thermal equilibrium at temperature T is distributed probabilistically as

$$P(E) = e^{\frac{-E}{KT}}, \tag{A4.13}$$

where $P(E)$ denotes the probability of achieving the energy level E, and k is called the

Boltzmann's constant. Equation (A4.13) implies that at high temperatures the system has nearly a uniform probability of being at any energy state; however, at low temperatures, the system has a small probability of being at a high-energy state. This indicates that when the search process is assumed to follow Boltzmann's probability distribution, the convergence of the simulated annealing algorithm can be controlled by controlling the temperature T. The Boltzmann's probability distribution can be implemented by using the Metropolis algorithm. In case of minimising a function, let the current design point be X_i , with the corresponding value of the objective function given by $f_i = f(X_i)$. Similar to the energy state of a thermodynamic system, the energy E_i at state X_i is given by

$$E_i = f_i = f(X_i) \tag{A4.14}$$

Then, according to the Metropolis criterion, the probability of the next design point X_{i+1} depends on the difference in the energy state or function values at the two design points given by

$$\Delta E = E_{i+1} - E_i = \Delta f = f_{i+1} - f_i = f(X_{i+1}) - f(X_i) \tag{A4.15}$$

The new state or design point X_{i+1} can be found using the Boltzmann's probability distribution:

$$P[E_{i+1}] = \min\left\{1, e^{-\frac{\Delta E}{KT}}\right\} \tag{A4.16}$$

The Boltzmann's constant serves as a scaling factor in the SA and is often set to 1, for simplicity. When $\Delta E \leq 0$, that is, when the value of the function decreases by moving from X_i to X_{i+1}, equation (A4.16) gives $P[E_{i+1}] = 1$, and hence the point X_{i+1} is always accepted. This is a logical choice in the context of minimization of a function. On the other hand, when $\Delta E > 0$, the value of the function increases by moving from X_i to X_{i+1}. According to most conventional optimization procedures, the point X_{i+1} cannot be accepted as the next point in the

iterative process. In the SA however, the probability of accepting X_{i+1} is high at high T, and is low at a low T.

The SA algorithm can be summarized as follows. Start with an initial design vector $X1$ (iteration number $i = 1$) and a high value of temperature T. Generate a new design point randomly in the vicinity of the current design point and find the difference in function values (Δf). If f_{i+1} is smaller than f_i (with a negative value of Δf), accept the point X_{i+1} as the next design point. Otherwise, when Δf is positive, accept the point X_{i+1} as the next design point only with a probability $e^{-\frac{\Delta E}{KT}}$. This means that if the value of a randomly generated number is smaller than $e^{-\frac{\Delta E}{KT}}$, accept the point X_{i+1}; otherwise, reject the point X_{i+1}. This completes one iteration of the SA algorithm. If the point X_{i+1} is rejected, then the process of generating a new design point X_{i+1} randomly in the vicinity of the current design point, evaluating the corresponding objective function value f_{i+1}, and deciding to accept X_{i+1} as the new design point, based on equation (A4.16) is continued. To simulate the attainment of thermal equilibrium at every temperature, a predetermined number (n) of new points X_{i+1} are tested at any specific value of the temperature T. Once the number of new design points X_{i+1} tested at any temperature T exceeds the value of n, the temperature T is reduced by a prespecified fractional value c ($0 < c < 1$) and the whole process is repeated. The procedure is assumed to have converged when the current value of temperature T is sufficiently small or when changes in the function values (Δf) are observed to be sufficiently small. The SA algorithm is shown as a flowchart in Figure A4-2.

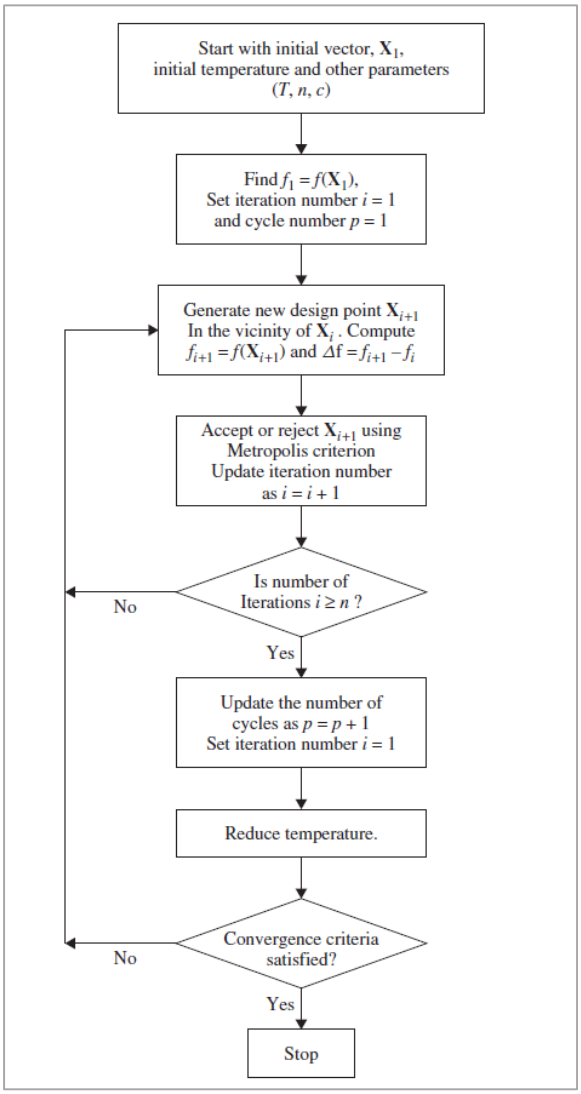

Figure A4-2. Recreated from [29]**: the flowchart of the SA algorithm**

Given a sufficiently large number of iterations at each temperature, SA is proved to converge in probability to the global minima. The choices of the initial temperature T, the number of iterations n before reducing the temperature, and the temperature reduction factor c play important roles in the successful convergence of the SA algorithm. In spite of all the research being done on SA algorithms, making these choices still remains an art and generally requirea a trial-and-error process to find suitable values for solving any particular type of optimization problems.

Some features of the SA make it a strong choice for solving model-based engineering optimisation problems. For example, because of the discrete nature of

the function and constraint evaluations, the convergence or transition characteristics of SA are not affected by the continuity or differentiability of the functions. In addition, the convergence of SA is also not influenced by the convexity status of the feasible design space.

Reference

[1] D.E. Kirk, Optimal control theory: an introduction, Courier Corporation, 2012.

[2] H.P. Geering, Optimal Control with Engineering Applications, Springer, 2007. doi:10.1007/978-3-540-69438-0.

[3] H. Geering, Optimal Control, in: Optim. Control with Eng. Appl., Springer Berlin Heidelberg, 2007: pp. 25–28.

[4] N. Kim, S. Cha, H. Peng, Optimal Control of Hybrid Electric Vehicles Based on Pontryagin's Minimum Principle, IEEE Trans. Control Syst. Technol. 19 (2010) 1279–1287. doi:10.1109/TCST.2010.2061232.

[5] L. Serrao, G. Rizzoni, Optimal control of power split for a hybrid electric refuse vehicle, Proc. Am. Control Conf. (2008) 4498–4503. doi:10.1109/ACC.2008.4587204.

[6] Q. Zhang, S. Stockar, M. Canova, Energy-Optimal Control of an Automotive Air Conditioning System for Ancillary Load Reduction, IEEE Trans. Control Syst. Technol. 24 (2016) 67–80. doi:10.1109/TCST.2015.2418322.

[7] M. Shams-Zahraei, A.Z. Kouzani, S. Kutter, B. Bäker, Integrated thermal and energy management of plug-in hybrid electric vehicles, J. Power Sources. 216 (2012) 237–248. doi:10.1016/j.jpowsour.2012.05.055.

[8] R. Johri, W. Liang, R. McGee, Hybrid Electric Vehicle Energy Management With Battery Thermal Considerations Using Multi-Rate Dynamic Programming, in: ASME Dyn. Syst. Control Conf., 2013: pp. 1–10. doi:10.1115/DSCC2013-4050.

[9] M. Debert, T.M. Padovani, Implementation of comfort constraints in dynamic programming for hybrid vehicle energy management, … J. Veh. …. (2012).

[10] S. Zhang, R. Xiong, Adaptive energy management of a plug-in hybrid electric vehicle based on driving pattern recognition and dynamic programming, Appl. Energy. 155 (2015) 68–78. doi:10.1016/j.apenergy.2015.06.003.

[11] A.A. Malikopoulos, Supervisory Power Management Control Algorithms for Hybrid Electric Vehicles: A Survey, in: IEEE Trans. Intell. Transp. Syst., 2014.

[12] B. Sampathnarayanan, Analysis and Design of Stable and Optimal Energy Management Strategies for Hybrid Electric Vehicles, Ohio State University, 2012.

[13] H. Waschl, I. Kolmanovsky, M. Steinbuch, L. Del Re, Optimization and

Optimal Control in Automotive Systems, Springer, 2014. doi:10.1007/978-3-319-05371-4.

[14] L. Serrao, A Comparative Analysis of Energy Management Strategies for Hybrid Electric Vehicles, Ohio State, 2009.

[15] E.D. Tate, S.P. Boyd, Finding Ultimate Limits of Performance for Hybrid Electric Vehicles, in: SAE Tech. Pap., 2000. doi:10.4271/2000-01-3099.

[16] J. Pu, C. Yin, Optimal control of fuel economy in parallel hybrid electric vehicles, Proc. Inst. Mech. Eng. Part D J. Automob. Eng. 221 (2007) 1097–1106.

[17] L. Guzzella, A. Sciarretta, Supervisory Control Algorithms, in: Veh. Propuls. Syst. Introd. to Model. Optim., Springer, 2007.

[18] C.-C. Lin, H. Peng, J.W. Grizzle, J.-M. Kang, Power management strategy for a parallel hybrid electric truck, Control Syst. Technol. IEEE Trans. 11 (2003) 839–849.

[19] C. Rostiti, S. Stockar, M. Canova, A Rule-Based Control for Fuel-Efficient Automotive Air Conditioning Systems, in: SAE Int., 2015. doi:10.4271/2015-01-0366.Copyright.

[20] D. Kum, H. Peng, N. Bucknor, Supervisory Control of Parallel Hybrid Electric Vehicles for Fuel and Emission Reduction, ASME 2011 Dyn. Syst. Control Conf. 13 (2011) 553–560.

[21] D. Kum, Modeling and optimal control of Parallel HEVs and Plug-in HEVs for Multiple Objectives, The University of Michigan, 2010.

[22] H. Khayyam, A. Bab-Hadiashar, Adaptive intelligent energy management system of plug-in hybrid electric vehicle, Energy. 69 (2014) 319–335.

[23] N.A. Kheir, M.A. Salman, N.J. Schouten, Emissions and fuel economy trade-off for hybrid vehicles using fuzzy logic, Math. Comput. Simul. 66 (2004) 155–172.

[24] Y. Zhu, Y. Chen, G. Tian, H. Wu, Q. Chen, A four-step method to design an energy management strategy for hybrid vehicles, in: Am. Control Conf., IEEE, 2004: pp. 156–161.

[25] Z. Chen, C.C. Mi, J. Xu, X. Gong, C. You, Energy Management for a Power-Split Plug-in Hybrid Electric Vehicle Based on Dynamic Programming and Neural Networks, IEEE Trans. Veh. Technol. 63 (2014) 1567–1580.

[26] E.D. Tate, J.W. Grizzle, H. Peng, SP-SDP for fuel consumption and tailpipe emissions minimization in an EVT hybrid, IEEE Trans. Control Syst. Technol. 18 (2010) 673–687.

[27] M. Shahverdi, M. Mazzola, S. Abdelwahed, M. Doude, D. Zhu, MPC-based power management system for a plug-in hybrid electric vehicle for relaxing battery cycling, in: IEEE Transp. Electrif. Conf. Expo, 2016: pp. 1–6.

[28] B. Gu, G. Rizzoni, An adaptive algorithm for hybrid electric vehicle energy management based on driving pattern recognition, in: ASME 2006 Int. Mech. Eng. Congr. Expo., American Society of Mechanical Engineers, 2006: pp. 249–258.

[29] S. Rao, Modern Methods of Optimization, in: Eng. Optim. Theory Pract., 4th ed., John Wiley & Sons, 2009. doi:10.1002/9780470549124.